Improving X-ray CT Dimensional Metrology with Simple Holeplates

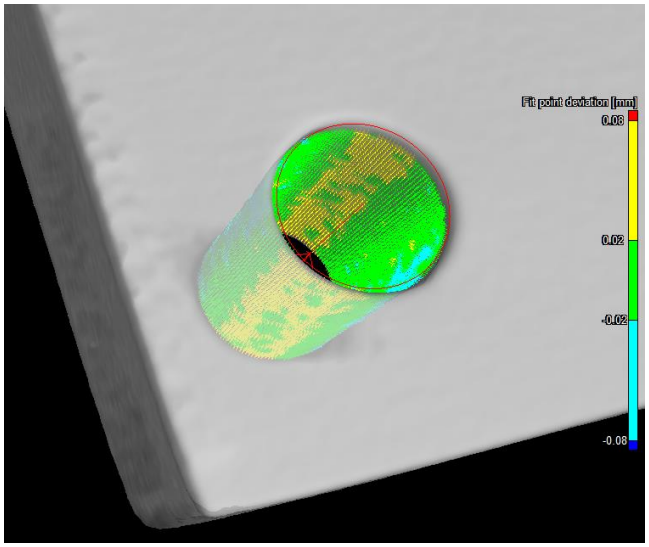

Hannah Clare Corcoran

Department of Civil, Environmental and Geomatic Engineering,
University College London

Supervisors: Professor Stuart Robson, Professor Robert Speller,
Mr Stephen Brown and Professor Michael McCarthy

Thesis for the Degree of Doctor of Engineering (EngD)
Virtual Environments, Imaging and Visualisation

2018

Declaration of Authorship

I, Hannah Clare Corcoran, confirm that the work presented in this thesis is my own. Where information has been derived from other sources, I confirm that this has been indicated in the thesis.

Signed……

Date ……..

In fide et in bello fortis

Abstract

X-ray computed tomography (XCT) is increasingly being used for the internal and external dimensional measurement of objects in many sectors. However, multiple factors affect the accuracy and precision of these dimensional measurements. Initial work found errors associated with the intensity and spectrum of the X-ray flux, both spatially and temporally over the imaging period. These variables were measured using a single ionisation chamber, an ionisation chamber array and a spectrometer, and their effects on dimensional metrology are discussed.

The main focus of this work is on the apparent surface deformation of the reconstructed holes within a holeplate. Measurements of a complex holeplate with multiple holes highlighted systematic deformations in the reconstructed geometry (± 60 µm) for a 2 mm radius hole. Observed systematic deformation patterns were correlated with holeplate orientation. The simplification needed to understand the problem was achieved through practical testing and numerical simulation of simple holeplates, each containing a single hole. Similar trends in the systematic deformation patterns between complex and simple holeplates were found with deformations in the geometry of ±30 µm for a 2 mm radius hole. Algorithms using a ray tracing method were used to simulate X-ray images which were subsequently reconstructed. Results had the same trends in deformation as the experimental data but were of a smaller magnitude, probably due to scatter not being modelled in the simulation.

Systematic deformation in the reconstructed geometry of the holes is caused by multiple factors: the orientation of the holeplate during imaging; the largest errors (<60 µm) were found when the holeplate was orientated at 45° to horizontal. The path length of the X-rays through the material and errors of <40 µm highlighted a correlation between the hole and the centre of rotation. Understanding these factors is essential to traceability in dimensional measurements using XCT.

Impact Statement

X-ray computed tomography (XCT) is increasingly being used in multiple sectors for the measurement of both external and internal dimensions in a variety of objects. As yet, these measurements are not traceable to the SI unit, the metre. This does not allow the user to have complete confidence in the results achieved. This in turn limits the size of features that a designer could propose in the knowledge that they could not be accurately measured.

An aluminium complex holeplate is being considered as a reference object for the international standard, ISO10360-11, which is dedicated to coordinate measuring machines that use the principle of X-ray computed tomography and is in the process of being revised. Various measurements will be included in the standard including radii of the holes and bidirectional lengths.

A similar holeplate along with four simple holeplates (with dimensions of 48 mm x 48 mm x 8 mm) were used in this study to highlight factors that cause apparent systematic deformation of the holes (nominal diameter 4 mm) in the reconstructed volume. These errors could pose particular issues with some of the measurements in the standard. However, as proven in this thesis, due to the systematic nature of the errors (such as the deformation due to the orientation of the object during imaging), the errors could be accounted for and corrected.

Acknowledgements

I would firstly like to thank all my supervisors for their support and guidance over the last four years. To Stuart Robson, for his seemingly endless knowledge on so many subjects, his confidence in me and his reassuring words that I will be able to “close the circle”. To Stephen Brown for his experimental knowledge and thirst for finding the answer (along with all the banter in the office and lab). To Robert Speller for his experience and ceaseless knowledge of X-rays and their behaviour; and last but not least to Michael McCarthy for his metrology knowledge and continued supervision after the changes at NPL. Thank you all for giving me this opportunity.

To Daniel O’Flynn and Nicholas Calvert (previously of Medical Physics, UCL) for their help with measuring the spectrum of the X-rays, use of their correction code and advice on simulations. To Ian Seaton in the CEGE workshop for his assistance in designing and making the stand for my holeplates. To everyone at NPL for the help with experiments including David Maughan, Ileana Silvestre Patallo and Ilias Billas in the Radiation group, for the loan of, and assistance with, the kit needed for the measurement of the cone beam intensity. To Wenjuan Sun and Nadia Flay for their advice and guidance with the NPL XCT system.

To Andrew Ramsey and David Bates at Nikon Metrology for answering my questions about their XCT system and reconstruction software.

To North Star Imaging for imaging two of my holeplates and for the free trial of their reconstruction software, efX-CT and to Guy Tolley, Sheng Yue and Joseph Schlecht for their help with the imaging and software.

To everyone in the 3DIMPact research group, the high jinks in the office and games nights always kept me entertained. Not forgetting all the birthday cakes and karaoke.

Special thanks to the Sisters of Nazareth; for their constant prayers, encouragement, understanding and patience.

To my dear friends, Anita Soni, Sarah Wise, Ruth Maniscalco and Chris Castell. You are always there for me and are a constant source of support, love and fun in all the antics that we get up to. Sarah, Thursdays are now synonymous with noodles, deep conversations and plenty of laughter. Ruth, you have been a source of calmness and kindness ever since we met in Newman House. Chris, your office does not just offer a comfy sofa but a friendly face and a conversation about something madcap. And, my partner in crime, Anita; who knew that when I worked with you for my MSc project you

would become my best friend. You are my EngD big sister and have always been there to prod me on with encouraging words of advice, I will never be able to thank you enough for your kind generosity.

And finally to my amazing and awesome family to whom I dedicate this thesis. You have been there for me through thick and thin; I could not have done this without you all, I am truly blessed. Mummy and Daddy, I wouldn't be half the person I am if it had not been for you. You have always supported my decisions and been there for me for absolutely everything, from giving advice on different situations to driving me and all my stuff up and down to London. To Lizzie (Sacred Sister #2) and Karl; for all the proof reading and random but useful questions on X-rays and the provision of well needed distractions along the way. I couldn't want for a more wonderful sister and brother-in-law. And to Thomas and Didi; for providing me with plenty of cuddles and for keeping me real! I love you all very much.

Ad Majorem Dei Gloriam, let the next adventure begin.

Glossary

Attenuation coefficient (μ) is a measure of the probability that a photon will interact per unit length for a specific material. The attenuation coefficient is proportional to the half-value layer (HVL) as described below: $\mu = 0.693/HVL$.

Bidirectional length measurement is the distance between two points on an objects surface

Coulomb force is the attraction of two differently charged particles and the repulsion of two particles with the same charge.

Half-value layer (HVL) is the thickness of a given material that will reduce the intensity of an X-ray beam to half its original value.

Ionisation is the process whereby a charged particle interacts with a medium with multiple electrons. As the particle passes by an electron a coulomb force is felt by the electron which causes an electron from the atom to be completely removed. A transfer in energy occurs which results in the velocity of the charged particle decreasing. Only about 1/500th of the particles energy is lost per nucleon (Knoll, 2010), therefore, the charged particle has multiple interactions before it finally stops.

Length measurement error is the discrepancy between a reference length and the measured length

Pair production is the creation of a positron-electron pair and occurs when a photon interacts with an atomic nucleus.

Planarity is defined as the flatness of a measured surface

Probing form error is the difference between the maximum and minimum radii of the measured shape.

Probing size error is the difference between the measured diameter and the reference diameter

Spatial resolution is the distance required between two objects for them to be distinguishable from each other.

Structural resolution is described as the smallest structure that can be measured within the specified error limits.

Thermionic emission is the discharge of electrons from a heated material. The heat allows the electrons to overcome the attractive force that is holding them to the material.

Unidirectional length measurement is the centre to centre distance between two fitted shapes

Table of Contents

Declaration of Authorship 3

Abstract 7

Impact Statement 8

Acknowledgements 9

Glossary 11

Table of Contents 13

List of Figures 20

List of Tables 31

List of Equations 32

Chapter 1: Introduction 33

1.1 Motivation of this research 33

1.2 Objectives of the research 34

1.3 Contributions to knowledge 34

1.4 Thesis outline 35

1.5 User survey 37

1.6 Initial work for MRes: Determination of true threshold 39

1.6.1 Experimental set up 39

1.6.2 Measurements taken 40

1.6.3 Orientation of spheres 41

1.6.4 Results: True threshold 42

1.6.4.1 Orientation of tube with spheres 44

1.7 Publications from this work 46

Chapter 2: State of the art 48

2.1 Introduction to X-ray computed tomography 48

2.1.1 Medicine to industry 49

2.2 Processes involved in imaging with XCT 49

2.2.1 Production of X-rays 52

2.2.1.1 Transmission/ reflection targets 54
2.2.1.2 Focal spot size 54
2.2.1.3 Inverse square law 56
2.2.2 Manipulator 56
2.2.3 X-ray interaction and attenuation 57
2.2.4 Shape of beam 58
2.2.5 Detectors 59
2.2.5.1 Scintillation detector 59
2.2.5.2 Thimble ionisation chamber 60
2.2.5.3 Ionisation chamber array 61
2.2.5.4 X-ray spectrometer 61
2.2.6 Image reconstruction 61
2.2.6.1 Filtered back projection 62
2.2.6.2 Feldkamp algorithm 63
2.2.7 Surface determination 64
2.2.7.1 ISO50 threshold 64
2.2.7.2 Gradient based edge detection 65
2.3 Artefacts 65
2.3.1 Beam hardening 65
2.3.2 Anode heel effect 66
2.3.3 Partial volume effect 67
2.3.4 Scattering 67
2.4 Workflow of data processing for this project 68
2.4.1 Shading correction 68
2.4.2 Reconstruction 68
2.4.2.1 Beam hardening correction 71
2.4.3 Surface determination 71
2.4.4 Registration 73
2.4.5 Shape fitting 74

2.5 Simulation packages 75
2.5.1 XCT simulation 75
2.5.2 X-ray spectrum simulation 75
2.6 Traceability and international standards 75
2.7 Critical factors affecting the MPE of XCT systems 79
2.7.1 X-ray source 79
2.7.1.1 Focal spot 80
2.7.1.2 Inherent filtration of source 80
2.7.1.3 Instability of flux 80
2.7.1.4 Temperature and humidity 81
2.7.2 Scattered radiation 81
2.7.3 System geometry and alignment 81
2.8 Reference objects 81
2.8.1 Complex holeplate 82
2.8.2 Beam hardening 84
2.8.3 Surface determination 85
2.8.4 Position of feature in object 86
2.8.5 Orientation of object 86
2.8.6 Magnification 87
2.8.7 Feldkamp effect 89
2.8.8 Noise 90
2.9 How industry is affected 91
Chapter 3: X-ray field variations and their effects on metrology 94
3.1 Temporal measurement of X-ray flux 94
3.1.1 Constant kV and µA 96
3.1.2 Varying kV, constant µA 99
3.1.3 Varying µA, constant kV 100
3.2 Spatial measurement of X-ray flux 102
3.2.1 Repeatability of data 109

3.2.2 Measuring flux with different voltages and currents 111
3.3 Measurement of X-ray energy spectrum 119
3.3.1 Data correction 123
3.3.2 Repeatability 123
3.3.3 Varying voltage 125
3.3.4 Filtered X-ray beam 127
3.3.5 Position in cone beam 128
3.4 Estimation of effect 131
3.5 Chapter summary 131
Chapter 4: Object related effects on metrology 133
4.1 Complex holeplate 133
4.2 Imaging of holeplates 134
4.2.1 Magnification 135
4.2.2 System settings 136
4.2.3 Volume alignment 139
4.2.4 Measurements 139
4.2.4.1 Lengths 139
4.2.4.2 Fit point deviations 139
4.2.4.3 Key to graphs 141
4.2.5 Lengths 145
4.2.6 Cylinder radii 148
4.2.7 Geometry 149
4.3 Simple holeplates 150
4.3.1 Repeatability 151
4.3.2 Fixing during imaging 153
4.3.3 Movement in between measurements 155
4.3.4 Amount of material – path length 156
4.3.4.1 Circular holeplate 156
4.3.4.2 HP1 and HP5 160

4.3.5 Beam hardening correction 163
4.3.6 Asymmetry 164
4.3.6.1 Inverse square law 166
4.3.7 NSI data 167
4.3.8 Orientation during imaging 169
4.3.9 Magnification 173
4.4 Error interactions 175
4.5 Chapter summary 176
Chapter 5: Simulation of X-ray images 179
5.1 Initial simulations 179
5.1.1 Results 179
5.2 Development of code 180
5.2.1 Assumptions 181
5.2.2 Steps in the code 182
5.2.3 Modelling polychromatic X-rays 185
5.2.4 Reducing computational time 186
5.2.5 Code verification 187
5.2.5.1 Mesh vs. primitive shapes 187
5.2.5.2 Path length averaging 191
5.2.5.3 Pixel size 195
5.2.5.4 Image comparison 197
5.3 Simulation of X-ray flux variation 201
5.3.1 Results 202
5.3.1.1 Horizontal gradient 204
5.3.1.2 Vertical gradient 205
5.3.1.3 Diagonal gradient 206
5.3.1.4 Temporal variation 206
5.3.2 Discussion 207
5.4 Simulation of holeplates 208

5.4.1 Orientation of holeplate during imaging 208
5.4.2 Amount of material – path length 213
5.4.2.1 Effective energy 217
5.4.3 Complex holeplate 219
5.4.4 Monoenergetic X-rays 225
5.4.5 Alignment of experimental components 226
5.4.6 Holeplate away from centre of rotation 227
5.4.7 Artefacts in CiHPSim deviations at 0° orientation 229
5.5 Discussion 231
5.6 Potential correction 234
5.7 Impact of simulation 234
5.8 Chapter Summary 235
Chapter 6: Conclusions and further work 237
6.1 Contributions to knowledge 238
6.2 Novelty 242
6.3 Link to International Standard and recommendations 244
6.4 Further work 246
References and bibliography 248
Appendices 259
Appendix 1: System specifications 259
Nikon XTH 225 M 259
NSI X5000 260
Perkin Elmer XRD Detector 260
Appendix 2: Complex holeplate 261
Appendix 3: Orientation 267
Simple holeplates imaged at 45° 267
Simple holeplates imaged at 90° 268
Appendix 4: Repeatability 269
Appendix 5: MATLAB code 270

Appendix 6: Image intensity gradient..... 276
Appendix 7: Survey results..... 278
Appendix 8: ISO report..... 281

List of Figures

Figure 1.1 XCT uses in industry 37
Figure 1.2 XCT industrial user's priorities 38
Figure 1.3 Greatest limitation in XCT for users 38
Figure 1.4 Spheres in tube (Corcoran, 2014) 40
Figure 1.5 Setup of spheres in tube. D_1 and D_2 represent different densities (Corcoran, 2014) 40
Figure 1.6 Measurements taken of spheres 41
Figure 1.7 Graph to determine the true threshold (Corcoran, 2014) 41
Figure 1.8 A foam block was used to hold the tube at varying orientations (Corcoran, 2014) 42
Figure 1.9 Difference in distances between pairs of Nylon and Acetal spheres for varying arbitrary thresholds 43
Figure 1.10 Difference in distances between pairs of Acetal and Polypropylene spheres for varying arbitrary thresholds (Corcoran, 2014) 43
Figure 1.11 Profile taken down image (green line) and results plotted on graph (top of image to the left of the graph) 44
Figure 1.12 As the orientation of the spheres increases the path length of the X-rays through the spheres increases 44
Figure 1.13 Variation in threshold for sphere pairs and different orientations 45
Figure 2.1 Schematic of layout of XCT system 50
Figure 2.2 Workflow for XCT showing some of the common file formats that are used during the process 51
Figure 2.3 Schematic of X-ray tube (Nikon Metrology, 2014) 52
Figure 2.4 Bremsstrahlung radiation production. V_1 and V_2, velocity before and after deceleration of electron 52
Figure 2.5 Characteristic radiation production 53
Figure 2.6 Spectrum for Tungsten target 54
Figure 2.7: Target types, transmission (a) and reflection (b) 54
Figure 2.8 Penumbra size with respect to focal spot size 55
Figure 2.9 Reflection target with angled edge to dissipate heat and narrow the electron beam. Tilt angle: Φ 55
Figure 2.10 Metal jet anode from Excillum uses a jet of metal flowing at very high speed (Excillum, 2015) 56
Figure 2.11 Schematic of the inverse square law. As the distance from the source doubles, the area across which the intensity is spread increases by a factor of 4 56

Figure 2.12 Dominant X-ray interaction depends on X-ray energy and atomic number of material (Evans, 1955) 57
Figure 2.13 Relationship between intensity and thickness of material where I is transmitted intensity, I_0 is the incident intensity, μ is the attenuation coefficient at a given energy (E) and t is the thickness of the material for a single line integral 58
Figure 2.14 Shape of beam and subsequent detector shape (a) cone beam, (b) fan beam and (c) Helical scanning. GE speed|scan CT 64 (GE Measurement and Control, 2013) 59
Figure 2.15 Schematic of a scintillation detector 60
Figure 2.16 Schematic of an ionisation chamber. Based on Johns and Cunningham, 1983 61
Figure 2.17 Back-projection schematic. Description seen below 62
Figure 2.18 Intensity profile before (top) and after (bottom) of ramp filter based on figures from (Smith, 1997) 63
Figure 2.19 Only data in the torus shape will be collected if Tuy-Smith conditions are not met 63
Figure 2.20 Determination of ISO50 using a histogram of voxel greyscale values 64
Figure 2.21 Greyscale across a uniform water phantom (Barrett & Keat, 2004) 66
Figure 2.22 Streaks visible in the image of a heat exchanger (Lifton, Malcolm & Mcbride, 2013) 66
Figure 2.23 Anode heel effect and amount of beam hardening in the three X-ray path lengths 67
Figure 2.24 Partial volume effect 67
Figure 2.25 Screenshot of the CT Pro interface. A 2D image can be seen on the right 69
Figure 2.26 Five step workflow of CT Pro 69
Figure 2.27 Screenshot of VGStudio Max after a volume has been imported. Images to the left and top middle are 2D sections through the volume. The 3D volume can be seen at the bottom 72
Figure 2.28 Area containing background selected (red and yellow box) 72
Figure 2.29 Area containing material selected (yellow box) 73
Figure 2.30 Histogram of greyscale values for background and material 73
Figure 2.31 Stages of registration of holeplate volume (grey) (a) imported CAD model (pink) (b) Simple registration (c) Best fit registration 73
Figure 2.32 Deviation of fit points from determined surface and fitted cylinder 74
Figure 2.33 Fitting of reference object (a) red points chosen by user (Exaggerated size for ease of viewing) (b) all points used by software to fit cylinder 74

Figure 2.34 NIST standard SRM 2087. The PTFE spheres have diameters of 5.556 mm and 7.144 mm (National Institute of Standards & Technology, 2012) 76
Figure 2.35 Test objects along with measurements taken by Kraemer et al., (2017) ... 79
Figure 2.36 Direction of unidirectional and bidirectional measurements 82
Figure 2.37 NIST reference object. Holeplate containing spheres in each hole (NIST, 2018) 83
Figure 2.38 Comparison of volume and STL for iron holeplate simulated with polychromatic X-rays (Kasperl et al., 2014) 84
Figure 2.39 2D projection of a steel pin in steel step gauge (Tan et al., 2014) 85
Figure 2.40 Glass fibre array by Carmignato et al., (2009) 85
Figure 2.41 Reference object used (a) and different distances that are heavily dependent (top) or minimally dependent on the value used to determine the surface (b) (Kiekens et al., 2010) 86
Figure 2.42 Step gauges in various materials (Angel et al., 2015) 86
Figure 2.43 Geometric shapes used in study by Villarraga-Gómez & Smith, (2015). They had dimensions of 60 mm x 20 mm x 40 mm, the holes a radius of 10 mm 87
Figure 2.44 Test objects used by Nardelli et al., (2012) multi-wave standard (a), polyoxymethylene step cylinder (b) and calibrated production workpiece (c) 88
Figure 2.45 Ruby spheres, 5 mm in diameter glued to carbon fibre plate (Müller et al., 2012) 89
Figure 2.46 Circular cone beam (a) and helical scan set up (b) 89
Figure 2.47 Calibrated cube used by Muders et al., (2011) 90
Figure 2.48 Test objects used for interlaboratory comparison (Carmignato, 2012) 90
Figure 2.49 Multiple uses of XCT outputs. CT model, form deviations, porosity and wall thickness plot (clockwise from top left) (Kruth et al., 2011) 91
Figure 2.50 (a) Micro milling cutter and micro holes with diameters of 0.55 mm to 4 mm (De Chiffre et al., 2014). (b) AM injection nozzle (De Chiffre et al., 2014). (c) Aluminium casting (NSI, 2018). (d) Cylinder head (Yxlon, 2016) 92
Figure 2.51 Top: Values of standard tolerance grades (British Standard, 2010). Bottom: Machining processes and IT grades ((Oberg et al., 2016) 93
Figure 3.1 Mean greyscale of images throughout the time of one measurement 95
Figure 3.2 Thimble ionisation chamber (circled) positioned in XCT system at NPL 95
Figure 3.3 Constant kV, constant current for 20 minutes 97
Figure 3.4 Comparison of average output for different voltages 97
Figure 3.5 Normalised output for multiple voltage, constant current 98
Figure 3.6 Ionisation chamber output for varying voltages (with offsets) 98
Figure 3.7 Voltage changed without switching off X-rays, constant current (300 µA) ... 99

Figure 3.8 Comparison of average output for different voltages (80-220 kV)..... 100
Figure 3.9 Ionisation chamber output for various currents, constant voltage (100 kV) 101
Figure 3.10 Comparison of average output for different currents 101
Figure 3.11 Grid layout for chamber position on image 102
Figure 3.12 Output for ionisation chamber in various location in cone beam. Numbers at top specify position (see Figure 3.11). Grey band indicates central location 103
Figure 3.13 Different values used in drift correction 104
Figure 3.14 Corrected output for ionisation chamber at different locations around cone beam for 150 kV 104
Figure 3.15 Corrected output for ionisation chamber measurements at corners for 100 kV, 150 kV and 200 kV 106
Figure 3.16 Contour plot of Corrected output for ionisation chamber measurements at corners for 100 kV, 150 kV and 200 kV..... 107
Figure 3.17 Ionisation chamber array position in XCT system at NPL..... 108
Figure 3.18 Layout of chamber array within the XCT system 108
Figure 3.19 Lead triangle placed in front of array to determine the orientation of the array 109
Figure 3.20 Standard deviation expressed as a percentage of the mean for five repeated measurements for varying voltages. Each square represents an ionisation chamber in the array 110
Figure 3.21 Standard deviation expressed as a percentage of the mean for five repeated measurements for varying currents. Each square represents an ionisation chamber in the array 111
Figure 3.22 Circular wave front of X-rays travelling from source and the subsequent dose captured on detector..... 112
Figure 3.23 Movement of cone beam with focal spot movement..... 113
Figure 3.24 Dose across cone beam for different voltages. Normalised between 0 and 1 (maximum and minimum taken from across all datasets). Each square represents an ionisation chamber array. Dashed line indicates elliptical shape 114
Figure 3.25 Dose across cone beam for different currents. Normalised between 0 and 1 (maximum and minimum taken from across all datasets). Each square represents an ionisation chamber array..... 115
Figure 3.26 Area of cone beam that hits detector, varying voltages. Normalised for each data set. Each square represents an ionisation chamber array..... 117
Figure 3.27 Area of cone beam that hits detector, varying currents. Normalised for each data set. Each square represents an ionisation chamber array Beam filtering 118

Figure 3.28 140 kV and 100 µA with varying thicknesses of copper filter 119
Figure 3.29 Spectral detector positioned between source and detector (top) and close up of spectrometer (bottom) 120
Figure 3.30 Schematic of collimator housing for spectrometer (not to scale) 121
Figure 3.31 Local maxima of number of counts along X, Y and rotational axes of the manipulator 121
Figure 3.32: Comparison of noise for two different measurement durations 122
Figure 3.33 Difference between centre of image and centre of cone beam 122
Figure 3.34 Average of repeated measurements of spectrum at 160 kV. Error bars are standard deviation of the five results 124
Figure 3.35 Comparison of repeated measurements at 160 kV to SpekCalc simulated spectrum 125
Figure 3.36 Spectra for different voltages 126
Figure 3.37 Varying thickness tungsten filters simulated in SpekCalc 127
Figure 3.38 160 keV spectra filtered with differing thicknesses of copper from 0.1 mm to 1.0 mm 128
Figure 3.39 Mean energy for 160 keV spectra filtered with varying thicknesses of copper 128
Figure 3.40 Spectra at the centre at the beginning, the middle and at the end of the position experiment 129
Figure 3.41 Spectra when spectrometer is offset along the Y axis 130
Figure 3.42 Expected variation in spectra depending on amount of target material X-rays have travelled through (I_1 shortest distance, I_2 middle distance, I_3 longest distance) 131
Figure 4.1 Schematic and photo of complex holeplate. Numbers indicate hole number referred to in text 134
Figure 4.2 2D X-ray image of holeplate being imaged at 45° orientation 134
Figure 4.3 NPL's Nikon system (left) and NSI system (NSI, 2017) (right) 135
Figure 4.4 Difference between XCT and CMM distance measurements for ball-bar. 1 is at the top of the image, 5 at the bottom 136
Figure 4.5 Close up view of reconstructed hole in VGStudio Max. Noise within the hole prevents fitting a cylinder confidently. Green points are fit points as described in 4.2.4.2 137
Figure 4.6: Differences between Unidirectional and bidirectional length measurements (Corcoran et al. 2016) 139
Figure 4.7 The orientation of the bearings around the circumference of the cylinder 140
Figure 4.8 Schematic of area from which mean of deviation, bearing and greyscale are taken 140

Figure 4.9 Fit points for HP3 depending on maximum number of fit points used 141
Figure 4.10 Key to radial graphs used in thesis. Mean taken for every 5° interval, scale bars are the standard deviation for points in that interval 142
Figure 4.11 Key to line graphs used in thesis. Mean taken for every 5° interval, scale bars are the standard deviation for interval 142
Figure 4.12 Key to unrolled cylinder graph. Graph based on every fit point used to fit cylinder (black dot on graph) 143
Figure 4.13 Screen shots from VGStudio Max (a) reconstructed holeplate (b) cross section across a hole (c) cross section through two holes. White line indicates defined surface 144
Figure 4.14 Screen shots from VGStudio Max. Unidirectional lengths (a) reconstructed holeplate (b) cross section across a hole (c) cross section through two holes. Red line indicates defined cylinder 144
Figure 4.15 Screen shots from VGStudio Max. Bidirectional lengths (a) reconstructed holeplate (b) cross section across a hole (c) cross section through two holes 145
Figure 4.16 Unidirectional discrepancy results for complex holeplate. Error bars equal to standard deviation of population 146
Figure 4.17 Unidirectional discrepancy results for complex holeplate after scale factor applied 146
Figure 4.18 Bidirectional discrepancy results for complex holeplate. Error bars equal to standard deviation of population 147
Figure 4.19 Cylinder radii, discrepancy between CMM and XCT values. Error bars equal to standard deviation of population (Corcoran et al. 2016) 148
Figure 4.20 Fit point deviations for Cylinders 1, 17 and 19 150
Figure 4.21 Schematic of simple holeplates, HP1, HP3 and HP5 from left to right 151
Figure 4.22 Deviation in geometry for repeated runs of HP3 152
Figure 4.23 Mean of five repeated measurements of HP3. Error bars are standard deviation for each 5° interval for all 5 runs 152
Figure 4.24 Alignment of the centre of the image and centre of rotation was required when the holeplate was being imaged at multiple angles 153
Figure 4.25 Holeplate stand fitted on manipulator in XCT system 154
Figure 4.26 Deformation of HP3 with carbon fibre stand (left) and plastic stand (right) 154
Figure 4.27 Comparison of deformation of HP1. Results show the mean of the five repeated measurements, the error bars are the standard deviation for each of the five results. Left: holeplate remains in stand, right: holeplate taken out and replaced in stand in between each imaging run 155

Figure 4.28 Circular holeplate deviations 156
Figure 4.29 Difference between deviation found for HP3 and CiHP 157
Figure 4.30 Deviations found in HP3 when imaged at 0° 158
Figure 4.31 Path length through holeplate calculated from edge to edge of holeplate (red circles) through centre of hole in question. 72 measurements taken in total at 5° intervals 158
Figure 4.32 Path length of X-rays through holeplate versus deviation with colour coded quadrants for HP3 159
Figure 4.33 Comparison of path length and deviation for HP3 159
Figure 4.34 Deviations found in HP1 when imaged at 0° 160
Figure 4.35 Path length of X-rays through holeplate versus deviation with colour coded quadrants for HP1 161
Figure 4.36 Comparison of path length and deviation for HP1 161
Figure 4.37 Deviations found in HP5 when imaged at 0° 162
Figure 4.38 Path length of X-rays through holeplate versus deviation with colour coded quadrants for HP5 162
Figure 4.39 Comparison of path length and deviation for HP5 163
Figure 4.40 Fit point deviations for HP1exp with the use of different beam hardening corrections 164
Figure 4.41 Comparison of path length and deviation for HP5 (areas described in text) 165
Figure 4.42 Schematic plan view of the voxel position and size at different distances along the cone beam as holeplate rotates 180° 166
Figure 4.43 Cylinder deviations for complex holeplate imaged at NSI 168
Figure 4.44 Fit point deviations for HP1 imaged at NSI 169
Figure 4.45 The three different orientations of the holeplate during imaging 169
Figure 4.46 Deformation in cylinder geometry depending on angle of orientation during imaging 171
Figure 4.47 Vertical profile of path length taken down centre of CiHP from two different imaging angles (see Figure 4.48 for positon of holeplate) 172
Figure 4.48 Position of holeplate discussed above. From the perspective of the detector, looking towards the source. (a) front view (b) back view 172
Figure 4.49 Position of holeplate discussed above. From the perspective of the detector, looking towards the source. (a) Parallel (b) Perpendicular 173
Figure 4.50 Comparison of HP3 imaged with two magnifications (×1.6 and ×5) 174
Figure 4.51 Fit point deviations for CIHP and HP5 imaged at 45° (top) and HP5 imaged at 0° (bottom) 175

Figure 5.1 Fit point deviations when there is variation in intensity across the image (please note the varying scales in the colour bar) 180
Figure 5.2 Single ray represents intensity of pixel as opposed to the whole area in the experimental set up 181
Figure 5.3 Flow diagram of major steps in algorithm for the three functions used in the simulation 182
Figure 5.4 Coordinate system used in MATLAB simulations 184
Figure 5.5 Direction of rotation of holeplate due to rotation matrices Rx (a) and Rz (b) 184
Figure 5.6 Attenuation coefficient for Aluminium 185
Figure 5.7 Simulated spectrum generated in SpekCalc 185
Figure 5.8 Weighting for generated spectrum 186
Figure 5.9 Schematic of 2D image. Path lengths taken from along black central line 187
Figure 5.10 Difference in path lengths between images taken at 0° and 180° 188
Figure 5.11 Difference in path lengths between images taken at 0° and 90° 188
Figure 5.12 Mesh of circular holeplate 189
Figure 5.13 Mesh of circular holeplate with increased number of vertices 189
Figure 5.14 Difference in path lengths between images taken at 0° and 180° 190
Figure 5.15 Path length between images taken at 0° and 90° 190
Figure 5.16 Number of points and spacing used when averaging pixels 191
Figure 5.17 Path lengths at edge of the hole, averaged pixels (green line indicates true edge) 192
Figure 5.18 Path lengths at centre of the hole, averaged pixels 192
Figure 5.19 Cylinders fitted to CiHP termed in this work inside and outside 193
Figure 5.20 Deviation from cylinder of CiHPSim when no pixels are averaged 193
Figure 5.21 Deviation from cylinder of CiHPSim when 4 pixels are averaged 194
Figure 5.22 Deviation from cylinder of CiHPSim when 16 pixels are averaged 194
Figure 5.23 Path lengths at edge of the hole, decreasing pixel size (vertical line indicates true edge) 195
Figure 5.24 Path lengths at centre of the hole, decreasing pixel size 196
Figure 5.25 Deviation from cylinder of CiHPSim with 0.1 mm wide pixels 197
Figure 5.26 Simulated image of HP1. Black border is to show edge of image 198
Figure 5.27 Experimental image of HP1. Black border is to show edge of image 198
Figure 5.28 Profile of the greyscale values through the holeplate in the experimental and simulated images 199

Figure 5.29 Views of reconstructed volume for simulated data (top) and experimental data (bottom). Green line indicates profile from which cross section imaged is viewed 200
Figure 5.30 Greyscale values from profiles taken through reconstructed volumes using simulated and experimental images 201
Figure 5.31 Direction of gradient applied to each image 202
Figure 5.32 No gradient applied to images, average deviation of fit points, inside cylinder (a) outside cylinder (b) 203
Figure 5.33 No gradient applied to images. Fit points of inside and outside fitted cylinders 204
Figure 5.34 Horizontal gradient applied to images, average deviation of fit points, inside cylinder (a) outside cylinder (b) 205
Figure 5.35 Vertical gradient applied to images, average deviation of fit points, inside cylinder (a) outside cylinder (b) 205
Figure 5.36 Diagonal gradient applied to images, average deviation of fit points, inside cylinder (a) outside cylinder (b) 206
Figure 5.37 Different uniform change in intensity applied to each image, average deviation of fit points, inside cylinder (a) outside cylinder (b) 207
Figure 5.38 Average fit point deviations for CiHP imaged at 0° orientation, inside cylinder (a) outside cylinder (b) 208
Figure 5.39 Contour plot of all fit points used for CiHPSim imaged at 0° orientation, inside cylinder (a) outside cylinder (b) 209
Figure 5.40 Average fit point deviations for CiHP imaged at 45° orientation, inside cylinder (a) outside cylinder (b) 210
Figure 5.41 Contour plots of fit points for CiHPSim imaged at an orientation of 45°, inside cylinder (a) outside cylinder (b) 211
Figure 5.42 Contour and profile plot of all fit points used for inside cylinder of CiHPSim imaged at 45° orientation 212
Figure 5.43 Contour and profile plot of all fit points used for outside cylinder of CiHPSim imaged at 45° orientation 213
Figure 5.44 Schematic of holeplates, HP1 (a) and HP3 (b) used in numeric simulations 213
Figure 5.45 Contour plot for HP1Sim of all fit points 214
Figure 5.46 Radial plot showing fit point deviations HP1exp (a) and HP1Sim (b) 215
Figure 5.47 Path length (a) and effective energy (b) for HP1 215
Figure 5.48 Radial plot showing fit point deviations HP3exp (a) and HP3Sim (b) 216

Figure 5.49 Radial plot showing fit point deviations for HP3, both simulated and experimental 216
Figure 5.50 Path length (a) and effective energy (b) for HP3 217
Figure 5.51 Fit point deviation verses effective energy for HP1Sim 218
Figure 5.52 Fit point deviation verses effective energy for HP3Sim 219
Figure 5.53 Fit point deviations for Cylinder 1 experimental (a) and simulation (b).... 220
Figure 5.54 Effective energy for Cylinder 1 in CompHP 220
Figure 5.55 Fit point deviations of cylinder in Cylinder 1 in CompHPSim compared to effective energies around cylinder 221
Figure 5.56 Fit point deviations for Cylinder 17 in CompHP, experimental (a) and simulation (b) 221
Figure 5.57 Effective energy for Cylinder 17 in CompHP 222
Figure 5.58 Fit point deviations of cylinder in Cylinder 17 in CompHPSim compared to effective energies around cylinder 222
Figure 5.59 Fit point deviations for Cylinder 19 both experimental (a) and simulation223
Figure 5.60 Effective energy for Cylinder 19 in CompHP 223
Figure 5.61 Fit point deviations of cylinder in Cylinder 19 in CompHPSim compared to effective energies around cylinder 224
Figure 5.62 Comparison of unidirectional length discrepancy for simulated and experimental results for CompHP. Error bars equal to standard deviation of population 224
Figure 5.63 Fit point deviations for HP3Sim simulated using a monoenergetic X-rays 225
Figure 5.64 Comparison of energy spectrums when used to simulate images of HP3 226
Figure 5.65 Comparison between HP3 with perfect alignment on Z axis compared to a translation of 1 mm 227
Figure 5.66 CiHPSim is positioned 14.5 mm from the centre of rotation 228
Figure 5.67 Radial plots for CiHPSim when imaged off-centre from rotational axis ... 228
Figure 5.68 Position of CiHPSim during rotation. Arrow indicates bearing of 90° where the large deviation seen in Figure 5.67 occurs 229
Figure 5.69 Deviations for inner and outer cylinder fitted to CiHPSim imaged at 0° .. 230
Figure 5.70 Deviations for inner and outer cylinder fitted to CiHPSim. Reconstructed with a 35° initial angle 230
Figure 5.71 Deviations for inner and outer cylinder fitted to CiHPSim when volume rotated 35° in VGStudio Max 231
Figure 5.72 Comparison of fit point deviations for HP1Sim and HP3Sim 232

Figure 5.73 Comparison of HP1 and HP3 for the experimental and simulated data ..233
Figure 5.74 Comparison of Cy1, Cy17 and Cy17 in CompHP for the experimental and simulated data 234
Figure 6.1 Schematic of simple holeplates, HP1, HP3 and HP5 from left to right 239
Figure 6.2 Comparison of simple holeplates experimentally imaged at 0° (with and without error bars).....240
Figure 6.3 Comparison of CiHPExp imaged at different orientations (with and without error bars).....240

List of Tables

Table 1.1 Sphere material and density 39
Table 2.1 Coefficients used in beam hardening correction in this study 71
Table 2.2 National standards and operating procedures 78
Table 3.1 Voltage and current settings for each set up for repeated measurements . 109
Table 3.2 Settings for system for ionisation chamber array measurements 111
Table 4.1 Settings used for different experiments 138
Table 4.2 Mean and standard deviation of deviation in length measurements 147
Table 4.3 Area under fit point deviation graph and radius of fitted cylinders for simple holeplates 163
Table 4.4 Intensity of X-ray energy at each voxel position as seen above 166
Table 4.5 Factors considered in this chapter and the errors observed 176
Table 5.1 Range in data and average of standard deviations for graphs in Figure 5.20, Figure 5.21 and Figure 5.22 195

List of Equations

Equation 1.1 Calculation used in the determination of the true threshold. Difference (d), separation between spheres (S) and radii of spheres one 1(r_1) and 2(r_2) 41
Equation 2.1 Polynomial curve for beam correction. X initial greyscale value, Y equals corrected grey scale and a to f are coefficients that depend on the level of correction chosen by the user..... 71
Equation 3.1: Equation to calculate mean energy of spectrum..... 127
Equation 4.1 Calculation of bearing (θ) around circumference 140
Equation 5.1 Intensity of x-rays $I0$ is equal to original intensity, PL is equal to path length through object and μ is equal to the attenuation coefficient for a given energy and material..... 186
Equation 5.2 Intensity of X-ray where $I0$ is equal to original intensity, w is equal to the spectrum weighting, PL is equal to path length through object and μ is equal to an array containing the attenuation coefficients in 1 keV intervals..... 186
Equation 5.3 Determination of attenuation coefficient for a given length of material .. 217
Equation 5.4 Transformation matrix to move CiHPSim away from the centre of rotation 228

Chapter 1: Introduction

X-ray computed tomography (XCT) is now an important tool in the non-destructive testing sector. Its ability to be able to “see inside” an object and to obtain dimensional measurements of both internal and external features without destruction of the part is unique and is a highly powerful dimensional metrology tool. It is used in an increasingly wide range of sectors including manufacturing, aerospace, automotive, medicine, heritage and geology, imaging a variety of materials such as: metals and plastic castings, additive manufacturing, electrical components, mummies and antiquities. XCT can be used for highlighting defects and voids, reverse engineering and material composition analysis and is increasingly being used for dimensional metrology.

The fundamental purpose of XCT is the reconstruction of a 3D volume from 2D radiographic images. The intensity of the images is based on the transmission and attenuation of X-rays travelling through an object. The physics and algorithms used throughout the whole process will be discussed in Chapter 2.

1.1 Motivation of this research

Dimensional measurements, be it length measurements or geometry comparisons, acquired using XCT are subject to errors that are not fully understood. As yet, the results achieved are not traceable to the metre and are difficult to verify, unlike other systems such as the Cartesian coordinate measuring machine (CMM). A XCT user’s survey was carried out by the author (see Section 1.5) and it highlighted the importance of accurate dimensional measurements for the users. This work, carried out jointly between University College London (UCL) and the National Physical Laboratory (NPL), aims to characterise some of these measurement errors.

Initially the aim of the project was to study the traceability of dimensional measurements on multi-material objects. Preliminary experiments, carried out as part of an MRes that was completed for the EngD process, examined the effect of the threshold choice on dimensional measurements. This experiments indicated that fundamental issues needed to be better understood before looking at multi-material objects. These included the effect of the orientation of the object and the gradient of the X-ray intensity across the image. An outline of these experiments and results can be seen in Section 1.6.

Further to the apparent gradient seen in the intensity of the image the intensity of the X-rays in the cone beam were measured both spatially across the cone beam and temporally throughout the time it takes for a set of images to be acquired.

Parallel to these investigations an aluminium holeplate was being considered as a reference object for the international standard, ISO10360-11. As NPL are participating in the international work to determine traceability of results obtained using XCT, it was decided to image a similar holeplate. Systematic errors were found in the unidirectional and bidirectional length measurements and in the geometry of the holes. These errors appeared to also be related to the orientation of the holeplate during imaging along with the position of the hole within the holeplate. The geometry of the reconstructed holes within the holeplate became the main focus of this research along with the cause of these errors.

1.2 Objectives of the research

The above motivations led to these five main objectives:

- Investigation into the cause of the errors in unidirectional and bidirectional length measurements and geometry of the holes, in particular:
    - The effect of the orientation of the holeplate during imaging
    - The position of the hole within the holeplate
- Simplify the trends seen in the complex holeplate with the use of simple holeplates to understand the cause of the errors
- Simulation of 2D projections of the various holeplates used in the experimental imaging to replicate the errors seen, thereby assisting in the understanding of the cause of the errors and allowing a correction to be calculated
- Investigation into the variation of the X-ray flux, both spatially and temporally on the system at NPL. The spectrum was also to be measured and compared to a simulated spectrum for the same settings as the XCT system
- Variation in intensity across each individual 2D X-ray image, as measured in the X-ray flux investigation, to be applied to simulated images of a cylinder. Effects on dimensional metrology to be studied.

1.3 Contributions to knowledge

Imaging, reconstruction and measurement of the complex holeplate highlighted a variety of systematic trends in the geometry of the different holes within the holeplate. This deformation appeared to be related to both the orientation of the object during imaging and the position of the hole within the holeplate.

Four simple holeplates were designed to simplify these trends. The holes were positioned in the holeplates to create as much imbalance in the material around the hole as possible. Results from these holeplates indicate deformations due to the orientation

of the holeplate of up to 60 µm. The maximum deformation, found at an orientation of 45°, is seen at the top and bottom of the reconstructed cylinders and indicates that the cylinders have an apparent tilt. The position of the hole within the holeplate causes varying trends in deformation to the hole's geometry, the shapes vary from ellipses to star patterns. When results from a circular holeplate were compared to a square holeplate with a single hole in the middle, it can be seen that the path length of the X-rays through the holeplate affects the deformation. This is due to the X-rays have varying effective energies when reaching the detector after passing through the holeplate. The deformation of the holes in the other holeplates appears to be related to the position of the hole with respect to the centre of rotation.

A numerical simulation, which was written by the author in MATLAB, enabled 2D images of the holeplates to be simulated using a ray tracing method. A replication of the experimental system was set up and a polychromatic X-ray spectrum was used. The holeplates were modelled with primitive shapes. Results for the simple holeplates indicated similar systematic deformations when compared to the experimental data but of smaller magnitude. The complex holeplate's results have the same trends in deformation as the experimental data and the errors are of the same magnitude. The simulation also confirmed the theory that more deformation occurs when the feature being measured is away from the centre of rotation. A cause for this is the decrease in X-ray intensity as it travels away from the source; the cross section of an object will be recorded with two different intensities when it is closest and then furthest away from the source.

Detailed monitoring of the X-ray flux was carried out with ionisation chambers and a spectrometer. Results indicate that there is a 10% variation in the intensity both through the period of imaging and across the detector. These results were used in simulated images of a cylinder and the reconstructed volumes showed errors in the reconstructed cylinder geometry of up to 4 µm. The form or pattern that the deviations took depended on the direction of the gradient in the intensity of the 2D images.

1.4 Thesis outline

This thesis is formed of six main chapters, this introductory chapter being the first.

Chapter 2 begins with a description of the XCT workflow in general and also the particulars for this research; from setting up the system to the analysis of the reconstructed volume. The physics and algorithms associated with each step are then discussed. This chapter also includes a review of the current state of the art methods

used to understand and quantify the errors associated with dimensional measurements and XCT.

Chapter 3 is the first of three experimental chapters included in this thesis. It discusses experiments carried out to determine the variation of the X-ray intensity and spectrum. Results indicate that there is a variation in the intensity of the X-rays both over time (2%) and across the cone beam itself (10%).

Chapter 4 focusses on the imaging and analysis of a series of 5 holeplates, all having dimensions of 48 mm x 48 mm x 8 mm. One is a complex holeplate with 28 holes all of which have a nominal diameter of 4 mm. Three are simple holeplates that are based on the complex holeplate but only contain one hole in various positions. The last is a circular holeplate containing a single, central hole. Findings indicate that the geometry of the reconstructed holes show systematic deformation with errors in the region of ±30 µm. The trend in the deformation is dependent on the orientation of the object during imaging with maximum errors of 60 µm being seen at an orientation of 45°. The systematic trends are also affected by the position of the hole within the holeplate and the path length of the X-rays travelling through the holeplate. The magnitude of the errors depends on the magnification at which the holeplate is imaged.

Chapter 5 discusses a numerical simulation written by the author to replicate 2D images generated by an XCT system. The simulation uses a ray-tracing method with the holeplates being modelled using primitive shapes. Images were simulated that replicated intensity variations recorded in Chapter 3, results indicate errors of ±5 µm in the geometry of cylinders with a diameter of 48 mm. Further images of the holeplates were simulated; these highlighted similar systematic trends in the apparent deformation of the holes seen in the experimental data, however, the magnitudes were smaller (<10 µm compared to <30 µm). The deviation is correlated to the effective energy of the X-rays as they pass through the holeplates.

Chapter 6 outlines the contributions of the research to the ongoing international work on traceability of dimensional measurements using XCT. The novel outputs from the thesis are discussed along with the new methods developed throughout the thesis. The chapter also discusses the impact of the findings on the international standard, ISO10360-11, which is currently under review. Further work that could be carried out to continue the investigation into the errors associated with the geometry of objects imaged using XCT along with possible corrections are also considered.

1.5 User survey

In 2015 a XCT user's survey was compiled and distributed to users by the author. It was sent to both industrial and medical users to determine what systems were being used, in what sector and for what purpose. The survey also asked what the user's priorities were when it comes to using XCT, along with any expectations and limitations that they have with their systems. Of the 47 users who completed the survey, 21 were in industry and research and 26 were in medicine. The purpose of the survey was to give an overview of the situation with regards to XCT at that time, i.e. what are people using XCT for and what sort of systems were they using.

The user survey highlighted that the main sectors using XCT, after medical (68%), were the manufacturing (12%), automotive (11%) and aerospace (9%) industries. It was also being used by the electronics and watch industries, geological sciences and by the military/defence sectors. The use of XCT in these industrial sectors can be seen in Figure 1.1.

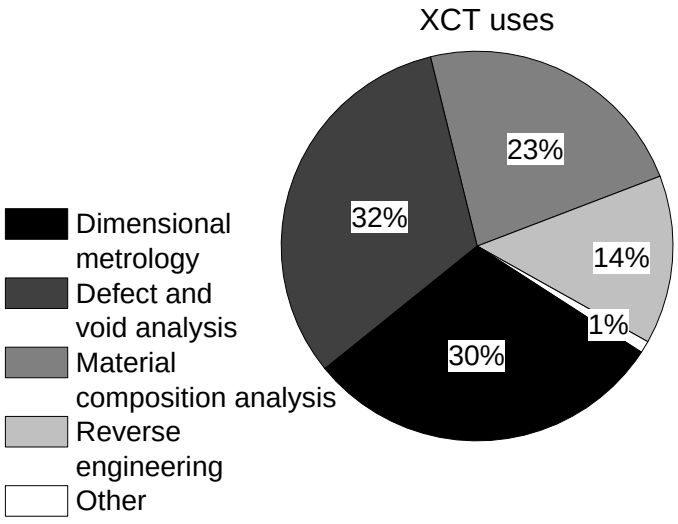

Figure 1.1 XCT uses in industry

The industrial user's priorities can be seen in Figure 1.2, for medical users the main priority (86%) is visualisation for medical diagnosis. It can be that the XCT systems are used predominantly for visualisation, however, it is also used for acquiring dimensional measurements and to compare an object to a CAD model.

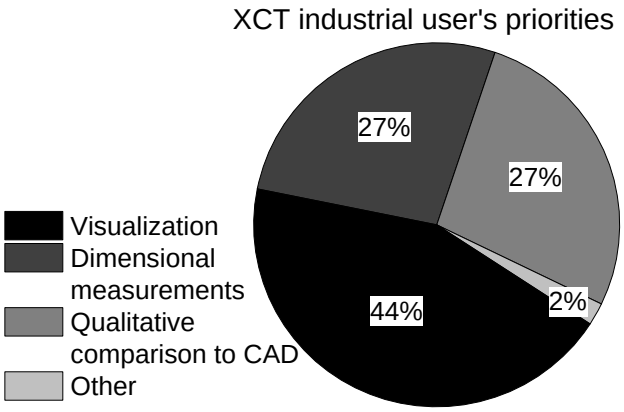

Figure 1.2 XCT industrial user's priorities

Materials imaged using XCT include castings of both metal and plastic, additive manufacturing, geological samples, electrical components and foam.

When the industrial users were asked how important dimensional measurements were to them on a scale of 1 to 5, 1 being not at all important and 5 being very important, the average amongst those who use XCT for dimensional metrology and material composition analysis was 4.3, for defect and void analysis, 4.2 and for reverse engineering, 4.1. This indicates that it is crucial to have accurate dimensional measurements as they are key to XCT users.

For all the users the greatest limitations were found to be beam hardening and noise, see Figure 1.3.

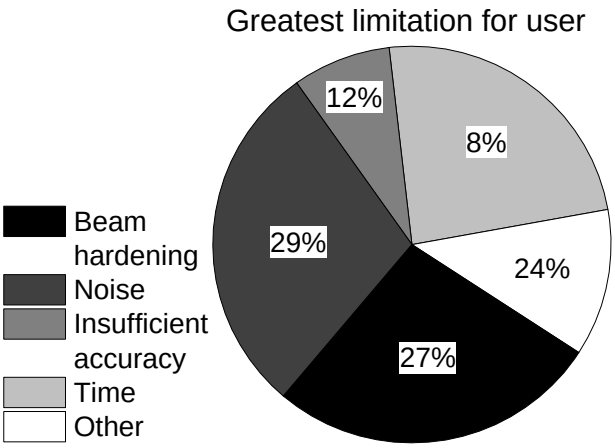

Figure 1.3 Greatest limitation in XCT for users

As the survey showed, XCT is used to image many objects from multiple sectors. Dimensional metrology and comparison to CAD play an important part in the use of XCT which is why it is essential to understand any factors that may affect these results. Both of these uses are dependent on findings in this project as it is predominantly

concentrating on the apparent deformation in the geometry of the imaged object which will, in turn, lead to errors in length dimensions.

All of the questions and results for the survey can be seen in Appendix 7.

1.6 Initial work for MRes: Determination of true threshold

The EngD programme at UCL involves obtaining an MRes in the first year of the 4 year programme, a summary of the work carried out by the author for the MRes is outlined in this section as it highlighted fundamental issues that were researched further in this EngD thesis.

Preliminary experiments were carried out to initially determine the effects of the threshold on dimensional measurements of multi-material objects. This work highlighted that the threshold that provided the correct dimensional measurements varied depending on the location of the object with respect to the position on the detector. The main causes for this were thought to be either due to the flux of the X-rays not remaining stable or errors within the detector.

To ensure correct dimensional measurements, the correct threshold value has to be determined, as described in Section 2.2.7. To determine the true threshold these experiments utilised the geometric relationship between spheres

1.6.1 Experimental set up

Measurements were carried out on four spheres that were placed in a polystyrene tube. The plastic spheres had a nominal diameter of 12 mm and were made of varying types of material, the densities of which varied and can be seen in Table 1.1. All imaging in this chapter was carried out on NPL's XCT system a Nikon XTH 225 M.

Material Type	Abbreviation	Density (gcm^{-3})
Polypropylene	P	0.90-0.92
Nylon	N	1.14
Acetal	A	1.42
Fluoroelastomer	F	1.99
Ruby	R	4.00
Zirconia	Zr	5.68

Table 1.1 Sphere material and density

The spheres were arranged in a polystyrene tube and were held in place with a rubber stopper and foam to prevent any movement during imaging, see Figure 1.4. The lower

sphere was not used in the measurements; it was just used to elevate the spheres and remove them from any scattered X-rays that may be produced from the manipulator.

Figure 1.4 Spheres in tube (Corcoran, 2014)

Spheres with different densities were placed in the tube and were alternated as seen in Figure 1.5

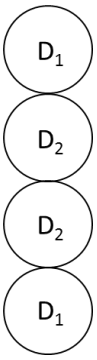

Figure 1.5 Setup of spheres in tube. D_1 and D_2 represent different densities (Corcoran, 2014)

1.6.2 Measurements taken

The geometric relationship between spheres was used to determine the true threshold, this would allow for the correct dimensional measurements to be achieved. Three measurements were taken: the radii of the spheres, the separation between two adjacent spheres and the coordinates of the sphere centres (see Figure 1.6).

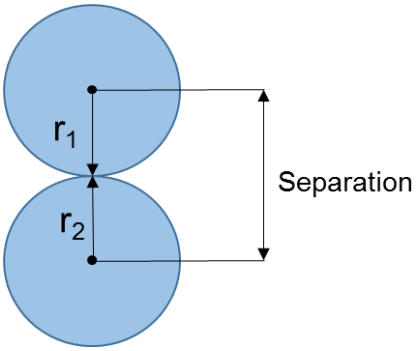

Figure 1.6 Measurements taken of spheres

A threshold was manually chosen in VGStudio Max 2.2 and a surface was fitted to the reconstructed surfaces. See Section 2.4.3 for the processing workflow used. Reference spheres were fitted to the reconstructed spheres and the dimensions noted. The sum of the two radii for the two adjacent spheres was subtracted from the separation of the two spheres (Equation 1.1). The threshold was changed and the process repeated.

$$d = S - (r_1 + r_2)$$

Equation 1.1 Calculation used in the determination of the true threshold. Difference (d), separation between spheres (S) and radii of spheres one 1(r_1) and 2(r_2)

These differences in distance were plotted against the arbitrary threshold on a scatter graph and a line of best fit was drawn. The true threshold lies where the differences in the distances is equal to zero, see Figure 1.7.

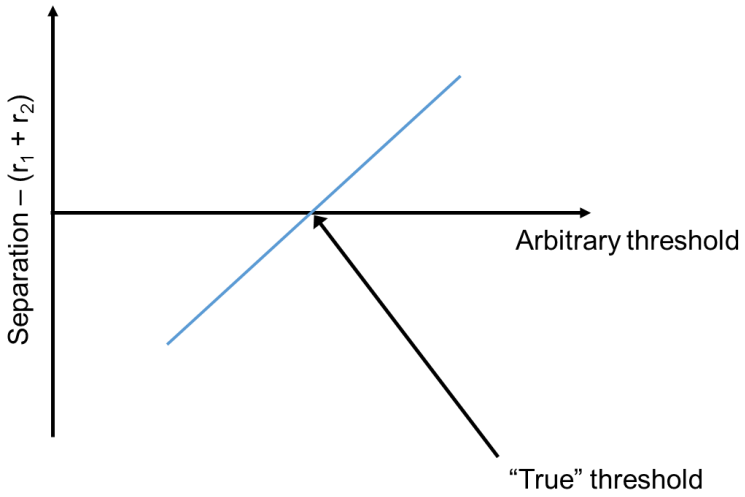

Figure 1.7 Graph to determine the true threshold (Corcoran, 2014)

1.6.3 Orientation of spheres

To determine if the orientation at which the spheres were imaged had any impact on the results, the tube was mounted in a foam block in which holes had been made. The tube

could be fixed at approximately 90°, 75°, 65°, 55° and 40° from horizontal. All of the spheres were made of Fluoroelastomer, this material was chosen as the density is the most different from that of the test tube allowing them to be more easily distinguishable from the test tube when setting the threshold.

Figure 1.8 A foam block was used to hold the tube at varying orientations (Corcoran, 2014)

The spheres were aligned using the manipulator to ensure that the central two spheres were in the centre of the image during rotation.

1.6.4 Results: True threshold

The relationship between the change in threshold and change is size of the object is clear to see in Figure 1.9 and Figure 1.10. As the threshold increases the radii of the spheres is decreasing; effectively removing material from the volume. When comparing the correct threshold between the different sphere pairs it can be seen that the threshold varies depending on the pair, with the top pair of spheres having a lower threshold than the bottom pair.

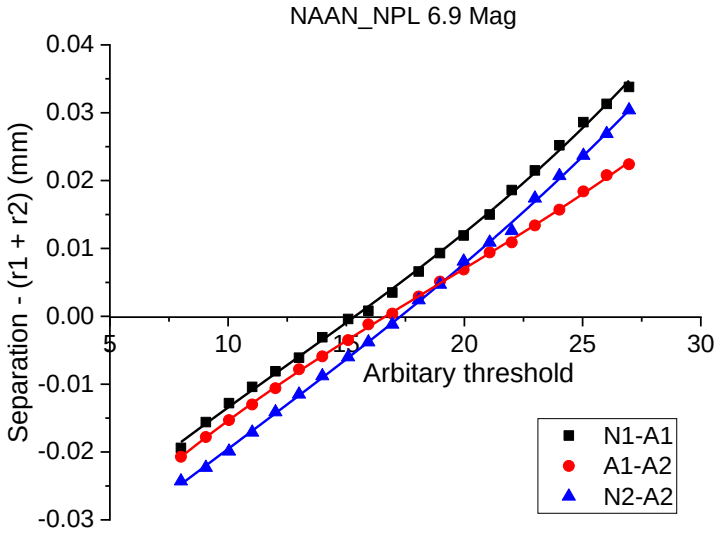

Figure 1.9 Difference in distances between pairs of Nylon and Acetal spheres for varying arbitrary thresholds

This pattern occurs for both set ups where the spheres are of different densities. This indicates that this finding is not related to the actual attenuation of the spheres but the apparent attenuation caused by a variation in the intensity of the 2D image. An increase in the threshold would indicate that the intensity of the image is decreasing down the image.

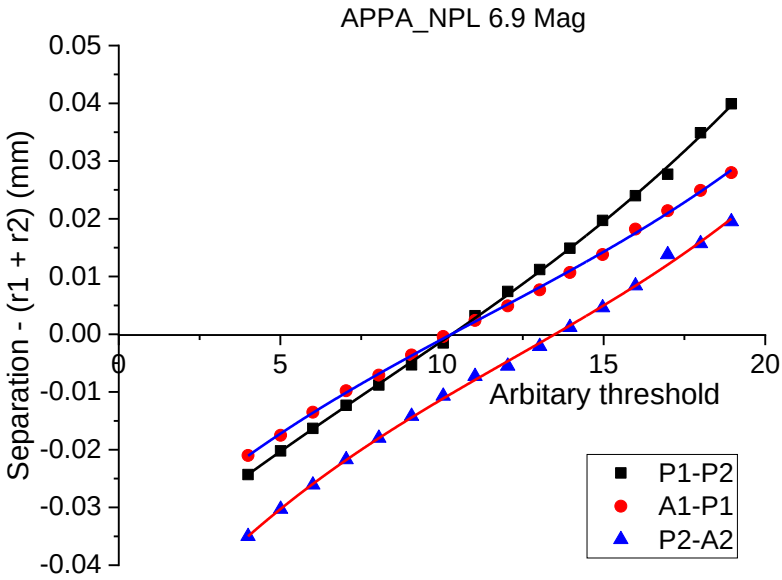

Figure 1.10 Difference in distances between pairs of Acetal and Polypropylene spheres for varying arbitrary thresholds (Corcoran, 2014)

This is confirmed when an image in studied in ImageJ; Figure 1.11 highlights the decrease in greyscale down the image. The profile line was not drawn to the bottom of the image as the foam holder is just visible. The increase in greyscale values, around 1000 pixels on the graph, highlights that the gradient is not constant.

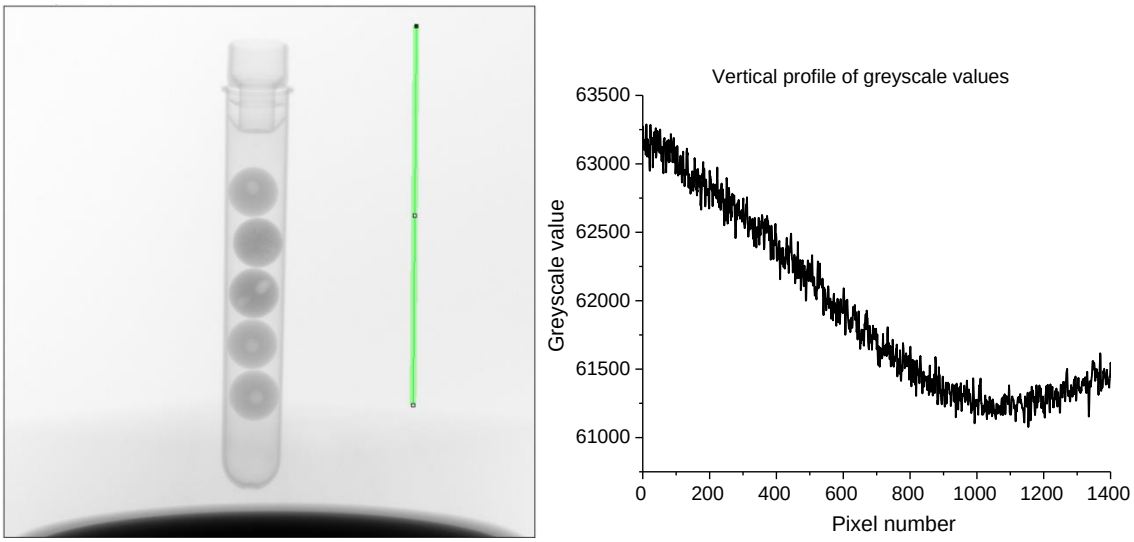

Figure 1.11 Profile taken down image (green line) and results plotted on graph (top of image to the left of the graph)

1.6.4.1 Orientation of tube with spheres

When two pairs of spheres of the same density were imaged at multiple angles it can be seen in Figure 1.13 that the difference in the two thresholds varies depending on the orientation at which they were imaged. The optimum angle, where the thresholds are most similar is found at 65°. Working with the conclusions from the previous results that the change in threshold is due to a change of intensity down the image, the decrease in difference between the thresholds could be due to the fact that the spheres now occupy a smaller area on the detector and therefore the variation does not change so much over a smaller vertical area.

The data becomes noisy and does not follow such a clear trend at an orientation of 55° and 45°, this is due to the X-rays having to travel through more material as the spheres are now sitting in a line in between the source and detector, see Figure 1.12.

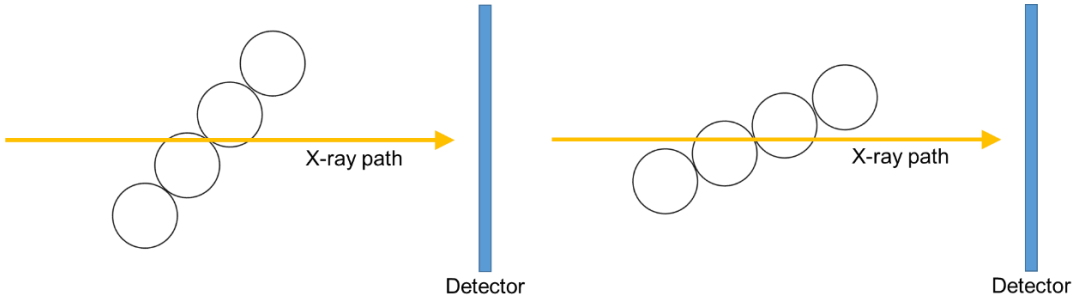

Figure 1.12 As the orientation of the spheres increases the path length of the X-rays through the spheres increases

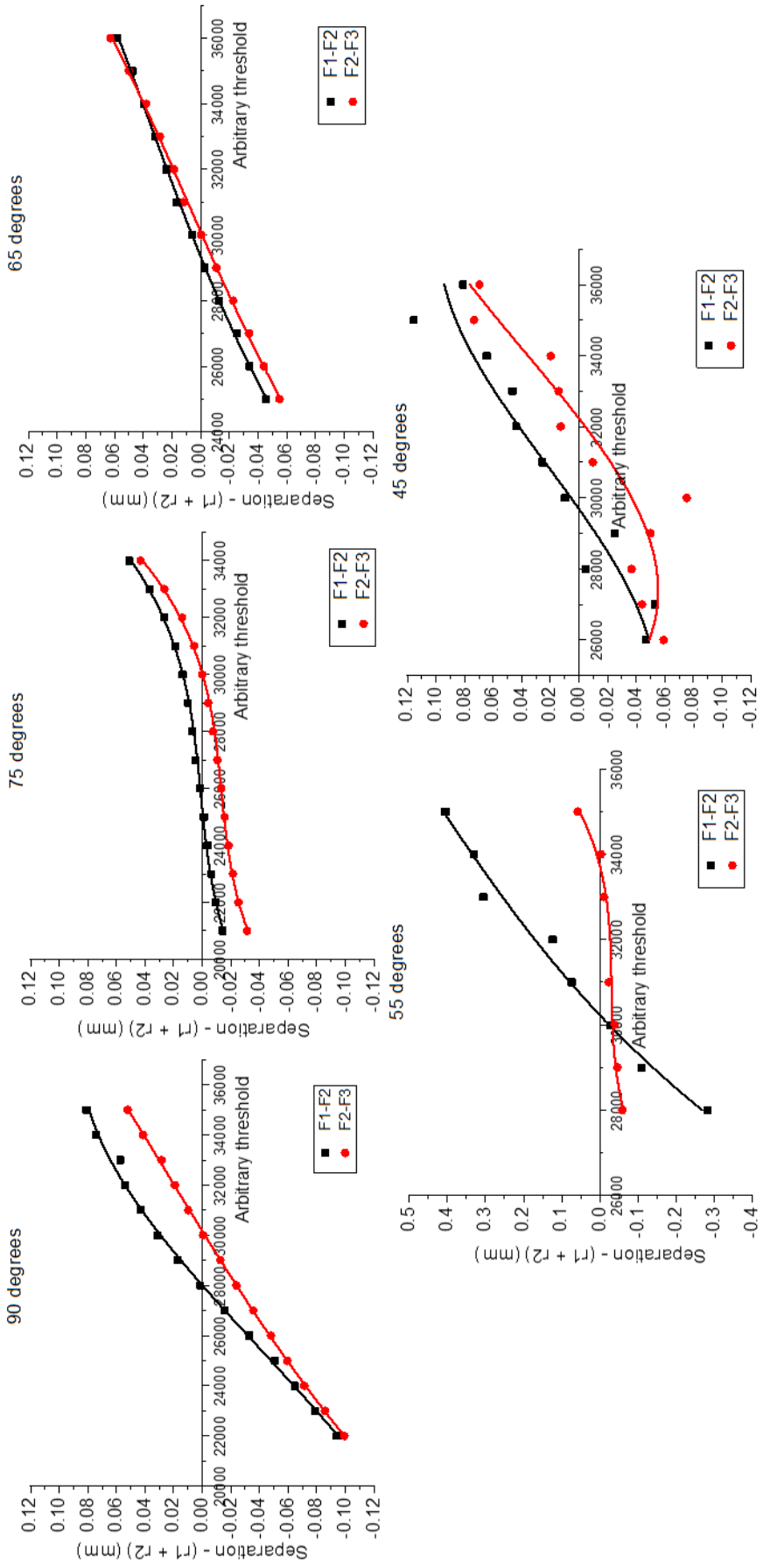

Figure 1.13 Variation in threshold for sphere pairs and different orientations

This work indicated that the cause, and potential affects, of the change in greyscale across the image needs to be investigated further.

1.7 Publications from this work

A list of the papers and presentations based on this research can be seen below. They consist of conference proceedings and presentations given at academic and industrial conferences.

Conference proceedings

Corcoran, H.C., Brown, S.B., Robson, S., Speller, R.D., McCarthy, M.B., 2016. Observations on the performance of X-Ray computed tomography for dimensional metrology, in: *International Archives of the Photogrammetry, Remote Sensing and Spatial Information Sciences - ISPRS Archives.* Prague, pp. 25–31.

Corcoran, H.C., Brown, S., Robson, S., Speller, R., McCarthy, M., 2017. How beam hardening influences the dimensional geometry in X-ray computed tomography, in: iCT2017 *7th Conference on Industrial Computed Tomography.* Leuven.

Conference Presentations

Corcoran, H.C., Brown, S.B., Robson, S., Speller, R., McCarthy, M., 2015. State of the art of X-ray Computed Tomography for Dimensional Metrology, in: *European Portable Metrology Conference.* Manchester.

Corcoran, H.C., Sun, W., Brown, S.B., Robson, S., Speller, R., McCarthy, M., 2016. Characterisation of X-ray Source for X-ray Computed Tomography for Dimensional Metrology, in: *iCT2016 6th Confrence on Industrial Computed Tomography*. Wels.

Corcoran, H.C., Brown, S., Robson, S., McCarthy, M., Speller, R., 2016. Observations on the performance of X-ray computed tomography when measuring a holeplate, in: *Dimensional X-Ray Computed Tomography Conference*. Teddington.

Corcoran, H.C., Brown, S., Robson, S., Speller, R., McCarthy, M., 2017. A study into the use of simple holeplates to measure the apparent distortion in the geometry of reconstructed volumes, in: *Dimensional X-Ray Computed Tomography Conference*. Warwick.

Corcoran, H.C., Robson, S., Speller, R., Brown, S., McCarthy, M., 2017. Limiting factors in the X-ray CT metrology of holeplates, in: *VEIV Showcase and Exhibition*. London.

Journal Paper

To be submitted to Measurement Science and Technology:

Corcoran, H.C., Brown, S.B., Robson, S., Speller, R., McCarthy, M.. The use of simple holeplates to improve X- ray CT dimensional metrology

Chapter 2: State of the art

Chapter 2 introduces the reader to the processes and physics associated with imaging using XCT. The chapter starts with a description of the workflow from start to finish, from imaging to measurement along with the general set up of a system. The path of the X-ray and the physics involved is described, from the production of the X-rays, their interaction with material and their final detection by a detector. This is followed by an explanation of the algorithms used for both reconstruction of the 3D volume and surface determination. The cause of various artefacts is also discussed.

The next main section of the chapter illustrates the workflow used in this project including the different software packages used. This section was written to provide enough detail to allow the reader to repeat the processing and to follow a similar approach. The national standards being used to accomplished traceability to the unit length, the metre, are discussed briefly.

The final part of the chapter discusses the factors affecting the maximum permissible error (MPE) of XCT systems and reports on multiple reference objects that are used to quantify the effect of these factors on dimensional metrology. This is followed by a section on the impact on industry and manufacturing.

2.1 Introduction to X-ray computed tomography

X-ray computed tomography (XCT) enables an object to be viewed in 3D allowing visualisation of external and internal structures. Along with visualisation of a volume, various types of software allow for the dimensional measurement of these internal and external structures and surfaces. The ability to “see” inside an object is beyond the scope of other traditional coordinate measuring systems, be it Cartesian coordinate measuring machines (CMM) or laser scanners, as they are only able to analyse external surfaces of an object. In some cases, for example Cartesian CMMs, they often physically touch the surface with a probe. XCT was originally established as a form of medical imaging, however, with the increase in technology and the enhanced nature of XCT compared to other imaging techniques, it has increased in popularity with many industries and manufacturers. This, however, has led to a demand to quantify the errors associated with these dimensional measurements along with providing an estimation of precision and accuracy.

The principle behind XCT is the production of a 3D volume from 2D images. These images are based on the attenuation of X-rays as they travel through a material. The attenuation is a function of the material, object thickness and X-ray energy. The intensity

of the X-rays measured on the detector, after they have travelled through the object, is proportional to the attenuation. The 2D images collected at the detector are used for the tomographic reconstruction of the 3D volume.

2.1.1 Medicine to industry

XCT was invented in the 1960s by Godfrey Hounsfield (Kalender, 2011) and was primarily used in the medical sector, however in the last decade it has been increasingly used by many industries, along with CMMs, for the inspection of many different objects.

The main difference between medical and industrial XCT is that in industrial XCT the object rotates, whereas in medical XCT the patient remains stationary and the source and detector are fixed to a gantry that rotates around the patient. Additionally, much lower X-ray energies are used in medicine (<200 keV) whereas in XCT for metrology, energy levels can reach 15MeV (Cantatore & Müller, 2011).

In medical environments the speed with which a scan can be carried out is important. Patient movement is inevitable, therefore a scan needs to be completed as quickly as possible to reduce the likelihood of artefacts, (Barrett & Keat, 2004). Although this is fundamentally not a problem with inanimate objects it is becoming an issue with in-line inspection in a manufacturing setting.

Another significant difference between medical and industrial needs is the use of the final reconstructed volume, it is a matter of qualitative vs. quantitative. For medical purposes, visualisation is the most important objective whereas in industry the output has multiple uses including comparison to a CAD model and acquiring dimensional measurements.

2.2 Processes involved in imaging with XCT

This section discusses the theory behind XCT systems including the geometry and technology of the systems, the physics involved in the production and attenuation of X-rays and the algorithms used for reconstruction of the volume and determination of the object's surface.

The workflow for imaging an object has many steps and these can be seen outlined in Figure 2.2. The figure also highlights some of the common data types that are generated by the different steps.

The primary stages in industrial imaging using XCT are:

1. Rotation of the object in the system using a rotating stage mounted on to a turntable in between the X-ray source and detector

2. Capture of 2D radiographs from multiple projections detailing the X-ray transmission through the object being imaged along the individual ray paths

3. Reconstruction of a 3D volume from the 2D images.

An XCT system is composed of many components, the main parts being the X-ray source, the manipulator and the detector; all of these will be discussed below along with the physics that is involved in each step of the process.

The geometry of XCT systems in industry is usually based on the source and detector having a fixed position and the object rotating somewhere between the two. The object is moved along the X, Y and Z axis on a manipulator, see Figure 2.1. During the imaging process, the object rotates, aided by a mechanical rotary stage, about the Y axis.

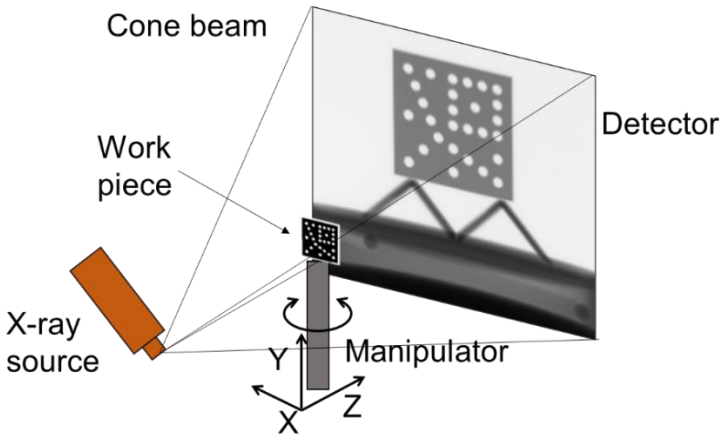

Figure 2.1 Schematic of layout of XCT system

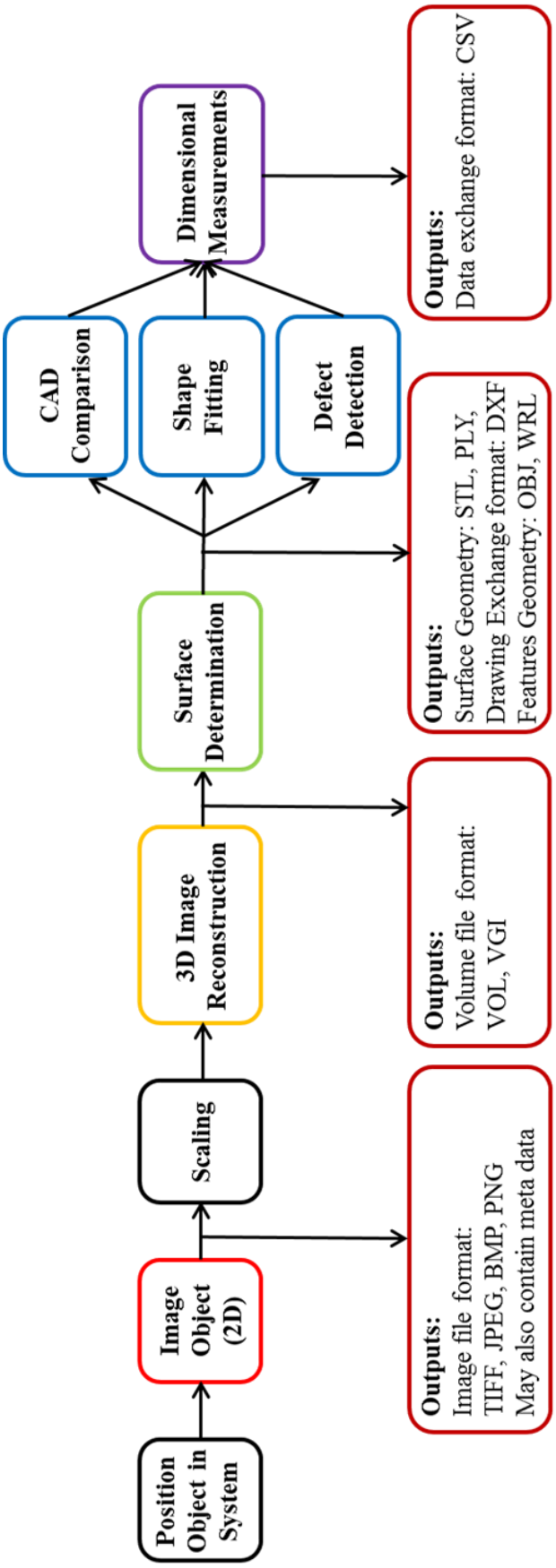

Figure 2.2 Workflow for XCT showing some of the common file formats that are used during the process

2.2.1 Production of X-rays

X-rays are produced when electrons are accelerated towards a target within an X-ray tube. The electrons are emitted from a filament or cathode, through which a current is applied. This results in the filament becoming hot and electrons being emitted by a process known as thermionic emission (Young & Freedman, 2008). The X-ray tube also contains an anode, or target. A potential difference is applied between the cathode and anode causing the electrons emitted by the filament to travel towards the target at high speeds, see Figure 2.3. The electrons are controlled and focussed into a beam by electrodes, magnetic deflectors and lenses (Kruth *et al.*, 2011).

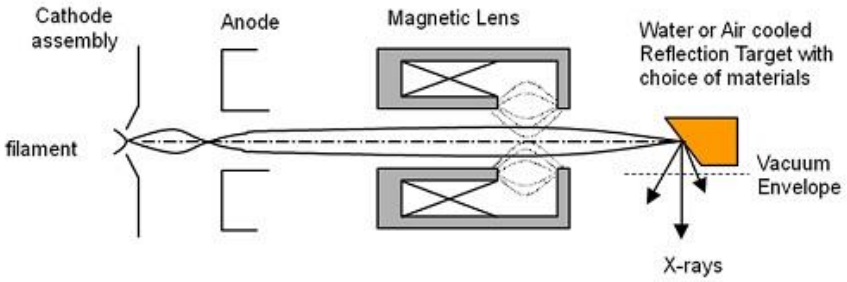

Figure 2.3 Schematic of X-ray tube (Nikon Metrology, 2014)

Once the X-rays hit the target they interact with the material and start to produce X-rays. X-rays are produced by two different processes. The first interaction is known as Bremsstrahlung radiation and emits a continuous spectrum of X-rays. When the electrons hit the target at high velocity they come close to the nucleus of an atom. This causes the electron to decelerate and change direction, losing some of its energy see Figure 2.4. Conservation of energy means that the energy is converted to heat (99%) and X-rays (1%) (Reid-Paul, 2012).

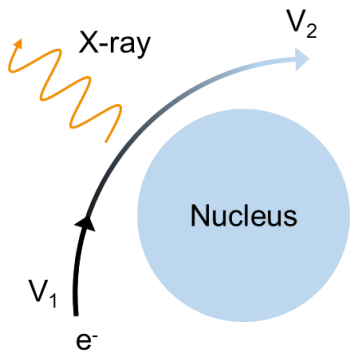

Figure 2.4 Bremsstrahlung radiation production. V_1 and V_2, velocity before and after deceleration of electron

The second process of X-ray production is known as characteristic radiation and produces X-rays with discrete energies. When an accelerated electron from the filament

hits the target, if its energy is great enough, it can eject an electron from the atom's inner shell. This electron along with the original electron (which now has a much slower velocity) are ejected, this causes the atom to become ionised. As a result an electron from an outer shell transitions into the vacancy which causes an X-ray to be emitted, see Figure 2.5. The X-ray energy will depend upon the energy of the emitted electron and the electron that filled the vacancy. This depends on the material and atomic number of the target.

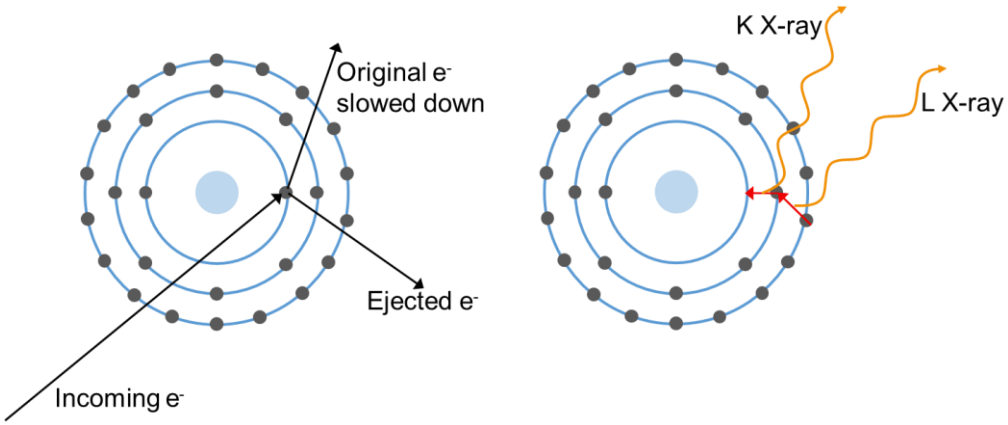

Figure 2.5 Characteristic radiation production

These two types of production create a spectrum of X-rays of varying energies, an example of which can be seen in Figure 2.6.

X-ray energies can vary, and are often referred to as soft or hard. For example, soft X-rays being in the range of 0.12 keV to 12 keV and hard X-rays from 12 keV to 120 keV (Sun, Brown & Leach, 2012). The target material changes the X-ray spectrum that is produced, higher atomic number materials produce spectrums with higher energy. Common material types include: Tungsten (Z=74), Copper (Z=29), Rhenium (Z=75) and Molybdenum (Z=42). The material type is chosen depending on the attenuation of the material being imaged with higher atomic numbers being chosen for materials that have higher attenuation.

The exposure of the image can be increased by increasing the number of photons produced; this is achieved by increasing the tube current.

The system used for this study contains a Tungsten target (Z = 74) so is more suitable for imaging denser materials.

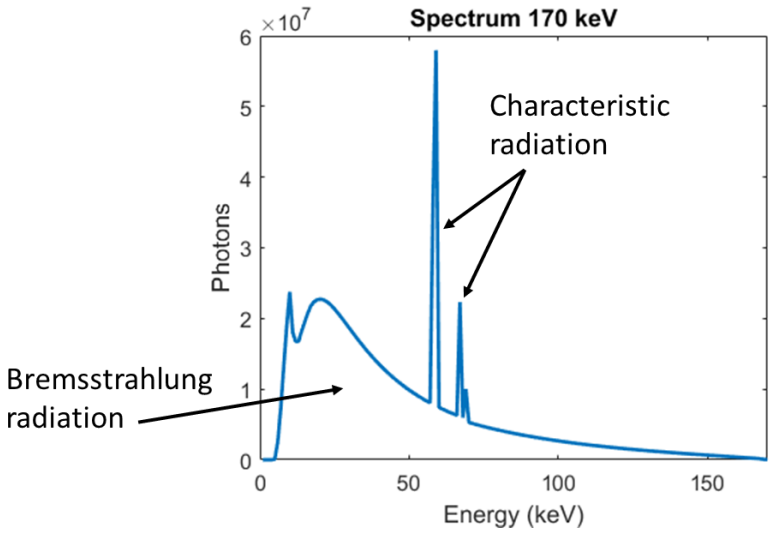

Figure 2.6 Spectrum for Tungsten target

2.2.1.1 Transmission/ reflection targets

There are two types of X-ray targets, transmission and reflection, see Figure 2.7. The type used depends on the application. For high resolution, high magnification applications, transmission targets are used. However, if higher power is required for penetrating a high density object, a large amount of heat will be produced therefore a reflection target is preferred because it can be cooled down. A reflection target is found in the system used for this study.

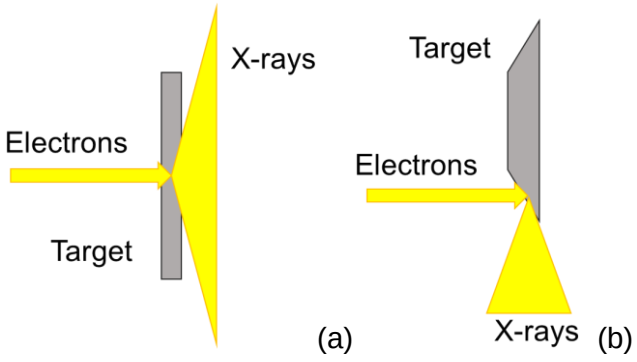

Figure 2.7: Target types, transmission (a) and reflection (b)

2.2.1.2 Focal spot size

The focal spot is the area of the anode hit by the beam of electrons. The size of the spot will affect the sharpness of the image (Figure 2.8); the resolution of the image is limited by the size of the focal spot and the magnification being used.

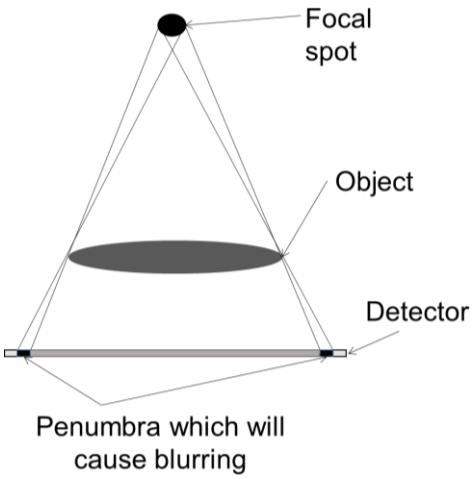

Figure 2.8 Penumbra size with respect to focal spot size

As previously stated in Section 2.2.1, 99% of the energy produced from the interactions is converted to heat, this can cause damage and pitting to the target itself. For this reason, the electron beam is made wider to dissipate the heat across a larger area, this however, leads to a larger focal spot which leads to blurring of the image leading to reduced structural resolution; a compromise therefore has to be achieved. This is often carried out by placing the anode at an angle (Fosbinder & Orth, 2011). An angled anode can be seen in Figure 2.9. The wide electron beam that distributes the heat across a large area hits the target; the surface of the target anode angled relative to the impinging beam causes the apparent dimension of the focal spot to be smaller. The aspect ratio of the incoming and outgoing beam width varies as a function of the tilt angle.

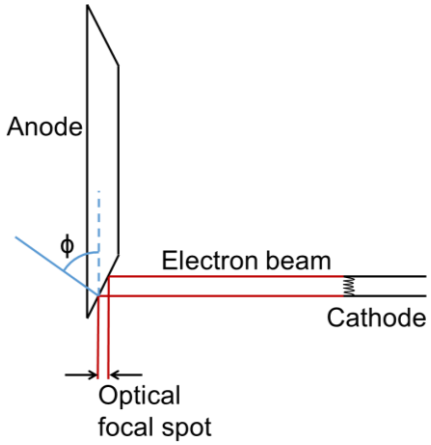

Figure 2.9 Reflection target with angled edge to dissipate heat and narrow the electron beam. Tilt angle: Φ

In most systems the anodes can be rotating or stationary. Excillum, who are a manufacturer of X-ray guns based in Sweden, have developed a metal jet anode that features a liquid target allowing for higher power on the electron beam whilst still maintaining a small spot size (see Figure 2.10). The spot size can remain small as the

power is not limited by the melting point of the anode (Excillum, 2015). The liquid metal is made of gallium and indium alloys which have Kα emission lines of 9.2 keV and 24.2 keV respectively.

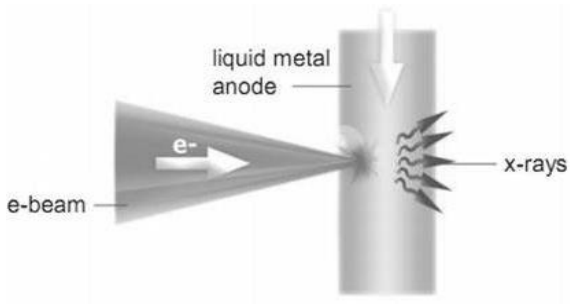

Figure 2.10 Metal jet anode from Excillum uses a jet of metal flowing at very high speed (Excillum, 2015)

2.2.1.3 Inverse square law

For a perfect point source, electromagnetic energy is emitted with equal intensity in all directions. As the distance from the point source (r) increases, the intensity of flux decreases by $1/r^2$, also known as the inverse square law. Therefore, the radiation, as it moves further away from the source is spread over a greater area. This relationship can be seen in Figure 2.11.

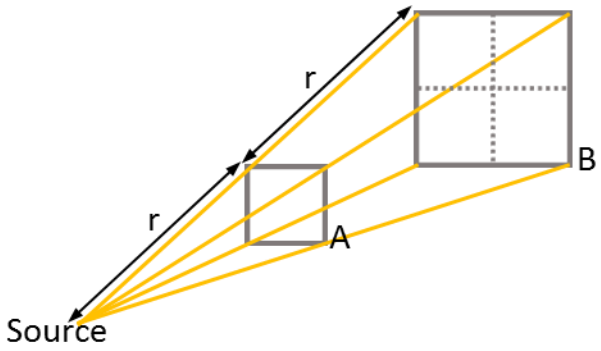

Figure 2.11 Schematic of the inverse square law. As the distance from the source doubles, the area across which the intensity is spread increases by a factor of 4

2.2.2 Manipulator

The object to be imaged is placed on a rotary table which is located on a 3-axis manipulator. The X and Y axis of the manipulator are used to position the object within the field of view, the Z axis of the manipulator determines the magnification at which the object is imaged (see Figure 2.1). The rotary table is used to rotate the object in steps to allow it to be imaged from multiple projections. Knowledge of relative position of the source, the object being measured (the position of the rotary table) and the detector are crucial to the accuracy of the reconstruction and therefore the final dimensional

measurements (Ferrucci *et al.*, 2015). To determine the position of the object within the system, distance sensors are used to measure the translation of the stage; the rotation is measured by an angular encoder. Manipulators are commonly made of steel with a granite base for high precision and stability.

2.2.3 X-ray interaction and attenuation

X-rays can interact with material in three different ways: they can pass through unaffected; this is called transmission. Alternatively, their energy is entirely transferred to the material and they are absorbed. Lastly, they can be scattered in a new direction.

X-rays are attenuated by the material of the object by various processes, the three most common are: Compton scatter and photoelectric effect which are discussed below and pair production which is described in the Glossary. The energy of the X-rays and the atomic number of the materials the X-rays are being absorbed by determines which interactions occur, see Figure 2.12.

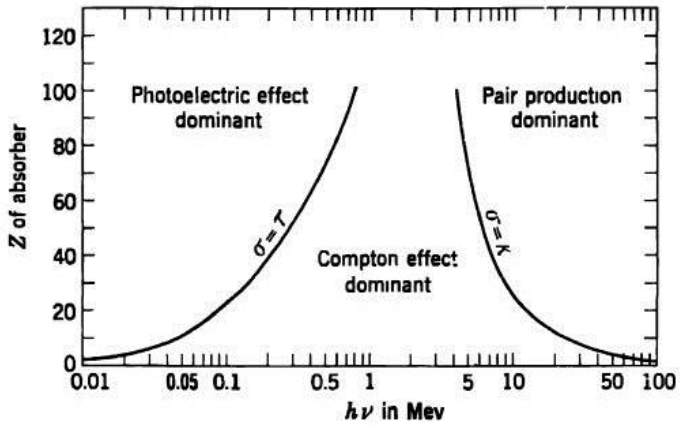

Figure 2.12 Dominant X-ray interaction depends on X-ray energy and atomic number of material (Evans, 1955)

Compton scatter is the interaction of the X-ray with a loosely bound or free electron within the object being imaged. As the electron recoils from the photon, some of the photon's energy is transferred to the electron as kinetic energy. The angle at which the electron is struck dictates the energy of the electron, the lower the angle, the lower the amount of energy that is transferred.

The interaction between an X-ray and an inner shell or bound electron is known as the photoelectric effect. If a photon collides with a bound electron in one of the shells, and has an energy greater than the binding energy of that electron, it can eject that electron from the shell. All of the energy of the photon is used up and the photon ceases to exist. The ejected electrons are known as photoelectrons. Like the production of characteristic radiation in the X-ray tube, electrons drop from a higher shell to fill the vacancy resulting

in the production of X-rays. However, the energy of these X-rays will be very much lower than in the target and they will be absorbed into the material.

Most of the imaging in this study takes place between 150 kV and 200 kV, therefore, the main interactions taking place during attenuation are the photoelectric effect and Compton scattering.

The attenuation of X-rays is related to the initial intensity of the X-rays along with the attenuation coefficient and thickness of the material that the photons are travelling through. This is illustrated in Figure 2.13 which also states the equation that defines the exponential curve.

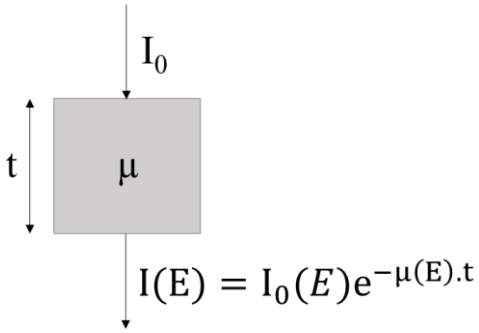

Figure 2.13 Relationship between intensity and thickness of material where I is transmitted intensity, I_0 is the incident intensity, μ is the attenuation coefficient at a given energy (E) and t is the thickness of the material for a single line integral

2.2.4 Shape of beam

The geometry of the beam can also vary, it can be a cone beam or a fan beam, the shape determines what type of detector is used. In order to decrease the scan time, a cone beam is used with a flat panel detector. The cone beam allows the whole object to be scanned in one rotation, in this work the systems used have a cone beam.

A fan beam is used in 2D-CT to image an object slice-by slice (Figure 2.14). A linear detector is used to capture the X-rays, for example as employed by a Nikon XT H 450 (Nikon Metrology, 2015). The X-ray beam and detector are well collimated which allows for a reduction in scattering artefacts such as noise and an increase in the signal to noise ratio. This therefore leads to an increase in image quality (Brunke, 2012), but to the detriment of increased scanning times.

Another method is to use a helical set-up, this involves the object rotating whilst it or the source and detector move laterally along the Y axis. It has been found by Hiller et al., (2010) amongst others, that helical scanning (using a cone beam) can decrease errors in form and size due to the removal of Feldkamp artefacts (distortions caused by

incompleteness of projections), this was also found by Kruth et al., (2011), see Section 2.8.7. Pelc, (2014) also states that helical scanning is quicker.

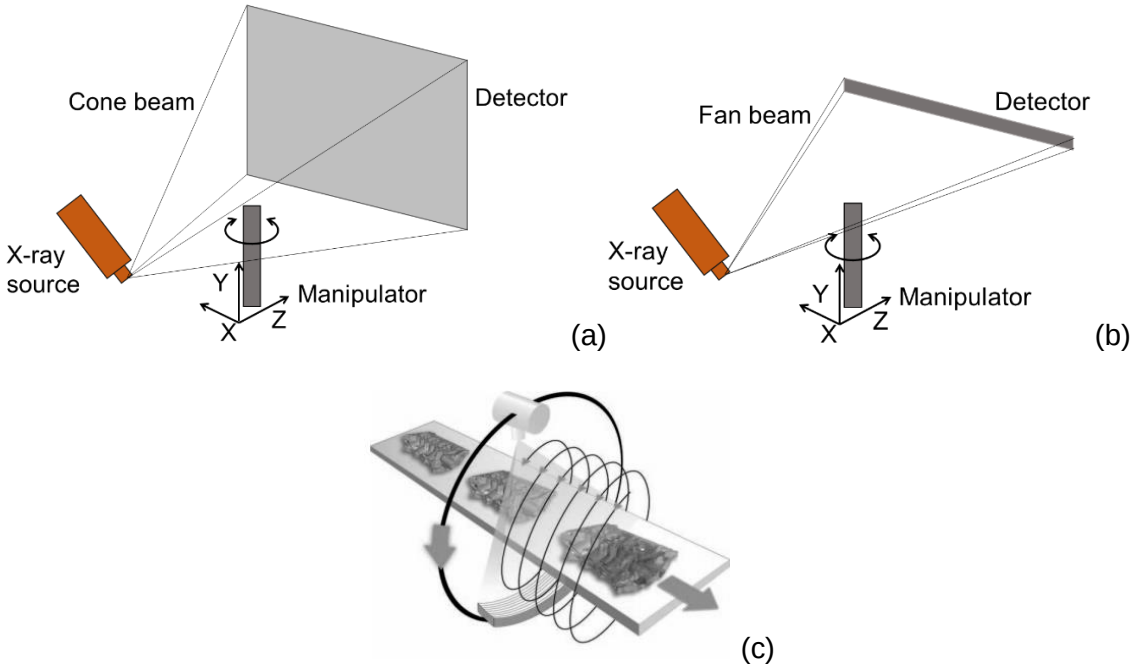

Figure 2.14 Shape of beam and subsequent detector shape (a) cone beam, (b) fan beam and (c) Helical scanning. GE speed|scan CT 64 (GE Measurement and Control, 2013)

2.2.5 Detectors

X-ray detectors are a crucial component of the system and are used to measure the X-ray transmission through the object being imaged along the individual ray paths from the focal spot to the detector. Requirements of an XCT detector include high dynamic range and quantum absorption efficiency. Other requirements are rapid temporal response and decay and low electronic noise.

Dynamic range is defined as the range in intensity that the detector can process. Quantum absorption efficiency defines the fraction of X-ray energy that is detected at points of X-ray interaction (Dössel & Schlegel, 2009).

This section discusses the digital flat panel detector array commonly used in XCT systems along with thimble ionisation chambers and spectrometers which were used in this study. The shading correction used for the scintillation detector will also be discussed.

2.2.5.1 Scintillation detector

Digital flat panel detector arrays contain a scintillator made of a material such as sodium-activated caesium iodide (Menefee, Cho & Swinehart, 1967). This is placed in front of a

photodiode array, forming an indirect flat panel detector. Scintillation detectors are suitable if high attenuation coefficient is required (Nikl, 2006).

As described earlier in Section 2.2.3 when X-rays interact with material the atoms and molecules can become excited which results in energy being released. When X-rays enter a scintillating material, that energy is released as light. The amount of light produced by this interaction is proportional to the energy of the photon that deposited the energy. This light is detected by a photodiode which converts it into an electrical signal, this process can be seen in Figure 2.15.

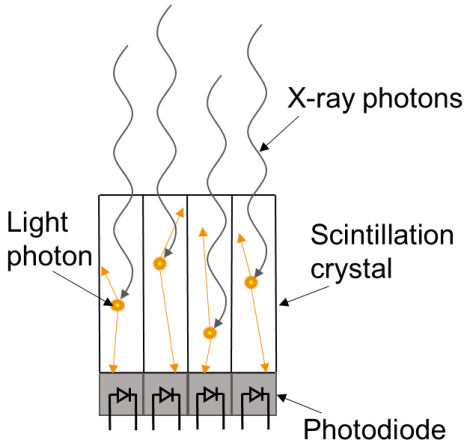

Figure 2.15 Schematic of a scintillation detector

2.2.5.2 Thimble ionisation chamber

Another form of radiation detector is an ionisation chamber. The fundamental theory of how an ionisation chamber works is based on the effects caused by a fast charged particle passing through a gas. X-rays produced at the target interact with the wall of the ionisation chamber and create charged particles. These charged particle ionises the neutral molecules along its path. The resulting positive ion and free electron are known as an ion pair. This ion pair is the basic initiation of an electric signal within the ionisation chamber.

In an ion chamber the initial ionisation takes place in the air wall material around the chamber, the free electron that is produced enters the gas where it then ionises the molecules in this gas. The ion pair created are attracted to their respective electrode due to the electric field. This creates an ionisation current that is measured with an electrometer. This ionisation current allows the total number of ion pairs that were created along the radiation path to be calculated. A schematic of an ion chamber can be seen in Figure 2.16.

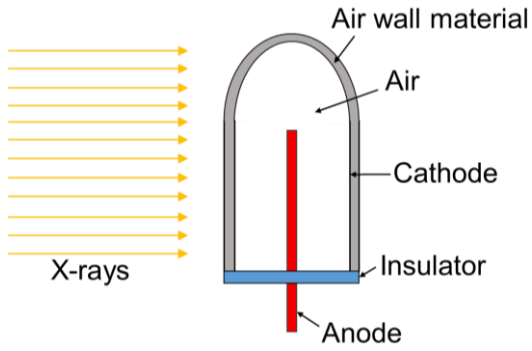

Figure 2.16 Schematic of an ionisation chamber. Based on Johns and Cunningham, 1983

2.2.5.3 Ionisation chamber array

The ionisation chamber array used in these experiments uses the same technology as thimble ionisation chamber, as seen in Section 2.2.5.2. The main difference is that it consists of 729 chambers (27 x 27) which are arranged in a 2D array. The accumulated ionisation current is measured over a period of time; the results are recorded as a measure of dose.

The ionisation chamber array used in these experiments was used mainly for the calibration of medical radiology devices and was calibrated in terms of air kerma which is a measure of dose.

2.2.5.4 X-ray spectrometer

To measure the energies of X-rays hitting the detector, pulse-height or energy spectrometry is used (Cherry, Sorenson & Phelps, 2012). Pulse-height uses the amplitude of the signals from a detector to determine the energy of the radiation that created the signal. This can only be carried out if the detector outputs a signal that has amplitudes that are proportional to the energy of the radiation detected.

The spectrometer will consist of a suitable detector, in the case of the system used in this study a CdTe detector, a preamplifier, an amplifier and a pulse processor. The Amptek X-123CdTe used in this study contains a pulse processor that processes the signal from the preamplifier and detects the peak amplitude. This value is binned in a histogram allowing a spectrum to be generated (Ametek, 2017).

2.2.6 Image reconstruction

Image reconstruction is the construction of a 3D volume from 2D images or set of projections taken of the object from multiple angles. Reconstruction is usually carried out using filtered back-projection (Kruth *et al.*, 2011). This is based on a mathematical model developed by Radon in 1917 known as linear integral transformation (Radon, 1917). This

model defines the amount of X-ray absorption when they are travelling through material with varying attenuation coefficients. This is based on the Beer-Lambert law as defined in Section 2.2.3.

2.2.6.1 Filtered back projection

An intensity profile is taken across each image, this is taken from the greyscale value of the pixels. This profile is used as the input for the reconstruction. These intensities are projected back across the volume for each projection. The summation of them will result in a reconstructed volume. Figure 2.17 illustrates the main stages of back projection, the description of which is described below Figure 2.17.

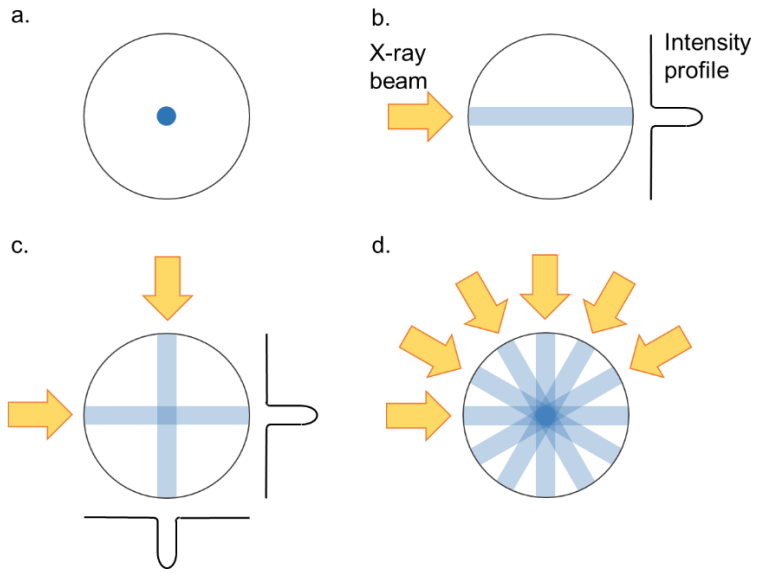

Figure 2.17 Back-projection schematic. Description seen below

a) Homogeneous sphere surrounded by air
b) X-rays are attenuated by the sphere and produce an intensity profile. The attenuation is projected back along that line
c) This process is repeated for another projection
d) After multiple projections the sphere reconstructs

As Figure 2.17(d) shows, back projection produces blurring around the object being reconstructed. To reduce this, a filter is applied to the 2D image, hence the name filtered back projection. CT Pro, the Nikon software used in this study, uses a ramp filter which is a high pass filter. This means that it removes low frequencies that cause blurring. It is known as a compensatory filter and will eliminate the star artefact (Lyra *et al.*, 2014) seen in Figure 2.17(d). The change in the intensity profile after filtering can be seen in Figure 2.18.

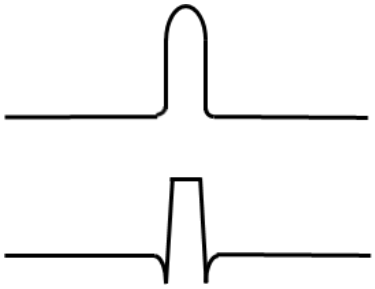

Figure 2.18 Intensity profile before (top) and after (bottom) of ramp filter based on figures from (Smith, 1997)

2.2.6.2 Feldkamp algorithm

The back projection method for reconstruction described above is based on an assumption that the rays coming from the source to the detector are parallel. It provides a 2D solution. However, in the case of a cone beam, as used in this study, a 3D solution needs to be applied to consider the fact that the voxels do not stay in the same horizontal plane as they rotate. To take the cone beam shape into account the Feldkamp algorithm is used (Feldkamp, Davis & Kress, 1984).

Kalender and Kyriakou, (2007) state that the Feldkamp algorithm has varying performances, with high quality images only being achieved in the central plane. This degradation in the image is known as the cone-beam effect. Maire and Withers, (2014) explains that a circular cone beam set up will result in an incomplete data set due to Tuy-Smith condition not being satisfied. For Tuy-Smith condition to be met all of the surface of an object must be intersected by a X-ray trajectory at least once (Hsieh *et al.*, 2013). This condition is only true for the central plane of the cone beam. Hiller et al., (2010) state that the Radon data is only collected inside a torus as seen in Figure 2.19, outside this area a shadow is created where there is a lack of data.

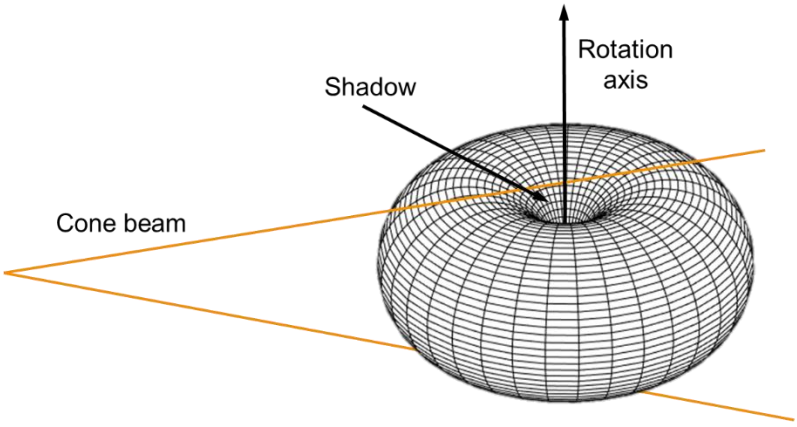

Figure 2.19 Only data in the torus shape will be collected if Tuy-Smith conditions are not met

Due to the fact that the Feldkamp algorithm assumes a perfect alignment between the source, centre of rotation and detector, any misalignment, no matter how small, can cause errors (Schulze *et al.*, 2011).

Effects on the dimensional metrology of the cone beam effect will be discussed later in Section 2.8.7.

2.2.7 Surface determination

Following the reconstruction of the 3D volume, in order to carry out dimensional measurements, it is necessary to segment the voxels associated with the object, from the voxels associated with the surrounding air. This is carried out by determining a threshold value which is dependent on the X-ray settings and materials. Two methods commonly used to determine the threshold value will be discussed below, these include the ISO50 method (see Section 2.2.7.1) which utilises a histogram of voxel intensities and a gradient based edge detection (see Section 2.2.7.2) which uses the rate of change in intensity between voxels.

The correct threshold is essential for dimensional measurements as incorrect values can lead to an apparent change in the size of the object. This will be discussed further in Section 2.8.3 and can be seen in Section 1.6.4.

2.2.7.1 ISO50 threshold

Following reconstruction, the greyscale values for the volumetric model are plotted on a histogram. If the object is homogeneous and made of a single material, the histogram will consist of two peaks, one for the air, the other for the object. The ISO50 value is half way between the two peaks, see Figure 2.20. If the greyscale value of the voxel is greater than the ISO50 value it is considered the object, likewise if it is below it is classified as air (Weckenmann & Kramer, 2009).

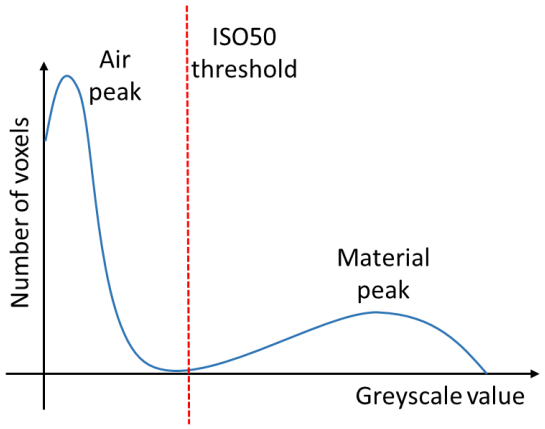

Figure 2.20 Determination of ISO50 using a histogram of voxel greyscale values

However, this global threshold can only be accurate if the object is made of a single, homogeneous material and the volume does not contain any artefacts, such as beam hardening or scattering, that could result in local dimming or lightening of the XCT image (BSI, 2011).

In practice the ISO50 method can result in the edge being defined in the incorrect position (Kiekens *et al.*, 2010). Kruth *et al.*, (2011) states that work carried out at K.U.Leuven indicates that the ISO50 method results in parts appearing too small. They state that the optimal threshold is found at around 35-45% on a greyscale histogram.

2.2.7.2 Gradient based edge detection

An alternative to the ISO50 method is to determine a local threshold that is dependent on the rate of change between the voxel greyscale values. There are many types of edge detection algorithms including Sobel and Canny.

For any of these algorithms to work an initial surface is required, this is defined using the ISO50 method which gives a starting value. Around this surface, within a given search distance, the local gradient is evaluated along the three main directions (x, y and z). The edge of the object is defined at the gradient maxima. Work, for example that carried out by Yagüe-Fabra *et al.*, (2013) allows sub-voxel spatial resolution to be obtained.

2.3 Artefacts

Artefacts are discrepancies between what the true image should be and the actual image that is captured, they can be translated into the 3D volume. It is a feature in the image that is not present within the object itself. Knowledge is plentiful with regards as to what causes artefacts and potential ways of removing them (Boas & Fleischmann, 2012).

2.3.1 Beam hardening

Beam hardening occurs when a polychromatic X-ray beam passes through an object. The lower energy X-rays are attenuated preferentially along the X-ray path due to their higher attenuation coefficients (Cantatore & Müller, 2011). This results in the mean energy of the remaining X-rays becoming higher as they travel through an object, i.e. the X-rays are becoming harder. Because of the lower attenuation coefficients, the harder X-rays are less likely to be absorbed. The total attenuation, given by the logarithmic ratio of the un-attenuated and attenuated beam, is now not a linear function of the object's thickness unlike if the X-rays were monoenergetic.

Beam hardening will result in a change in the measured attenuation making it difficult to quantitatively interpret data, this leads to problems with surface determination. Artefacts seen within the images include cupping (Figure 2.21) and streaking (Figure 2.22).

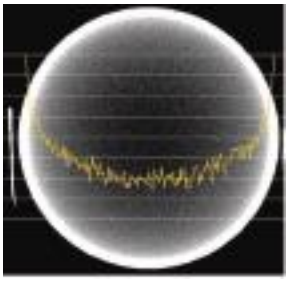

Figure 2.21 Greyscale across a uniform water phantom (Barrett & Keat, 2004)

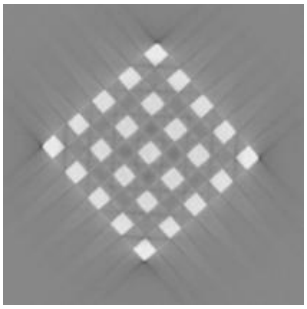

Figure 2.22 Streaks visible in the image of a heat exchanger (Lifton, Malcolm & Mcbride, 2013)

The implications of this effect on dimensional metrology will be discussed further in Section 2.8.2.

2.3.2 Anode heel effect

The anode heel effect is an inherent filtering that occurs within the target material itself. As the electrons hit the target they penetrate a small distance, the resulting X-rays that are dispersed in the cone will therefore travel through varying amounts of target material, see Figure 2.23. This will result in the x-rays being hardened by varying amounts. It is mainly the Bremsstrahlung spectrum that is filtered (Fritz and Livingston, 2009).

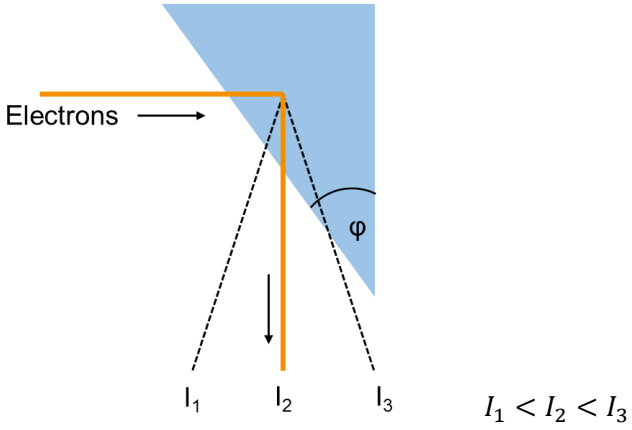

Figure 2.23 Anode heel effect and amount of beam hardening in the three X-ray path lengths

2.3.3 Partial volume effect

The partial volume effect is dependent on the resolution of the detector and causes blurring at the edges of an object. It most situations the edge of an object will not be aligned with the edge of a pixel (Figure 2.24), therefore the pixel associated with this edge will record an intensity that is linearly averaged over the width of the pixel (Buzug, 2010). This effect will be more noticeable in systems with limited resolution.

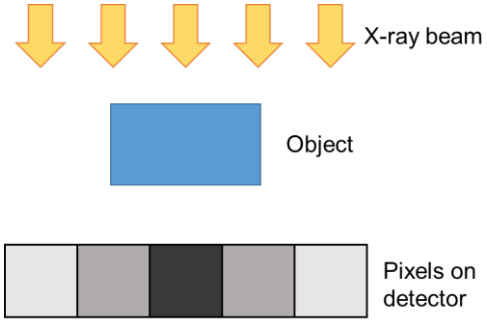

Figure 2.24 Partial volume effect

2.3.4 Scattering

X-rays can become scattered due to interaction with the object being images or the XCT system itself. These interactions, which have been discussed previously in Section 2.2.3, cause the X-rays to deviate from their straight path and leads to errors in the correct intensity recorded at the detector. This in turn leads to noise in the image which results in lower contrast. The effects on metrology will be discussed further in Section 2.8.8. In the case of high attenuation objects such as metal, scatter can cause streaks in the reconstructed data due to the greater than expected number of photons reaching the detector ((Boas & Fleischmann, 2012).

The amount of scatter recorded on the detector depends on the distance between the object being imaged and the detector. When the object is close to the detector more scatter will be collected due to the larger angle subtended at the detector by the object. If the object is further away this angle is smaller and less scatter will be recorded.

2.4 Workflow of data processing for this project

This section will be dedicated to describing the particular methods and algorithms found in the software that was used in this project. Being proprietary software, the actual algorithms are not shared but the user manuals were used to decipher what processes were being used as much as possible.

2.4.1 Shading correction

Software used to run the XCT system, the Nikon XTH 225 M (see Section 4.2), is known as Inspect-X. It applies a shading correction to all images acquired by the system. The manual states that this is to compensate for the variation in the detector's pixel response. Two reasons for the variations are given in the manual for the software; one is the variation internally within the system's detector and the second is a decrease in the flux due to the inverse square law (explained in Section 2.2.1.3) resulting in darker regions at the corners of the image compared to the centre.

Before imaging of the object begins, images of an empty field of view are taken both with the X-rays switch on and off. These are then used in the software to correct each image for any variation in the flux across the detector. This is only based on the initial images and does not take into account temporal changes.

2.4.2 Reconstruction

In this study reconstruction of the 3D volume from the 2D images was carried out using mainly CTPro, Nikon's proprietary software. After carrying out a scan the images were stored in a folder with a parameter file, a .xtekct file, which was opened in CT Pro. The interface can be seen in Figure 2.25.

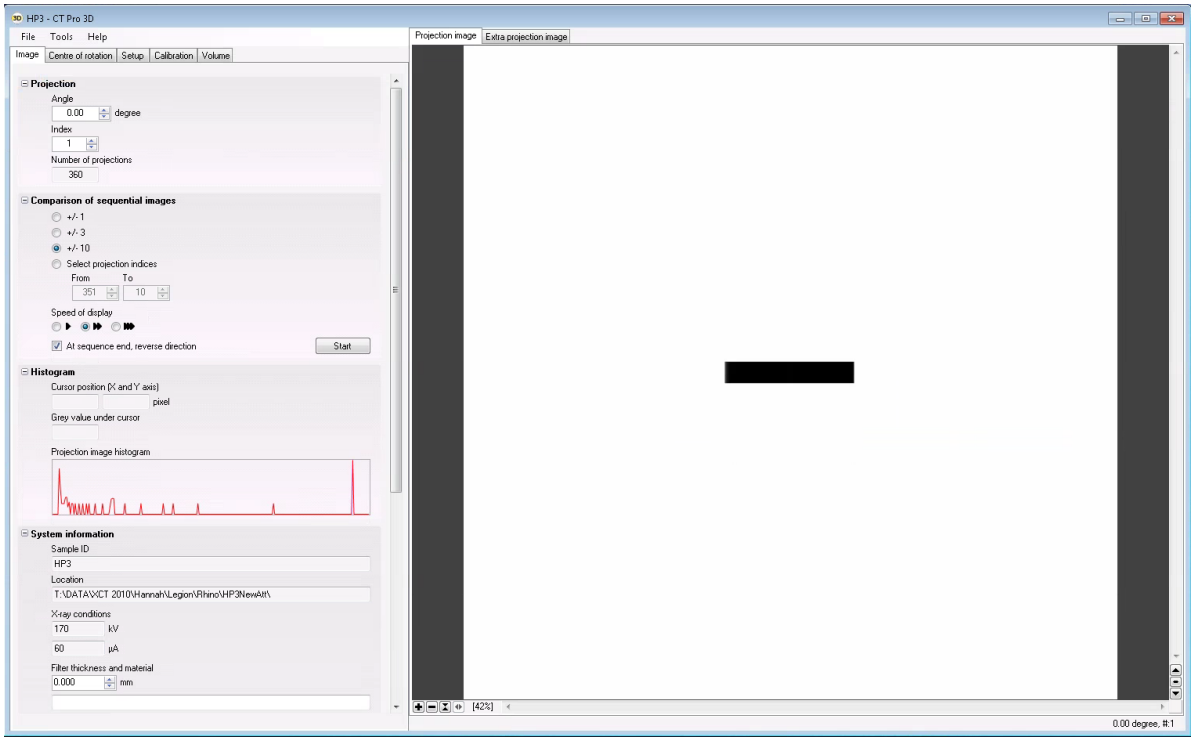

Figure 2.25 Screenshot of the CT Pro interface. A 2D image can be seen on the right

Reconstruction of the volume in CT Pro follows a five step procedure which can be seen in Figure 2.26, the steps are described below.

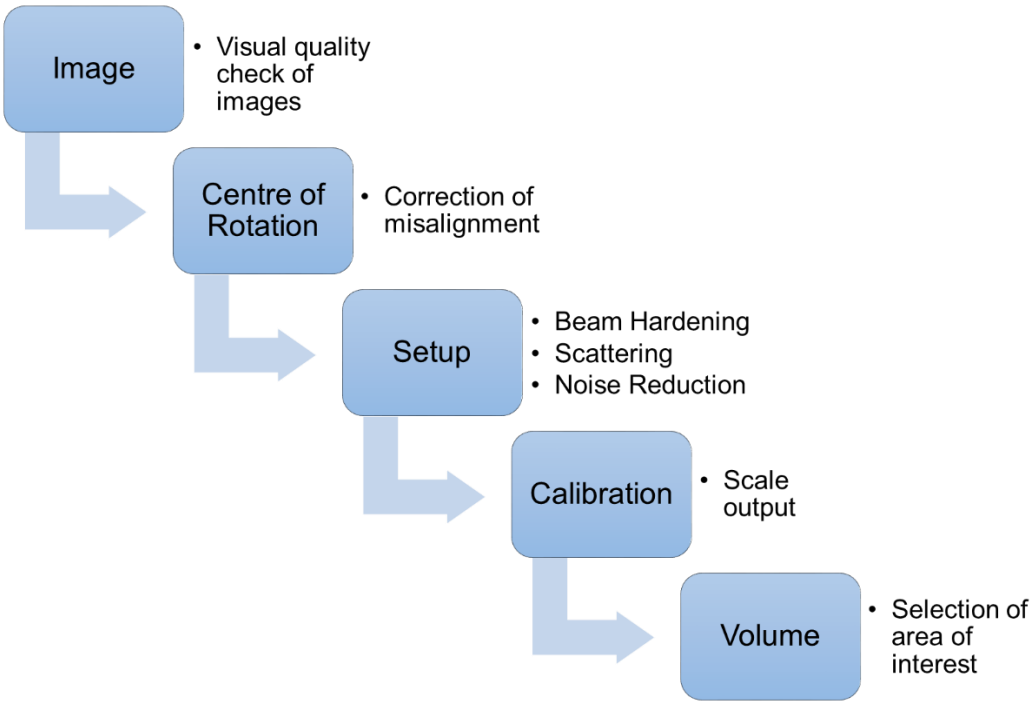

Figure 2.26 Five step workflow of CT Pro

1. This step is for a visual inspection of the data. Sequential images can be viewed along with the first and last images. This is to ensure that no movement of the object has occurred during imaging
2. A Centre of Rotation correction is carried out by the software. Reconstruction algorithms assume that the projection images are centred on the rotation axis and are perfectly vertical. In reality this is never possible due to misalignment of the system's components. To correct for these errors, the sharpness of a test slice in the centre of the volume is evaluated. The projections are shifted by one pixel and the process is repeated, this allows the required shift to be estimated. This process continues as an iterative process until the quality required is achieved.
3. Once the data is sharp the next set of corrections can be carried out.
    a. Beam hardening is described in Section 2.3.1 and can be corrected most effectively if the object being measured only contains one material (Nikon Metrology, 2013a). The corrections use the decrease in the X-ray attenuation coefficient in the material as a function of the material thickness for the conditions used. There are six pre-set values from which the user selects the one which best eliminates the effects of beam hardening. The value is chosen by studying a profile of the greyscale through the object. The profile with least cupping but also the least removal of material will be deemed to be the most suitable. (See Section 2.4.2.1 for description of correction).
    b. Scatter can cause an increase in the intensity of the data with the effect being linear, this correction removes this excess intensity. This correction was never applied to the data sets used in this project.
    c. Volumes are reconstructed using filtered back projection, however, this can lead to noise within the images being enhanced. If the correct filter is used the background noise can be cancelled out. Six filtering options are given, the option that removes the most noise but the least detail is chosen. This is again carried out by studying a profile through the object.
4. Calibration is only required if a specific area of the object has a known output value. It was not used in this project.
5. In the final tab the volume to be reconstructed is defined as the region of interest. This area is chosen by selecting an area on two projections at 0° and 90° views.

2.4.2.1 Beam hardening correction

The beam hardening correction used in Nikon's CT Pro applies a linearization technique based on polynomial curves (Léonard *et al.*, 2014).

An ideal greyscale value would be acquired using a mono energetic X-ray beam, if this is plotted against the path length of the X-rays a straight line intersecting the origin of the graph would be seen. When polyenergetic X-rays are used a curve would be produced instead of a straight line. Linearization is the procedure by which the polyenergetic values are projected onto the straight line. To do this a polynomial function is used, the values for which can be acquired experimentally from the radiographs of reference objects of similar materials (Kasperl *et al.*, 2002). However, with CT Pro, pre-set values for these coefficients have been defined and the user chooses the correction level based on how much each level corrects for the cupping effect. It is presumed that the pre-set values are based on varying materials as the attenuation coefficient of different materials will vary the amount of beam hardening that is occurring.

The equation and coefficients used in this study can be seen below in Equation 2.1 and Table 2.1.

$$Y = a(b + cX + dX^2 + eX^3 + fX^4)$$

Equation 2.1 Polynomial curve for beam correction. X initial greyscale value, Y equals corrected grey scale and a to f are coefficients that depend on the level of correction chosen by the user

Correction level	Coefficients					
	a	b	c	d	e	f
1	1	0	1	0	0	0
2	1.32	0	0.75	0.25	0	0
3	1.94	0	0.5	0.5	0	0

Table 2.1 Coefficients used in beam hardening correction in this study

2.4.3 Surface determination

Surface determination was carried out in the software VGStudio Max 2.2. This software was used as this was the software available at NPL. A .VGL file (which is produced by CT Pro) is opened in VGStudio Max 2.2 (Volume Graphics GmbH, Heidelberg, Germany). A screenshot of the interface can be seen in Figure 2.27.

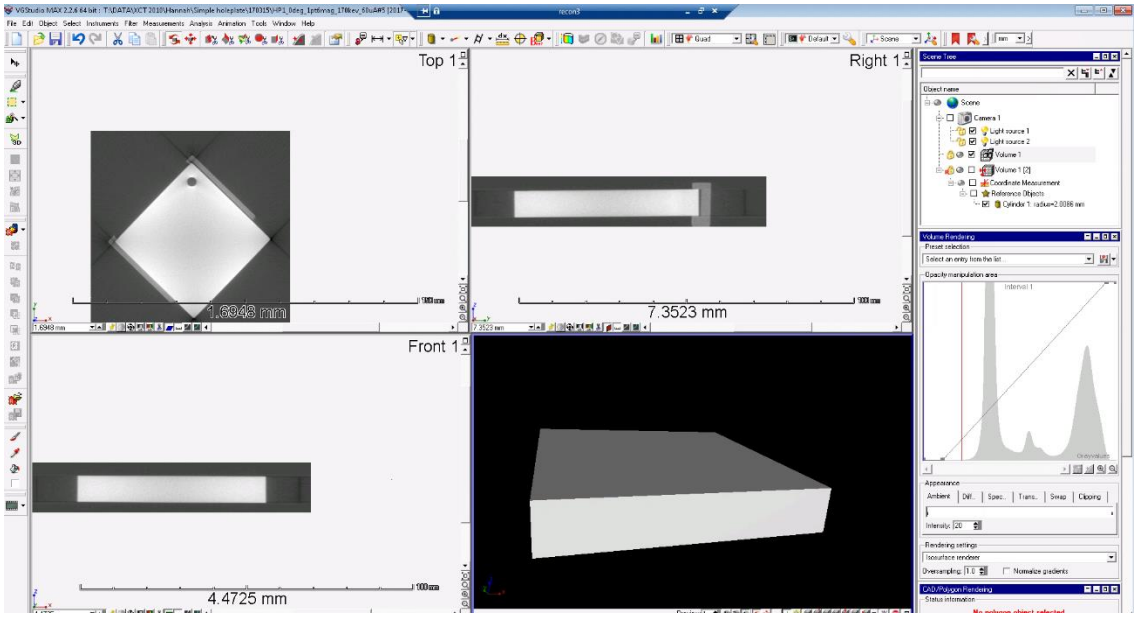

Figure 2.27 Screenshot of VGStudio Max after a volume has been imported. Images to the left and top middle are 2D sections through the volume. The 3D volume can be seen at the bottom

To determine the surface of the holeplate the ISO50 method is used initially. As described in Section 2.2.7.1, this method uses the midpoint between the peak in the greyscale for the air and the peak in the greyscale for the material as the greyscale value of the threshold or interface between the air and material. Using the 2D sections, the user manually selects an area of the background (Figure 2.28) and then another area containing the material of the object in question (Figure 2.29). From this data a histogram is drawn and the ISO50 is defined (Figure 2.30). This initial surface is used as a starting value for an algorithm that searches locally for the greatest rate of change in greyscale value in between the air and the object. At the point of maximum gradient, a new surface is defined. This method was described further in Section 2.2.7.2.

Figure 2.28 Area containing background selected (red and yellow box)

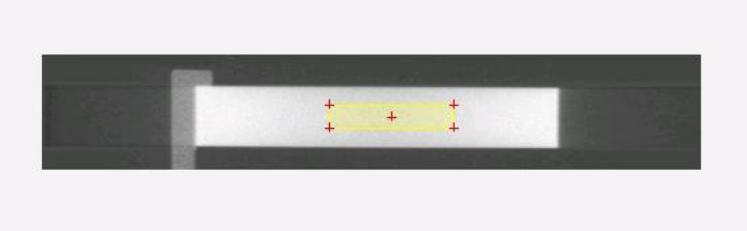

Figure 2.29 Area containing material selected (yellow box)

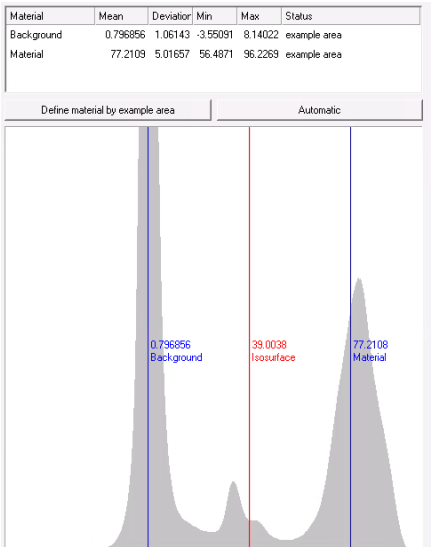

Figure 2.30 Histogram of greyscale values for background and material

2.4.4 Registration

To ensure the coordinates used to define the reference objects are aligned to a common coordinate system the volume is registered to an imported CAD model of the holeplate (Figure 2.31 (a)). The initial stage of registration is to manually rotate and position the volume to align it with the CAD (Figure 2.31 (b)).The final stage is to use the best fit technique that considers the current transformation of the volume and uses a Gaussian best fit method (Figure 2.31 (c)).

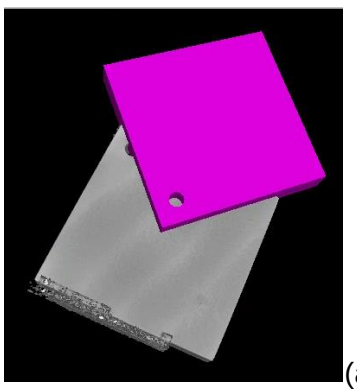
(a)
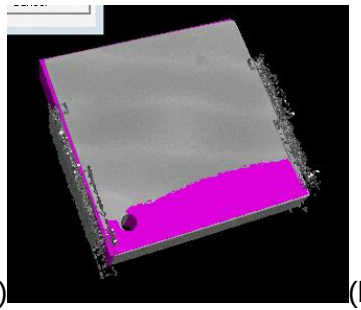
(b)
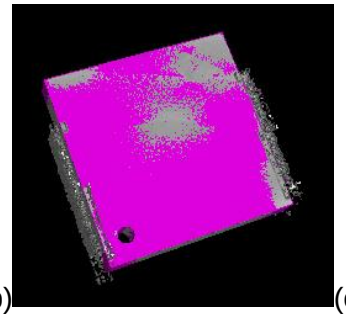
(c)

Figure 2.31 Stages of registration of holeplate volume (grey) (a) imported CAD model (pink) (b) Simple registration (c) Best fit registration

2.4.5 Shape fitting

In VGStudio Max, after the surface of the reconstructed volume has been determined, and it has been registered to ensure the correct alignment to a common coordinate system, reference objects such as cylinders can be fitted to the volume, see Figure 2.32. Fit points are used by the software to fit a shape using an iterative process.

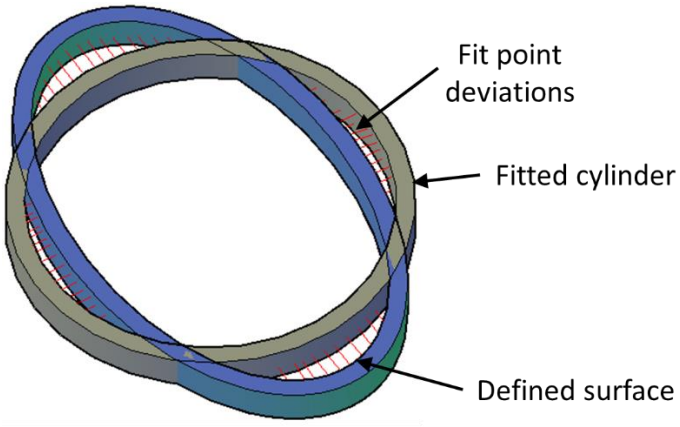

Figure 2.32 Deviation of fit points from determined surface and fitted cylinder

The user manually selects at least three points distributed across the surface where the cylinder is to be fitted (Figure 2.33 (a)), these points are used to fit an interim reference object. From this object a new set of uniformly distributed points is generated across the surface of the volume. The reference object will be defined by a parametric model; the sum of the residuals between the object and the points will be calculated, this will then be taken into account and a new reference object will be fitted, this process repeats using an iterative least-squares technique until the smallest sum of residuals is found or the maximum number of iterations is reached. The deviation of the final points from the surface are colour coded (Figure 2.33 (b)) and are listed along with their 3D coordinates. The cylinder's centre coordinates, direction and radius are also defined.

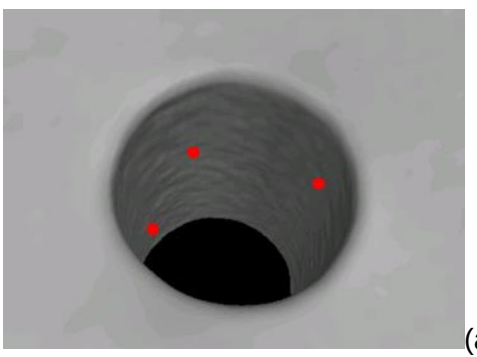
(a)
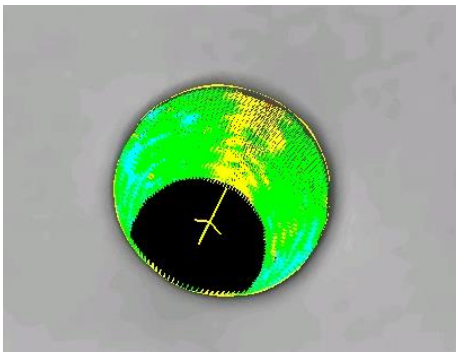
(b)

Figure 2.33 Fitting of reference object (a) red points chosen by user (Exaggerated size for ease of viewing) (b) all points used by software to fit cylinder

The VGStudio Max User Manual states that by using the least squares method to fit a reference object, the distribution of the fit points will usually result in a Gaussian shape and the sum of the negative deviations will equal the sum of the positive deviations.

2.5 Simulation packages

2.5.1 XCT simulation

A few commercial XCT simulation software packages are available, these include Scorpius XLab® by Fraunhofer (Hiller & Reindl, 2012), aRTist by BAM (Bellon *et al.*, 2012) and Geant4 (Agostinelli *et al.*, 2003). They can either be based on the Monte Carlo method or ray tracing algorithms. Due to the nature of the algorithms used, the ray tracing methods are much quicker to process.

Scorpius XLab® and aRTist both generate projections using the ray tracing method and allows objects to be modelled either by using solid geometry shapes or by importing a .stl file. Amongst other factors, the material of the object can be changed along with the size and drift of the focal spot, scatter and misalignment of the geometry.

Geant4 uses the Monte Carlo method, this software also allows for various system geometries and object shapes and materials to be simulated. It tracks particles through the material and takes into account external electromagnetic fields. Unlike the other software packages and the simulation written for this study, Geant4 includes calculations accounting for scatter of X-rays.

2.5.2 X-ray spectrum simulation

SpekCalc (Poludniowski *et al.*, 2009) is a software the is used in this project to simulate a theoretical spectrum for different settings that are defined by the user. It combines both semi-empirical models of X-ray production and Monte Carlo methods which trace individual particles. To reduce the computation cost the probabilities of electron survival at given depths within a target and the energy distribution of that electron have been pre-calculated. The Bremsstrahlung cross-section, or area in which the electron decelerates, along with the inherent filtration within the target is based on empirical methods.

2.6 Traceability and international standards

Traceability is ensuring that a measurement obtained with any system is an accurate representation of the measurement being taken. The international Vocabulary of Basic and General Terms in Metrology define it as “the property of the result of a measurement or the value of a standard whereby it can be related to stated references, usually national or international standards, through an unbroken chain of comparisons all having stated

uncertainties" (International Organization for Standardization, 1993). This allows the user of the instrument to have confidence in the result being obtained.

In order to provide traceable results back to the SI unit, in this case the metre, an error budget has to be calculated taking into account the various errors that influence the result. At the present point in time, measurements of dimension and form obtained with an XCT system are not traceable back to the metre and any measurements calculated using XCT cannot be accompanied by a statement of uncertainty (Lifton, 2017). It is for this reason that research into the critical factors affecting XCT dimensional measurements are being studied internationally.

Material standards available from National Institute for Standards and Technology (NIST) in the U.S. supply both density and dimensional standards for XCT (SRM 2088 and SRM 2087, respectively). The dimensional standard comprises of 16 spheres supported in a plastic structure (Figure 2.34). The sphere diameters have a confidence interval of ±25 µm.

In Japan, NMIJ/AIST (National Institute of Advanced Industrial Science and Technology) have, since 2008, been working on standardisation of XCT for dimensional metrology and in 2013 published a standard terminology for dimensional CT reference JIS B 7442 (Bartscher *et al.*, 2014).

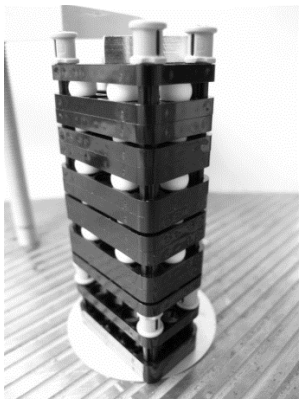

Figure 2.34 NIST standard SRM 2087. The PTFE spheres have diameters of 5.556 mm and 7.144 mm (National Institute of Standards & Technology, 2012)

In the US, the ASTM has written guidelines for NDT (ASTM E 1665) and advice on problems found with XCT systems (American Society for Testing and Materials, 2014). This, however, is not for dimensional metrology.

In Germany the VDI/VDE have produced the document VDI/VDE 2630 which is a guideline for the application of DIN EN ISO 10360 for coordinate measuring machines with CT sensors.

Verification of coordinate measuring machines is the focus of International Standardisation International (ISO) Technical Committee 213 Working Group 10. A future output will be an additional ISO verification document focused on XCT.

A summary of the national standards and operating procedures can be seen in Table 2.2.

Standard	Date	Title of document
ISO 15708-1	2002	Non-destructive testing – Radiation Methods – Computed Tomography – Part 1: Principles
ISO 15708-2	2002	Non-destructive testing -- Radiation methods - Computed tomography - Part 2: Examination practices
BS EN 16016-1	2011	Non destructive testing. Radiation methods. Computed tomography. Terminology
BS EN 16016-2	2011	Non destructive testing. Radiation methods. Computed tomography. Principle, equipment and samples
BS EN 16016-3	2011	Non destructive testing. Radiation methods. Computed tomography. Operation and interpretation
BS EN 16016-4	2011	Non destructive testing. Radiation methods. Computed tomography. Qualification
ASTM E1672 - 12	2012	Standard Guide for Computed Tomography (CT) System Selection
ASTM E1441 - 11	2011	Standard Guide for Computed Tomography (CT) Imaging
ASTM E1695 - 95	2013	Standard Test Method for Measurement of Computed Tomography (CT) System Performance
ASTM E1570 - 11		Standard Practice for Computed Tomographic (CT) Examination
VDI/VDE 2630 - 1.1	2009	Computed tomography in dimensional measurements – Basics and definitions
VDI/VDE 2630 - 1.1	2014	Computed tomography in dimensional measurements – Fundamentals and definitions
VDI/VDE 2630 - 1.2	2010	Computed tomography in dimensional measurements – Influencing variables on measurement results and recommendations for computed tomography dimensional measurements
VDI/VDE 2630 - 1.3	2011	Computed tomography in dimensional measurements – Guidelines for the application of DIN EN ISO 10360 for coordinate measuring machines with CT-sensors
VDI/VDE 2630 - 1.4	2010	Computed tomography in dimensional measurements – Measurement procedure and comparability
VDI/VDE 2630 - 2.1	2013	Computed tomography in dimensional measurements – Determination of the uncertainty of measurement and the test process suitability of coordinate measurement systems with CT sensors

Table 2.2 National standards and operating procedures

One method to understand and estimate the measurement uncertainties of results obtained using XCT is to use a calibrated test object that has been previously measured with an instrument that is traceable, for example a CMM. Villarraga-Gómez et al., (2018) used a truncated aluminium cone of approximately 40 mm, containing internal circular voids. Differences of up to 4 µm were found in the diameters of the voids. Kraemer et al., (2017) used two industry inspired test objects, seen in Figure 2.35, to study the accuracy of two different XCT systems. The uncertainty was estimated and based on, amongst other factors, the uncertainty due to the calibration of the XCT system and the uncertainty due to noise. The uncertainty was calculated to be 10 µm for all the different measurands.

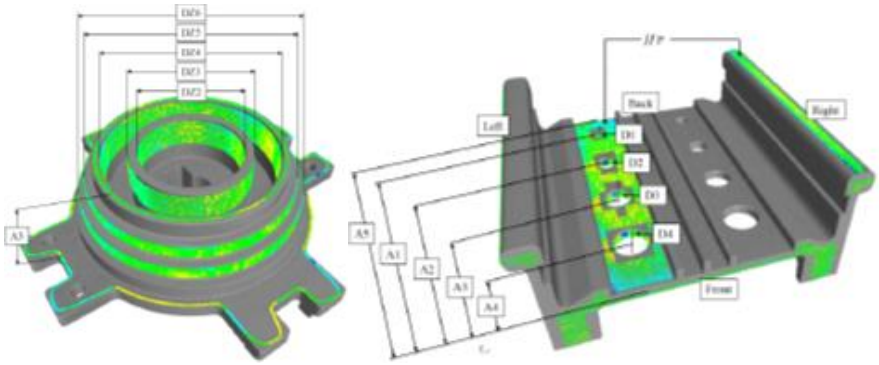

Figure 2.35 Test objects along with measurements taken by Kraemer et al., (2017)

In order to provide a maximum permissible error (MPE) for measurements, manufacturers of XCT systems have developed their own calibration methods, this makes comparison of different systems very difficult.

2.7 Critical factors affecting the MPE of XCT systems

As already discussed there are many variables that can affect the dimensional measurement results of XCT. The guidance document by VDI/VDE (VDI/VDE-Richtlinien, 2010) list these variables and gives a brief description of the possible effects. This list will be the basis for the following discussion on these variables and critical factors.

2.7.1 X-ray source

This section will look into the issues associated with the X-ray source, including drift of the focal spot, inherent filtration within the target material and the causes of variation in the X-ray flux.

2.7.1.1 Focal spot

The point at which the electrons hit the target is known as the focal spot. The position and shape of this focal spot is known to move on the target which causes a source of movement (Affenzeller *et al.*, 2015). This in turn leads to apparent movement in the object being imaged leading to errors in the reconstruction (Vogeler *et al.*, 2011). Flay, (2016) carried out experimental and simulation work on the drift of the focal spot in the system used in this study and it was found that the drift in the X and Y coordinates was no greater than ±0.2 pixels at a magnification of x130. This equates to a discrepancy in the diameter, when measuring a 1 mm iron sphere, of -0.05 µm and a form error of 1.38 µm. These values are smaller than the errors studied in this work so will not be considered further.

2.7.1.2 Inherent filtration of source

Filtration of the X-rays within the source is known as the anode heel effect and is discussed in more detail in Section 2.3.2. Work carried out by Braun et al., (2010) has found that there is not a smooth transition between the different fields of view which results in a bevel-like artefact caused by there being different thickness of filtration on neighbouring pixels. Emission spectra were modelled by Fritz and Livingston (2009) and it was found that the intensity varied across the image.

After an extensive literature search there does not appear to have been any research into the consequence of this filtering on dimensional metrology. This work looks at the effects of the anode heel effect and measurements of the spectra and intensity were collected, further details can be seen in Chapter 3.

2.7.1.3 Instability of flux

Instability in the flux has been noted by many authors including Baek et al., (2015) and Cuadra et al., (2017). Titarenko et al., (2010), who works in synchrotron-based micro-tomography, describes how these time dependent variations can lead to the shading corrections, carried out at the beginning of an imaging period, becoming ineffective. They go on to describe how applying a shading or flat field correction can lead to ring artefacts. Eigen flat fields were used by Van Nieuwenhove et al., (2015) to correct for the flux variations. Araujo et al., (2011) states that the fluctuations in X-rays are due to the wave form of the voltage being applied to the tube.

Again, a literature search has not highlighted any work done by other authors relating to X-ray flux instability and dimensional metrology, however, it was part of this study and can be found in Chapter 3 and Chapter 5.

2.7.1.4 Temperature and humidity

The temperature of the target during imaging can cause the focal spot to drift, especially during a warm up period when the X-rays are initially produced (Flay *et al.*, 2015). However, as already described in Section 2.7.1.1 about focal spot drift, the errors in measurement associated with this movement are negligible in this study.

2.7.2 Scattered radiation

Radiation due to scatter relates to the scatter within the cabinet itself and not that associated with scatter within the object. A study carried out by Schuetz et al., (2014) simulated scatter from the detector stand and the walls of the cabinet. A lead-iron combination was used initially for the stand but was changed to a carbon fibre reinforced polymer design, scatter reduced from 2.5% to 0.3%. The walls were originally concrete but were lined with tin and lead, this reduced scatter from 1% to 0.1%. Experimental data using a step cylinder showed an increase in contrast of 36%.

2.7.3 System geometry and alignment

The accurate positioning and the stability of the manipulator and the axes along which the object being imaged moves is crucial to the clarity of the images and the scaling that is applied to the reconstructions. Work carried out by Ferrucci et al., (2015) on the length of a 2 mm ball bar found errors of 0.5% when the error of the position of the source and manipulator was 100 µm. Simulation work carried out by Wenig and Kasperl, (2006) shifted the rotation axis towards the Y-direction by up to 700 µm. A 100 mm alloy test object was used which had multiple lengths and diameters that could be measured. Relative measurement errors were found to be up to -2% of the lengths measured. This indicates that measurement accuracy would vary depending on the position of the object in the field of view.

Hermanek et al., (2017) are proposing an object to study the geometry and it comprises of markers placed in circular and helical patterns. So far, only simulated scans of the object have been carried out.

Errors in the rotational axis and hence the centre of rotation can cause artifacts known as tuning fork artifacts (Cheng *et al.*, 2018). These would lead to errors in the greyscale values and subsequent errors in the reconstructed volume.

2.8 Reference objects

This section discusses the various reference objects that have been designed to study particular effects and factors associated with XCT some of which appear in the guidance

document by VDI/VDE (VDI/VDE-Richtlinien, 2010) which was mentioned above in Section 2.7. The reference objects can also be used, if their dimensions are already known from another measurement technique, to verify the metrological performance of a system.

2.8.1 Complex holeplate

The holeplate, which is described and used in Chapter 4, is based on a holeplate designed by the German National Measurement Institute (PTB), (Bartscher et al., 2014). It was designed to optimise the assessment strategy of ISO 10360-2, VDI/VDE 2630-1.3 and ISO 10360-11 that requires five length measurements along seven different spatial directions. Length measurements are the distances between the centres of two cylinders (unidirectional) and the distances between two points on the surface (bidirectional). Figure 2.36 illustrates the directions along which the measurements are to be taken to ensure they fulfil the requirements of the assessment strategy of the various standards. To minimise X-ray attenuation, the holeplate was manufactured from aluminium. Another design feature is that at least 5% of the X-ray intensity reaches the detector at any projection. Another holeplate was also manufactured in steel but was much smaller at only 6 mm x 6 mm compared to 48 mm x 48 mm for the aluminium holeplate.

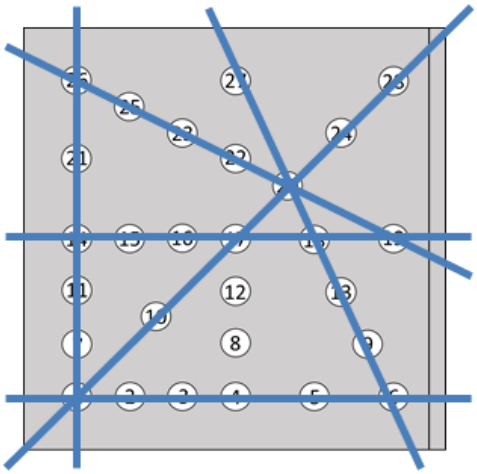

Figure 2.36 Direction of unidirectional and bidirectional measurements

The complex holeplate was again analysed by Bartscher et al., (2016) when the predominant measurements carried out were bidirectional lengths, 10 in total, using both inside and outside edges of the holes. The holeplate was imaged at an orientation of both 0° and 45° to horizontal. Length measurement errors when the holeplate was orientated at 0° were in the range of ±11 µm, for 45° they were found to be -13 µm to 1 µm.

Using the Fraunhofer software Scorpius XLab® Bartscher et al., (2014) carried out a simulation of the imaging of the holeplate in a vertical position. Unidirectional length measurements were taken and found to be within ±2 µm. The author does note deviation in the surface for both simulated and experimental data at the top and bottom of the holes but determines that they are due to the holeplate being imaged in a vertical position which then causes errors in the reconstruction. They state that if the holeplate had been orientated differently the errors would not have occurred, however, in Chapter 4 and Chapter 5 this study shows that is not the case.

Kasperl et al., (2014) used the holeplate made in aluminium and iron to look at the effects of the material on measurement errors. Both experimental and simulated data was calculated. Length measurements, probing errors and planarity errors are investigated and will be discussed in Section 2.8.2.

Villarraga-Gómez et al., (2016) used the smaller steel plate to study the measurement uncertainties when the holeplate was tilted in different directions. It should be noted that the measurements and analysis in this thesis had already been carried out before the release of this work. Further details can be found in Section 2.8.5 which discusses the errors associated with object orientation during imaging.

NIST, the National Institute of Standards and Technology in the US, indicate on their website, that they are considering using spheres within the complex holeplate, see Figure 2.37. It is assumed by the author that the sphere to sphere centre distances would be considered in the same way that the unidirectional lengths are taken between the different holes, see Section 4.2.5.

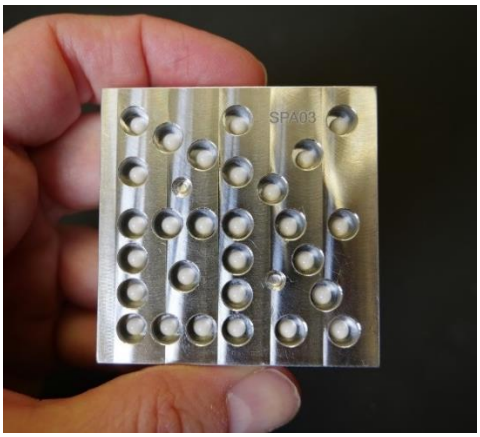

Figure 2.37 NIST reference object. Holeplate containing spheres in each hole (NIST, 2018)

2.8.2 Beam hardening

As described in Section 2.3.1, beam hardening is the attenuation of soft, low energy polychromatic X-rays in an object resulting in an increase in the overall mean X-ray energy and hence, an incorrect greyscale value being assigned. This in turn would lead to the incorrect threshold between the air and material being assigned which would lead to the surface of the object being defined incorrectly. This would cause the object to be the incorrect size leading to spatial errors.

Kasperl et al., (2014) used the complex holeplate described in Section 2.8.1 to study the influence of the material on the measurements obtained. Two different simulations for two different materials, aluminium and iron, were carried out. The reconstructed volumes were compared to a model of the holeplate, see Figure 2.38. The visible streaks seen are attributed by the author to beam hardening and lead to error in length measurements of ±50 µm for lengths of up to 50 mm. They also state that the artefacts are worse with the iron holeplate. Probing errors for the aluminium holeplate were found to between 55 µm and 85 µm and planes fitting to the surfaces showed planarity errors of 70 µm to 110 µm.

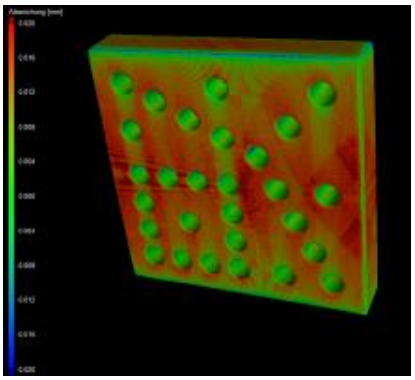

Figure 2.38 Comparison of volume and STL for iron holeplate simulated with polychromatic X-rays (Kasperl et al., 2014)

Tan et al., (2014) used experimental and simulated methods to investigate the effects of beam hardening on the dimensions of a 4 mm diameter steel pin, see Figure 2.39. The pin was surrounded by a step cylinder and the diameter of the pin was compared to CMM results. Maximum errors, with no beam hardening correction, are in the range of 6 µm.

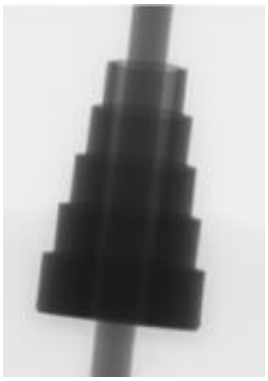

Figure 2.39 2D projection of a steel pin in steel step gauge (Tan *et al.*, 2014)

A step cylinder was also used by Kasperl et al., (2013) when developing a correction for beam hardening. The errors in the radii of the cylinders were found to be <17 µm for cylinders with diameters in the range of 15 mm to 55 mm.

2.8.3 Surface determination

As previously mentioned in Section 2.2.7, surface or threshold determination is crucial with regards to dimensional metrology. A test object was designed by Carmignato et al., (2009) to include external and internal features to test the chosen threshold values. It contains 12 fibres and 12 holes both of which have nominal diameters of 125 µm. Both a Cartesian CMM with a tactile probe and electron microscopy were used to calibrate the features. Differing greyscales of 49 to 61 (in a scale from 0 to 225) were used to define the threshold which caused errors in the diameters of the fitted cylinder of ±6 µm. The diameters and their discrepancies depending on threshold varied depending on whether it was an internal or external cylinder. As threshold values increased, the diameter of the inner features increased and vice versa for the external features.

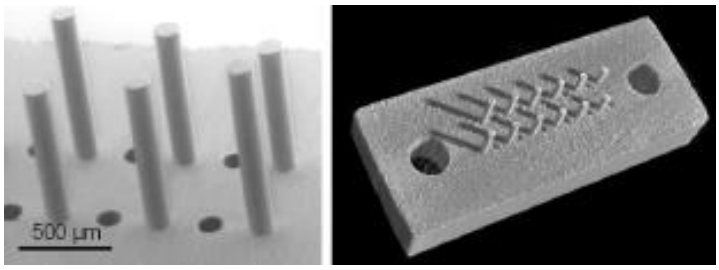

Figure 2.40 Glass fibre array by Carmignato et al., (2009)

Another reference object that highlighted errors with respect to the threshold of the object during imaging was an aluminium cube that contained internal grooves (Figure 2.41. The cube was designed by Kiekens et al., (2011) and highlighted the most accurate method to define lengths so that the threshold had the least effect, see Figure 2.41. The top diagram of Figure 2.41 (b) indicates a method where the length measurement is highly

dependent on the greyscale value chose for the surface. An incorrect greyscale value will result in incorrect dimensions, whereas the bottom diagram indicates a much more robust method that is not dependent on the greyscale value, because it takes two similar edges i.e. right to right not left to right in the other method.

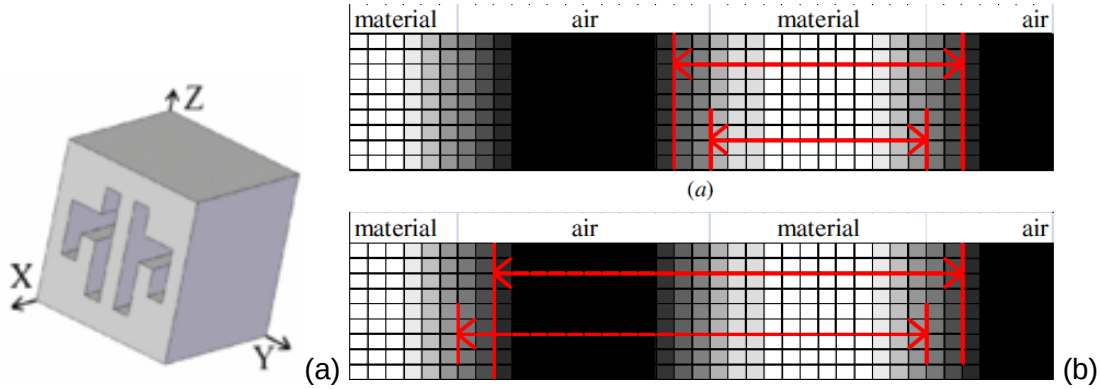

Figure 2.41 Reference object used (a) and different distances that are heavily dependent (top) or minimally dependent on the value used to determine the surface (b) (Kiekens et al., 2010)

2.8.4 Position of feature in object

The shape of the object being imaged can have an influence on the accuracy of distance measurements. Kiekens et al., (2011), who used a test object that was a cube with parallel cubes in its interior (Figure 2.41(a)), found that planes perpendicular to the rotational axis are subject to more noise due to scattering which in turn leads to inaccurate results.

2.8.5 Orientation of object

A study carried out by Angel et al., (2015) found that the orientation of the object during imaging affected unidirectional and bidirectional length measurements on step gauges of various materials (Figure 2.42). Maximum errors in the 2 mm lengths were found to be no greater than 6-7 µm, repeatability was found to be worse when the step gauge was in a vertical position. The authors state that scatter is the cause of the errors and this is why the errors vary depending on the material of the object.

Figure 2.42 Step gauges in various materials (Angel *et al.*, 2015)

As mentioned previously in Section 2.8.1, Villarraga-Gómez et al., (2016) used the smaller steel complex holeplate to study the effect of object orientation on unidirectional and bidirectional length measurements along with roundness of holes. Results indicated that the uncertainties in the measurements were minimised if the orientation is at 10°. They start to increase as the orientation starts to become greater than 35°.

The same authors (Villarraga-Gómez & Smith, 2015) used a series of aluminium blocks to study the effects of orientation Figure 2.43. The blocks contained holes, the roundness of which had been measured on a CMM. Deviations in roundness of up to 55 µm (radius 10 mm) were measured when the orientation of the object was of 40° and above.

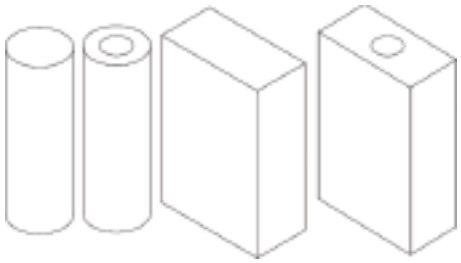

Figure 2.43 Geometric shapes used in study by Villarraga-Gómez & Smith, (2015). They had dimensions of 60 mm x 20 mm x 40 mm, the holes a radius of 10 mm

2.8.6 Magnification

The effects of magnification on XCT dimensional metrology has been studied by a few authors who have used various objects to measure the effects.

Nardelli et al., (2012) tested the influence of many different variables such as magnification and system set up on the shape of multiple test objects seen in Figure 2.44. Measurements were acquired from the different objects including a profile of the circumference of an aluminium multi-wave standard (described below in next paragraph after the figure) which has a nominal diameter of 76 mm, a step cylinder (nominal diameter of 74 mm) and a toothbrush head (nominal diameter of 13.4 mm). All of the objects were measured on a CMM to obtain reference data. The quality of the results was defined by the root-mean-square deviation parameter which is based on the reference radius for the objects. The multi-wave standard highlighted errors of between 3 µm and 4.5 µm. For the step cylinder, for a voxel size of 120 µm the RMS value was 7.7 µm, for a lower magnification with a voxel size of 320 µm the RMS was 11.4 µm. The author states that errors due to magnification are systematic and homogeneous across a feature so can be corrected for.


(a)
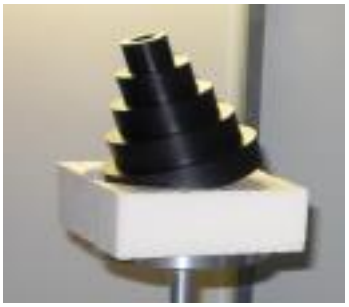
(b)

(c)

Figure 2.44 Test objects used by Nardelli et al., (2012) *multi-wave standard (a), polyoxymethylene step cylinder (b) and calibrated production workpiece (c)*

In contrast to form measurements of standard shapes such as cylinders, a multi-wave standard allows for a measurement procedure that acquires data over a broad spectral band (PTB, 2000). The standard consists of a cylinder with form deviations that are defined by a sinusoidal function consisting of multiple wavelengths. This sinusoidal function creates a spatial signal which corresponds to a line spectrum which can be compared to the calibrated line spectrum.

Silicon Nitride spheres were used by Shi et al., (2014) who studied the effect of differing magnifications on probing form error and probing size error. Probing form error is the difference between the maximum and minimum radii of the measured sphere. Probing size error is the difference between the measured diameter and the reference diameter. Five different spheres were used with sizes ranging from 4 mm to 50 mm. Results, which are just listed as probing error, indicate a decrease in error from 50 µm to 5 µm as the magnification is increased from ×1 to ×20.

A simple ball bar was used by Weckenmann and Krämer, (2009). The distance between the centres of the two spheres was measured (nominally 20 mm) for two different magnifications, ×1 and ×2. The difference between the XCT and reference lengths was -18 µm for the lower magnification and -7 µm for the higher magnification.

A ball plate, see Figure 2.45, was used by Müller et al., (2012) to explore factors effecting the reconstructed image's quality, one of these factors was magnification. Sphere centre positions, sphere diameters, centre to centre distances and form errors were measured. The ball plate was imaged in a vertical position. Sphere distance errors were found to be ±30 µm for high magnifications but reduced to ±10 µm for lower magnifications. This is the opposite of what was found by the other authors who obtained lower magnitude errors at higher magnifications. Müller et al., (2012) put the errors down to the Feldkamp effect (discussed in 2.2.6.2) and the resultant artefacts in the images.

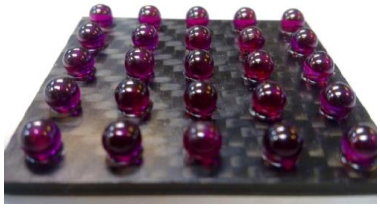

Figure 2.45 Ruby spheres, 5 mm in diameter glued to carbon fibre plate (Müller et al., 2012)

2.8.7 Feldkamp effect

Also known as the cone beam effect, the Feldkamp effect causes artefacts such as blurring (Villarraga-Gómez & Smith, 2015) at the outer edges of the projection image. As seen in Section 2.2.4, it has been suggested that errors, such as those described above by Müller et al., (2012), can be reduced with the use of helical scanning. Simulated data of spheres with a 4 mm diameter was used by Hiller et al., (2010) using both circular and helical scanning and reconstruction. The spheres were positioned in different positions within the cone beam. It was found that for the helical scanning the probing form errors for all the spheres were between 5.4 µm and 7.9 µm. For circular scanning the central spheres had form errors of 4.3 µm and 6.3 µm, however, for spheres on the outer edges of the cone beam, errors of 22.7 µm to 24.3 µm were present indicating that helical scanning can reduce Feldkamp errors. This is because when helical scanning is being used a complete data set is captured and all the surfaces will be intersected by at least one X-ray trajectory, as described in Section 2.2.6.2. This can be illustrated in Figure 2.46 which shows how all surfaces will intersect with an X-ray trajectory when helical scanning us used, unlike the cone beam where the top and bottom of an object may be missed resulting in shadows in the data.

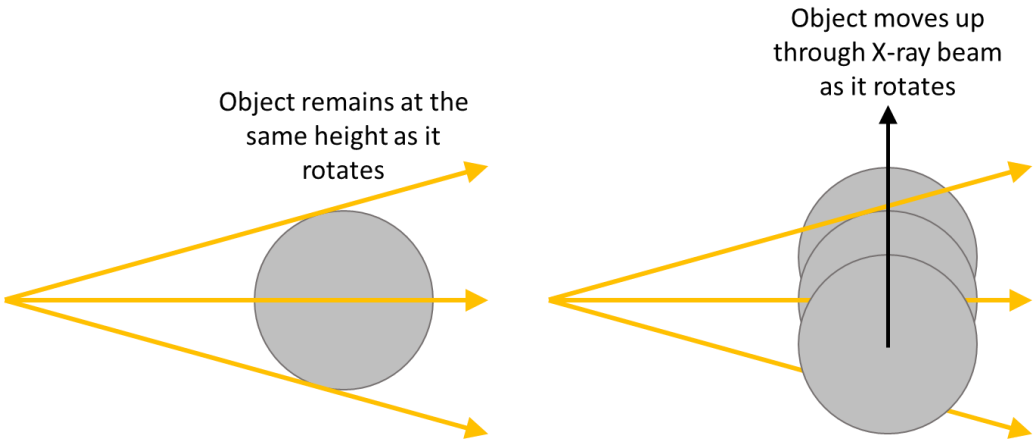

Figure 2.46 Circular cone beam (a) and helical scan set up (b)

A calibrated cube with spherical caps (see Figure 2.47) was used by Muders et al., (2011) to study the difference between circular and helical reconstruction. Both experimental

and simulation data was collected. The results were contradictory to those seen above in that the form and length deviations were higher for the helical scanning. The authors state that this was due to certain parameters, such as detector offset, being manually chosen for the helical scanning which was not the case for the circular scan.

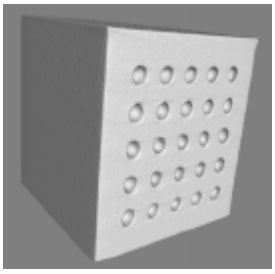

Figure 2.47 Calibrated cube used by Muders et al., (2011)

2.8.8 Noise

Buzug, (2010) states that noise in reconstructed images can be divided into two categories; quantum noise and detector noise. Quantum noise is a result of the stochastic fluctuations that are a due to absorption and scattering of the X-rays as they pass through an object. Due to the random nature of the radiation, no two images in the same set up will be identical. With an increase in intensity comes a linear increase in quantum noise. The detector noise is a result of the electrons within the detector and is not related to X-ray exposure.

An inter-laboratory comparison of four test objects, see Figure 2.48, was carried out by Carmignato, (2012). Measurements were carried out by 15 different research institutions and companies. Results indicate that noise is the largest influence on form measurements as opposed to length measurements. This is because length measurements are often based on an averaging calculation that removes outliers, which is not the case for form measurements. The author notes that the noise in the projection increases as the number of photons reaching the images decreases. This is crucial with the advance of in-line scanning systems that require very quick imaging times.

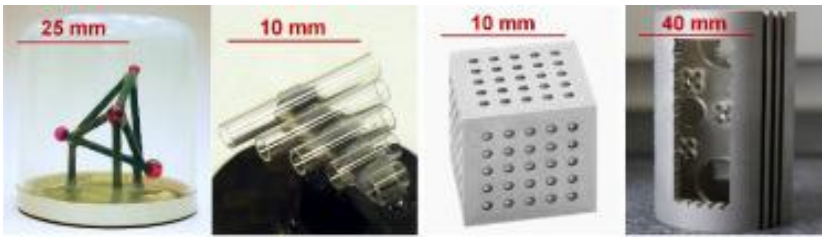

Figure 2.48 Test objects used for interlaboratory comparison (Carmignato, 2012)

Hermanek and Carmignato, (2017) state that if the tube current is increased a higher signal-to-noise ratio can be attained.

2.9 How industry is affected

XCT, as shown by the user's survey, is used in many industries and sectors including manufacturing. Within the manufacturing industry XCT allows for the testing of the product throughout the whole manufacturing process. XCT has many roles within the manufacturing industry, from qualitative visual inspection of pores and cracks for defect analysis to dimensional metrology which involves nominal/actual comparisons and dimensional measurements of form and geometry, see Figure 2.49. De Chiffre et al., (2014) summarises the many industries that use XCT including, manufacturing, casting and form, machining, injection moulding, assemblies and additive manufacturing.

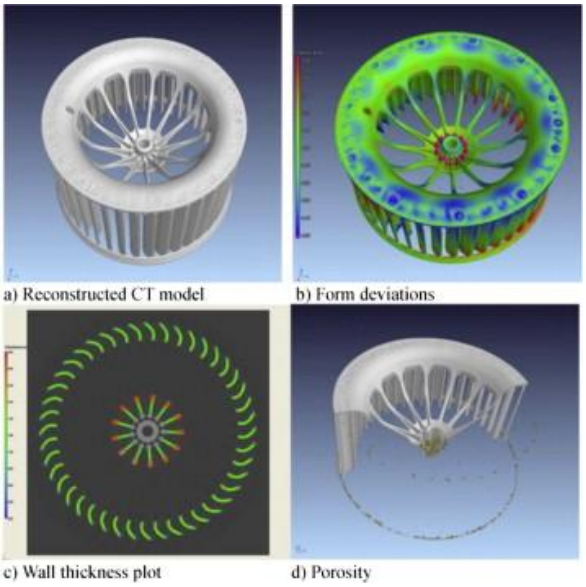

Figure 2.49 Multiple uses of XCT outputs. CT model, form deviations, porosity and wall thickness plot (clockwise from top left) (Kruth *et al.*, 2011)

This project is focussing on the geometry of objects, in particular the shape of cylinders. Figure 2.50 highlights a selection of manufactured objects, all of which contain holes in different positions and orientations within the object as a whole. As seen in Chapter 4 and Chapter 5 these two factors are crucial to the apparent geometry of a cylindrical shape imaged with XCT.

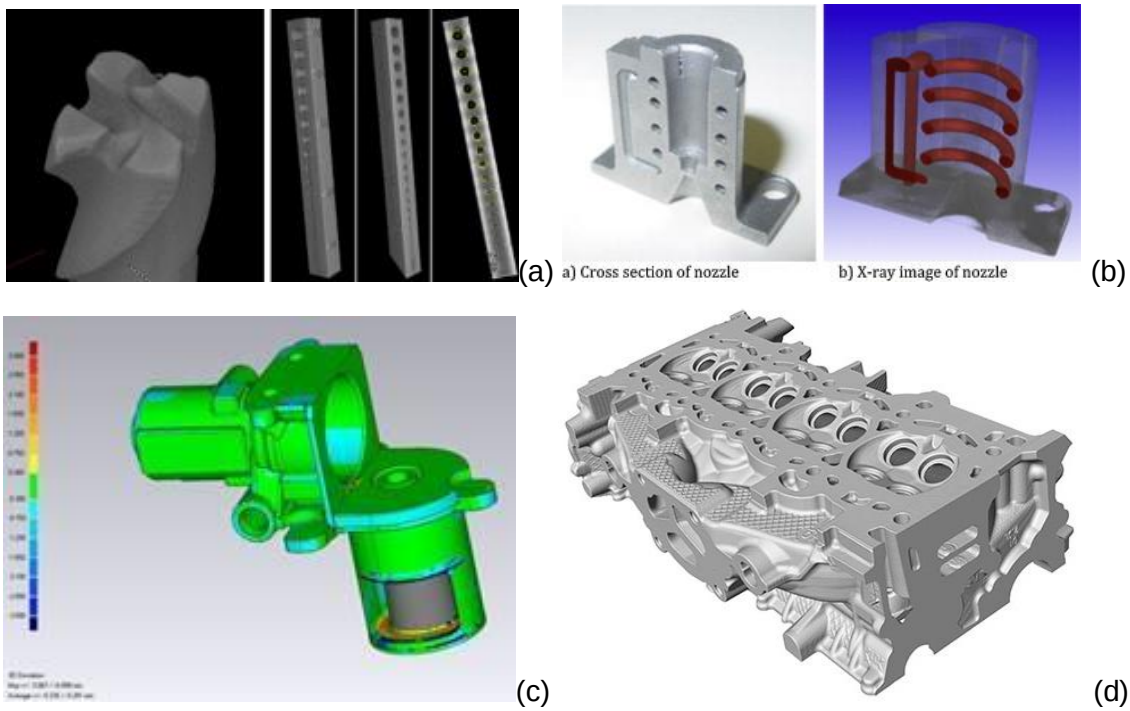

Figure 2.50 (a) Micro milling cutter and micro holes with diameters of 0.55 mm to 4 mm (De Chiffre *et al.*, 2014)*. (b) AM injection nozzle* (De Chiffre *et al.*, 2014)*. (c) Aluminium casting* (NSI, 2018)*. (d) Cylinder head* (Yxlon, 2016)

The British Standard ISO 286-1:2010 (British Standards Institution, 2010) outlines the limits and fits for machined workpieces. It specifies tolerances values that have to be considered, from the design stage through to manufacturing and finally quality control. As the top table in Figure 2.51 shows, for very precise manufacturing, the tolerance levels can be sub-micron. As the size of the object being manufactured increases it can be seen there is an increase in tolerance too. The bottom table in Figure 2.51 shows examples of some of the different manufacturing processes that would use the different tolerance grades. This will be discussed in Chapter 5 to determine if the results seen in this study will affect the manufacturing and quality control process.

Nominal size (mm)		Standard tolerance grades																	
Above	Up to and including	IT01	IT0	IT1	IT2	IT3	IT4	IT5	IT6	IT7	IT8	IT9	IT10	IT11	IT12	IT13	IT14	IT15	IT16	IT17	IT18
Standard tolerance values																					
		µm													mm						
—	3	0.3	0.5	0.8	1.2	2	3	4	6	10	14	25	40	60	0.1	0.1	0.3	0.4	0.6	1	1.4
3	6	0.4	0.6	1	1.5	2.5	4	5	8	12	18	30	48	75	0.1	0.2	0.3	0.5	0.8	1.2	1.8
6	10	0.4	0.6	1	1.5	2.5	4	6	9	15	22	36	58	90	0.2	0.2	0.4	0.6	0.9	1.5	2.2
10	18	0.5	0.8	1.2	2	3	5	8	11	18	27	43	70	110	0.2	0.3	0.4	0.7	1.1	1.8	2.7
18	30	0.6	1	1.5	2.5	4	6	9	13	21	33	52	84	130	0.2	0.3	0.5	0.8	1.3	2.1	3.3
30	50	0.6	1	1.5	2.5	4	7	11	16	25	39	62	100	160	0.3	0.4	0.6	1	1.6	2.5	3.9
50	80	0.8	1.2	2	3	5	8	13	19	30	46	74	120	190	0.3	0.5	0.7	1.2	1.9	3	4.6
80	120	1	1.5	2.5	4	6	10	15	22	35	54	87	140	220	0.4	0.5	0.9	1.4	2.2	3.5	5.4

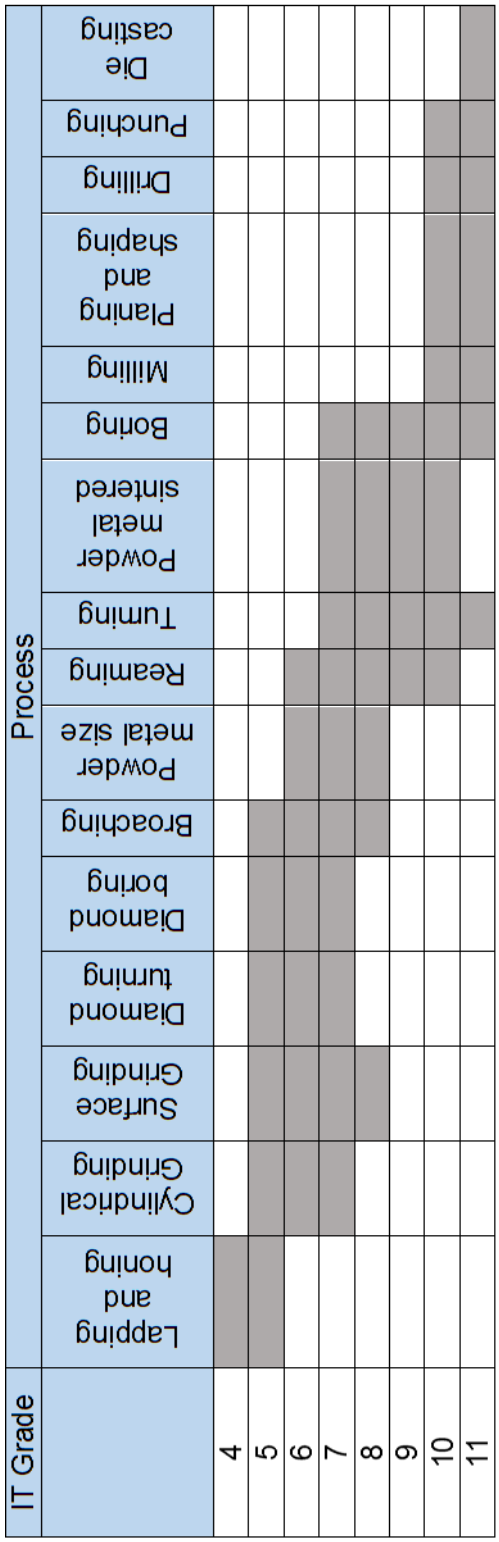

Figure 2.51 Top: Values of standard tolerance grades (British Standard, 2010). Bottom: Machining processes and IT grades ((Oberg et al., 2016)

Chapter 3: X-ray field variations and their effects on metrology

This chapter details the investigation, using ionisation chambers and a spectrometer, into the intensity variation of the X-rays emitted from the X-ray source across the cone beam and during the time it takes to image an object. Findings from a previous experiment, seen in Section 1.6, carried out by the author for an MRes dissertation, indicate that the threshold for the defined surface varied depending on the location of the sphere in the image. To determine if this was due to a variation in the X-ray intensity reaching the detector both across the detector and throughout time, a series of tests were devised to measure the flux of the X-rays using both ionisation chambers and a spectrometer. Results indicate that there is temporal variation in the intensity of the X-rays and spatial variation across the cone beam both in the intensity and the spectrum of the X-rays.

3.1 Temporal measurement of X-ray flux

When reconstructing images in CT Pro it could be seen that the first and last images were not always of the same intensity. To determine if this was caused by either a variation in the intensity of the X-rays or an issue with the detector a series of measurements was carried out to try to identify and quantify the cause.

Initially a set of images, with no object in the field of view, was acquired from the XCT system to determine the amount of change in the intensity of the images themselves. The voltage was set to 150 kV and the current to 50 µA. The mean greyscale of each image was calculated in MATLAB.

The mean intensity or greyscale value for the 3142 images taken over the usual imaging time (53 minutes) can be seen in Figure 3.1. As the graph shows, there are peaks and troughs in the intensity along with abrupt changes. This indicates that there is potentially a variation in the intensity or flux of the X-rays reaching the detector. Comparing the maximum and minimum throughout the time period it can be seen that the flux varies by approximately 2% throughout the measurement period.

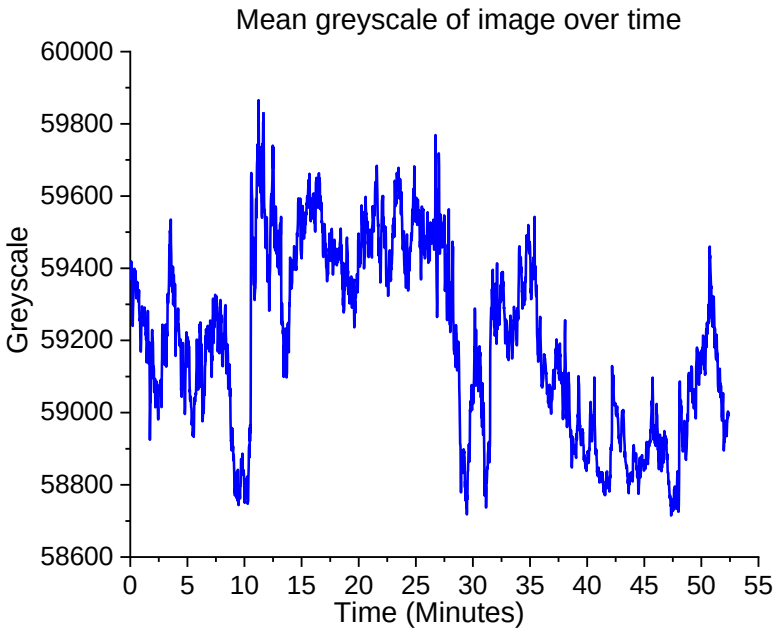

Figure 3.1 Mean greyscale of images throughout the time of one measurement

To measure the intensity of the X-rays throughout the time of imaging, a thimble ionisation chamber was used (a description of how this equipment works can be seen in Section 2.2.5.2). Various experiments were carried out using different voltages and currents with the ionisation chamber initially within the centre of the cone beam.

The ionisation chamber was placed between the source and the detector, giving a magnification of x2.9. The chamber was clamped in position on the manipulator, see Figure 3.2. Readings were taken every 0.5 seconds.

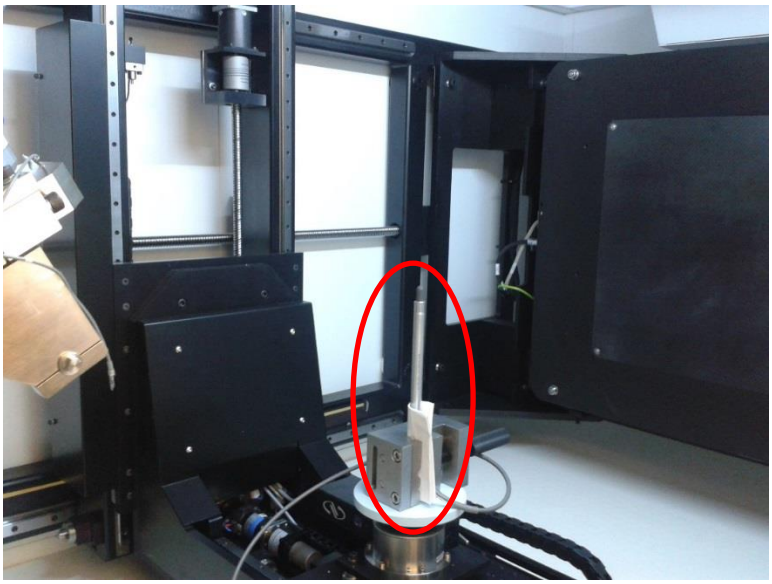

Figure 3.2 Thimble ionisation chamber (circled) positioned in XCT system at NPL

For the first experiment, the X-rays were switched off in between changing the voltage. In all the other experiments, the voltage and current of the X-ray gun and the position of the chamber were changed whilst keeping the X-rays on, thereby eliminating the need for stabilisation of the source (British Standards Institution, 2011).

The data is automatically corrected for temperature and pressure. As mentioned in Section 2.2.5.2, ion pairs are produced in the chamber resulting in positive and negative ions. An electric field is used to separate the ions and, in the case of the detector used in this study, a positive field was applied to collect the negative ions, therefore the outputs seen in the following graphs are all negative.

3.1.1 Constant kV and µA

For this experiment the ionisation chamber was placed in the centre of the image and the current and voltage were kept constant for 20 minutes. The output of the ionisation chamber was recorded for the whole period. The voltage was increased in 20 kV intervals and the measurement repeated. The voltage ranged from 100 kV to 200 kV, the current was kept constant at 300 µA.

When the output of the ionisation chamber is monitored over a 20 minute period, it can be seen that there is a settling period of less than a minute for all voltages apart from 200 kV where the results take approximately 3.5 minutes to become steady, as seen in Figure 3.3. It should be noted that when the first measurements (100 kV) were made the X-ray source had not been switched on for a significant amount of time and may not have stabilised completely. In between the other measurements the X-rays were only switched off for a maximum of a couple of minutes, therefore the source would be more stabilised. This, however, does not appear to have affected the results.

The intensity varies depending on the X-ray energy, however, an increase in voltage does not lead to an increase in output. This can be seen more clearly in Figure 3.4 which is comparing the results of the different voltages to the lowest voltage, i.e. the average output for each of the voltages is divided by the average for the lowest voltage, this value is termed factor.

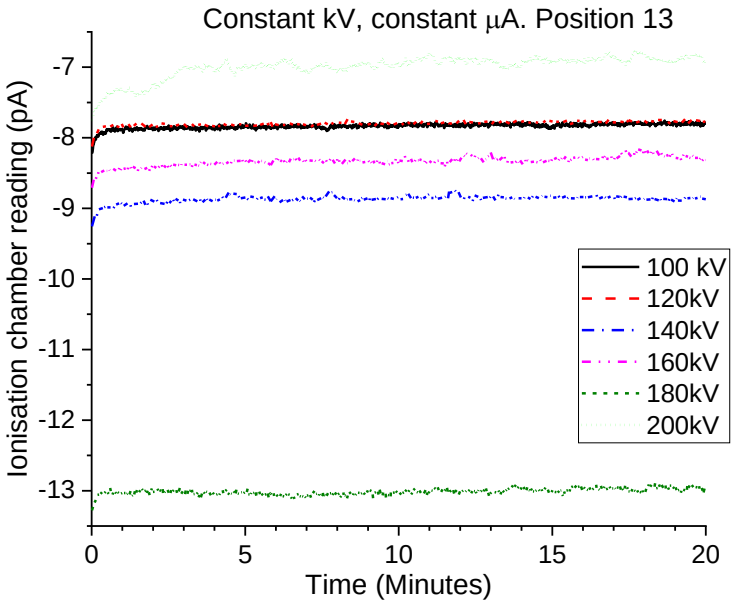

Figure 3.3 Constant kV, constant current for 20 minutes

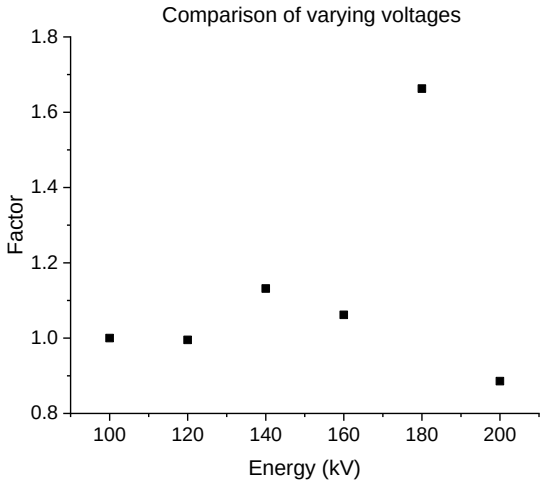

Figure 3.4 Comparison of average output for different voltages

Figure 3.5 illustrates normalised data, where the lowest and highest values, used for normalisation, are based on each voltage's individual data set. The range in standard deviations can be seen, noting particularly the higher standard deviation at 200 kV. The anomalies seen at 200 kV are discussed further at the end of Section 3.1.2. The range in data shows variation for the different voltages, this is indicative of the sudden spikes seen in in the data in Figure 3.1. The mean can be seen to be sitting in the upper regions for all the voltages.

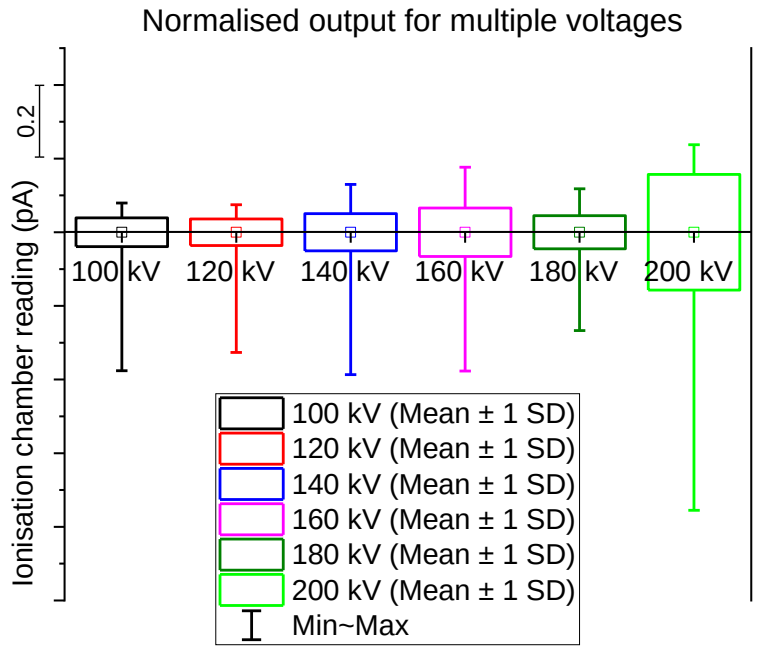

Figure 3.5 Normalised output for multiple voltage, constant current

When the data is plotted on a different scale, as seen in Figure 3.6, it can be seen that there is a drift over time in the data for all voltages, there is a steady increase in the output as time passes, this would explain the change in intensity seen in the first and last images observed during the reconstruction process.

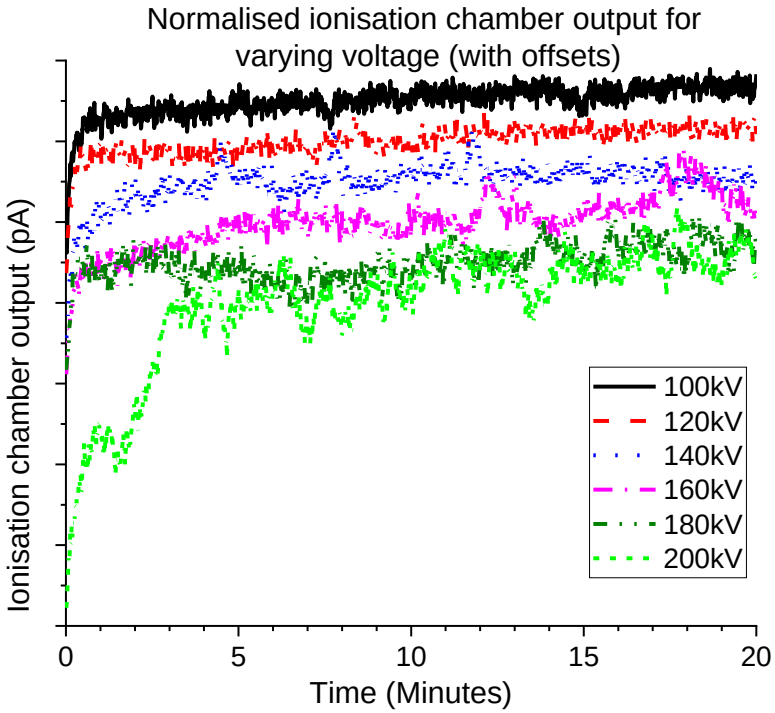

Figure 3.6 Ionisation chamber output for varying voltages (with offsets)

3.1.2 Varying kV, constant µA

The ionisation chamber outputs were now compared over a larger range of voltages, for a shorter time and without the X-ray tube being switched off between readings. The output was recorded for 5 minutes at each voltage. The voltage ranged from 80 kV to 220 kV in 20 kV intervals. The current was kept constant at 300 µA and the ionisation chamber was in the centre of the image.

As Figure 3.7 shows, the settling time seen in the data in Figure 3.3 is only visible at the beginning of the experiment. This indicates that the stabilisation of the data is due to the warming up of the X-ray tube.

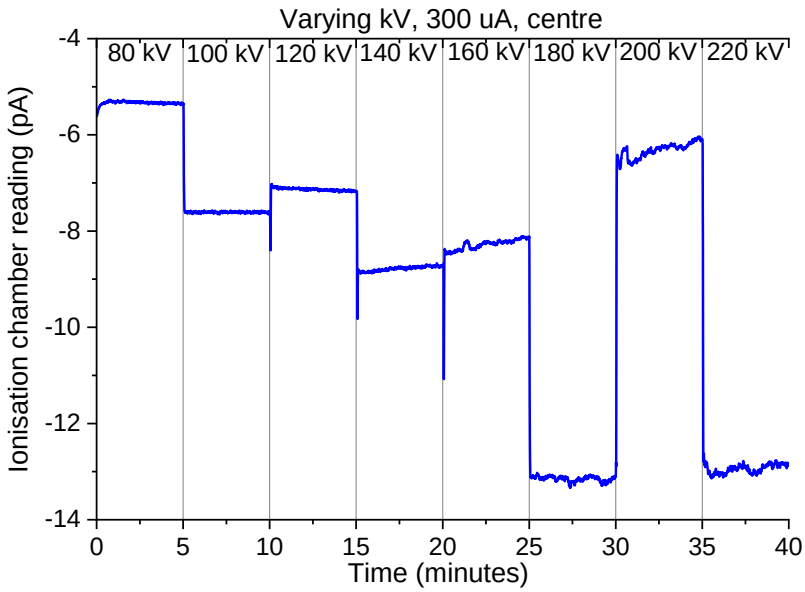

Figure 3.7 Voltage changed without switching off X-rays, constant current (300 µA)

If the results are compared with the lowest voltage, as before, it can be seen that the trend is for the factor to increase as the voltage increase, except at 200 kV again (Figure 3.8). The increase in energy and therefore increase in ionisation of the gas within the ionisation chamber is due to the higher energy X-rays being able to ionise more molecules therefore creating more ion pairs that will subsequently be detected.

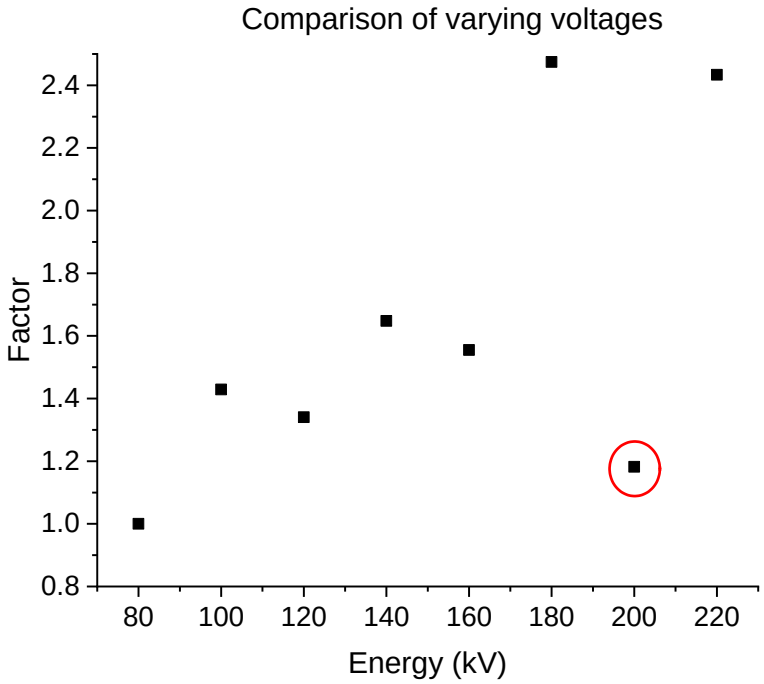

Figure 3.8 Comparison of average output for different voltages (80-220 kV)

These results indicate that the intensity at 200 kV is not following the usual trend and the XCT system does not perform as expected at that voltage. Following on from these findings it was found that discrepancies and instability had been noted by other users of this particular system. They reported sudden losses of intensity at 200 kV, the reason for this was unknown. For this reason, voltages for the rest of the experiments for this thesis were kept to below 185 kV.

3.1.3 Varying µA, constant kV

This is similar to the experiment above but in this case the current varied between 50 µA and 500 µA. The voltage was kept constant at 100 kV and the ionisation chamber was in the centre of the image. Measurements were taken for 5 minutes at each current.

When comparing outputs of the ionisation chamber when the current varies and the voltage remains constant (Figure 3.9), it can be seen that the signal becomes more negative as the current increases. This trend remains true until 400 µA when the signal becomes more positive up to 500 µA. The trend can also be seen in Figure 3.10 where the factor between the lowest result and the subsequent results shows an increase and then a decrease.

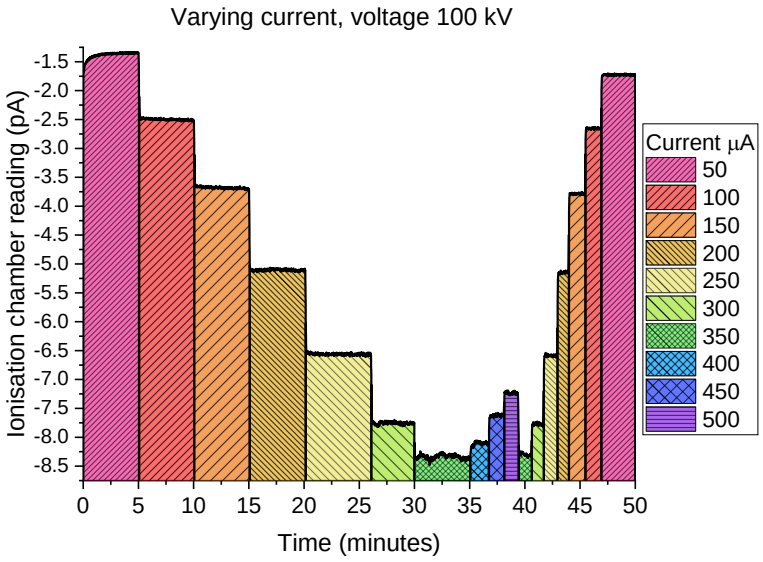

Figure 3.9 Ionisation chamber output for various currents, constant voltage (100 kV)

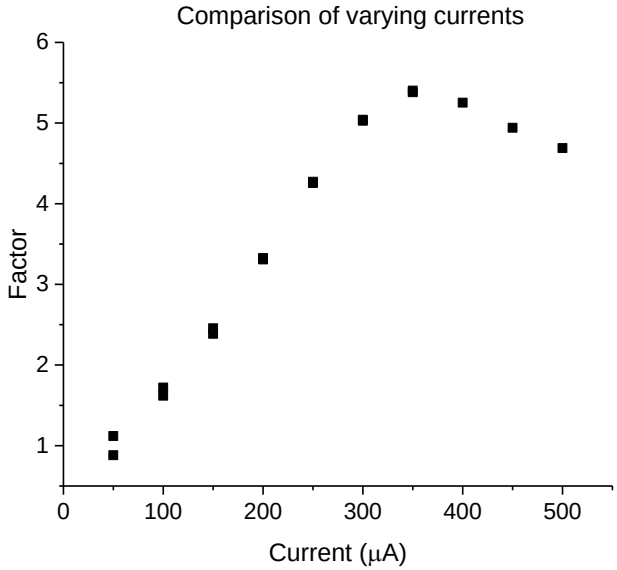

Figure 3.10 Comparison of average output for different currents

As the current is increased the number of electrons fired at the target increases, therefore the number of X-rays produced will increase leading to an increase in the number of ionisation events in the ionisation chamber.

A possible reason behind the decrease when the current reaches 400 μA is dead time within the ionisation chamber as the number of ionisation events increases. The efficiency of any given detector depends on the amount of time required for each event to be dealt with before it can deal with the next event. This interval is known as dead time and is the time interval between a particle arriving at the detector and it being able to process the arrival of another particle and can become an issue at high count rates

(Seco, Clasie & Partridge, 2014). Any event that occurs during this time will not be recorded and the detector will become saturated (Becares & Blazquez, 2012).

The temporal measurements of the X-ray flux carried out in this section indicates that if the X-ray source is allowed to warm up, the intensity of the X-rays in the centre of the cone beam can remain relatively stable as the voltage and current is increased, there can, however, be sudden changes in intensity of approximately 2% of the output but the stability does return. This is excluding when the X-ray source is at 200 kV, when unexplained anomalies can be seen. The sudden changes in intensity would explain the variation in the intensity of the images seen over time. There does appear to be an overall drift for all of the voltages over time.

3.2 Spatial measurement of X-ray flux

As variations in intensity had been seen down the 2D images the ionisation chamber was placed in different positions across the cone beam. The image on the detector was divided up into 25 equal sections (see Figure 3.11) and the X and Y coordinates of the manipulator were recorded for when the ionisation chamber was in the centre of each of these sections. When the chamber was moved, the coordinates were entered into the XCT software and the manipulator was moved automatically to decrease movement time in between different positions. The position only changed in the X and Y axes. Due to the height of the manipulator and chamber it was not possible to position it along the bottom of the detector.

1	2	3	4	5
6	7	8	9	10
11	12	13	14	15
16	17	18	19	20
21	22	23	24	25

Figure 3.11 Grid layout for chamber position on image

To check and correct for any drift over time, readings were taken in the centre at the beginning, the end and after subsequent measurements at different locations.

The sequence of positions was:

$$13 \rightarrow 1 \rightarrow 13 \rightarrow 5 \rightarrow 13 \rightarrow 11 \rightarrow 13 \rightarrow 15 \rightarrow 13 \rightarrow 16 \rightarrow 13 \rightarrow 20 \rightarrow 13$$

The experiment was repeated for different voltages: 100 kV, 150 kV and 200 kV all at 300 µA.

The results at 150 kV can be seen below in Figure 3.12 and they indicate that the intensity of the cone beam does indeed seem to vary in different locations.

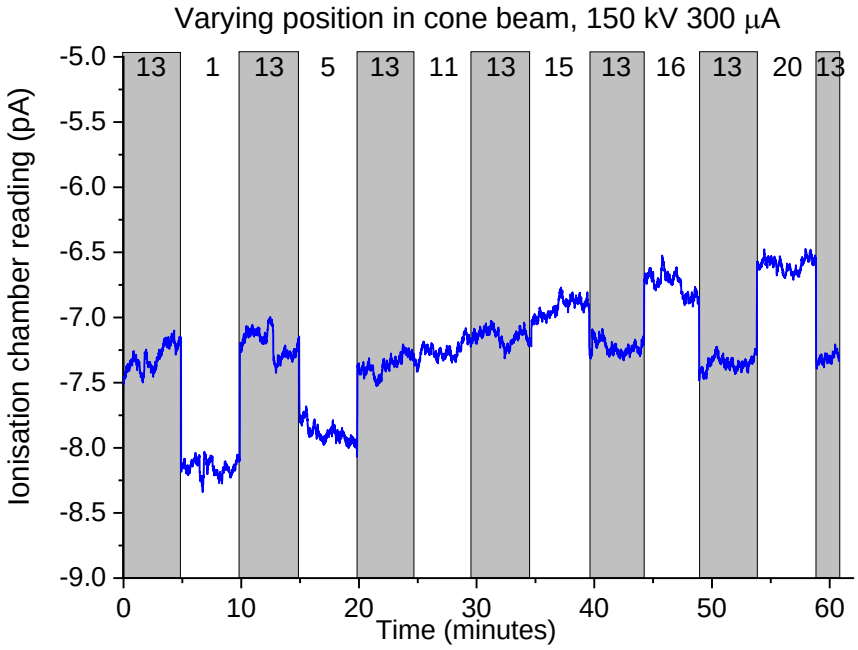

Figure 3.12 Output for ionisation chamber in various location in cone beam. Numbers at top specify position (see Figure 3.11). Grey band indicates central location

To verify if the differences between the centre values were significantly different or if drift had occurred, a two sample t-test (significance level of 0.05) was run on each consecutive central pair. A t-test is used to compare the means of two populations (NIST, 2013) and determines if they are significantly different from each other. The analysis was carried out in Origin Pro and it was run assuming both that the variances of the samples were the same and different.

The null hypothesis was that the means of the two samples would be equal i.e. (mean1 - mean2 = 0). The null hypothesis would be rejected if, at a level of 0.05, the difference in the means was significantly different from 0.

The results of the t-test showed that the results between the different central readings were significantly different, the null hypothesis was rejected, the drift, therefore, had to be corrected for, in both the centre readings and the corner readings.

These blocks of measurements at the centre will be subsequently called 13-1, 13-2, 13-3, etc. as the procedure is described below.

This drift was corrected for by firstly calculating the mean of both 13-1 and 13-2. The central time for the readings were used to calculate the time difference between the two

sets of readings (Figure 3.13). The correction for drift was calculated by dividing the difference in the means by the time difference.

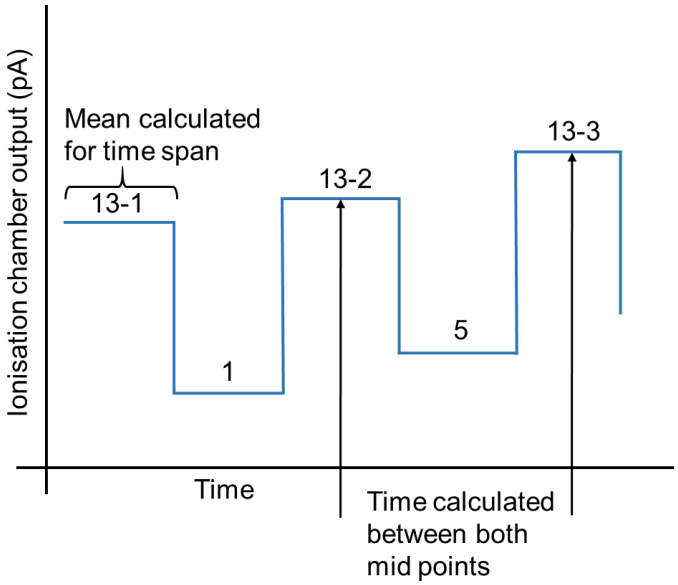

Figure 3.13 Different values used in drift correction

This scaling factor was applied to 13-2 and a new mean was calculated. The scaling factor was then applied to the data for positon 1. The process was repeated this time for 13-2 and 13-3 using the new mean for 13-2. The corrected results for 150 kV can be seen in Figure 3.14. After the correction, the difference in the means for the centre readings are no longer significantly different, but when compared with the results from other positions in the cone beam the null hypothesis was rejected indicating that there is still a significant difference from zero at a level of 0.05 between the two means.

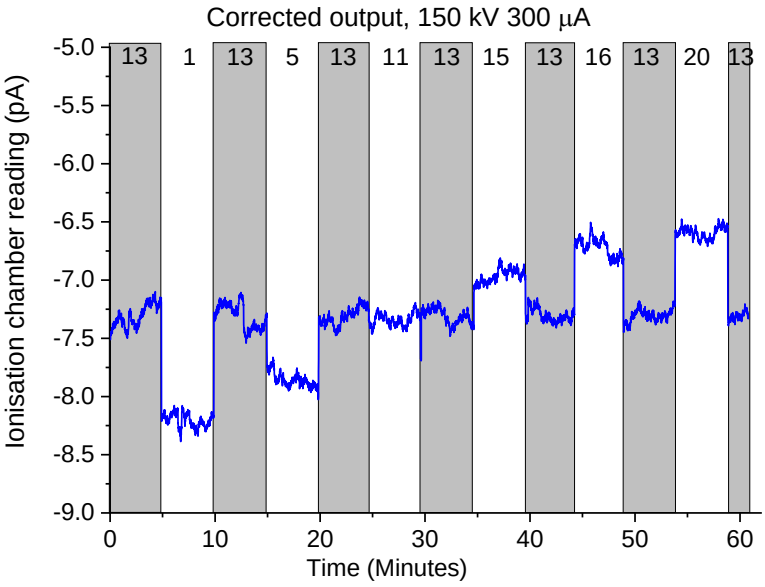

Figure 3.14 Corrected output for ionisation chamber at different locations around cone beam for 150 kV

Following on from this discovery it was decided to repeat the experiment and corrections, but this time just place the ionisation chamber in the corners (positions 1, 5, 16, 20) and with three different voltages (100 kV, 150 kV and 200 kV).

The results, seen in Figure 3.15, show similar trends in the rise and fall of the intensity depending on the position of the ionisation chamber within the cone beam. In positions 1 and 5, at the top of the beam, the results become more negative indicating a higher intensity than in the centre. Conversely, in the lower positions of 16 and 20, the results are more positive, indicating that the intensity is not as high as seen in the middle. The only difference between the results for the different voltages is that the range of intensities increases with the increase in voltage. There is also a difference horizontally across the detector with higher values seen on the right in positions 5 and 20.

The mean for each position was used to plot contour graphs, which can be seen in Figure 3.16. It should be noted that these plots are just based on the five points of measurement. All three plots show the change in intensity down the cone beam. This is what is seen in Figure 1.11 in Section 1.6 which indicated a decrease in the intensity down the image. This indicates that the change in intensity is due to a variation in the X-rays and not the detector.

It can be seen that at 150 kV there is a difference in the intensity of 10% from the top to the bottom of the detector. The influence of this on metrology will examined further in Chapter 5 where the gradient in intensity seen here will be applied to simulated images.

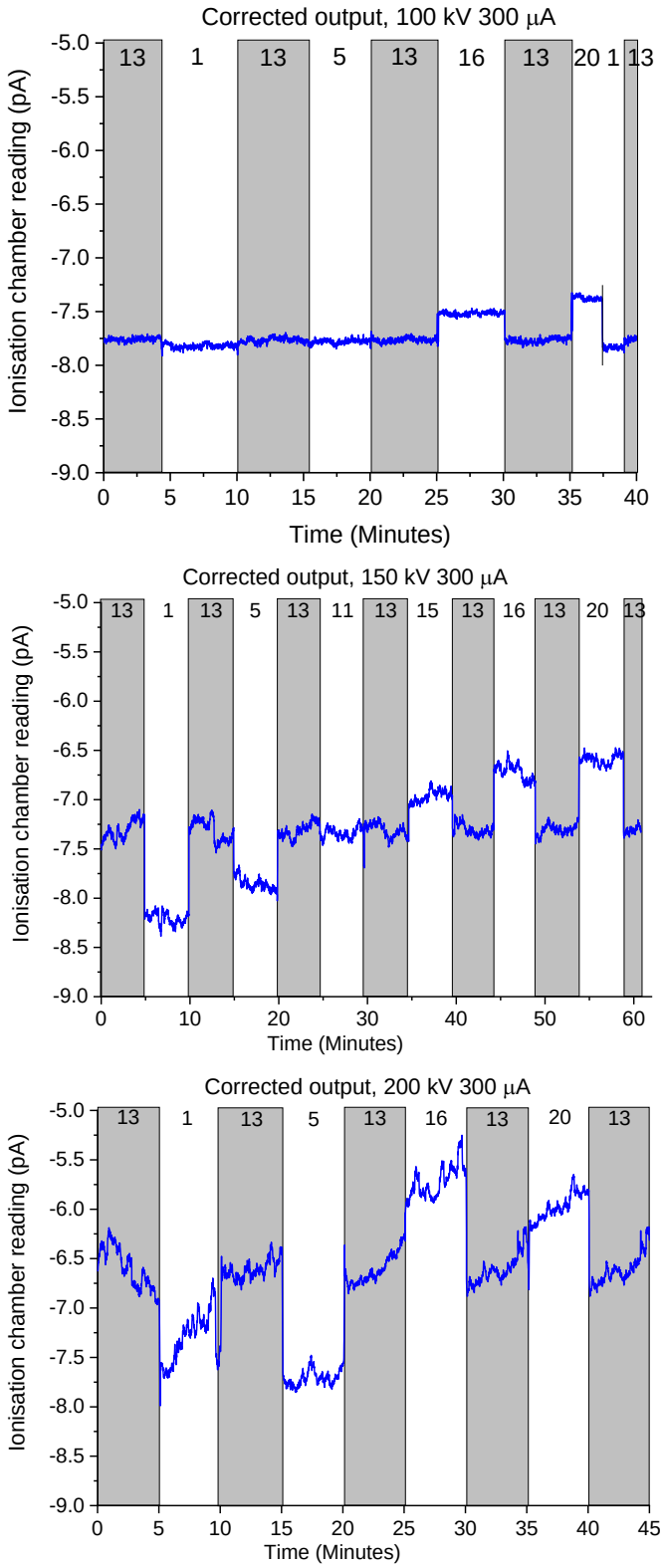

Figure 3.15 Corrected output for ionisation chamber measurements at corners for 100 kV, 150 kV and 200 kV

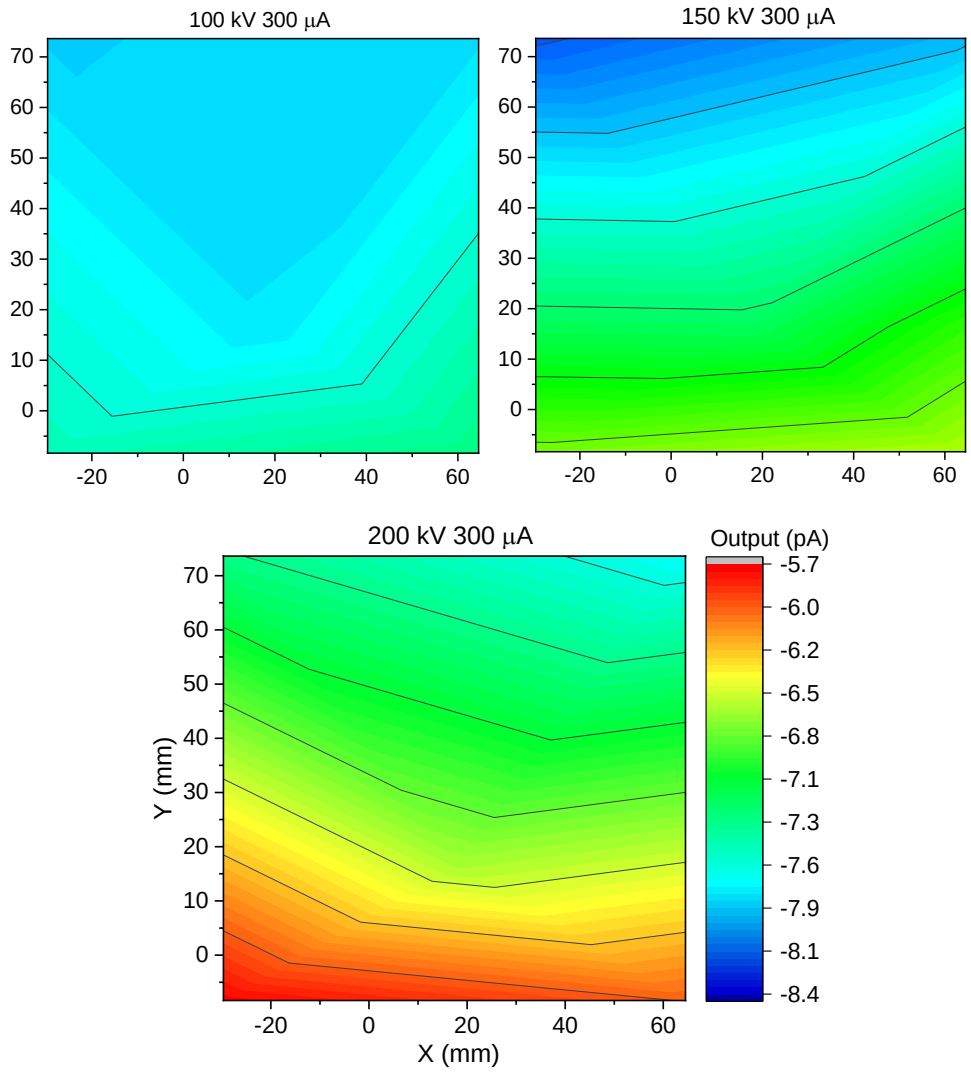

Figure 3.16 Contour plot of Corrected output for ionisation chamber measurements at corners for 100 kV, 150 kV and 200 kV

Although the results of the single ionisation chamber indicated a variation in the intensity of the X-ray flux depending on the position of the chamber, the density of the points across the cone beam was very sparse, therefore an array of ionisation chambers was used to get a more detailed view of the intensity profile across a section of the cone beam.

A PTW Octavius 729 was used to collect a more detailed view. A description of how this equipment works can be seen in Section 2.2.5.3. This detector contains as array of 27 x 27 ionisation chambers with each chamber measuring 5 mm x 5 mm x 5 mm. The centre to centre distance between chambers is 10 mm. The measured quantity is absorbed dose as it is usually used for calibrating systems used for radiotherapy. Absorbed dose is the amount of energy absorbed per unit mass, the units are the Gray (Gy). It is

assumed that the array has a uniform sensitivity as it is used to test hospital equipment and would therefore have to be calibrated correctly.

The chamber array was positioned on the manipulator and a clamp was used to keep the array horizontal, see Figure 3.17. The manipulator was positioned to ensure the complete extent of the cone beam was visible on the array, see Figure 3.18.

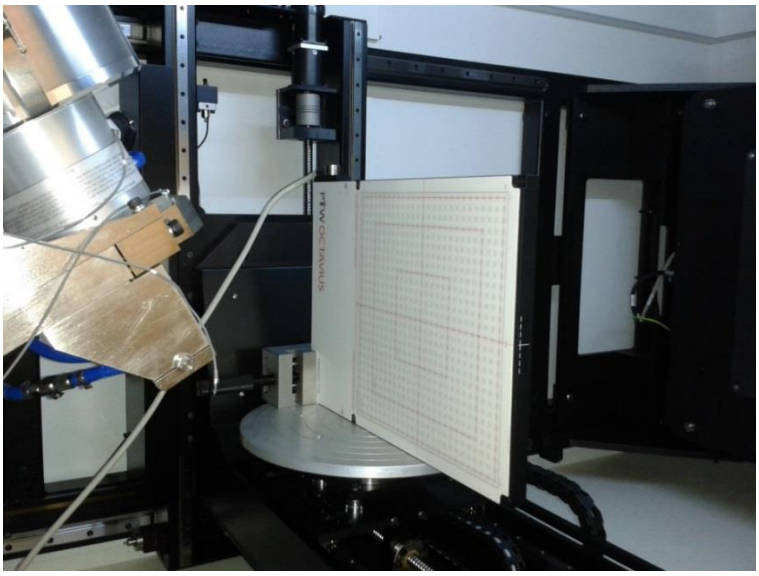

Figure 3.17 Ionisation chamber array position in XCT system at NPL

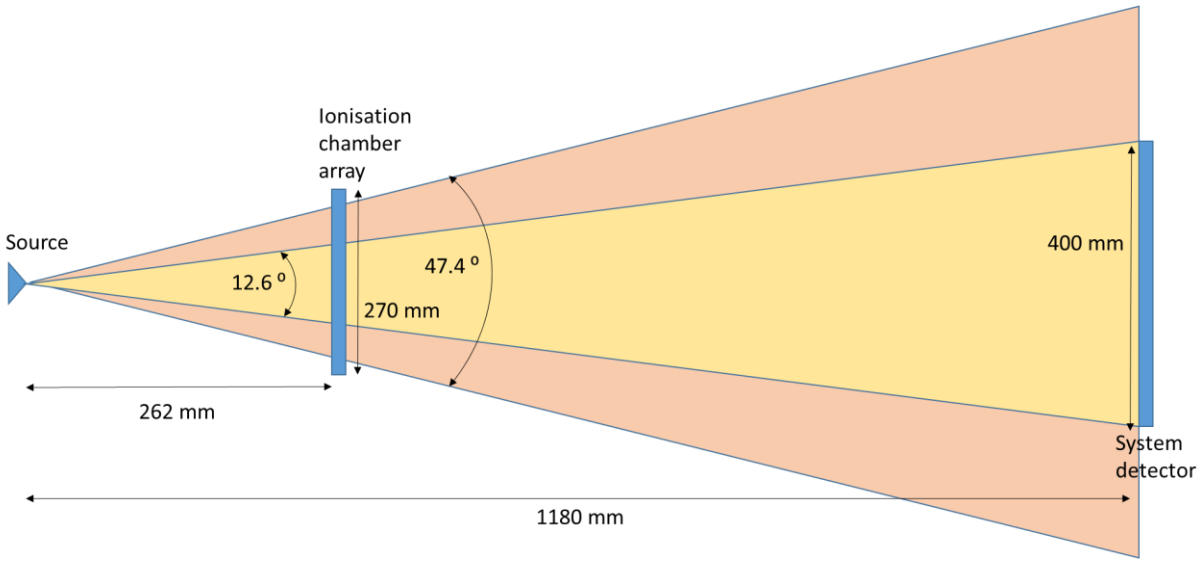

Figure 3.18 Layout of chamber array within the XCT system

A lead triangle was placed in front of the arrays to completely attenuate the X-rays in front of some of the chambers. This was used to determine the orientation of the data with respect to the system, see Figure 3.19.

The electronics for the detector had to be covered with a sheet of lead (thickness of 3 mm) to prevent any scattered X-rays hitting them.

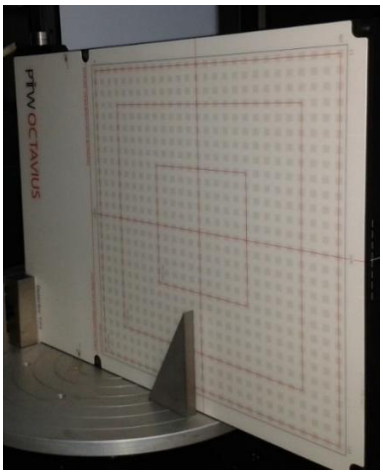

Figure 3.19 Lead triangle placed in front of array to determine the orientation of the array

3.2.1 Repeatability of data

Due to the fact that the array measures an accumulative dose over a longer period of time than the thimble ionisation chamber (1 minute vs 0.5 seconds) and the measurements could not be recorded constantly over a time period in the same way as the thimble ionisation chamber, a series of repeated measurements was carried out to determine if there was any notable change over time. Measurements were carried out at multiple voltages and currents across the range of the system, see Table 3.1. The X-rays were switched on and the accumulated dose was measured for 1 minute, this was carried out 5 times for each different set up.

Set up	Voltage (kV)	Current (μA)
1	80	100
2	140	100
3	200	100
4	160	50
5	160	250
6	160	400

Table 3.1 Voltage and current settings for each set up for repeated measurements

For each set up, the standard deviation of the results for the five measurements for each ionisation chamber was then calculated, this is expressed as a percentage of the mean value and can be seen in Figure 3.20 and Figure 3.21, which illustrate heat maps, each square of which represents an individual ionisation chamber in the array.

The results indicate that the X-ray flux remains relatively stable between the repeated measurements across most of the cone beam with a difference of <10% seen across the different tube voltages. Larger differences (<30%) can be seen around the edge of the cone beam, particularly at the lower voltages. When the current on the tube is at 250 µA there is a large difference in the amount of scatter reaching detector, this can be seen around the edges of the array. For both the high voltage and current, the cone beam appears to expand and fills the array.

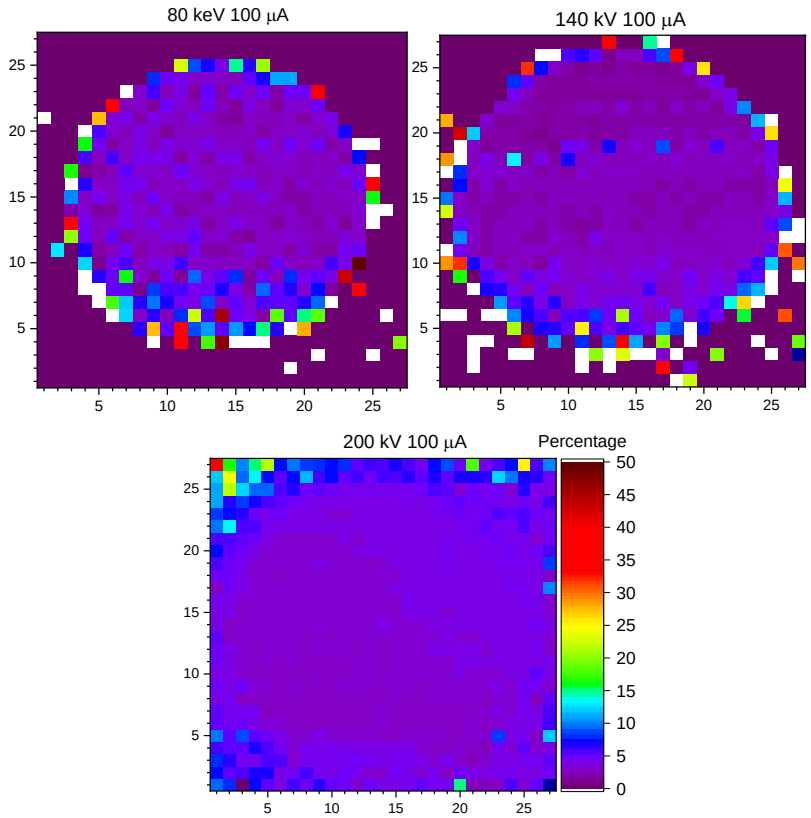

Figure 3.20 Standard deviation expressed as a percentage of the mean for five repeated measurements for varying voltages. Each square represents an ionisation chamber in the array

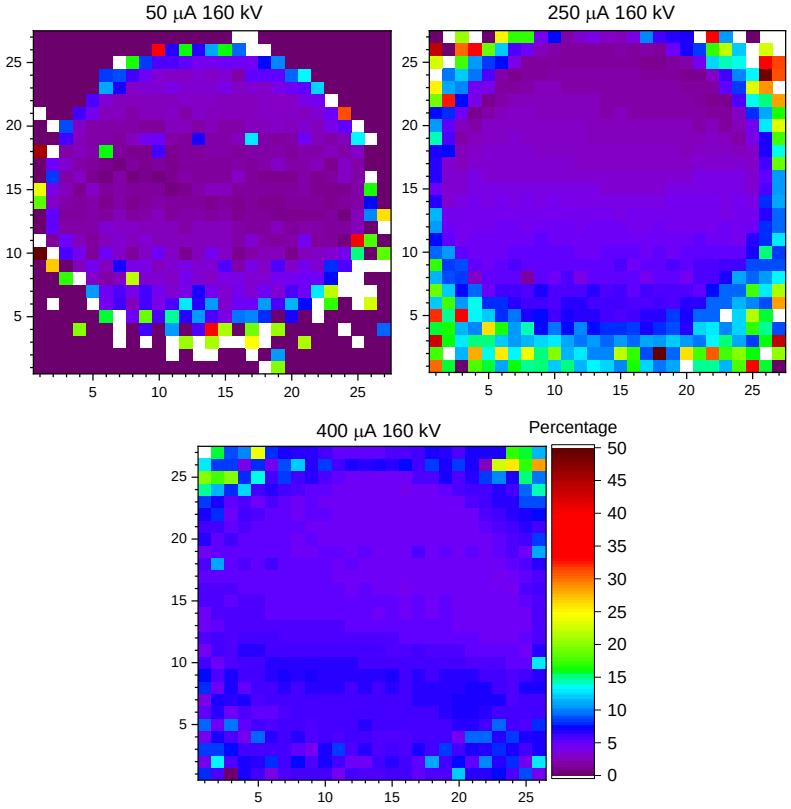

Figure 3.21 Standard deviation expressed as a percentage of the mean for five repeated measurements for varying currents. Each square represents an ionisation chamber in the array

3.2.2 Measuring flux with different voltages and currents

An experiment was designed to measure the variation in flux over the entire cone beam for different voltages and currents. The first set of experiments had a constant current of 100 µA and voltages ranging from 100 kV to 200 kV, increasing in 20 kV intervals. The second set of experiments had a constant voltage of 160 kV and currents ranging from 50 µA to 400 µA, increasing in 50 µA intervals, see Table 3.2. For both experiments, the accumulated dose was recorded over 1 minute.

Current when voltage is kept at 160 kV	Voltage when current kept at 100 µA
50 µA	80 kV
100 µA	100 kV
200 µA	120 kV
250 µA	140 kV
300 µA	160 kV
350 µA	180 kV
400 µA	200 kV

Table 3.2 Settings for system for ionisation chamber array measurements

The results for varying voltage can be seen in Figure 3.24 and show the intensity forms a bulls-eye pattern across the cone beam, the peak of the intensity, however, is not found centrally in the cone beam. As the voltage increases the centre appears to move around the cone beam. Within the X-ray gun the electrons follow a helical trajectory, therefore changing the voltage will rotate the position of the electrons on the target. However, this movement in itself is unlikely to cause a change in intensity across the beam. It is most likely that this movement is due to the position of the filament. When the filament is replaced in the target it is manually positioned, despite the most precise positioning it is not possible to align the filament 100% accurately.

When the voltage is constant and the current changes (see Figure 3.25) the centre of the bulls-eye is again off centre, although it does not appear to move as the current increases as it does with the change in voltage.

This bulls-eye pattern is a consequence of the isotropic nature of the radiation of the X-rays in all directions as they are emitted from the target (Cherry, Sorenson & Phelps, 2012) and hit the detector. The X-rays will travel out from the target in a spherical shape; as this sphere expands the energy of the X-rays remain the same, it is simply distributed over a larger area. The decrease in intensity of the X-rays is related to inverse square law, i.e. the intensity is inversely proportional to the radius of the sphere (Britannica Academic, 2018). Therefore, the areas at the side of the detectors will have a lower intensity compared to the centre, this is illustrated in Figure 3.22.

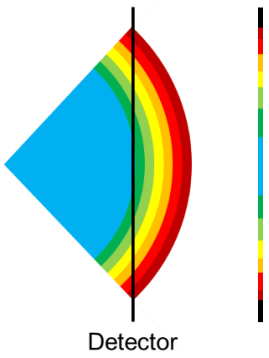

Figure 3.22 Circular wave front of X-rays travelling from source and the subsequent dose captured on detector

As mentioned previously, movement of the focal spot may occur, it can also be seen that the intensity of the X-rays follows a bulls-eye pattern. XCT systems contain an aperture close to the source to create the cone beam shape. As Figure 3.23 shows, if the focal spot moves, the cone beam will shift within the system. This will result in the bulls-eye pattern shifting on the detector.

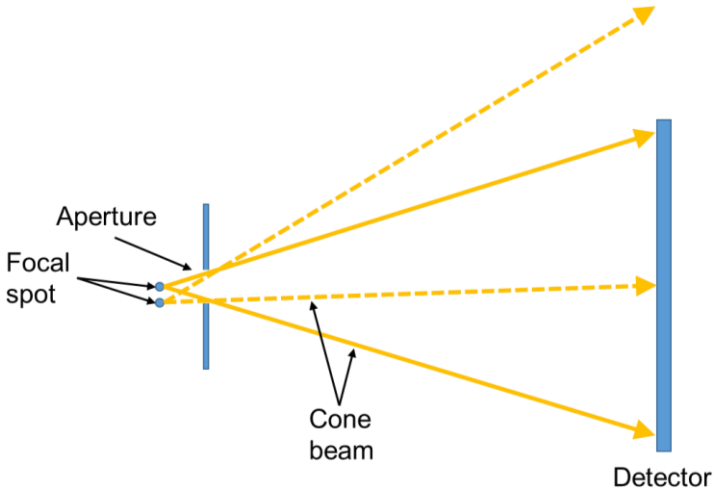

Figure 3.23 Movement of cone beam with focal spot movement

It can be seen that the background values around the cone beam are not at zero indicating that scattering within the chamber itself must be taking place. The amount of background scatter increases as the voltage increases. This is because the X-rays with a higher mean energy will still have sufficient energy remaining after hitting and deflecting off of the cabinet and manipulator and will be recorded as low energy X-rays on the detector (having lost some of their energy when colliding with the system).

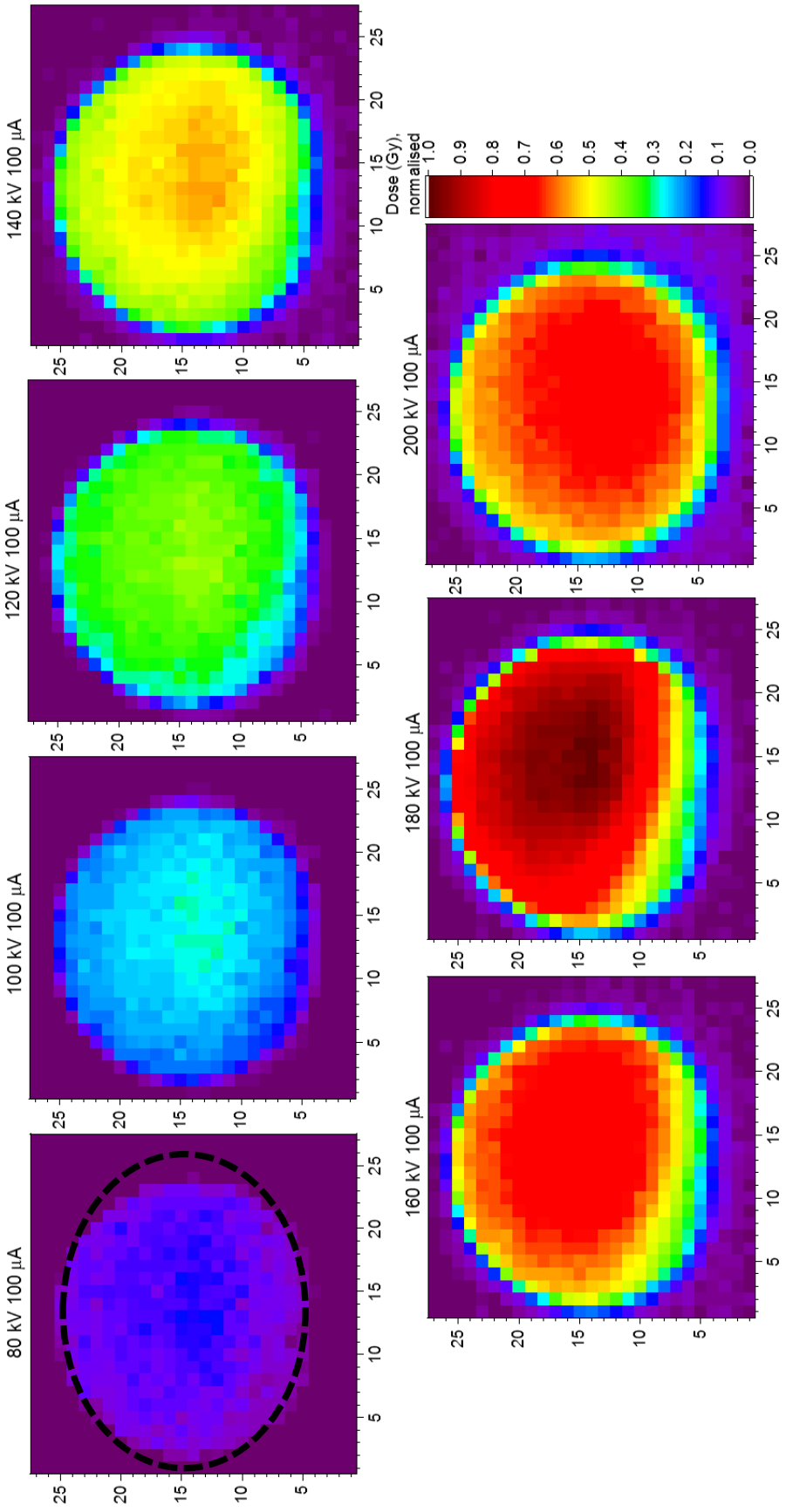

Figure 3.24 Dose across cone beam for different voltages. Normalised between 0 and 1 (maximum and minimum taken from across all datasets). Each square represents an ionisation chamber array. Dashed line indicates elliptical shape

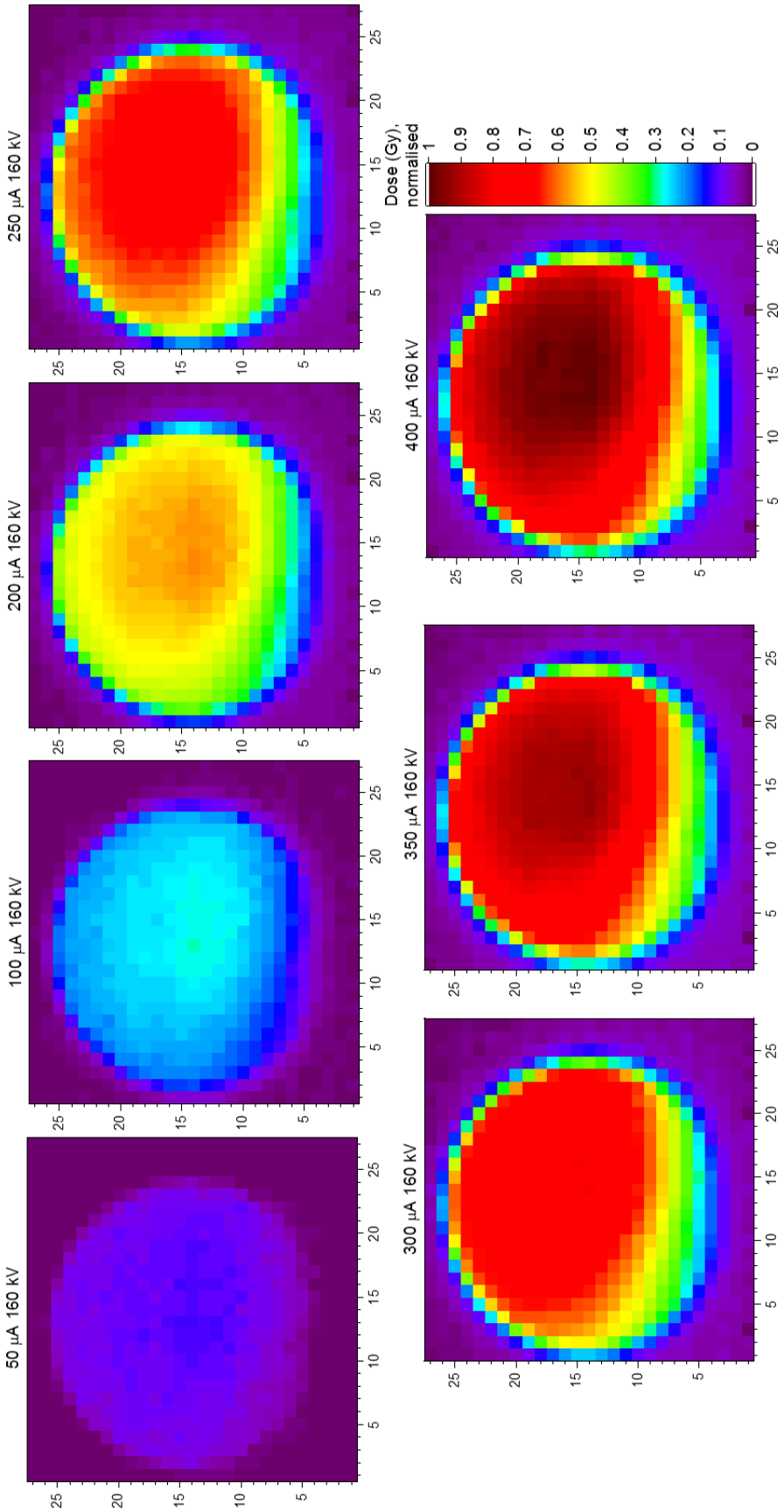

Figure 3.25 Dose across cone beam for different currents. Normalised between 0 and 1 (maximum and minimum taken from across all datasets). Each square represents an ionisation chamber array

The amount of variation for the part of the cone beam that hits the system detector can be seen in Figure 3.26 and Figure 3.27. The data has been normalised for each data set so that it is clearer to see the variation across the smaller area. When studying the results for the different voltages (Figure 3.26) it can be seen that there is a band running horizontally across the centre of the area where the dose is higher. As the voltage is increased the band moves down the Y-axis until it covers the bottom half at 200 kV. The exception to this is at 180 kV where the higher doses can be seen at the top of the area. This may be related to the issues in performance seen at the higher voltages described in Section 3.1.1. When studying the non-normalised data there is a 10% variation in dose across the detector.

When comparing the centre region for the varying currents (Figure 3.27), between 50 µA and 200 µA, the central band that was present in the lower voltages (Figure 3.26) is also present in this data. However, as the current is increased, the higher doses spread towards the top of the area. Between 300 µA to 400 µA the trend appears similar, with the higher doses found in the top half of the area.

These results correlate with the results seen in Section 1.6 that indicated that the threshold varied for the different sphere pairs. A change in dose down the detector would result in a change in energy deposited on the detector and therefore would result in a change in intensity down the image.

It can be seen in Figure 3.24 and Figure 3.25 that the cone beam front is not completely spherical and appears as an ellipse with the major axis running horizontally (see dashed line in Figure 3.24). The bottom of the cone beam appears as if it has been cut off. Also, the bulls-eye pattern is not centrally positioned within the cone beam. The vertical difference could be due to the anode heel effect, as described in Section 2.3.2, which results in the X-ray beam being filtered in the anode itself. The anode in this system is a cylinder laying horizontally. The cylindrical shape of the target would result in the X-rays being filtered both vertically and horizontally. The peak of the intensity has a skew with the higher values being on the right of the detector. Allisy-Roberts and Williams, (2008) state that the surface roughness of the target may increase the anode heel effect. The X-rays produced in the troughs on the anode would have to penetrate the peaks, resulting in increased filtration within the target material. This could explain the skew that is seen in the intensity of the X-rays across the detector. This will be discussed further in the next section where the spectrum is measured.

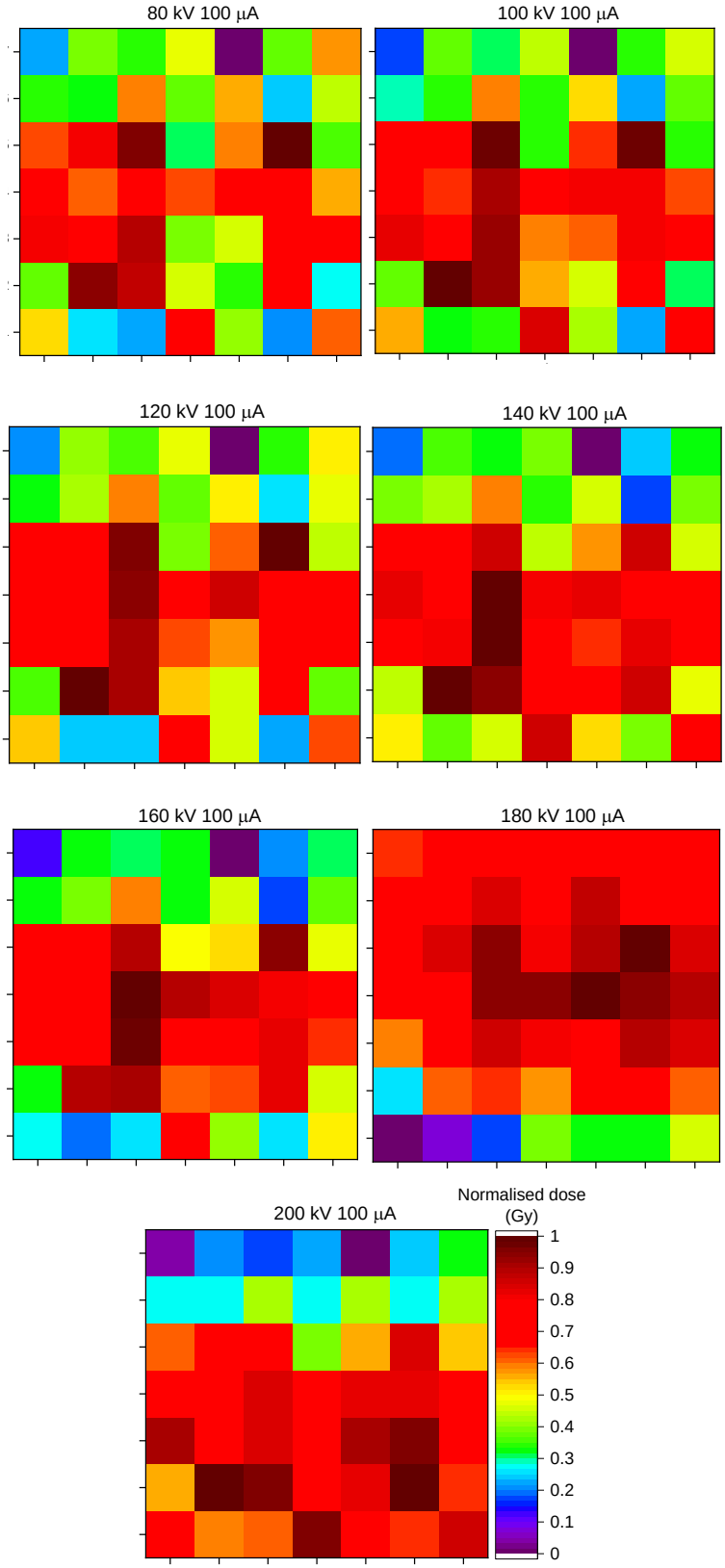

Figure 3.26 Area of cone beam that hits detector, varying voltages. Normalised for each data set. Each square represents an ionisation chamber array

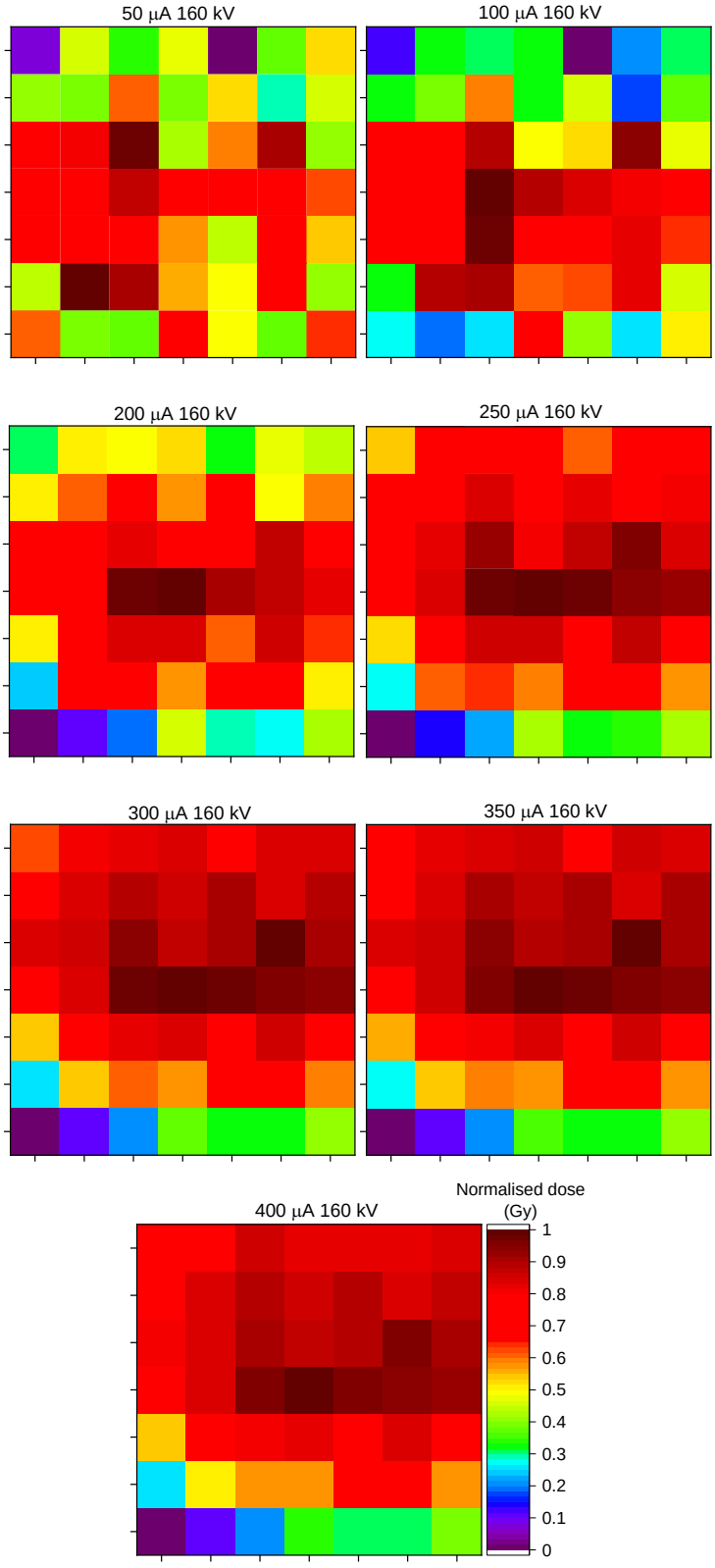

Figure 3.27 Area of cone beam that hits detector, varying currents. Normalised for each data set. Each square represents an ionisation chamber array Beam filtering

Following on from the repeatability tests, copper filters of thicknesses 0.1 mm, 0.3 mm, 0.5 mm and 1.0 mm were placed in front of the X-ray beam. A measurement was taken

once for each set up. The same set ups were used as the repeatability experiment (Section 3.2.1) and the voltages and currents can be seen in Table 3.1.

The pattern of the dose across the cone beam is very similar for all the different set ups so just one will be illustrated, as seen in Figure 3.28. As the filter thickness increases, the dose reaching the array decreases. This is because the lower energies are being attenuated by the filters, the increase in thickness leads to more attenuation.

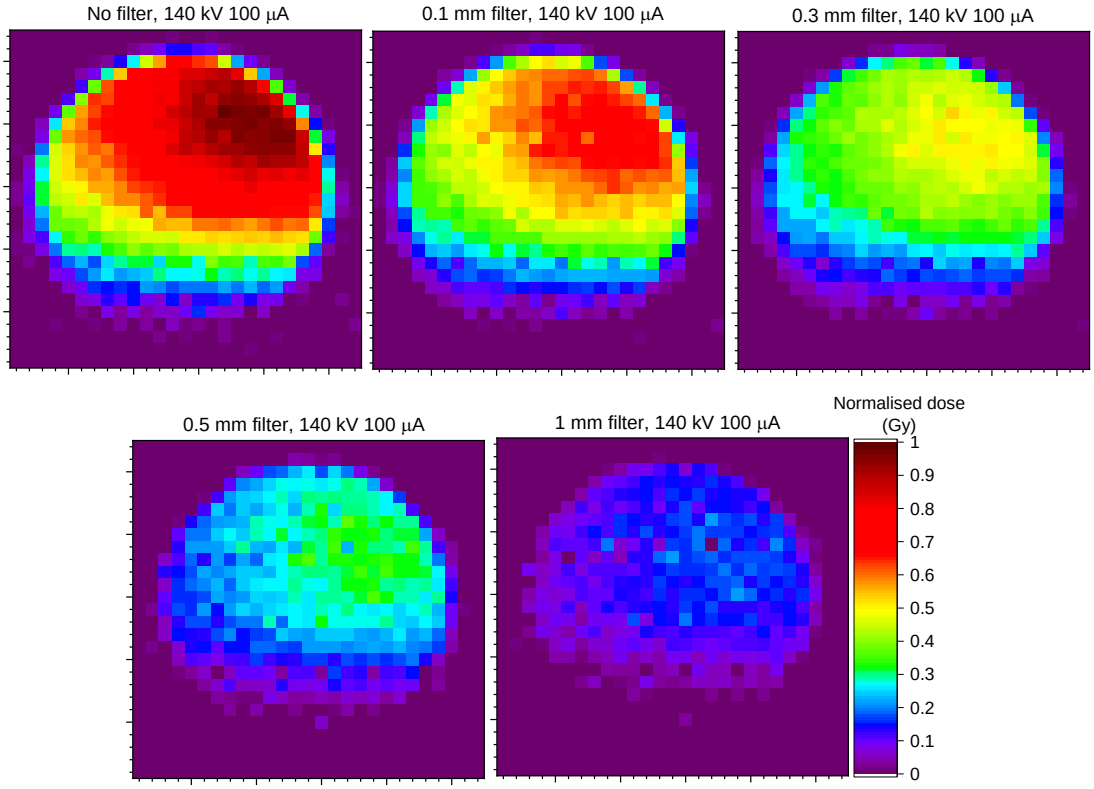

Figure 3.28 140 kV and 100 μA with varying thicknesses of copper filter

Results seen in this section, particularly those focussing on the area of the cone beam that would intersect with the detector indicate that the dose varies by 10% spatially across the area. This would lead to variation in intensity across the detector and explain the variation in the 2D images previously seen. This would in turn then lead to a different surface determination threshold having to be defined for an object depending on where it was positioned in the image.

3.3 Measurement of X-ray energy spectrum

In order to determine if the variation in intensity, as indicated in Section 3.2.2, was caused by a change in the X-ray energy spectrum, the spectrum was measured using a spectrometer. It is known that an inherent filtering of the X-ray beam can occur within X-ray targets (see Section 2.3.2 for description) and this test was designed to determine if it was present in this system.

To measure the spectrum an Amptek X-123CdTe X-ray spectrometer was used (see Section 2.2.5.4 as to how this works). The spectrometer was placed on the manipulator (as shown in Figure 3.29) in between the X-ray source and detector. A mounting stage was 3D printed so that the holder for the spectrometer could be screwed into it to ensure stability of the detector during measurement.

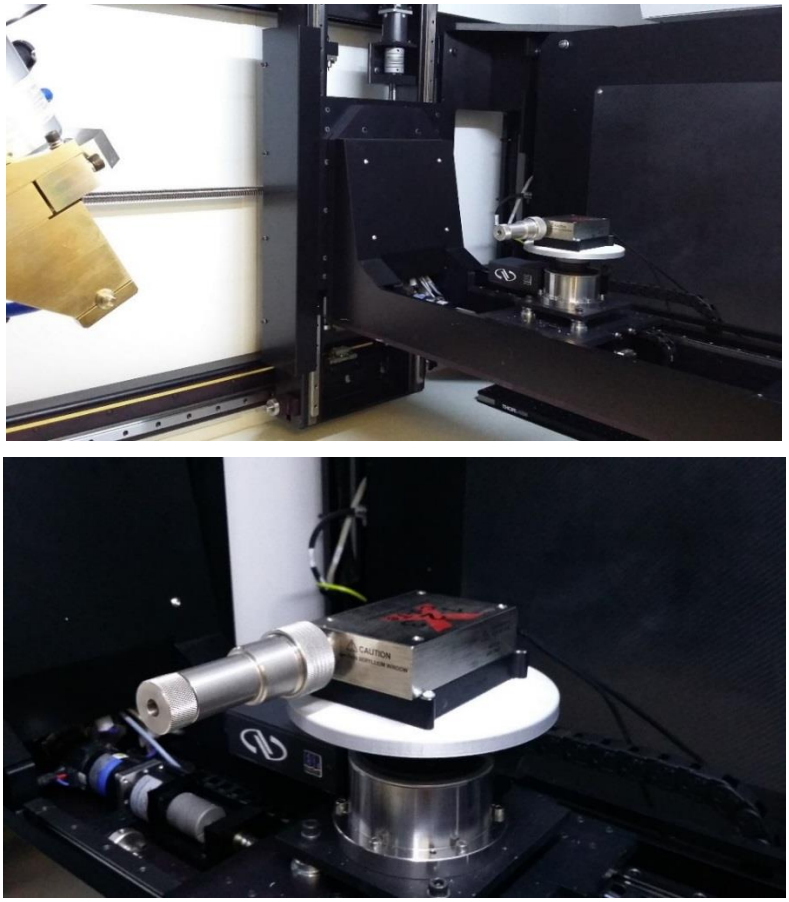

Figure 3.29 Spectral detector positioned between source and detector (top) and close up of spectrometer (bottom)

The spectrometer was initially placed in the centre of the image and a reading of the number of counts was taken. A 0.2 mm wide collimator is placed in front of the detector of the spectrometer (see Figure 3.30), this means that the centre of the X-ray beam and collimator have to be precisely aligned. To ensure this alignment the manipulator was moved along the X axis with repeated measurements being recorded until the local maxima was found. This was repeated for the rotational axis, the X axis again and then the Y axis to ensure the exact alignment was achieved, see Figure 3.31.

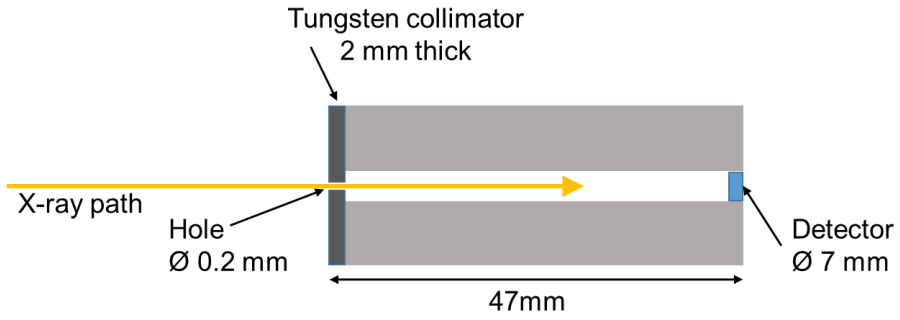

Figure 3.30 Schematic of collimator housing for spectrometer (not to scale)

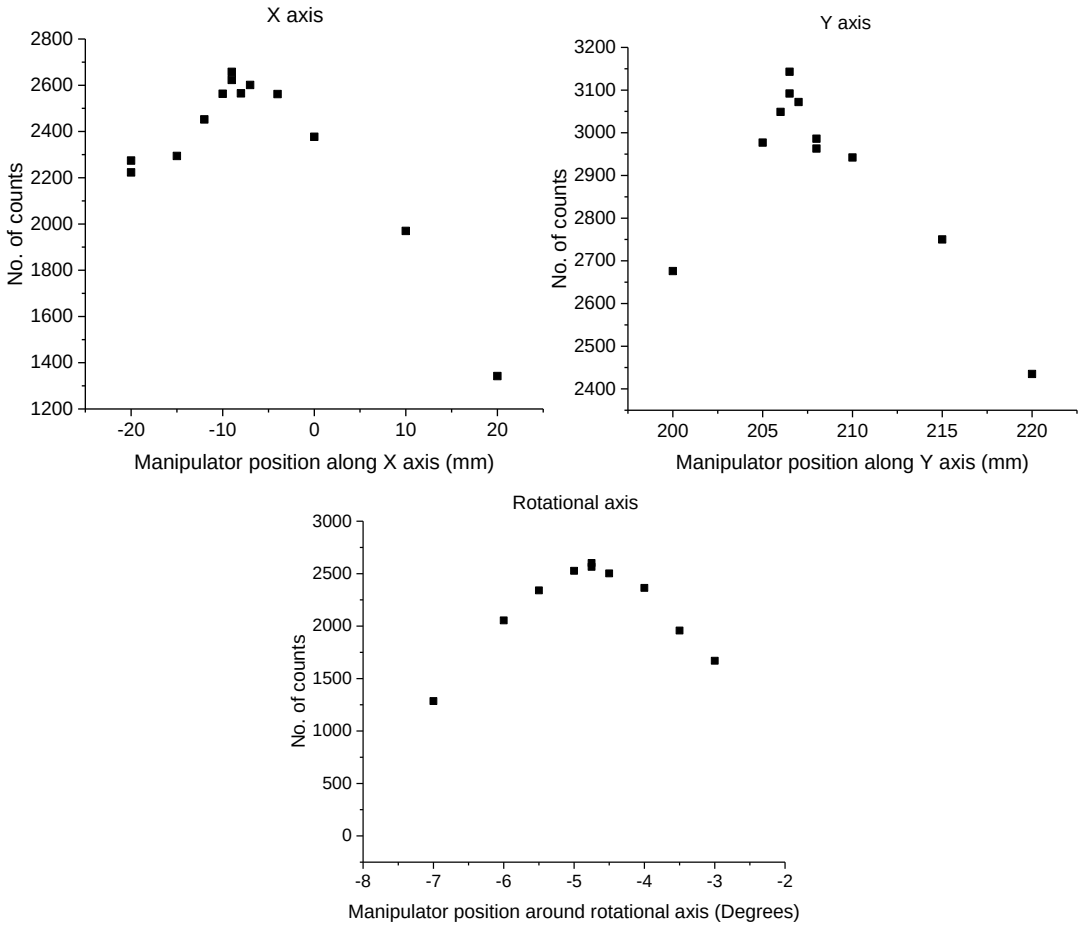

Figure 3.31 Local maxima of number of counts along X, Y and rotational axes of the manipulator

A low current had to be used to ensure the detector did not become saturated. It was noted that when the spectrum was measured for longer periods of time (300 seconds) the noise in the data was reduced, however, the shape or trend of the data did not vary, this can be seen in Figure 3.32. Therefore, for some of the tests, a shorter time of 60 seconds was used to ensure all the tests could be completed in the time that the spectrometer was available.

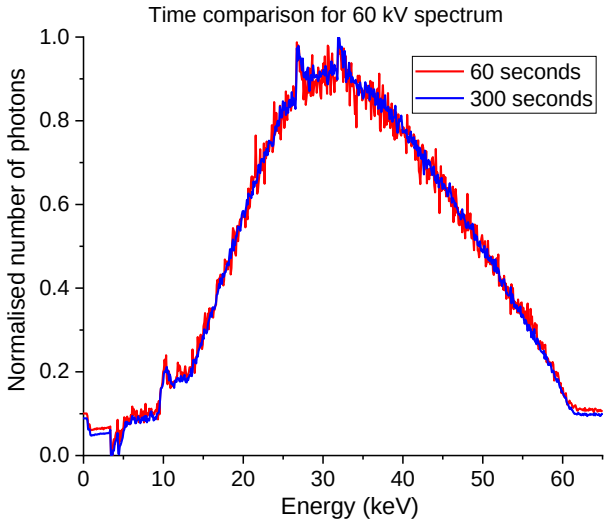

Figure 3.32: Comparison of noise for two different measurement durations

When the crosshair of the image was aligned with the centre of the collimator the manipulator was at position -23.510, 216.440, however after the alignment to find the maximum number of counts the manipulator was at position 13.510, -9.94, giving a distance of 16.7 mm between the centre of the image which is presumed to be the centre of the cone beam and the highest intensity of X-rays, see Figure 3.33. This ties in with the data seen in Section 3.2.2 which highlighted that the maximum intensity of the X-rays did not lie in the centre of the cone beam.

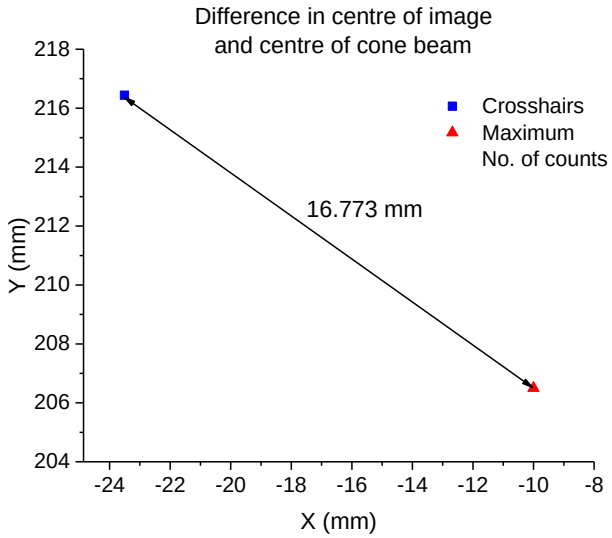

Figure 3.33 Difference between centre of image and centre of cone beam

The offset between the centre of the image and the peak in counts may be due to a misalignment within the system as discussed in Section 3.2.2.

3.3.1 Data correction

In this spectrometer the detector is made of Cadmium Telluride (CdTe) When an X-ray enters the detector it interacts with the CdTe and secondary X-rays are produced due to the processes discussed in Section 2.2.1. They escape the detector and therefore reduce the measured energy. This produces what are known as escape peaks on the measured spectrum which have to be corrected for. The Cd and Te both produce K_α and K_β peaks, this results in four escape peaks at 23.2 and 26.1 keV for Cd and 27.5 and 31.0 keV for Te (Redus *et al.*, 2009).

The data was corrected using MATLAB code written by and permission to use granted by Nicholas Calvert, formerly of Medical Physics, UCL. The code calculates the escape peak and photopeak ratio using Monte Carlo simulation data, these values are then interpolated depending on the energy values used in the experiment. The calculated number of counts is then subtracted from the measured counts to produce a final spectrum.

3.3.2 Repeatability

To determine how stable the spectrum was over repeated measurements, readings were taken for 1 minute, this was repeated five times. This was because a continuous reading could not be obtained over time and the stability of the spectrum needed to be determined. These measurements were taken at 160 kV and 15 µA. This value was chosen as it is a commonly used voltage within the NPL laboratory and is the voltage that was being used to image the complex holeplate at the time. The holeplate is described in Sections 2.8.1 and 4.1.

The repeatability of the multiple measurements can be seen in Figure 3.34. They indicate that the spectrum is stable, the mean standard deviation when comparing the repeated measurements is 34 photons with a maximum of 278 photons at the first k-shell peak (as described in Section 2.2.1). This small standard deviation ensured confidence in the measurements when taken just once.

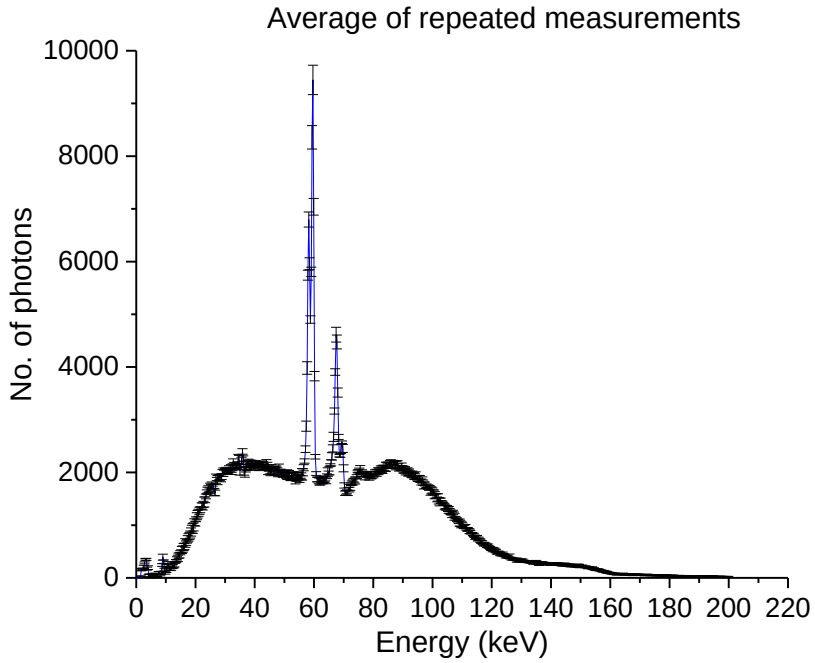

Figure 3.34 Average of repeated measurements of spectrum at 160 kV. Error bars are standard deviation of the five results

A software program known as SpekCalc (Poludniowskia & Evans, 2007) was used to simulate the expected X-ray spectrum for the system, see Section 2.5.2 for details of how the software calculates the spectrum. The results can be seen in Figure 3.35 and indicate that the measured spectrum has a different shape to the simulated spectrum. The results demonstrate that the lower energies are being attenuated, i.e. the beam is being hardened.

This filtering could be occurring somewhere within the housing of the X-ray gun. An alternative is described by Flay, 2016 who carried out work on the same XCT system, she showed that a secondary focal spot was being produced in the tungsten/copper alloy target housing. Flay explains that backscatter electrons are produced at the surface of the target, they subsequently interact with the metal in X-ray gun housing and produce more radiation. This radiation would most likely have a lower energy that the main X-ray beam (as it is derived from scattered radiation) and therefore contribute to the lower end of the spectrum.

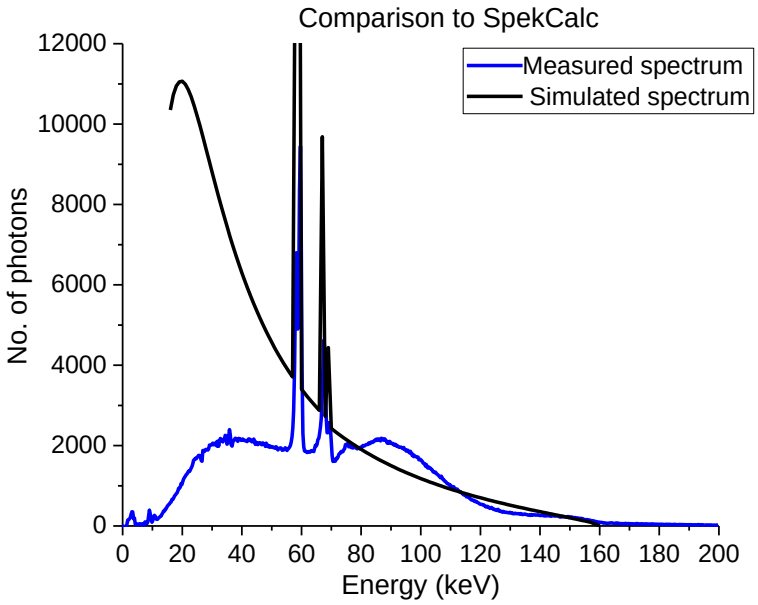

Figure 3.35 Comparison of repeated measurements at 160 kV to SpekCalc simulated spectrum

The increase in count to the right of the k peaks, at energies between 80 kV and 110 kV may be as a result of the photon experiencing an effect known as the Compton Continuum (Knoll, 2010). This is caused by Compton scattering where the higher energy X-rays are being scattered and producing X-rays of lower energies. This might explain the discrepancy between the simulated and measured spectrum seen between 110 keV and 140 keV. The higher energies are not being deposited on the detector as they are scattering and producing lower energy X-rays.

3.3.3 Varying voltage

The spectrum was measured over multiple voltages starting at 40 kV up to 200 kV which is the range over which this XCT system is used. The current was kept at a constant 15 µA throughout the measurements. The spectra were measured for 10 seconds for each measurement.

Figure 3.36, highlight a systematic decrease in the number of photons as the voltage decrease. The shape is similar for all the voltages except for 200 kV which cuts across the other lines with a much lower photon count. This anomaly ties in with the flux instability seen in the previous experiments carried out in Sections 3.1 and 3.2.2 where there was a decrease in intensity in the thimble ionisation chamber experiments. There was also a lower than expected dose with the chamber array experiments for 200 kV, again indicating issues with the system at higher energies as seen in Figure 3.3 and Figure 3.8.

For all the other voltages over 100 kV it can be seen that they exhibit the same trend as that seen in Figure 3.35 where there appears to be hardening of the beam, with a reduction in the number of photons with a lower energy in the Bremsstrahlung region (see Figure 2.6). They also have the same increase after the k line peaks.

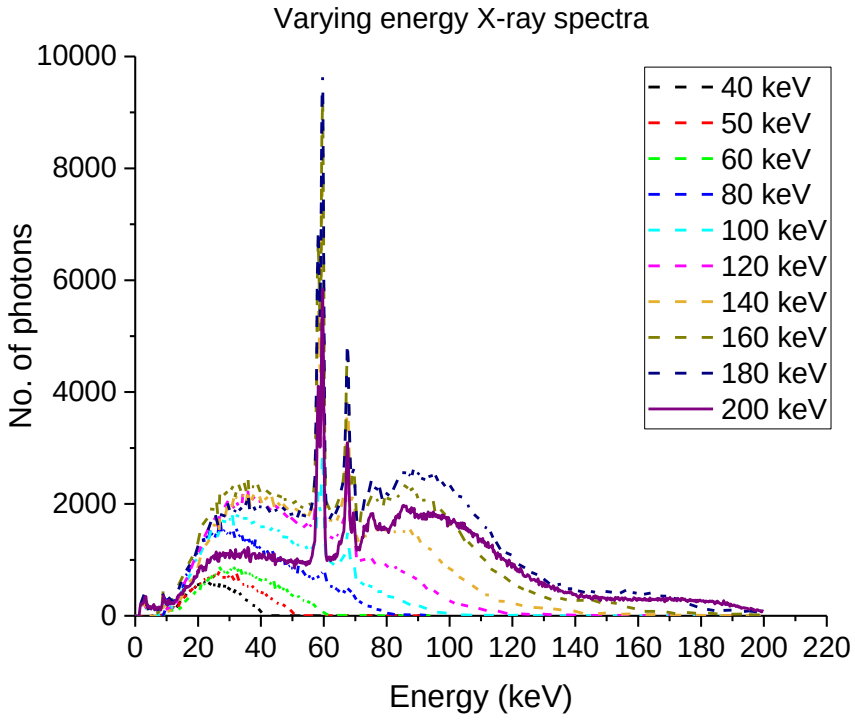

Figure 3.36 Spectra for different voltages

To determine if the shape of these spectra resembles that of a beam being filtered at the source, spectra were simulated again in SpekCalc but this time a filter was placed in front of the source. The anode angle was set to 60° and air thickness to 1000 mm.

Initially, to simulate the anode heel effect the filter was made of tungsten to replicate the material of the target. Varying thicknesses of tungsten filters were run and the spectrum compared to the measured spectrum from the spectrometer. It was found that the graphs were most similar when the tungsten was 0.08 mm thick, see Figure 3.37. This graph is indicative of the X-ray beam being attenuated in the target before it reaches an object.

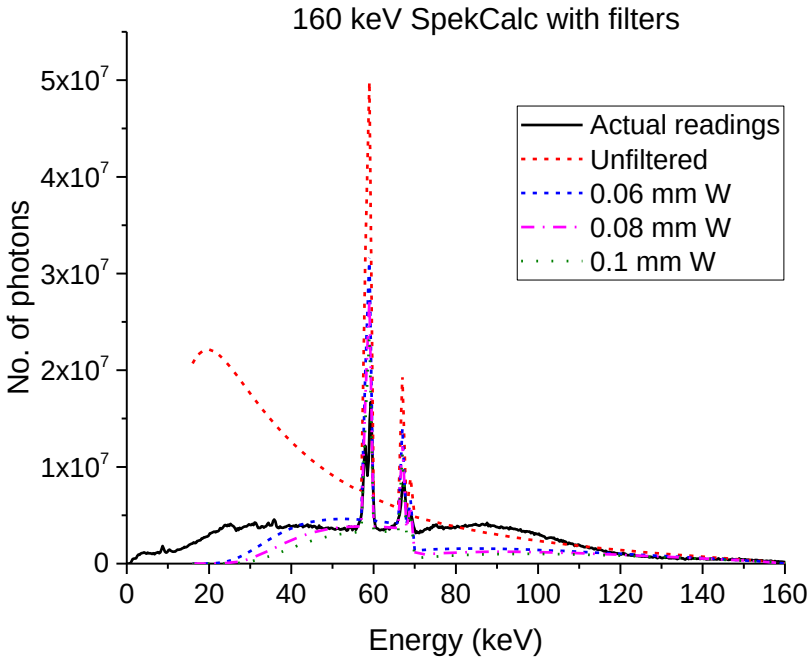

Figure 3.37 Varying thickness tungsten filters simulated in SpekCalc

3.3.4 Filtered X-ray beam

To replicate the findings from Section 3.3.3, a series of copper filters were placed in front of the X-ray source where it exits the housing. The voltage was set to 160 kV and the current to 15 µA. The filters had a range of thicknesses: 0.1 mm, 0.3 mm, 0.5 mm and 1.0 mm. The spectra were measured for 60 seconds.

Results, seen in Figure 3.38, highlight how the lower energies are attenuated by the filters. The amount of attenuation increases as the filter thickness increases, as expected. This attenuation of the lower energies results in an increase in the average energy of the spectrum, i.e. the beam is becoming hardened. The mean energy was calculated using Equation 3.1 The increase in mean energy as the filter thickness increases is illustrated in Figure 3.39 which shows a trend of increasing mean energy with increasing filter thickness. This increase, however, appears to be tailing off, the rate of increase is declining.

$$Mean\ energy = \frac{\sum(Energy\ \times\ number\ of\ photons)}{Total\ number\ of\ photons}$$

Equation 3.1: Equation to calculate mean energy of spectrum

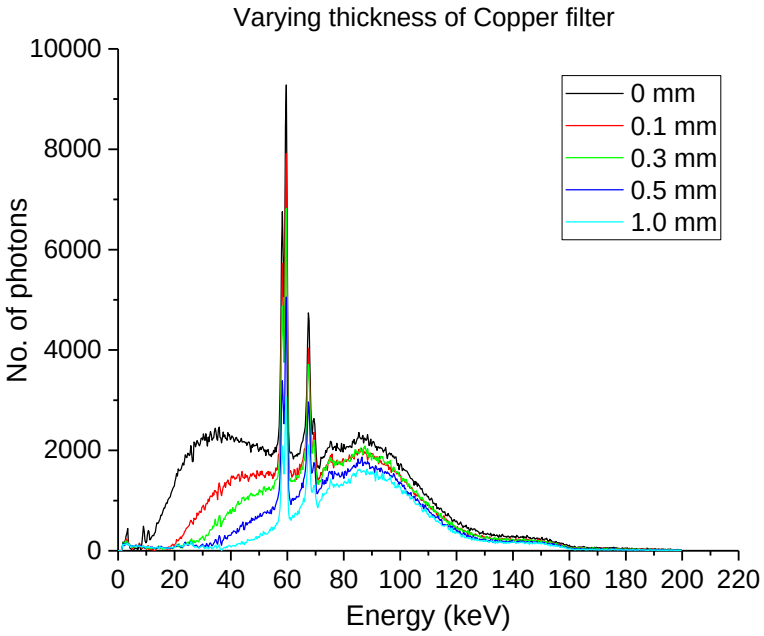

Figure 3.38 160 keV spectra filtered with differing thicknesses of copper from 0.1 mm to 1.0 mm

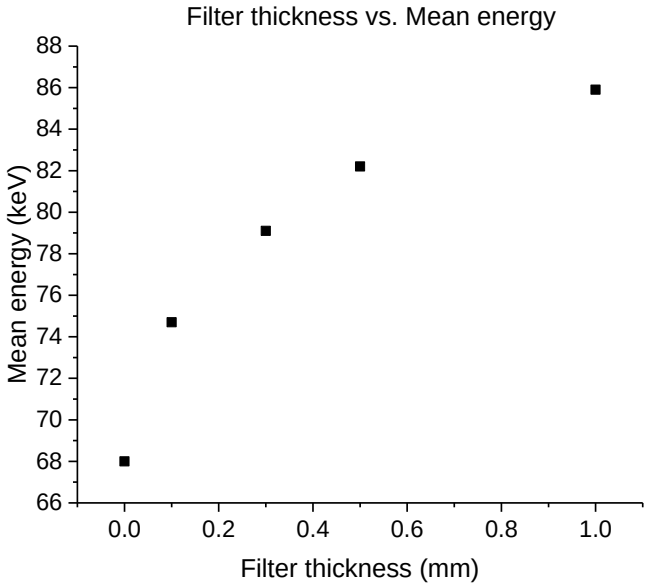

Figure 3.39 Mean energy for 160 keV spectra filtered with varying thicknesses of copper

Following on from measuring the spectrum in the centre of the cone beam it was decided to try and measure the spectra in other parts of the beam and this can be seen below.

3.3.5 Position in cone beam

To measure if there is any change in the spectrum spatially in the cone beam the spectrometer, on the manipulator, was moved vertically up the Y axis in 10 mm steps. Beyond 30 mm the spectrum became blocked by the collimator on the spectrometer. A voltage of 125 kV and a current of 15 µA was used. Measurements were taken for

10 seconds at each position. After the uppermost measurement and lowermost readings had been recorded the manipulator was placed back in the central position to ensure the spectra had not changed during the measurement. As Figure 3.40 shows, the different spectra for the central region have similar variations to the repeatability test seen in Section 3.3.2, there is therefore no significant drift during the measurement period.

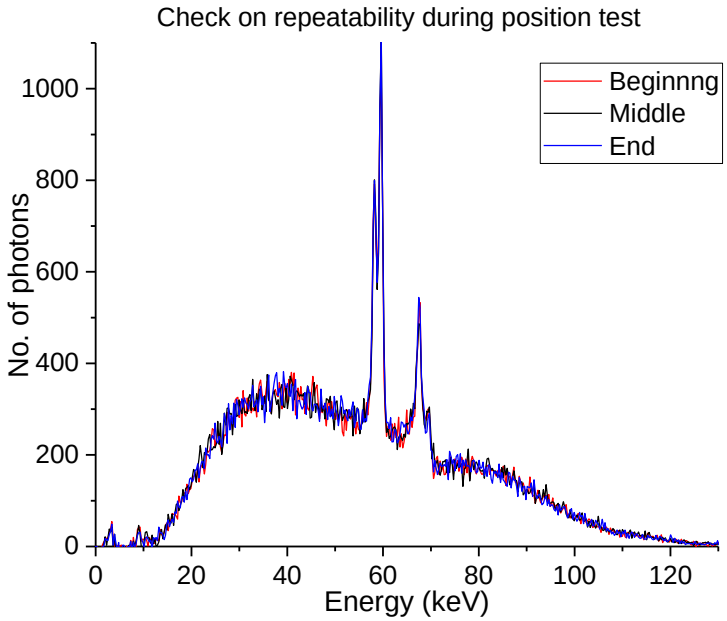

Figure 3.40 Spectra at the centre at the beginning, the middle and at the end of the position experiment

As seen in Figure 3.41, there is a change in the spectrum when the spectrometer is moved along the Y axis, i.e. when it is being moved in a vertical direction. For each 10 mm change in height, the number of photons of the lower energies (below 70 keV) decreases. This shows that the beam is being filtered away from the centre of the beam. However, the results are not as expected, if the results were due to the anode heel effect (see Figure 2.24 in Chapter 2) it would be expected that one spectrum would be higher than the one in the centre. Figure 3.42 illustrates the expected spectra for different path length distances of the X-rays through an anode. The change in spectrum can, at this point, only be explained by the X-rays being filtered by the collimator on the spectrometer

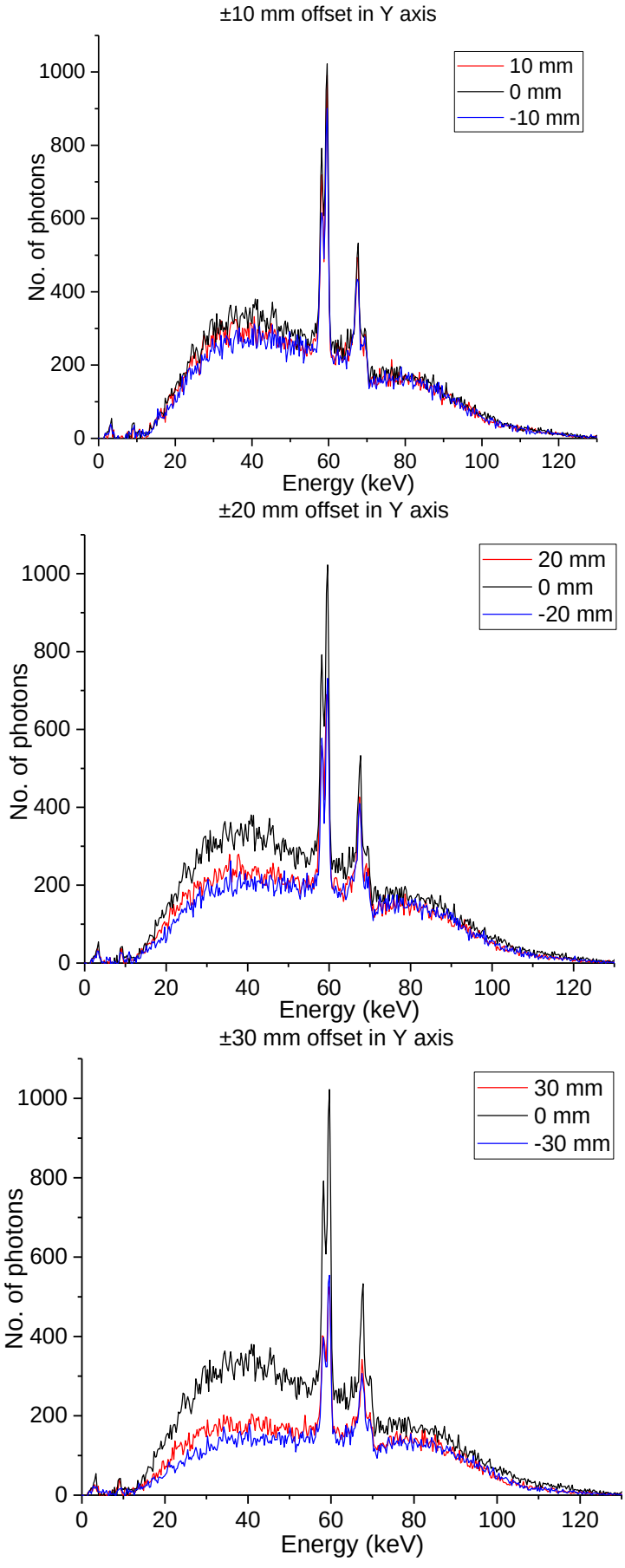

Figure 3.41 Spectra when spectrometer is offset along the Y axis

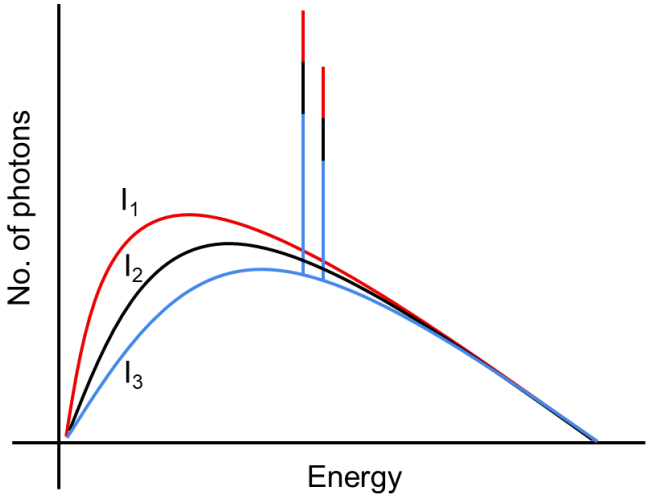

Figure 3.42 Expected variation in spectra depending on amount of target material X-rays have travelled through (I_1 shortest distance, I_2 middle distance, I_3 longest distance)

This series of experiments measuring the spectrum indicated that the spectrum remains stable throughout time although there does appear to be some filtering of lower energy X-rays within the X-ray gun housing before the X-rays reach the spectrometer. The maximum number of counts is found off centre of the detector, this replicates the results seen in Section 3.2.2 where the maximum dose was found away from the centre of the cone beam.

3.4 Estimation of effect

To determine the effects on the metrology of the factors seen in this chapter it the results were replicated in simulated images of spheres and cylinders. A change in intensity was applied to individual images to replicate the temporal changes seen, a gradient across the image was applied to duplicate spatial variations. The methods and findings can be seen in Chapter 5. Overall, for a cylinder with a diameter of 48 mm containing a hole with a diameter of 4 mm, maximum errors in the shape of the cylinders are ±4 µm. The shape of the cylinder varies depending on the direction of the gradient in the image. When comparing these values to the tolerance grades as outlined in Figure 2.51, it can be seen that this is acceptable for tolerances above IT5. Errors of ±4 µm are within the MPE of the system ((9 + L/50) µm where L is in mm), this indicates that at these tolerances they are acceptable.

3.5 Chapter summary

This chapter describes the investigation into the X-ray intensity of the cone-beam, both spatially and temporally using ionisation chambers. The spectrum emitted by the X-ray source was also investigated.

The stability of the X-ray flux is crucial with respect to the quality of the individual 2D images. If there are inaccuracies in the original image this can lead to problems further down the workflow. Manufacturers are aware that fluctuations do occur as they provide corrections such as shading corrections. However, as seen by the initial experiments, the gradient in the images and instability of the overall intensity is still visible despite corrections. Results indicate that there is a change in intensity over time but the shading correction used is based on an image acquired at the beginning of the imaging. This is discussed more in Section 5.3.2. This leads to errors in the threshold value being used to define the surface, resulting in an incorrect surface being defined and therefore inaccuracies in the dimensions of the object being measured.

The mean of blank images recorded during the imaging process with an empty field of view highlights peaks and troughs in the intensity values. This is also seen in the thimble ionisation chamber experiment where the output can also, at times be sporadic with changes of approximately 2%. When the ionisation chamber was placed in different positions in the cone beam, variations were seen in the results. This again corresponds to gradients seen in the original images.

Further measurements using an ionisation array found an uneven distribution of dose across the cone beam both across the whole section and also in the section populated by the system's detector. The maximum energy or intensity varies depending on the energy of the X-rays but is up to 10%.

Measurement of the spectrum of the X-rays and its comparison to simulated data indicated that the beam was being filtered before it even reached the spectrometer. This could be due either to the inherent filtering that occurs in the anode or it is occurring somewhere else in the housing of the X-ray gun. The maximum number of counts does not lie within the centre of the image, this correlates with the trends seen in the array experiments.

These different factors and their effect on the dimensional measurement of objects will be explored further in Chapter 5 in which X-ray images will be simulated and the intensity of the images manipulated.

Chapter 4: Object related effects on metrology

This chapter describes the use of a series of holeplates to study the factors that affect the measured dimensions and geometry of objects. These factors include orientation and fixing of the holeplate during imaging and the path length of the X-rays through the object. The holeplates used were a complex holeplate with multiple holes and four simple holeplates, each with just a single hole.

The geometric results for the complex holeplate (CompHP) were intricate, therefore it was decided to simplify the problem by constructing four simple holeplates. Results indicate that the geometry of the reconstructed holes show systematic trends in deformation. These systematic trends vary depending on the position of the hole within the holeplate and also on the orientation of the object during imaging. The magnitude of the trends depends on the magnification of the object during imaging.

4.1 Complex holeplate

A complex holeplate was designed by Physikalisch-Technische Bundesanstalt (PTB) to measure the effects of beam hardening on unidirectional and bidirectional length measurements (Bartscher et al. 2014). The number and position of the holes within the holeplate is optimised to acquire five length measurements in seven different spatial directions. This is a requirement of the ISO10360 acceptance and reverification test along with the VDI/VDE 2630-1.3 standard. Although the shape of a holeplate is not ideal when considering XCT, due to the angular shape, their use follows on from the reference standards used to assess length measurement errors in coordinate measuring machines and is therefore a natural evolution of the standard.

A similar holeplate was manufactured, imaged, reconstructed and measured at NPL. It is made of aluminium and consists of 28 cylindrical holes, each with a nominal radius of 2 mm. It is 48 mm x 48 mm x 8 mm in size, see Figure 4.1. The holeplate was measured on the NPL Zeiss UPMC 550 Cartesian CMM with an MPE of (1.2 + L/400) µm providing traceable reference measurements.

NPL manufactured the holeplate with the intention of using it as a reference object for an inter-laboratory experiment. It was during the initial imaging of the holeplate, by the author, that the errors in bidirectional lengths were seen, this led to an investigation into the cause of these errors. This work focussing on the apparent systematic deformation in the geometry of the holes is therefore a continuation of the work started by Bartscher *et al.*, (2014) as it contributes to the discussion involving the use of a holeplate with

respect to the international standards. It also discusses the apparent shape of the holes which has not been previously studied.

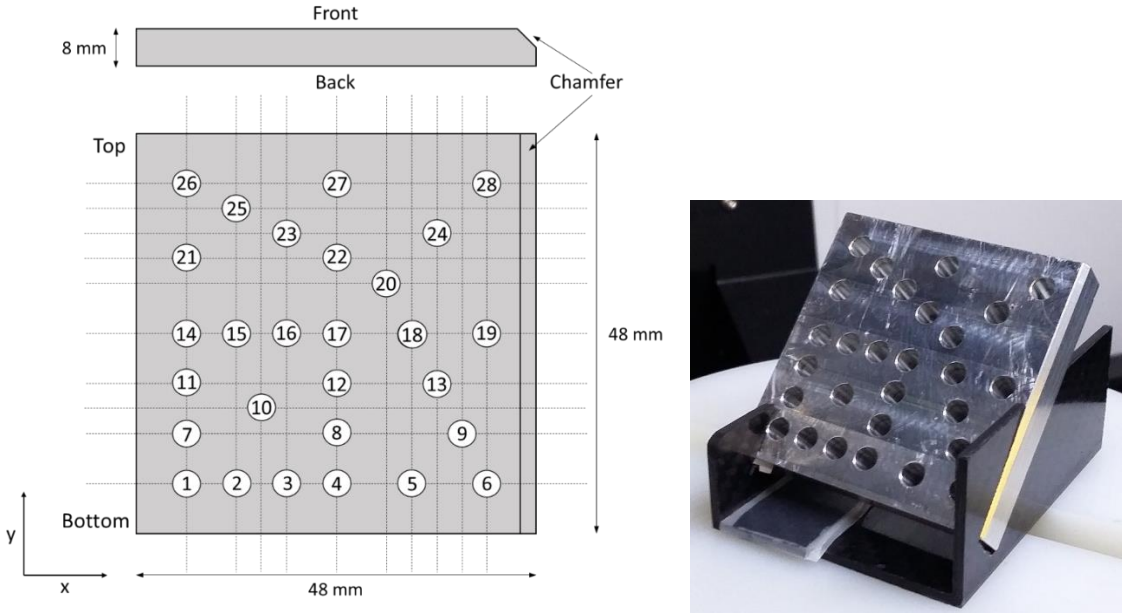

Figure 4.1 Schematic and photo of complex holeplate. Numbers indicate hole number referred to in text

A single projection image of the complex holeplate can be seen in Figure 4.2 and the reconstructed volume and a close up of a hole can be seen further on in this chapter in Figure 4.13.

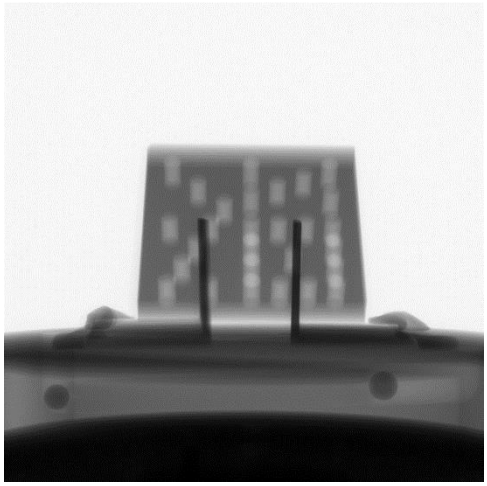

Figure 4.2 2D X-ray image of holeplate being imaged at 45° orientation

4.2 Imaging of holeplates

Most of the holeplate imaging was carried out on the XCT system at NPL, a Nikon 225 Metrology system which has an MPE of (9 + L/50) µm where L (length of measurement) is in mm. Nikon state that the accuracy is certified according to VDI/VDE 2630. A couple

of sets of images were collected on a North Star Imaging system, an X5000 which is not a metrology system, the system capability is given as the overall maximum system resolution which is approximately 500 nm. NSI do not state how they have accomplished this but with a pixel size of 0.2 mm and a geometric magnification of >x3000, it would be possible to achieve a voxel size of approximately 67 nm. This system was at the NSI UK headquarters in High Wycombe. The full specifications for both systems can be seen in Appendix 1. Both systems can be seen below in Figure 4.3. Unless specified the results are from the Nikon system.

Figure 4.3 NPL's Nikon system (left) and NSI system (NSI, 2017) *(right)*

A detailed explanation of the workflow process of imaging, reconstruction and analysis using XCT in this project can be found in Section 2.4.

4.2.1 Magnification

The holeplates were imaged at two different magnifications, ×1.6 and ×5. These two magnifications were at the extremes of the magnification range with the manipulator being as far away and as close to the source as possible whilst still being able to capture the whole holeplate in the image.

During initial imaging of CompHP it was positioned on a platform on the manipulator that contained a ball bar, the length of which had been measured on a CMM. This ball-bar was placed in five positions along the Y axis at approximately equal distances. The ball bar was imaged, reconstructed and the centre to centre distance between the two spheres measured. These lengths was compared to the CMM measurements, the results, seen in Figure 4.4 indicate a scaling error as the error in the length varies depending on the position along the Y axis. It is a systematic error which could be corrected for by using the equation of the straight line of the graph. For this reason most of the imaging was at a magnification of ×1.6, this meant that there was as small a

variation along the Y axis (vertical axis as shown in Figure 2.1) as possible thereby limiting the scaling error.

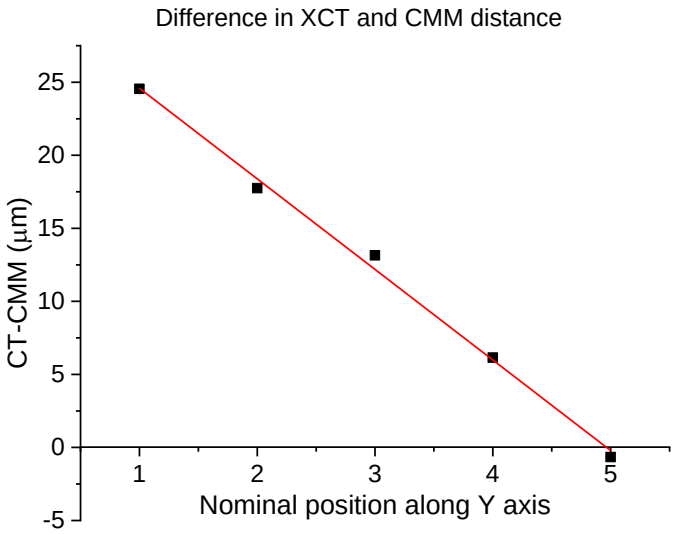

Figure 4.4 Difference between XCT and CMM distance measurements for ball-bar. 1 is at the top of the image, 5 at the bottom

4.2.2 System settings

Initially when imaging CompHP the voltage and current used were based purely on obtaining a clear live image of the holeplate ensuring a good contrast. However, this method is very subjective and is based on the user. ISO 15708-2 (International Organization for Standardization, 2002) states that the transmission should be 14%, i.e. where the average thickness multiplied by the attenuation coefficient is equal to 2. This value is a balance between contrast and noise at higher and lower transmissions respectively. Knowing the dimensions of the holeplate it was possible to calculate the average attenuation of the X-rays (based on the average length) and therefore the required monoenergetic X-ray energy.

The steps for this process can be seen below:

1. $attenuation\ coefficient\ (\mu) = \frac{2}{Average\ path\ length\ (cm)} = \frac{2}{3.8} = 0.53\ cm^{-1}$
2. From the NIST attenuation coefficient table the required monoenergetic energy for an attenuation of 0.53 cm^{-1} is equal to 74 keV
3. Sprawls 1995 states that the monoenergetic beam is 30-40% of the equivalent energy of a polyenergetic beam, therefore the equivalent polyenergetic X-ray energy is 170 kV

This method was used to calculate the voltage for imaging the simple holeplates and the repeat imaging of CompHP. The current was chosen based on the histogram of the live

image in the Nikon software, Inspect-X. The current was adjusted until the peak of the data was in the centre of the histogram, this ensured the X-rays were fully penetrating the object but the image was not saturated.

During projection set up the Inspect-X software allows the user to optimise the number of projections used, for this set-up the value was 3142. The optimal number of projections, as specified by the Inspect-X manual (Nikon Metrology, 2013b), is pi/2 times the number of voxels required along the X or Y axis. As the whole volume was being reconstructed (2000 x 2000 voxels) the optimal number of projections was 3142. For each projection, one frame was acquired for 1000 ms.

The values used for various settings for each holeplate measured can be seen in Table 4.1.

The beam hardening and noise reduction values given in Table 4.1 refer to the values chosen in CTPro during the reconstruction (see Section 2.4.2 for full description). As it was not known if the errors were caused by beam hardening, it was decided to keep the corrections to a minimum. However, in some cases, if no correction was applied the data was too noisy resulting in the holes becoming infilled (see Figure 4.5) this meant that cylinders could not be fitted. In this case the lowest possible correction was applied.

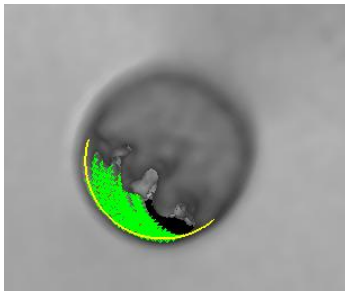

Figure 4.5 Close up view of reconstructed hole in VGStudio Max. Noise within the hole prevents fitting a cylinder confidently. Green points are fit points as described in 4.2.4.2

4.2.3 Volume alignment

To ensure that the coordinates of the fitted shapes were aligned consistently in the same coordinate system the reconstructed volumes were registered to a CAD model that was imported as a .stl file into VGStudio Max. To register the volume, it was initially aligned manually to the model. Following on from this a Gaussian best fit method is used which minimises the distance deviation between the considered surface of the volume and the model. It was chosen to use this method as opposed to the feature matching method that matches three planes, two lines and a single point as reference objects in both the

volume and the model because when this method was being used it kept flipping the holeplate diagonally.

Date	Experiment	Voltage (kV)	Current (μA)	Mag.	No. of images	BH	NR
7/3/16	CompHP 0°	120	140	×1.6	3142	2	2
9/3/16	CompHP 45°	170	70	×1.6	3142	2	2
9/3/16	CompHP 90°	190	80	×1.6	3142	2	2
25/1/17 & 14/3/17	HP1 0° Still	170	60	×1.6	3142	2	2
14/317	HP1 0° Moving	170	60	×1.6	3142	2	2
25/1/17	HP1 0°	170	60	×5	3142	2	3
26/1/17	HP1 45°	170	60	×1.6 & ×5	3142	1	1
27/1/17	HP1 90°	170	60	×1.6 & ×5	3142	1	1
13/2/17	HP3 0°	170	60	×1.6	3142	2	2
13/2/17	HP3 0°	170	60	×5	3142	2	3
31/1/17	HP3 45°	170	60	×1.6 & ×5	3142	1	1
30/1/17	HP3 90°	170	60	×1.6 & ×5	3142	1	1
15/2/17	HP5 0°	170	60	×1.6	3142	2	2
15/2/17	HP5 0°	170	60	×5	3142	2	3
16/2/17	HP5 45°	170	60	×1.6 & ×5	3142	1	1
15/2/17	HP5 90°	170	60	×1.6 & ×5	3142	1	1
3/4/17	CiHP 0°	170	60	×1.6	3142	1	1
22/5/17	CiHP 45°	170	60	×1.6	3142	1	1
24/5/17	CiHP 90°	170	60	×1.6	3142	1	1
15/3/17	Repeat CompHP 0°	185	75	×1.6	3142	2	2
1/6/17	Repeat CompHP 45°	185	75	×1.6	3142	2	2
15/9/17	Repeat CompHP 90°	185	75	×1.6	3142	2	2

Table 4.1 Settings used for different experiments

4.2.4 Measurements

Once the object has been reconstructed and surface defined, a series of measurements can be taken of the volume. In this study, lengths and the fit points used to fit the reference objects were of interest and they will be discussed in more detail below.

4.2.4.1 Lengths

Many industry standards, for example ISO/WD-CT (International Organization for Standardization, 2012) include the measurement of unidirectional and bidirectional lengths. In the holeplate these can both be taken between different holes. The differences between the two measurements can be seen below in Figure 4.6. As the figure shows, the unidirectional length would be more accurate as it is based on primitive shapes that are fitted to the surface of the reconstructed volume. As it is a centre to centre distance they are also independent of the threshold used, an issue that was found to cause dimensional errors in previous work by the author (Corcoran, 2014) and described in Section 1.6.

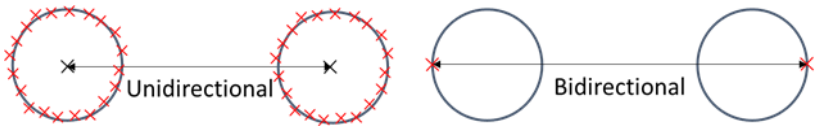

✓ Threshold independent	× Dependent on threshold
✓ Edge independent	setting
✓ Centre of cylinder is based on	× Influenced by material
it being fitted with many points	× Based only on two points

Figure 4.6: Differences between Unidirectional and bidirectional length measurements (Corcoran et al. 2016)

4.2.4.2 Fit point deviations

In VGStudio Max, fit points are used to fit a reference object to the reconstructed object (see Section 2.4.5). With the use of these points and their associated coordinate and deviation data, it is possible to determine the shape of the reconstructed cylinders as defined by the surface. The deviation is the distance of the surface to the fitted shape, negative deviations indicate the surface is outside the fitted cylinder, positive that the surface is inside the cylinder. For the purpose of visualisation and to highlight the shape of the hole geometry, in all of the graphs the signs have been reversed so that points outside the cylinder are positive and vice versa. In most cases, unless specified, approximately 10 000 points were used to fit the cylinders. The deviation and coordinates are exported into Microsoft Excel along with the coordinates of the centre of the cylinder. The bearing around the circumference is calculated using Equation 4.1, this converts the

rectangular coordinates into a polar coordinate system (Uren & Price, 2010). The Microsoft Excel Atan2 function was used to calculate the arctangent of the coordinates and the MOD function to ensure all the values were positive.

$$Tan\theta = \frac{x\ coordinate\ of\ fitpoint - x\ coordinate\ of\ centre\ of\ cylinder}{y\ coordinate\ of\ fitpoint - y\ coordinate\ of\ centre\ of\ cylinder}$$

Equation 4.1 Calculation of bearing (θ) around circumference

The orientation around the circumference can be seen in Figure 4.7 with 0° being at the top.

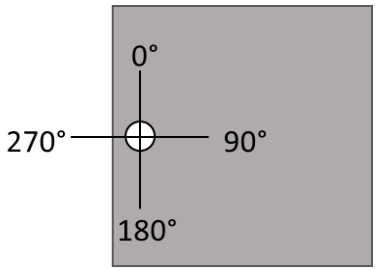

Figure 4.7 The orientation of the bearings around the circumference of the cylinder

This data was then exported to MATLAB where the average deviation, bearing and greyscale value for the whole length of the cylinder was calculated for all points within a 5° interval (Figure 4.8). The standard deviation for these values was also calculated for the interval. An interval of 5° was chosen to ensure sufficient coverage of fit points therefore allowing a mean to be calculated and ensuring a smooth trend in the graphs.

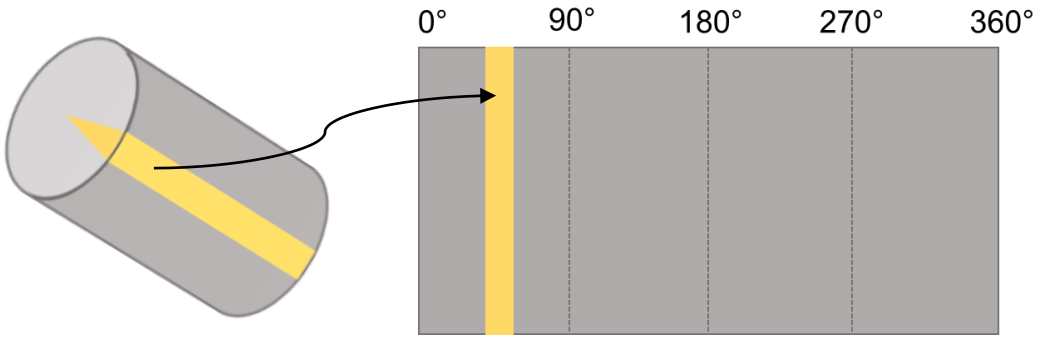

Figure 4.8 Schematic of area from which mean of deviation, bearing and greyscale are taken

It should be acknowledged that there may be variations within the fitting process and that different results could be found each time a shape is fitted. A study was carried out to determine if the parameters chosen when fitting a cylinder affected the shape. The parameters that can be changed include number of iterations and search distance between points. Changing the settings had little result on the results, compared to the

overall deformation they were so small that they were not considered significant. One example can be seen below in Figure 4.9 which was compares the maximum number of fit points used in the fitting process. As the graph shows the differences are a few micro meters so are not significant.

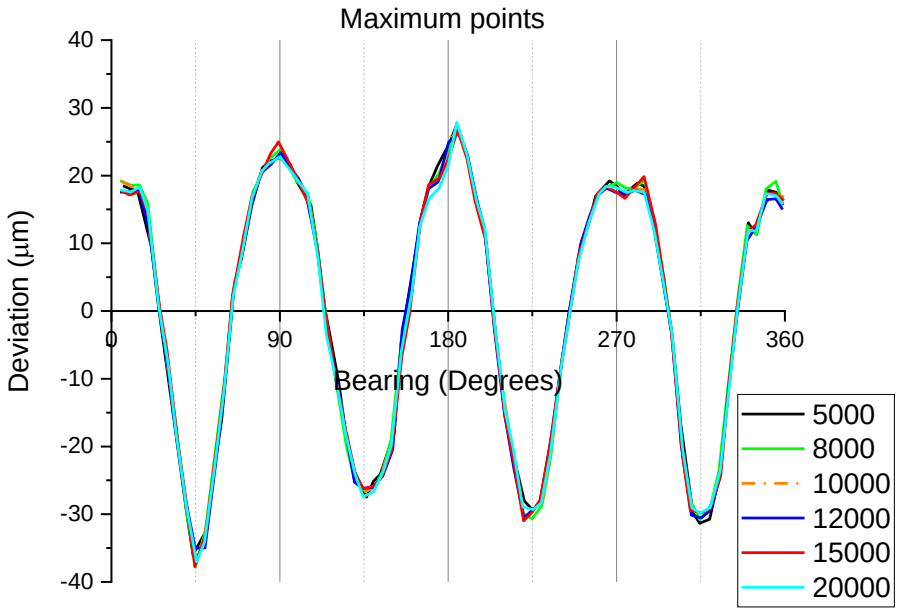

Figure 4.9 Fit points for HP3 depending on maximum number of fit points used

It is assumed that the variation in repeated fittings would be very small (< 5 µm) so is not significant to these experiments.

4.2.4.3 Key to graphs

Three types of graphs are predominantly used in this thesis, examples of which can be seen in Figure 4.10, Figure 4.11 and Figure 4.12. The black dots indicate the position of the fit points. The scale bars are equal to one standard deviation. Figure 4.12 illustrates the surface of an unrolled cylinder as seen above in Figure 4.8.

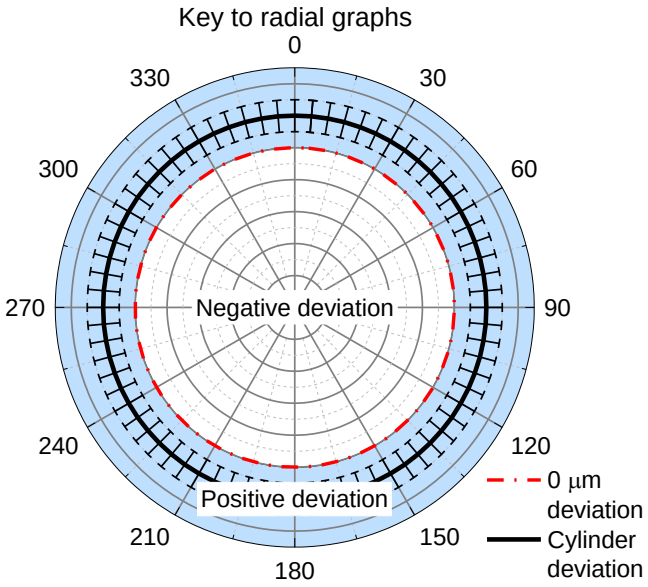

Figure 4.10 Key to radial graphs used in thesis. Mean taken for every 5° interval, scale bars are the standard deviation for points in that interval

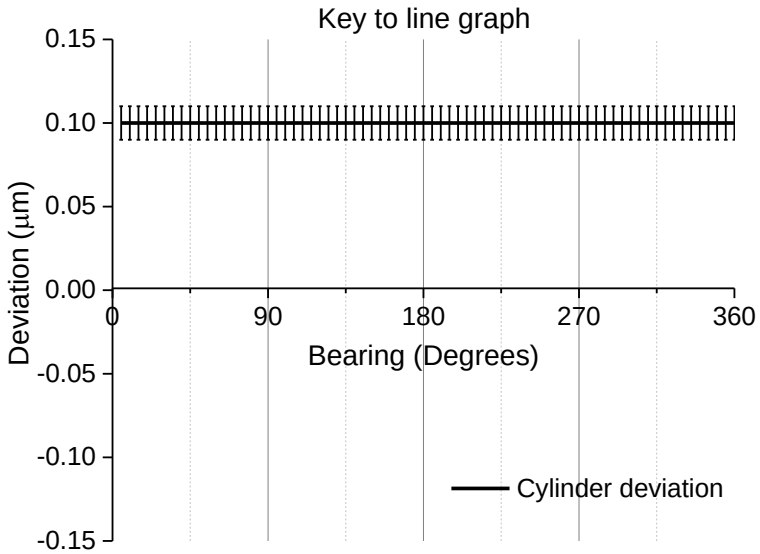

Figure 4.11 Key to line graphs used in thesis. Mean taken for every 5° interval, scale bars are the standard deviation for interval

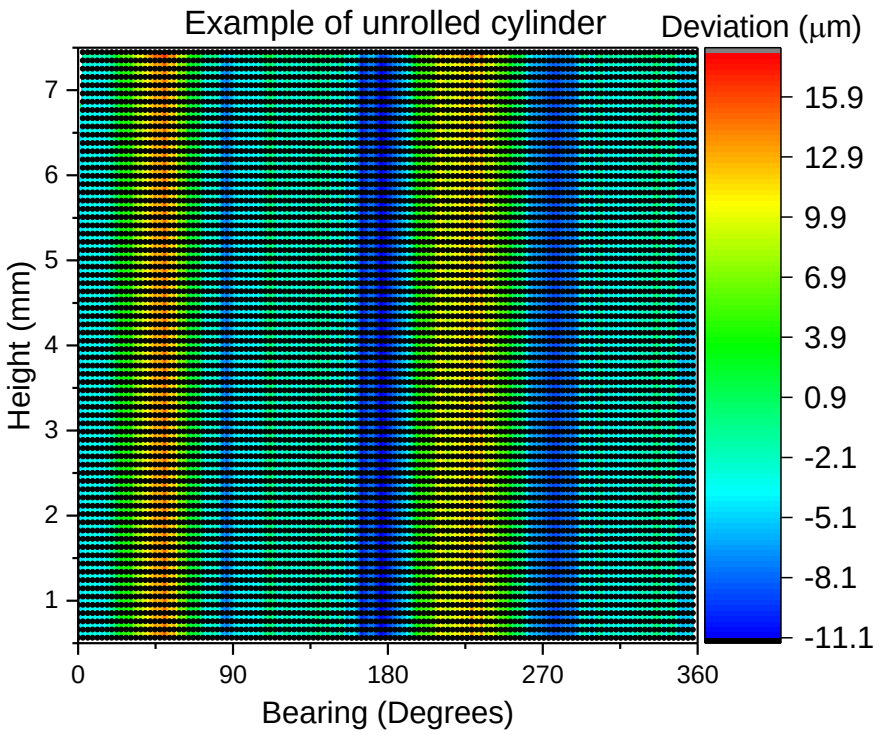

Figure 4.12 Key to unrolled cylinder graph. Graph based on every fit point used to fit cylinder (black dot on graph)

The holeplate was imaged at three approximate orientations, 0°, 45° and 90° to the horizontal and was supported on a carbon fibre frame made at NPL (see Figure 4.45). At 0° the holeplate laid on the stand to raise it above the manipulator slightly to reduce scatter. At 45° the holeplate slotted into the stand. At 90°, again, the holeplate placed on the stand. With this method, the holeplate was not fixed into position whilst the turntable rotated and the centre of the holeplate could only be aligned approximately with the centre of rotation. This could represent a situation in industry where a custom made stand would not necessarily be available.

After a surface was defined in the volume (as described in Section 2.4.3 and seen in Figure 4.13), the length measurements were collected in VGStudio Max using a template written by PTB, again as part of a potential comparison study of XCT systems in multiple labs as mentioned previously. The macro inserted three planes on three sides of the holeplate surface, from the intersection of these planes two lines were defined. A single point was then defined from the intersection of these two lines. The points for the bidirectional measurements were defined by intersections between planes and lines. It should be noted that when the holeplate was imaged at 90°, it was mistakenly placed upside down during imaging so that the holes 1 to 6 were at the top, it was decided at the time not to repeat as it was thought that it was not crucial.

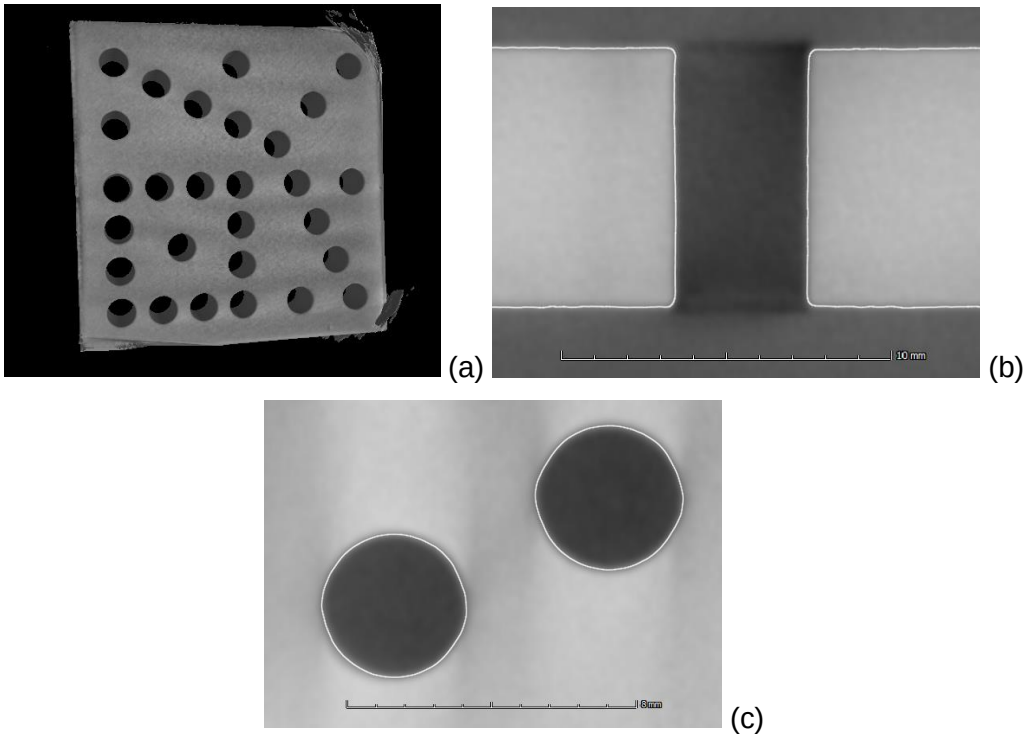

Figure 4.13 Screen shots from VGStudio Max (a) reconstructed holeplate (b) cross section across a hole (c) cross section through two holes. White line indicates defined surface

The points taken on the surface and the unidirectional and bidirectional lengths can be seen in Figure 4.14 and Figure 4.15.

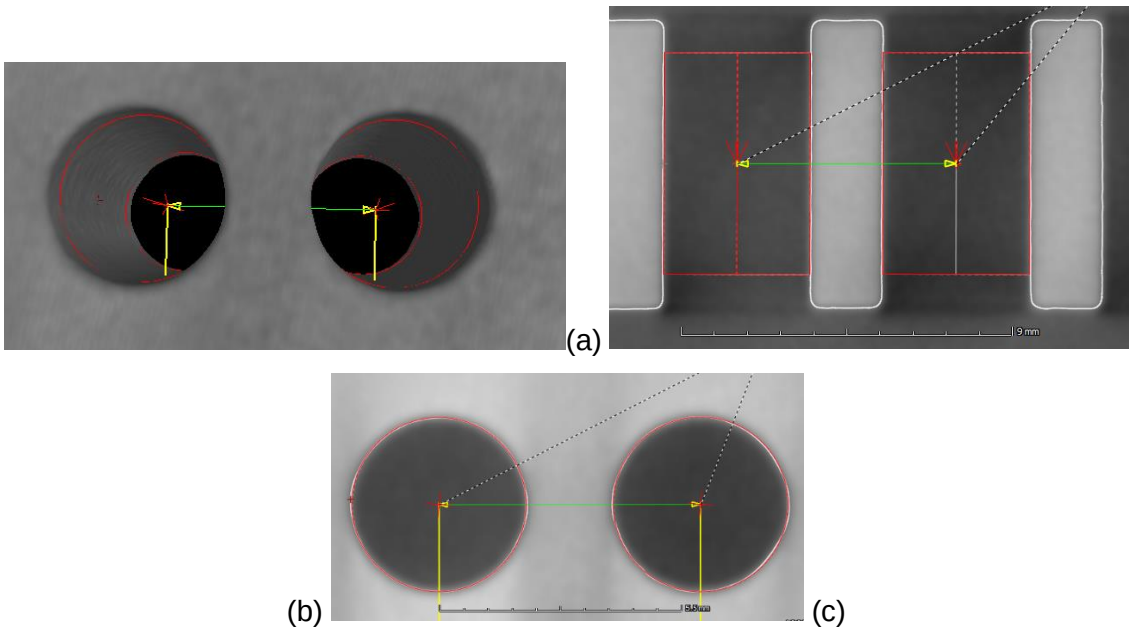

Figure 4.14 Screen shots from VGStudio Max. Unidirectional lengths (a) reconstructed holeplate (b) cross section across a hole (c) cross section through two holes. Red line indicates defined cylinder

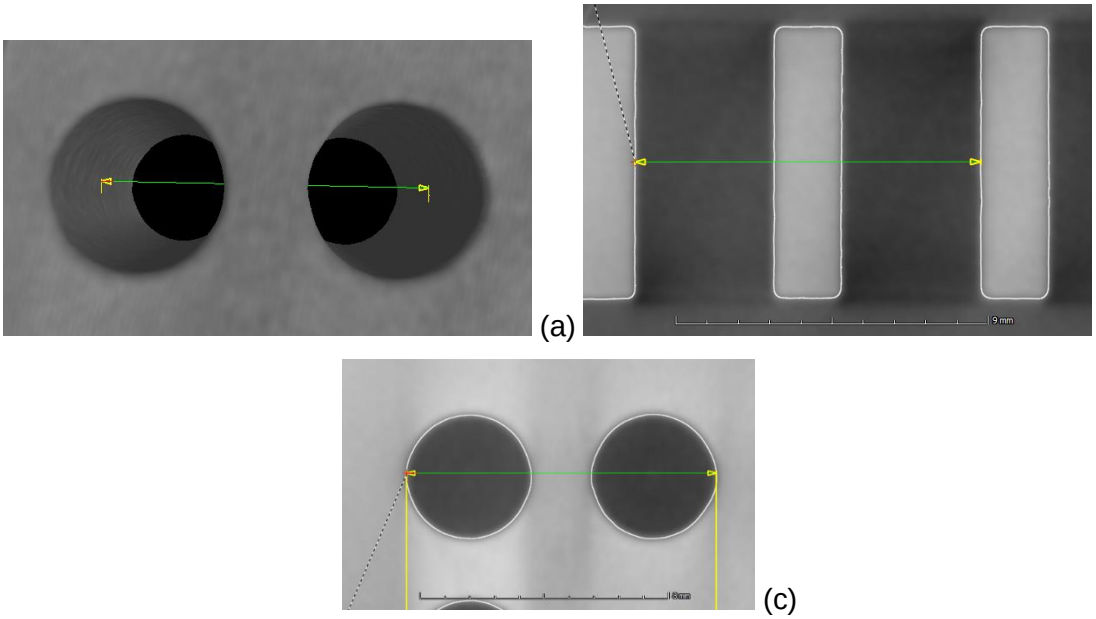

Figure 4.15 Screen shots from VGStudio Max. Bidirectional lengths (a) reconstructed holeplate (b) cross section across a hole (c) cross section through two holes

4.2.5 Lengths

Both unidirectional and bidirectional measurements were taken between cylinders. The path of these measurements can be seen previously in Figure 2.36. These paths were already defined by the PTB template and it was decided to use them for the initial imaging of the complex holeplate so that the results could potentially be compared to data taken from other institutions that were involved in a potential inter-laboratory study using the holeplate. The second time the holeplate was imaged, when it was fixed in the custom built stand, all of the cylinders were fitted manually and the PTB macro was not used. The distance between the cylinder centres was calculated using their centre coordinates and the distances between all of the different cylinders were calculated.

The CMM length measurements were subtracted from the XCT results, the unidirectional results can be seen below in Figure 4.16. The largest difference seen is 10 µm, this occurs when measuring a length of 50 mm when the holeplate was at 90°. This is within the MPE of the system ((9 + L/50) µm where L (length of measurement) is in mm) and would therefore be considered acceptable. However, the graph indicates that there is a scaling error, this appears to affect all orientations. If the error was in the X or Y axes, errors would only be seen when the holeplate was at 90°, therefore it indicates that the error is in the Z axis. This suggests that the error is in the magnification used during the reconstruction process. This error is systematic and can be corrected for by calculating the gradient of the slope of the line of best fit, see Figure 4.17.

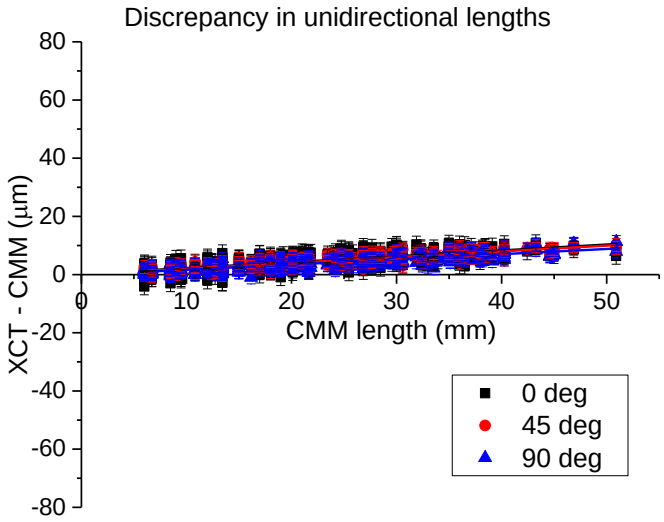

Figure 4.16 Unidirectional discrepancy results for complex holeplate. Error bars equal to standard deviation of population

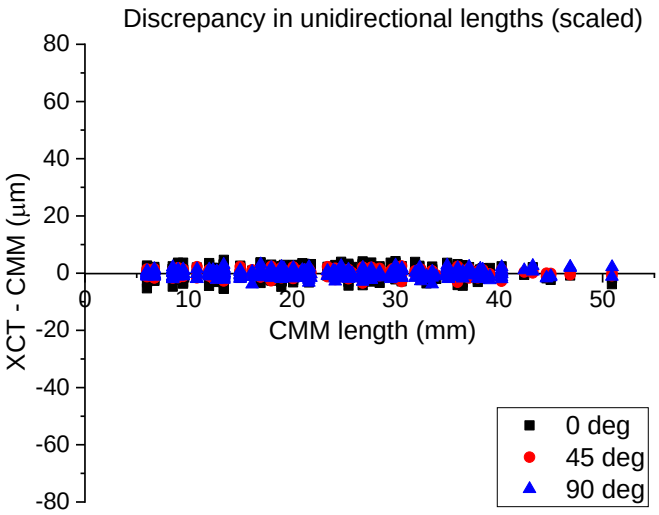

Figure 4.17 Unidirectional discrepancy results for complex holeplate after scale factor applied

When comparing these results to those achievable on the CMM the XCT results are an order of magnitude larger than the CMM. The MPE of the CMM is (1.2 + L/400) µm indicating that for a length of 50 mm the MPE would be 1.3 µm. This indicates that the XCT system is still not comparable, with respect to accuracy with the CMM.

When studying the bidirectional lengths (Figure 4.18) it can be seen the spread in the data is much greater than that of the unidirectional lengths and far exceed the MPE of the system. The standard deviations for the bidirectional lengths are an order of magnitude greater indicating a larger spread in the results, see Table 4.2. The scaling error is not as predominant in the bidirectional lengths, there is, however, systematic bias with respect to the accuracy of the data for the different orientations. When the holeplate is horizontal there is a negative bias, i.e. the lengths measured using XCT are smaller

than the CMM results; the mean deviation is equal to 16.9 µm. This is reversed with a positive bias when the holeplate is at 45° (mean equal to 5.5 µm) and 90° (mean equal to 19.3 µm).

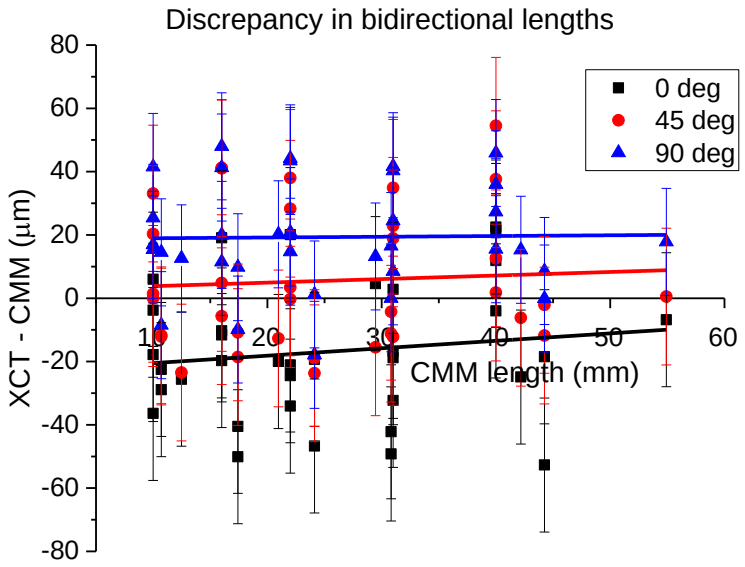

Figure 4.18 Bidirectional discrepancy results for complex holeplate. Error bars equal to standard deviation of population

Orientation	Unidirectional		Bidirectional	
	Mean (µm)	σ (µm)	Mean (µm)	σ (µm)
0°	4.8	2.8	-16.9	21.2
45°	4.5	2.2	5.5	21.6
90°	3.9	2.2	19.3	17.0

Table 4.2 Mean and standard deviation of deviation in length measurements

The scaling errors exist in both data sets, but are more predominant in the unidirectional results. This scaling error is a systematic error that could be accounted for and corrected. If longer lengths were being measured this error would become more problematic and greater discrepancies between the measured and true values would be seen.

The accuracy and spread of the bidirectional results indicates that the threshold plays a crucial role in these measurements. Larger errors occur when the measurements use a single point on the defined surface of the volume. However, if a primitive shape is applied to the surface, multiple points are used and an averaging effect occurs. The centre of this shape is therefore independent of the threshold which should result in more accurate lengths as long as the shape is positioned correctly.

4.2.6 Cylinder radii

The radius of a fitted cylinder can be defined by VGStudio Max, these were recorded for all of the holes in the holeplate and the results can be seen below in Figure 4.19. This data shows similar trends in accuracy and precision to the bidirectional length data. When the holeplate is imaged at 45° the results are more accurate than the other orientations. The most precise results however can be seen when the holeplate is imaged at 90°.

The measured radii appear to be independent of the position of the imaged hole when imaged at 0° and 45°. There does, however, at 90° appear to be a slight increase in the discrepancy as the hole identification number increases. As seen in Figure 4.1, the hole numbers increase along the Y axis of the holeplate, this therefore indicates that the radii changes depending on the position of the hole in the holeplate with respect to the Y axis. This scaling error correlates with the results seen in Section 3.2 where a change in intensity and therefore threshold can be seen down the image.

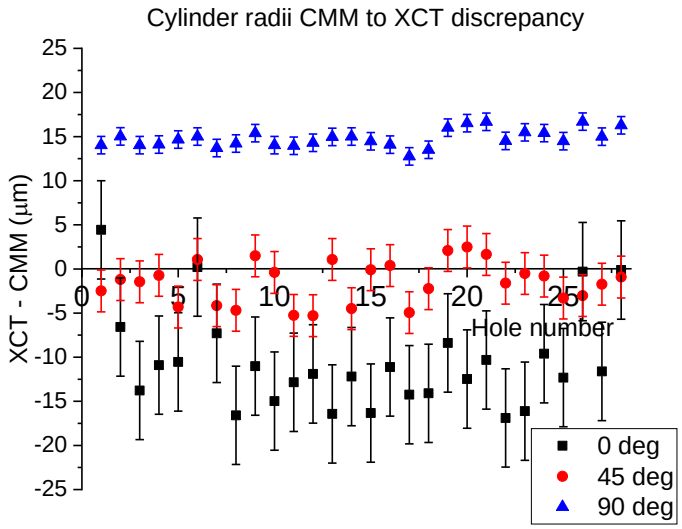

Orientation (°)	Mean (µm)	σ (µm)
0	-10.5	5.6
45	-1.6	2.4
90	14.8	1

Figure 4.19 Cylinder radii, discrepancy between CMM and XCT values. Error bars equal to standard deviation of population (Corcoran et al. 2016)

The cause of systematic offset in the radii of the cylinders, depending on the orientation of the holeplate, is one that needed to be investigated further. It is a crucial error when imaging objects that have features at varying orientations.

4.2.7 Geometry

Determining the cause of the errors in the bidirectional lengths led to studying the geometry of the cylinders, this was carried out by looking at the fit points of the reference objects.

The holeplate is imaged at 0° for the whole of this section. The fit point plots are seen below in Figure 4.20. Three cylinders were chosen to study as they represent extreme positions in the holeplate, Cylinder 1 is in the corner, Cylinder 17 in the centre and Cylinder 19 on the side. The graphs show three very distinctive trends to the cylinder geometry which are unique for each hole.

Cylinder 1 has a distinctive elliptical trend with deviations in the range of -16 µm to 24 µm, the standard deviation for the whole data set is 12 µm although data is much noisier when the deviations are positive, around a bearing of 135° and 315°. The trend appears to have two lines of symmetry running from 45-225° and 135-315°.

The deviations for Cylinder 17 exhibit a very distinctive star shape trend. The deviations range from -25 µm to 40 µm. The noise appears constant around the circumference of the cylinder. There are four lines of symmetry running vertically, horizontally and diagonally.

Cylinder 19 also has a distinctive shape with four lobes. The deviations range from - 18 µm to 19 µm. From 180° to 315° the deviations are no greater than 5 µm. The noise around the cylinder is consistent, it is slightly smaller at 60° and 120°. There is only one line of symmetry running from 90° to 270°.

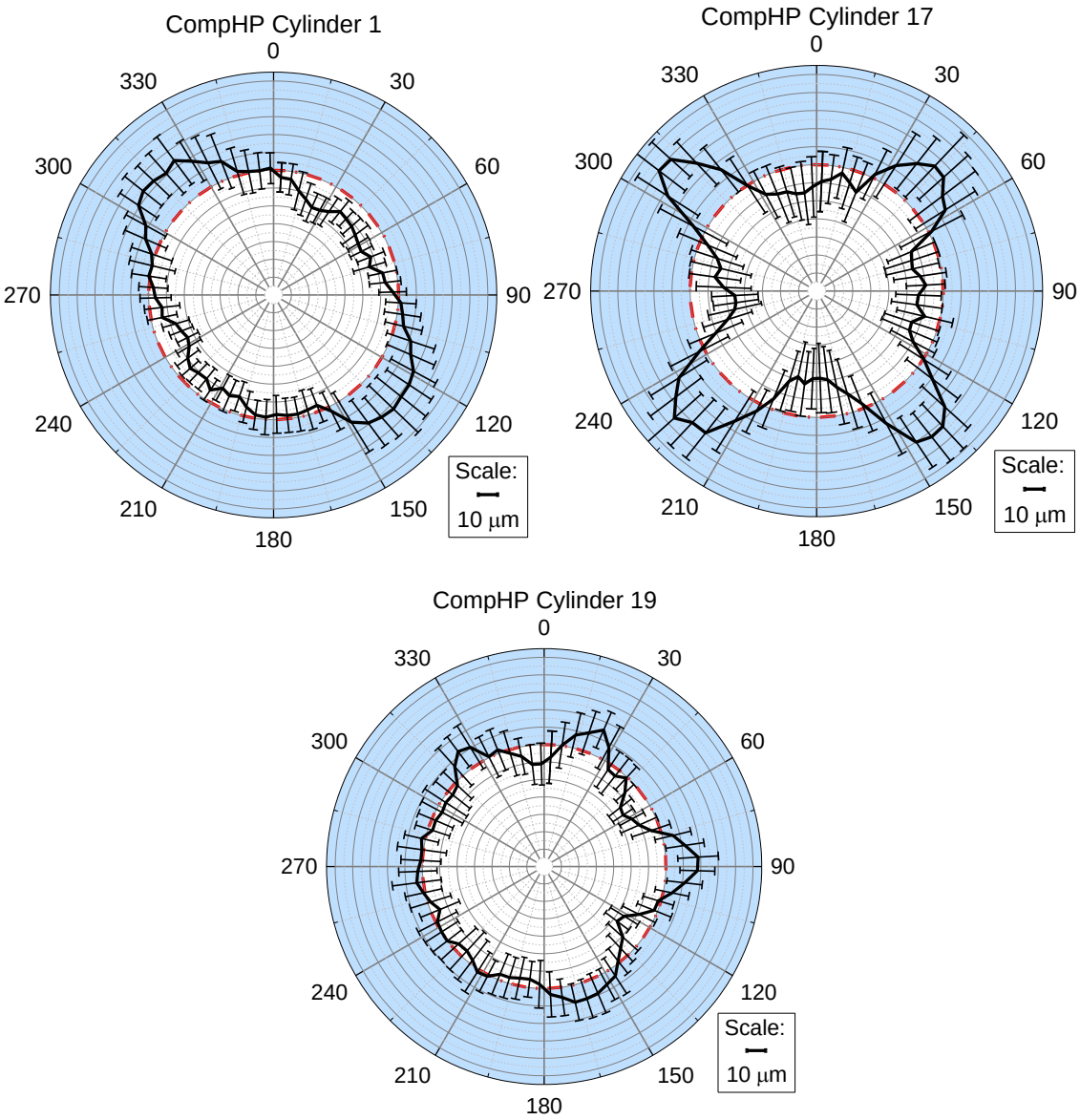

Figure 4.20 Fit point deviations for Cylinders 1, 17 and 19

CompHP was imaged again but this time was fixed in a purpose built holder (see Section 4.3.2). All of the cylinders were analysed and the graphs can be seen in Appendix 2.

Looking at the holes individually the observed deformations of up to 40 µm appear to be systematic, the trends are complex and not consistent between holes. To understand the factors causing these trends a simplification was required.

4.3 Simple holeplates

To simplify the trends seen in the geometry and dimensional measurements in CompHP it was decided to remove as many factors as possible. One of these was the number of holes within the holeplate. Therefore, based on the design of CompHP, three simple holeplates were designed and manufactured at NPL being drilled and then reamed. The

holeplates were made of aluminium, the same as CompHP and were of the same dimensions (48 mm x 48 mm x 8 mm). They all consisted of a single 2 mm (nominal) radius hole placed in the same position as one of the holes in CompHP. This was to allow for a comparison between the two holes. HP1 corresponds to Cylinder 1 in CompHP, HP3 corresponds to Cylinder 17 and HP5 corresponds to Cylinder 19 (see Figure 4.21).

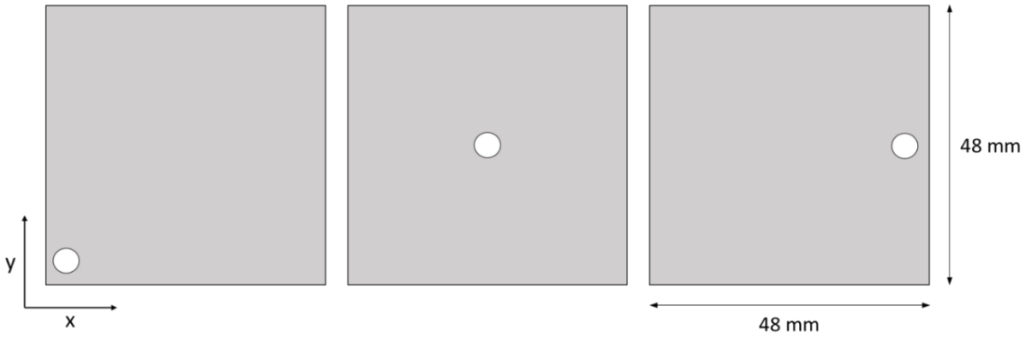

Figure 4.21 Schematic of simple holeplates, HP1, HP3 and HP5 from left to right

The holeplates were measured on a coordinate measuring machine (CMM) at NPL and the maximum deviation in the radius was found to be < 4 µm.

To determine if the trends seen in the geometry of CompHP data were random or systematic a series of experiments was carried out to identify and reduce the errors. The factors to be investigated were repeatability, the stability of the object during imaging, path length of X-rays through the holeplates, orientation of holeplate during imaging and position of the hole with respect to the centre of rotation. These are all discussed below.

4.3.1 Repeatability

Repeatability of dimensional measurements is essential in metrology to allow users to have confidence in the results. The ASTM standard E1441-00 (American Society for Testing and Materials, 2014) states the precision of a system can be determined by measuring a feature multiple times. It states that the object should be moved in between scans to replicate practical situations. To determine if the errors seen in the geometry were systematic or random, the simple holeplates were imaged multiple times and the results were compared. It was intended that each holeplate would be imaged 5 times, to accomplish this a macro was set up on the XCT system to repeat the imaging. Unfortunately, in some cases the system would crash and the 5 imaging sets were not obtained. Due to limited time on the system it was not possible to carry out more runs, the minimum number of runs was 3. Results for HP3 imaged at a 0° orientation can be seen in Figure 4.22 and Figure 4.23. All of the runs have similar trends and the largest

spread in data for all the runs is found at the maximum deviations at 0°, 90°, 180° and 270°. There is a systematic variation of approximately 60 µm, the cause of this deformation will discussed further in Section 4.3.4. As previously mentioned the holeplates were measured on a CMM and the maximum deviation in the radius is <4 µm, therefore the errors in the geometry seen here are significant. No particular run stands out from the others, there are no outliers. The maximum standard deviation between runs is 5.5 µm which is smaller than the systematic errors of 60 µm therefore it was decided that the difference seen between runs was not significant.

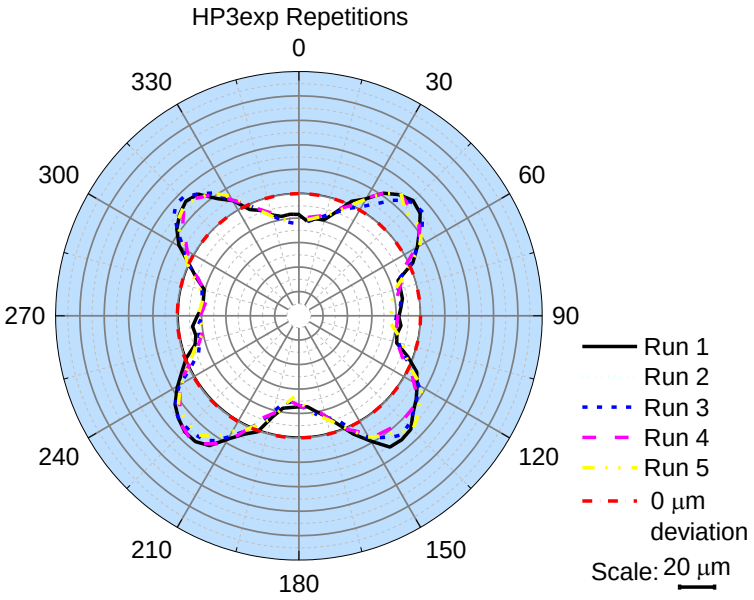

Figure 4.22 Deviation in geometry for repeated runs of HP3

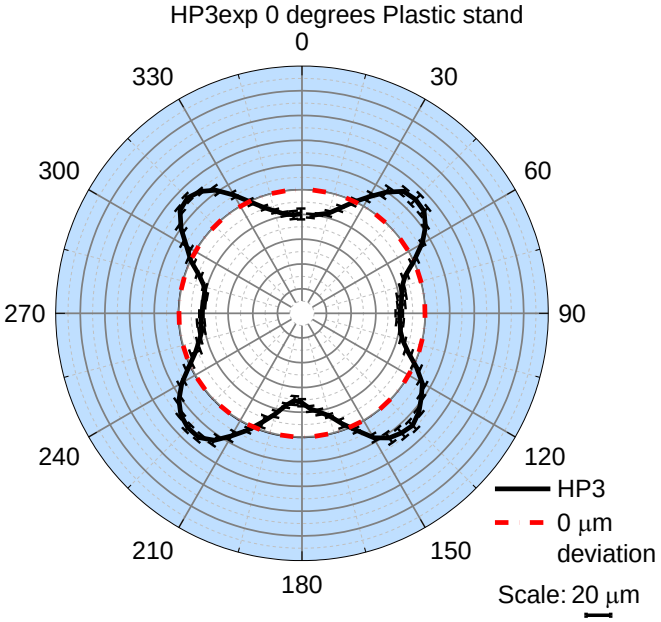

Figure 4.23 Mean of five repeated measurements of HP3. Error bars are standard deviation for each 5° interval for all 5 runs

This data shows that the data is repeatable to within approximately ± 6 µm; this is within the MPE of the system ((9 + L/50) µm where L is in mm). This experiment indicates that the apparent shape of the hole is indeed systematic for this hole with the maximum deviation seen by the lobes being found along the longest path length of the X-rays the most negative deviations seen at the shortest path length, this is discussed further in Section 4.3.4 .

Repeated measurements were carried out for HP1 and HP5 as well, the results can be seen in Appendix 4.

4.3.2 Fixing during imaging

Another factor to consider when identifying potential causes of the errors seen was the fixture and position of the holeplate with respect to the axis of rotation during imaging. It should be noted that CompHP was positioned roughly in the centre of the image and was not fixed rigidly in the carbon fibre stand.

To improve this situation a plastic stand was designed and manufactured by the UCL CEGE workshop, this stand was screwed onto a plate that could be attached to the manipulator and held securely. The whole set-up was designed to ensure that whatever the orientation of the holeplate during imaging (i.e. 0°, 45° or 90°) the centre was always at the same height along the Y axis and aligned with the centre of rotation, see Figure 4.24. The manipulator was positioned using the live X-ray image to align the centre of the holeplate with the centre of the image. The coordinates of the manipulator were recorded to ensure repeatability.

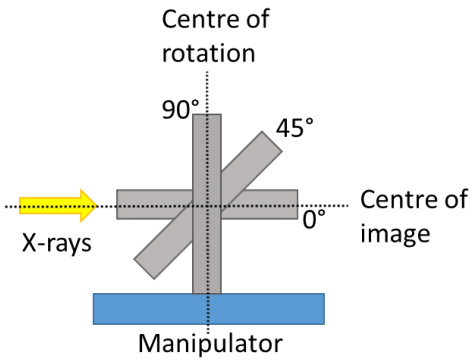

Figure 4.24 Alignment of the centre of the image and centre of rotation was required when the holeplate was being imaged at multiple angles

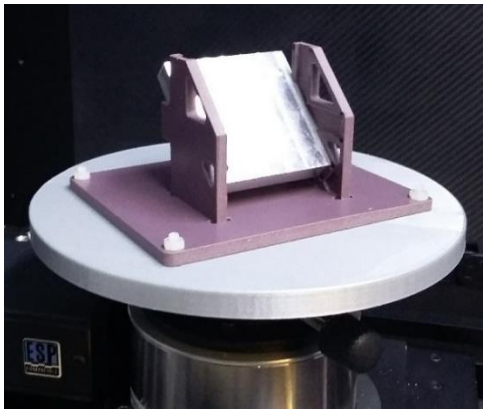

Figure 4.25 Holeplate stand fitted on manipulator in XCT system

To determine if the stability of an object on the manipulator whilst it is being measured affects the dimensional measurements two different set-ups (carbon fibre and plastic stand) were compared.

The results of the deviations along with the standard deviations can be seen in Figure 4.26. Despite the sparser nature of the data when the holeplate is in the carbon fibre stand the same general trends in deformation are present i.e. peaks at 45°, 135°, 225° and 315° and troughs at 0°, 90°, 180° and 270°.

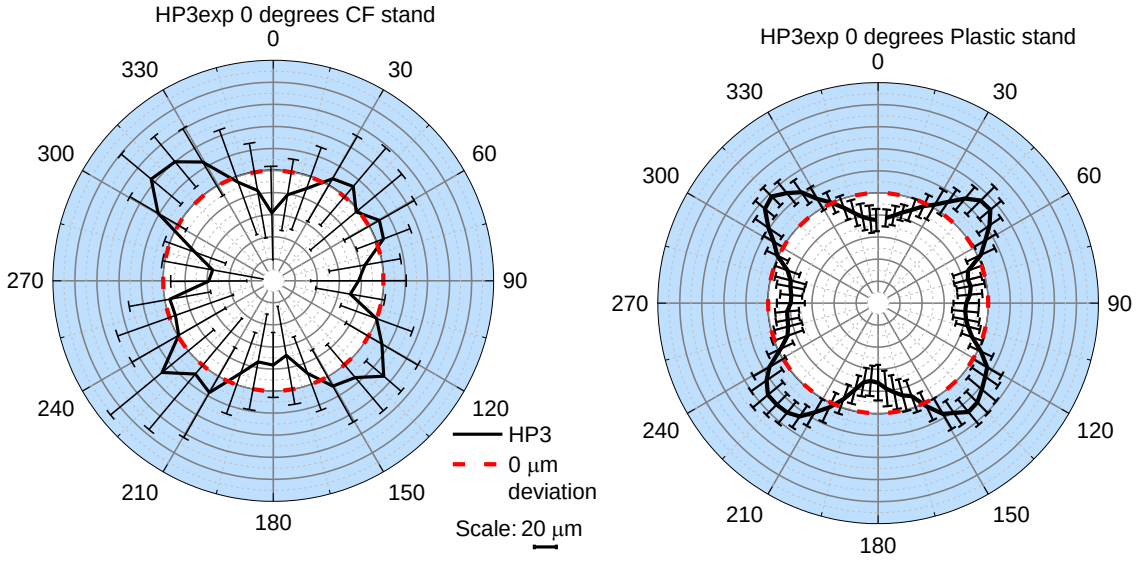

Figure 4.26 Deformation of HP3 with carbon fibre stand (left) and plastic stand (right)

For the carbon fibre stand, the deformations are up to 44 µm compared to a maximum of 37 µm when the holeplate is in the plastic stand. The carbon fibre stand measurements have a maximum standard deviation of 67 µm whereas when the holeplate is fixed in the plastic stand the errors have a maximum standard deviation of 18 µm.

This data highlights the importance of ensuring that the object being imaged is securely fixed and is aligned with the centre of rotation and the centre of the image. Using the

plastic stand reduced the noise dramatically. The use of the stand has brought the noise in the standard deviation down to within the region of the MPE of the system. This shows that any movement during imaging has a consequence on the trend in deformation and the level of measurement noise.

Further experiments were carried out to determine how much impact there was on an object being away from the centre of rotation. These were carried out in Section 5.4.6.

CompHP was imaged again in the new set up, the results can be seen in Section 5.4.3 and in Appendix 2.

4.3.3 Movement in between measurements

The repeatability of measurements depending on the fixing used was investigated above. To continue this further to determine if the shape of the whole was systematic and not random, HP1 was imaged ten times, the first five times the holeplate remained in the stand and the manipulator was kept stationary. In between the subsequent five measurements the holeplate was taken out of and then replaced in the stand and the manipulator was moved from its position before returning to the correct location. This was to check the repeatability if there was movement in between measurements.

Results seen in Figure 4.27 indicate that the standard deviation for the measurements at each 5° interval remain constant between the two different set ups. The data is noisier at 150° and 315° in both cases.

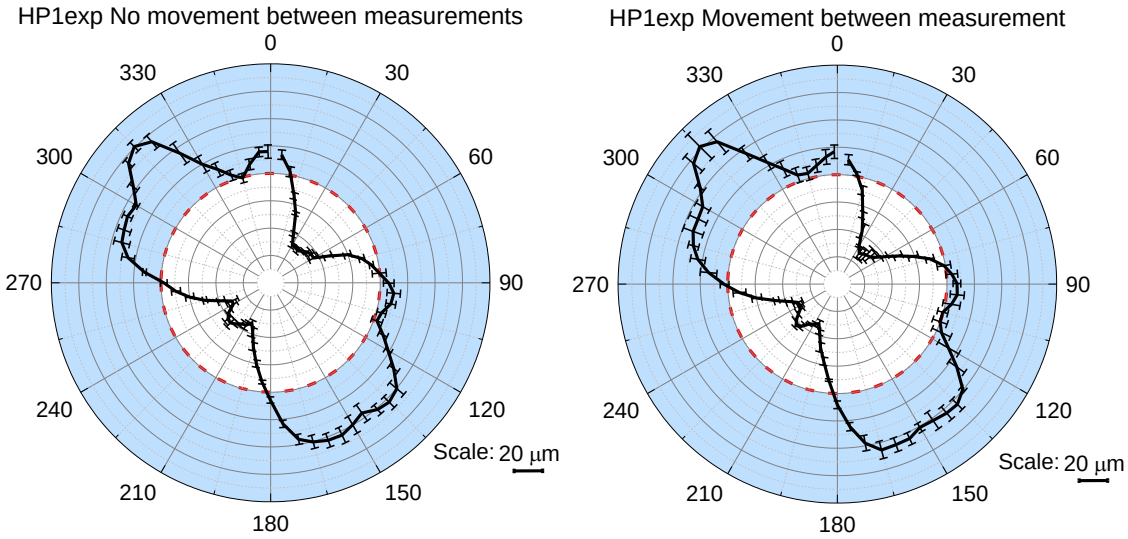

Figure 4.27 Comparison of deformation of HP1. Results show the mean of the five repeated measurements, the error bars are the standard deviation for each of the five results. Left: holeplate remains in stand, right: holeplate taken out and replaced in stand in between each imaging run

These results show that if a stand, which prevents movement during imaging is used, even if the object is removed from and replaced back in the stand, the results still remain repeatable with maximum standard deviations between runs of 6 µm. The deformations remain systematic.

4.3.4 Amount of material – path length

Having shown that the results are repeatable the next step was to look at the length of material that the X-rays are travelling through to determine if this was the cause of the errors in the geometry.

4.3.4.1 Circular holeplate

At the time of manufacturing, two of each simple holeplate were made. The second HP3 was cut into a circle with the hole remaining in the centre to form a circular holeplate (CiHP), this ensured a constant amount of material around the hole. It was fixed into the purpose built stand and imaged at 0°, the results can be seen below in Figure 4.28. A cylinder could only be fitted to the inside hole and not the outside as the data where the holeplate and stand met was too noisy.

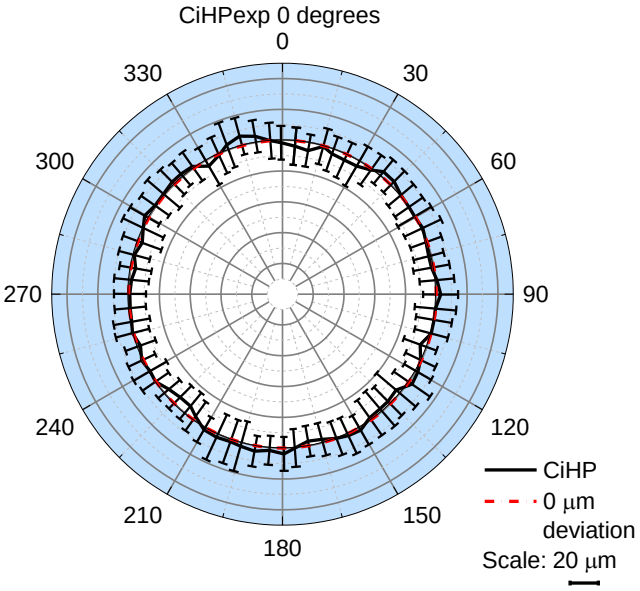

Figure 4.28 Circular holeplate deviations

CiHP has maximum deformations of ±6 µm, the readings have a maximum standard deviation of ±14 µm. This indicates that although the overall deformation is small the surface that the cylinder is being fitted to is fairly noisy. The 0 µm deviation line lies within the bounds of the error bars of the data (the standard deviation of the data for that 5° interval) indicating the errors are not significant and lie within the MPE of the system. This data indicates that the deformation is linked to material thickness around the hole.

To determine if the relationship between the path length of the X-rays through the aluminium and the apparent deformation of the holes is apparent, HP3, introduced earlier in Section 4.3, was imaged at 0° orientation.

Comparative results between HP3 and CiHP, shown in Figure 4.29, indicate an obvious difference between the two holeplates. HP3 has a similar trend as that seen in Cylinder 17 in CompHP. The only difference between HP3 and CiHP is the amount of material around the holes.

This error would be crucial for the dimensional metrology when imaging an object such as an aluminium casting as seen in Figure 2.50.

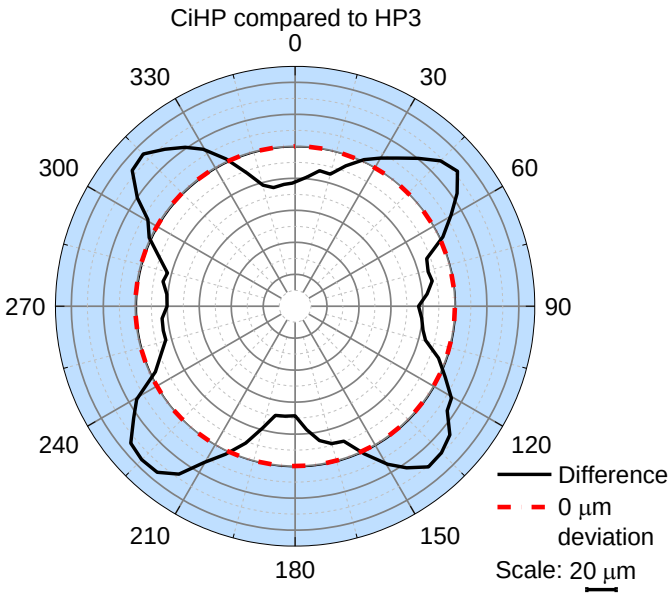

Figure 4.29 Difference between deviation found for HP3 and CiHP

Looking in more detail when HP3 was imaged horizontally at 0° (see Figure 4.30), the deformation has a very distinctive star shape that appears to be related to the amount of material the X-rays have travelled through. The peaks and troughs correspond to the path length of the X-rays as they travel through the holeplate. At the bearings of 0°, 90°, 180° and 270° (when the path lengths are at their minimum) the deformation maximum is -30 µm, however, in between these troughs are large peaks where the deformation can reach 37 µm, this is when the path lengths are at their maximum. The standard deviation of the results appears to increase from ±10 µm at the troughs to ±20 µm at the peaks.

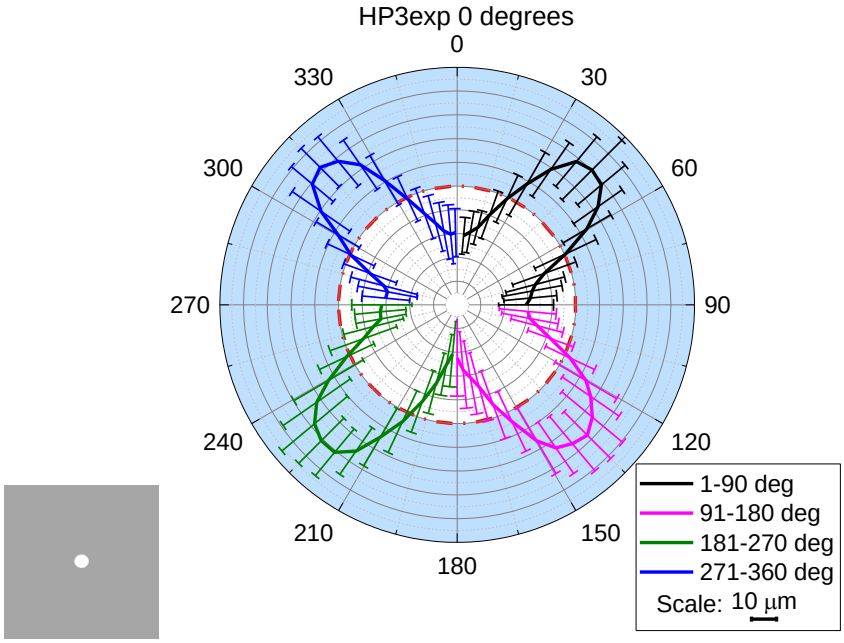

Figure 4.30 Deviations found in HP3 when imaged at 0°

To determine a quantitative correlation between material thickness and deformation, the path length of the X-rays from one edge of the holeplate to the other with the line running through the centre of the hole, was calculated using a MATLAB script written by the author, see Figure 4.31 for a schematic; lengths were calculated every 5° (see Appendix 5 for code). The line is taken on a plane with the surface of the holeplate. Although the volume is reconstructed from multiple paths, this method allows for a simplification to observe correlations.

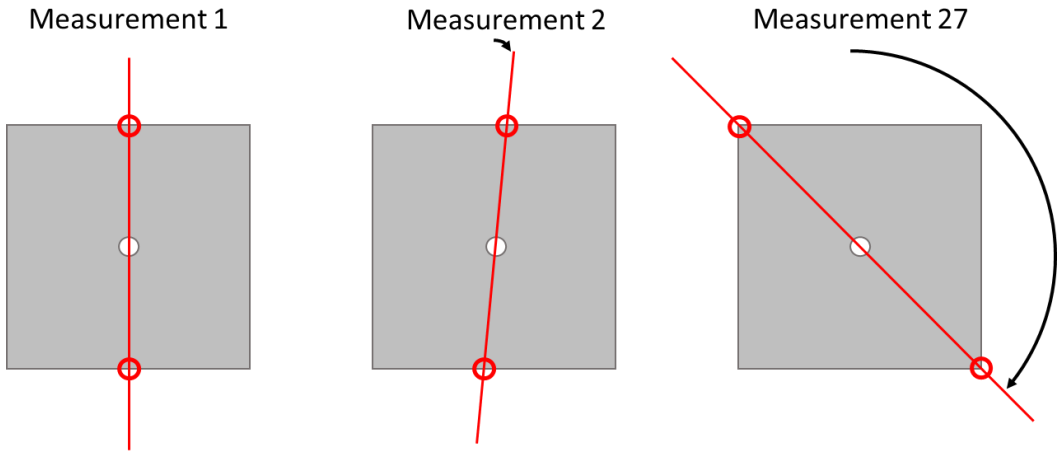

Figure 4.31 Path length through holeplate calculated from edge to edge of holeplate (red circles) through centre of hole in question. 72 measurements taken in total at 5° intervals

Results of the path length and deformation can be seen graphically in Figure 4.32 and Figure 4.33. The graphs indicate that there is a correlation between the two. As the path

length increases the deformation becomes more positive, i.e. the radius of the cylinder at that given point becomes larger. The optimum path length appears to be approximately 49 mm where the deformations are ±5 µm.

The results have been divided up into four quadrants (Figure 4.32), it can be seen that as the quadrants are all of the same shape the points for each individual quadrant are spread across the whole range of data.

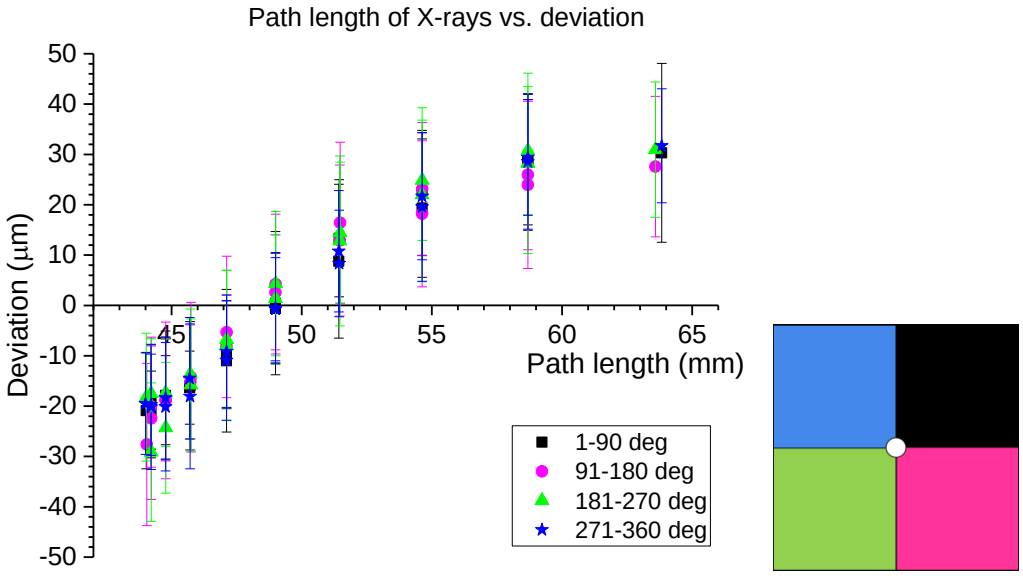

Figure 4.32 Path length of X-rays through holeplate versus deviation with colour coded quadrants for HP3

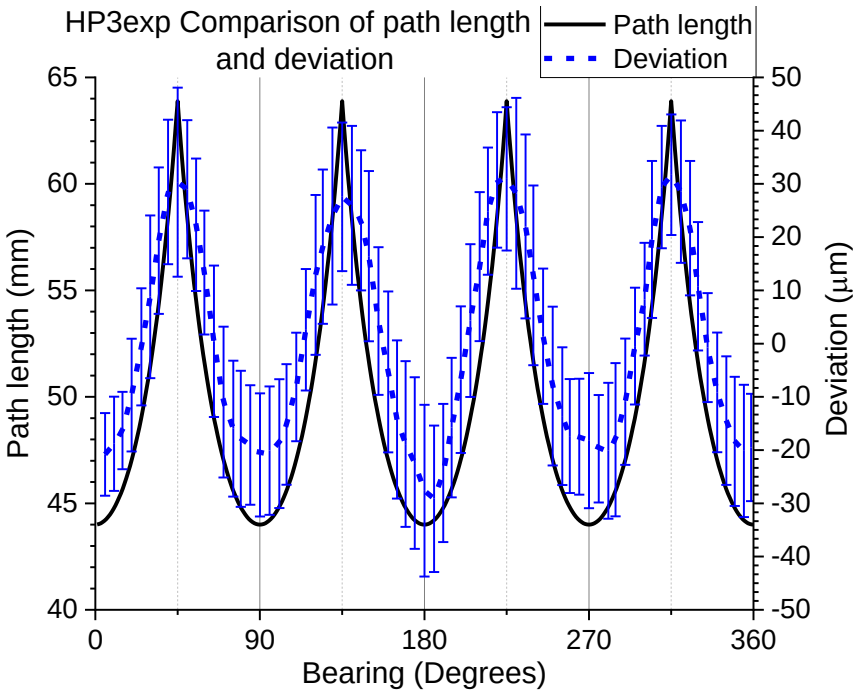

Figure 4.33 Comparison of path length and deviation for HP3

4.3.4.2 HP1 and HP5

To concentrate on the path length of the X-rays through the material, another two holeplates were imaged, HP1 and HP5, the results can be seen below.

HP1 has the maximum path length variations around the hole of each holeplate. The geometry of the hole has a very distinctive trend that has a line of symmetry between 45° and 225°, this is the same as the line of symmetry for the holeplate. The major axis of the ellipse lies along the line of smallest path length. Deviations range from -27 µm to 30 µm with the greatest standard deviation equalling 30 µm. The greatest noise is seen along the line between 135° and 315° where the more positive deviations and shortest path lengths can be found.

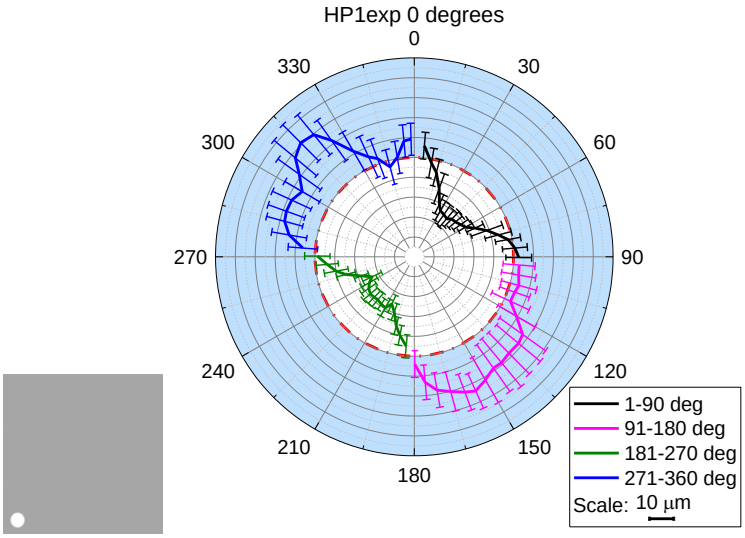

Figure 4.34 Deviations found in HP1 when imaged at 0°

When considering the deviations with respect to the path length of the X-rays the trend in data varies from that seen in HP3. In this case the data is divided up into two distinct regions both of which have systematic characteristics that are dependent on the quadrants, see Figure 3.20. The negative deviations are from the quadrant between 0° and 90° and the one opposite it from 180° to 270°. These correspond to where the path lengths are at their longest. The deviations appear to become more negative between path lengths of 45 to 55 mm and then they plateau. In the other two quadrants, where path lengths are at their shortest, exhibit positive deformations with a large spread. The noise is much lower for the longer path lengths. The negative trend can be seen clearly in Figure 4.36, however, it can also be seen that the deviations do not follow the path length smoothly, like HP3.

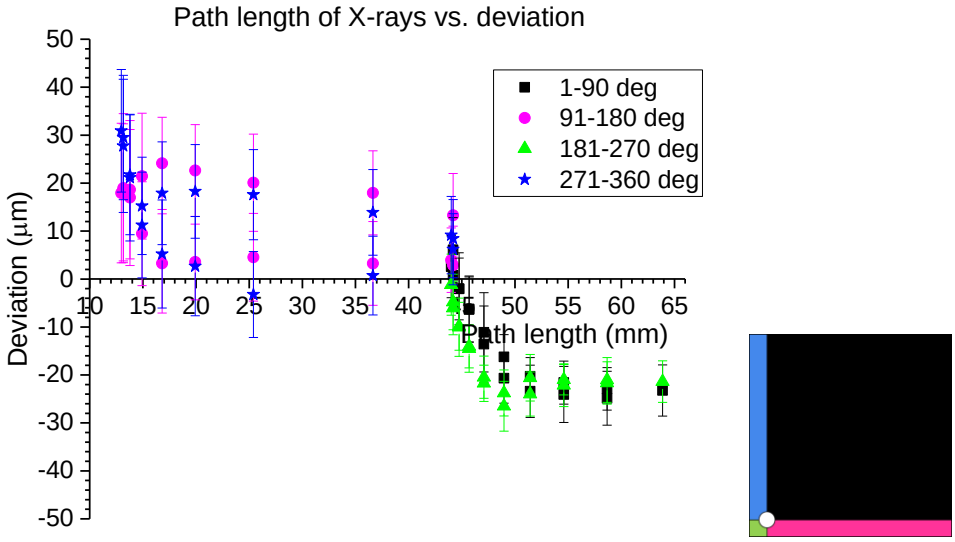

Figure 4.35 Path length of X-rays through holeplate versus deviation with colour coded quadrants for HP1

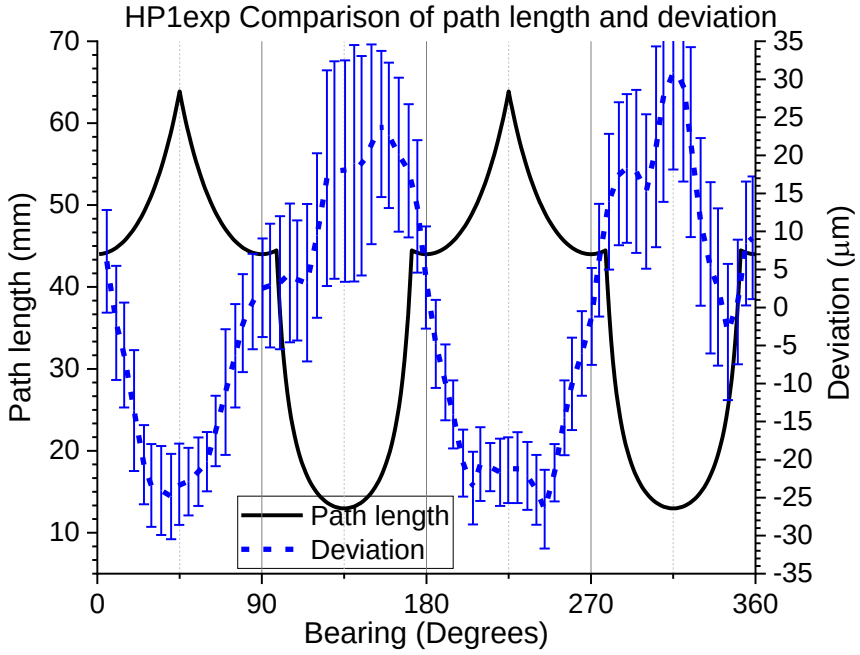

Figure 4.36 Comparison of path length and deviation for HP1

The results for HP1, highlight the biggest effect on the geometry presented in this thesis and illustrates a worst case scenario. Industrial cases such as the cylinder head seen in Figure 2.50 would be affected by these errors as they have differing amounts of material around the holes.

The deviations for HP5, as seen in Figure 4.37, also show a distinctive trend. There is a line of symmetry running from a bearing of 90° to 270°. This again corresponds to the line of symmetry in the holeplate itself. Deviations are in the range of -17 µm to 22 µm with the standard deviations reaching 16 µm.

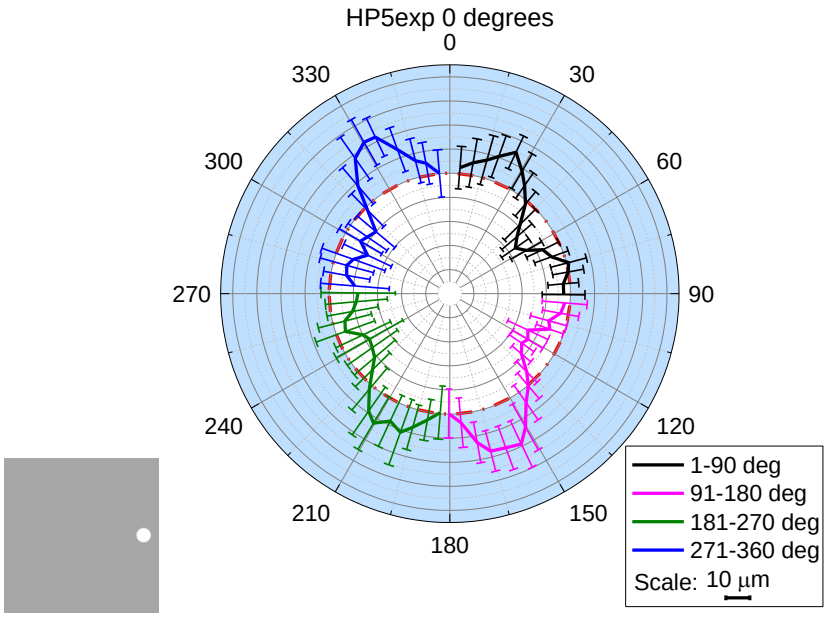

Figure 4.37 Deviations found in HP5 when imaged at 0°

When comparing the path lengths and fit point deviations in Figure 4.38 and Figure 4.39 there is a negative correlation; as the path lengths increase the deviations become more negative, this is similar to what was seen in HP1. The link between the quadrants is not as obvious as it was for HP1, there appears to be data from all quadrants distributed across the whole range.

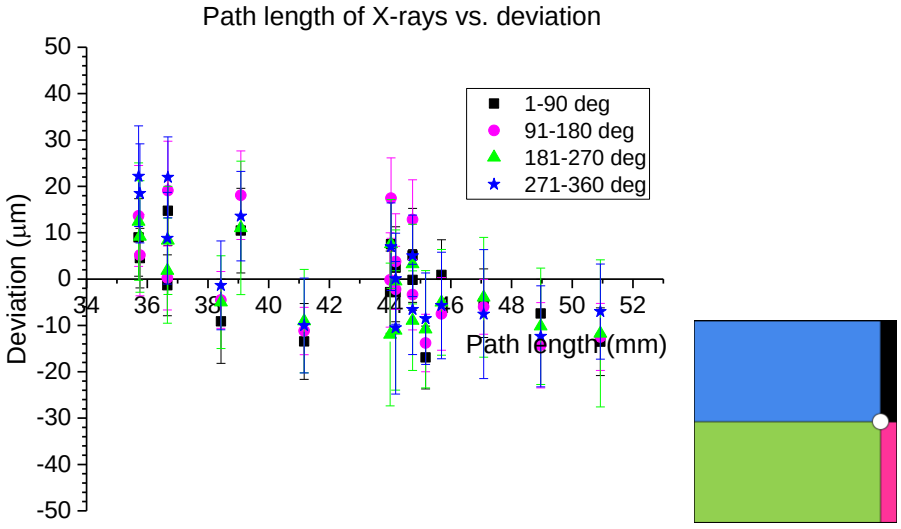

Figure 4.38 Path length of X-rays through holeplate versus deviation with colour coded quadrants for HP5

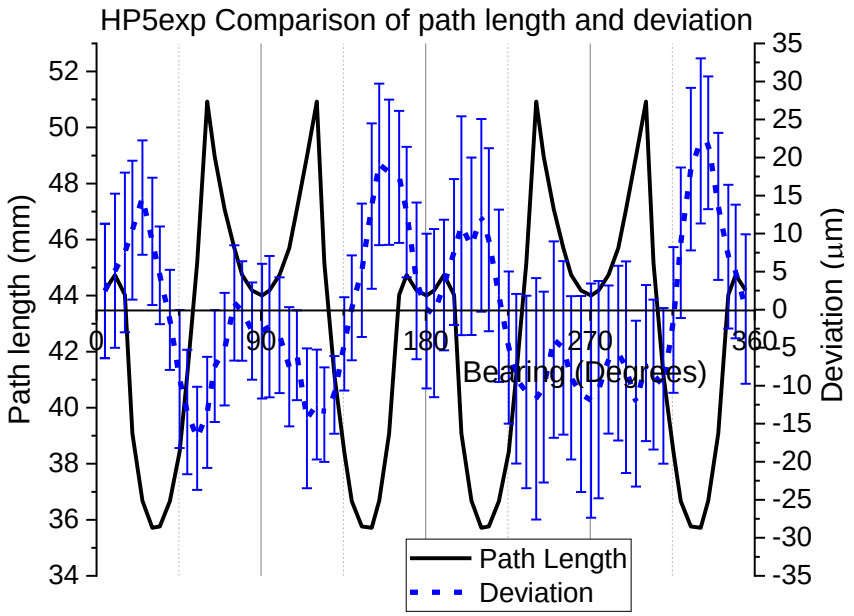

Figure 4.39 Comparison of path length and deviation for HP5

Holeplate	Area under graph	Radius (mm)
HP1	-254.5	2.008
HP3	248.5	2.001
HP5	-69.3	1.975

Table 4.3 Area under fit point deviation graph and radius of fitted cylinders for simple holeplates

Path length of the X-rays through the object and the subsequent effective energy of the X-rays that reach the detector have a major influence on the apparent systematic deformation of the holes. The shape, which can have errors of ±30 µm varies depending on the position of the hole within the holeplate and the amount of material around the hole. This is clearly seen when comparing CiHP with HP3.

The systematic characteristics seen here are revisited in Chapter 5 when numerical simulations are used to study the effects of varying path lengths. The effective energy of the X-rays for these different path lengths and their effect on the geometry of the holes is discusses later in the thesis in Section 5.4.2.1.

4.3.5 Beam hardening correction

Beam hardening is often deemed the cause of measurement errors (Kasperl *et al.*, 2014), it is presumed that if beam hardening corrections are applied during the reconstruction process the errors can be reduced. Six different pre-set levels of beam hardening can be applied in CTPro, these are discussed in Section 2.4.2.1.

HP1 was reconstructed using 5 of the different settings and cylinders were fitted. The deviations of the fit points for the different setting can be seen in Figure 4.40. The graph shows that there is deformation in the geometry for all of the levels of correction. For BH5 and BH6, the highest level of corrections, it can be seen that even more deviation is caused at a bearing of 225°. However, at 45° it appears to correctly reduce the deformation.

Although the beam hardening correction may correct any cupping effects seen in the images (as seen in Section 2.3.1), this graph shows that the corrections do not necessarily reduce the apparent deformation in the geometry and in some cases even exacerbates it.

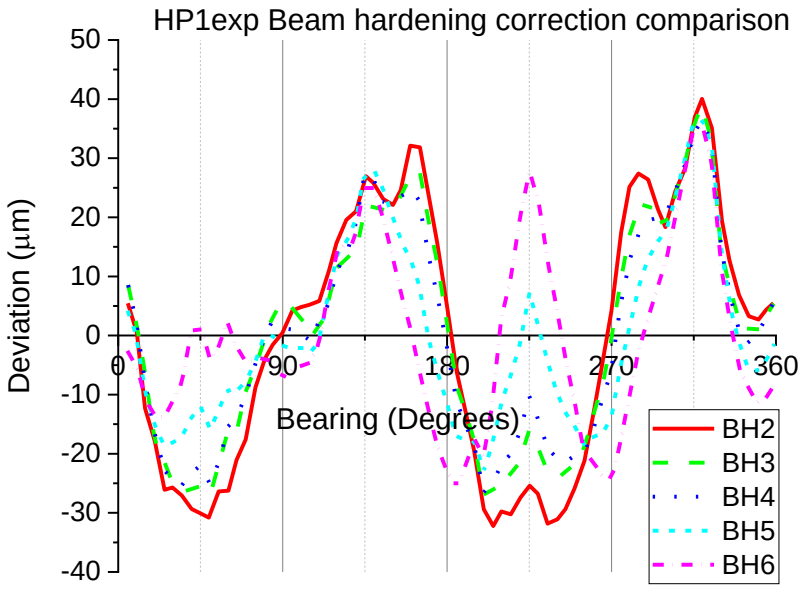

Figure 4.40 Fit point deviations for HP1exp with the use of different beam hardening corrections

As explained in Section 2.4.2.1, the different levels of correction are using pre-set values that are applied to a polynomial function that is used for the linearization of the polyenergetic curve. As these values are designed to cover a vast range of objects of varying materials a perfect correction will be unlikely to be found.

To identify what was happening to the data for each of the pre-set values of the beam hardening corrections it may have been beneficial to have used different objects of varying geometries.

4.3.6 Asymmetry

To make any trends more obvious the path lengths and deviations were plotted on the same graph against the bearing around the circumference of the cylinder (Figure 4.41).

The negative correlation between the path length and deviation is clear to see as they approximately follow the same opposite trends. An interesting point to note is that although the path lengths repeat after 180°, this is not the case with the deviations. The path length is the total path length, attenuation of the X-rays along that line should be equal from both directions. The intensity value is calculated from the total attenuation therefore if the deviations are a factor of the attenuation each side of the hole should have the same greyscale and therefore deviation. However, as most clearly seen at 90° and 270° (Area B in Figure 4.41) the deviation varies between the two. The side with the least material, 90°, has a deviation of -3 µm whereas at 270°, the side of most material, the deviation is -12 µm. At 25° the deviation is 14 µm but at 205° the deviation is only 8 µm (Area A in Figure 4.41). Area C in Figure 4.41 indicates a discrepancy of 9 µm between 150° and 330°. Although using just one path length is a very simplified way of looking at the reconstruction, in practice the voxels are reconstructed from X-rays traversing from all directions, this method gives an approximation to allow correlations between the errors to be seen.

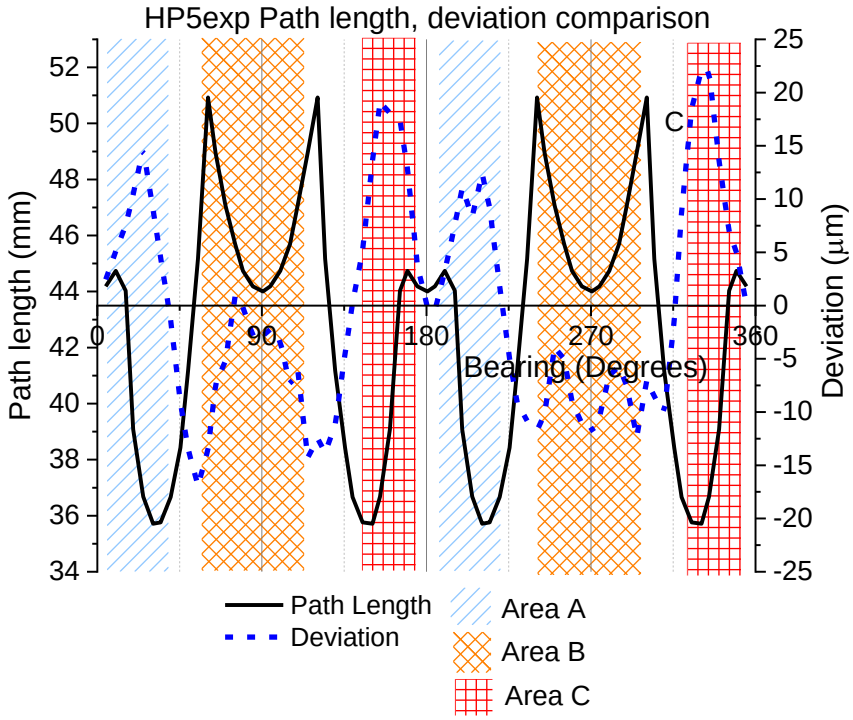

Figure 4.41 Comparison of path length and deviation for HP5 (areas described in text)

This discrepancy can also be found in the HP1 data along the 45° and 225° line and the 0° and 180° line.

This anomaly indicates that other factors must be having an influence on the deviations, one of which is the decrease in X-ray intensity as the distance from the source increases, this is discussed further in the next section.

4.3.6.1 Inverse square law

One of the influences on the discrepancies in the geometry, as seen in the previous section, is the difference in intensity of the X-rays at a given point on an object depending on where it is positioned within the cone beam. When an area in an object, for example the surface of the hole, is close to the source, the energy emitted from the source is spread across a given area, see cross section A in Figure 4.42. However, due to the nature of how X-rays propagate (as seen Section 3.2.2) as the X-rays travel further from the source the same amount of energy is spread across a larger area (cross section B). This results in a lower intensity in the same area when it is further away from the source.

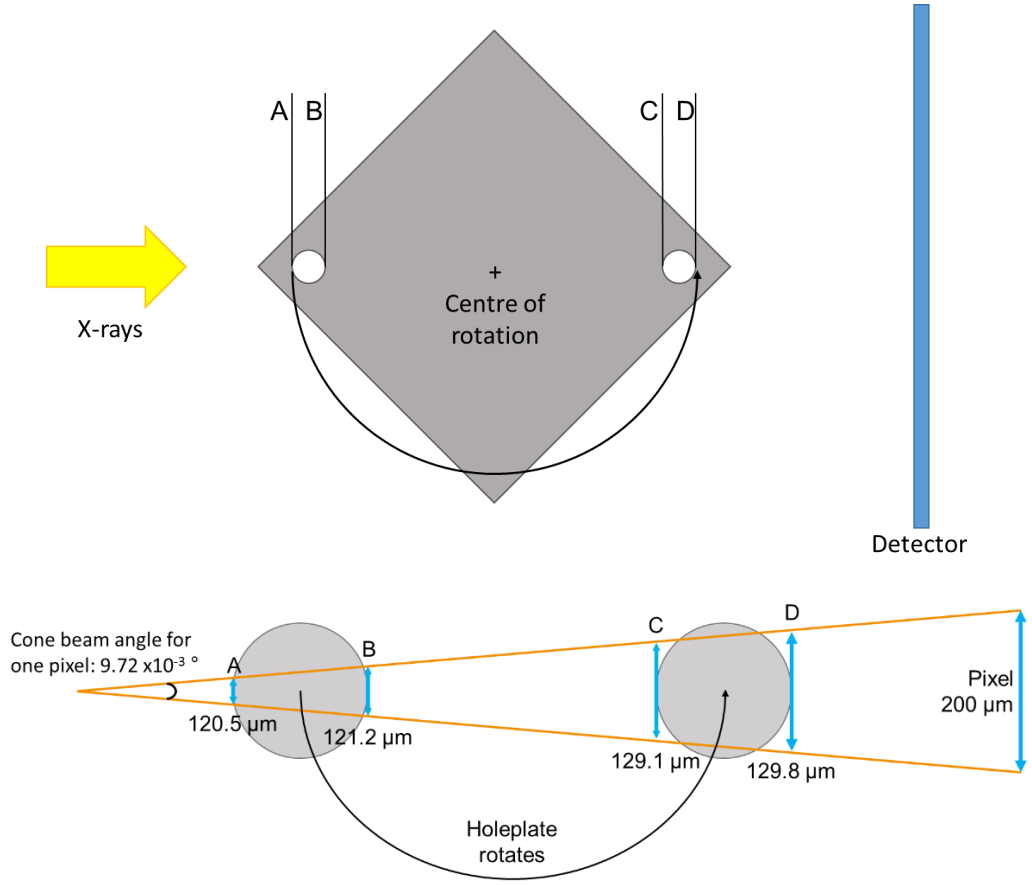

Figure 4.42 Schematic plan view of the voxel position and size at different distances along the cone beam as holeplate rotates 180°

Position	Intensity %
A	100
B	99
C	87
D	86

Table 4.4 Intensity of X-ray energy at each voxel position as seen above

This decrease in intensity is known as the inverse square law ($1/d^2$) where d is the distance from the source (Cherry, Sorenson & Phelps, 2012). Figure 4.42 illustrates the most extreme examples for HP1 when imaged at 0°. The hole is at its nearest and furthest away position from the source, Table 4.4 indicates that for the same size in area there is a 14% loss in intensity that will appear on the detector from position A to position D.

The algorithms for cone beam reconstruction do take this into account but it appears that it may not be sensitive enough for some metrology requirements (such as standard tolerance grades below IT7 seen in Figure 2.51) as discrepancies of up to 9 µm are occurring.

4.3.7 NSI data

To determine that the errors seen in the geometry were not a random error caused by the particular system the holeplates were imaged on and the software that was being used for the reconstruction process, CompHP and HP1 were imaged on a NSI system and reconstructed on their software, efx-CT.

The holeplates were fixed into the same custom made plastic stand and imaged at a magnification of x1.58, voltage of 170 kV and 140 µA. These parameters were chosen to keep the images comparable to the images captured with the Nikon system to ensure as many factors remained the same.

When fitting the cylinders to CompHP in VGStudio Max only 450 points were used. This led to a sparse point cloud meaning that the average deviations could only be calculated every 10° instead of 5° as used previously. It was decided that as this imaging was to determine the overall shape of the hole and as the NSI system was not a metrology system, the lack of points was not a problem as the shape is still visible.

Figure 4.43 illustrates the geometry of Cylinders 1, 17 and 19. The trends in the geometry are very similar to those seen when the Nikon system was used. The errors lie in the region of -30 µm to 20 µm. This is the same order of magnitude as those seen in the Nikon data.

Figure 4.44 shows the deviations for HP1, in this case the deviations range from -30 µm to 50 µm. These deviations are ±10 µm larger than those seen with the Nikon metrology system.

NSI state that their system is not a metrology system. Comparing the specifications for both systems, the main difference appears to be the precision of the manipulator. The

Nikon system is initially set up using a distance measuring laser interferometer to provide correction data for the Z-axis, linear guideway (which varies the magnification). The specifications for the NSI system make no mention of the precision capabilities of their manipulator. An accurate measurement of the manipulator leads to greater accuracy during the scaling in the reconstruction process.

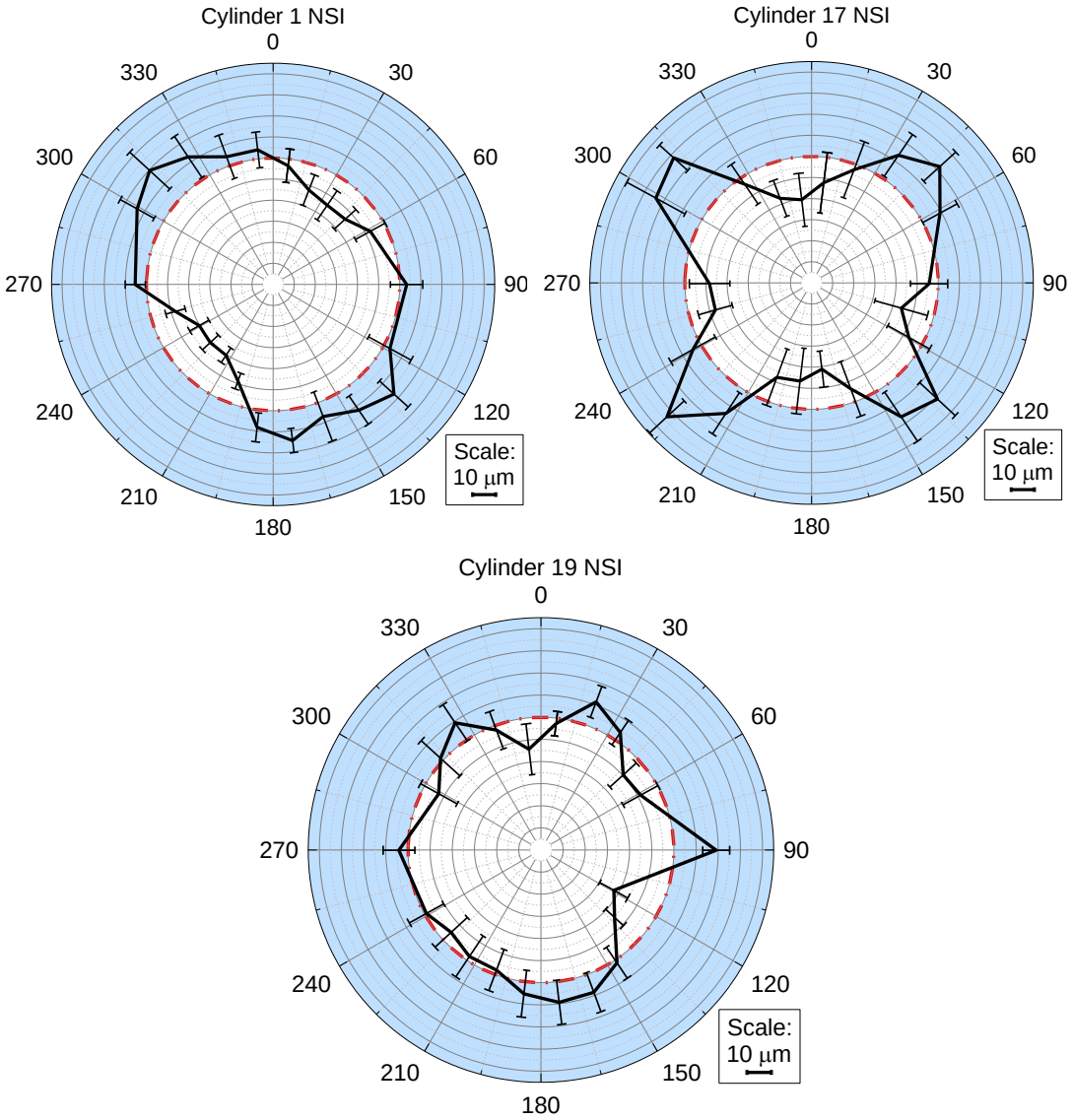

Figure 4.43 Cylinder deviations for complex holeplate imaged at NSI

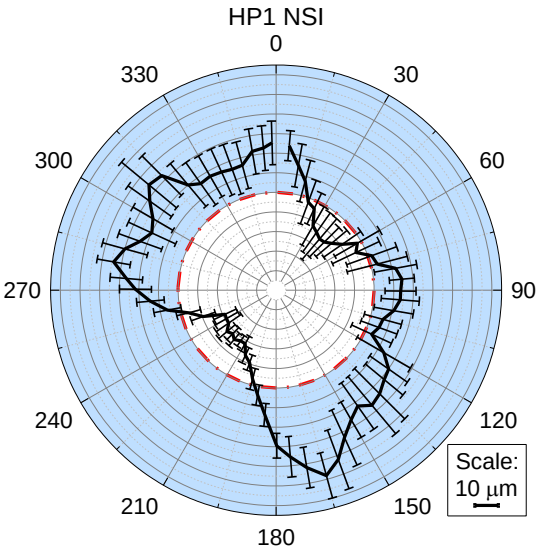

Figure 4.44 Fit point deviations for HP1 imaged at NSI

These results indicate that these trends in the shape of the holes are a function of the physics involved in XCT in general and not a particular system.

4.3.8 Orientation during imaging

Another factor which affected the complex holeplate length measurements was the orientation of the holeplate whilst it was being imaged. This was also apparent in Chapter 1 when the spheres were imaged.

The circular holeplate (CiHP) was imaged at three different orientations, 0°, 45° and 90°, see Figure 4.45 for schematic of holeplate orientations. CiHP was used as the path length around the hole would be constant thereby eliminating one factor. The identification of errors associated with the orientation of an object is crucial if an object that has multiple components at varying orientations is being imaged.

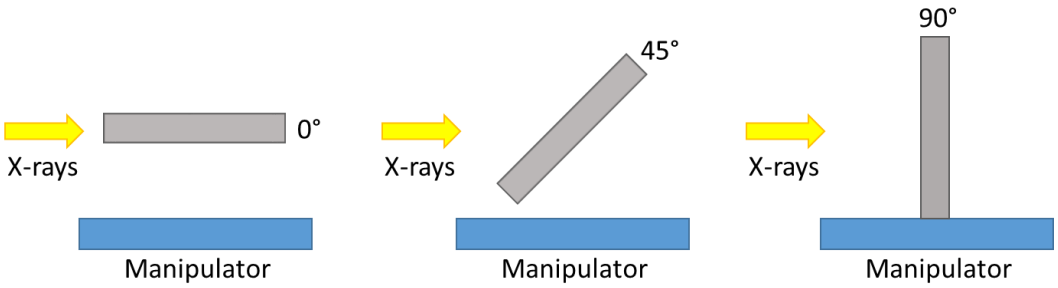

Figure 4.45 The three different orientations of the holeplate during imaging

Results shown in Figure 4.46 indicate that the orientation of the object does indeed have an impact on the cylinder geometry.

At an orientation of 0°, the maximum deformation in the cylinder is ±6 µm. The maximum standard deviation is 16 µm. The deviation is below the MPE of the system so would be considered negligible.

When CiHP is imaged at 45° a different trend can be seen. At a bearing of 90° and 270° the deformation is at its lowest at approximately -10 µm. This deformation continues for 30° either side of the quadrant where the radius of the cylinder becomes greater (up to 20 µm). This continues for 30° until it peaks to 60 µm at 0° and 180°. The noise in the data also increases here.

Having an orientation of 90° during imaging causes similar deformations as those seen at an imaging angle of 45°, however, the magnitude of the deformation is not so great. The maximum deformation, seen at a bearing of 0° and 180°, is in the range of 20 µm.

When considering the measurement noise of the three simple holeplates, it is greatest when the holeplate is at 0° and the smallest at 45°.

Holeplates HP1, HP3 and HP5 were also imaged at the three varying angles and showed similar trends (see Appendix 3 for graphs). This indicates that the main factor causing these particular trends is the orientation and not the amount of material or position of the hole within the holeplate.

Weckenmann and Krämer (2009) carried out measurements on a ball bar and found errors in the distances ranging between -15 µm and -10 µm depending on the orientation of the ball bar, see Section 4.3.9. They had form errors in the spheres of 20 µm to 70 µm. Villarraga-Gómez & Smith (2015) determined with the use of blocks with a single hole running through them (see Figure 2.43), that the deviation from CMM results for the roundness of the holes decreases when the orientation is above 40°. This is contrary to the observations seen in this chapter. Neither paper offers an explanation as to the cause of such findings.

Step gauges of different materials were used by Angel et al. (2015) to determine the effects of orientation on the object. The deviations from a reference length were between -5 µm and -2 µm. They state that the main cause of the errors is scattering and depends on the material of the object being imaged.

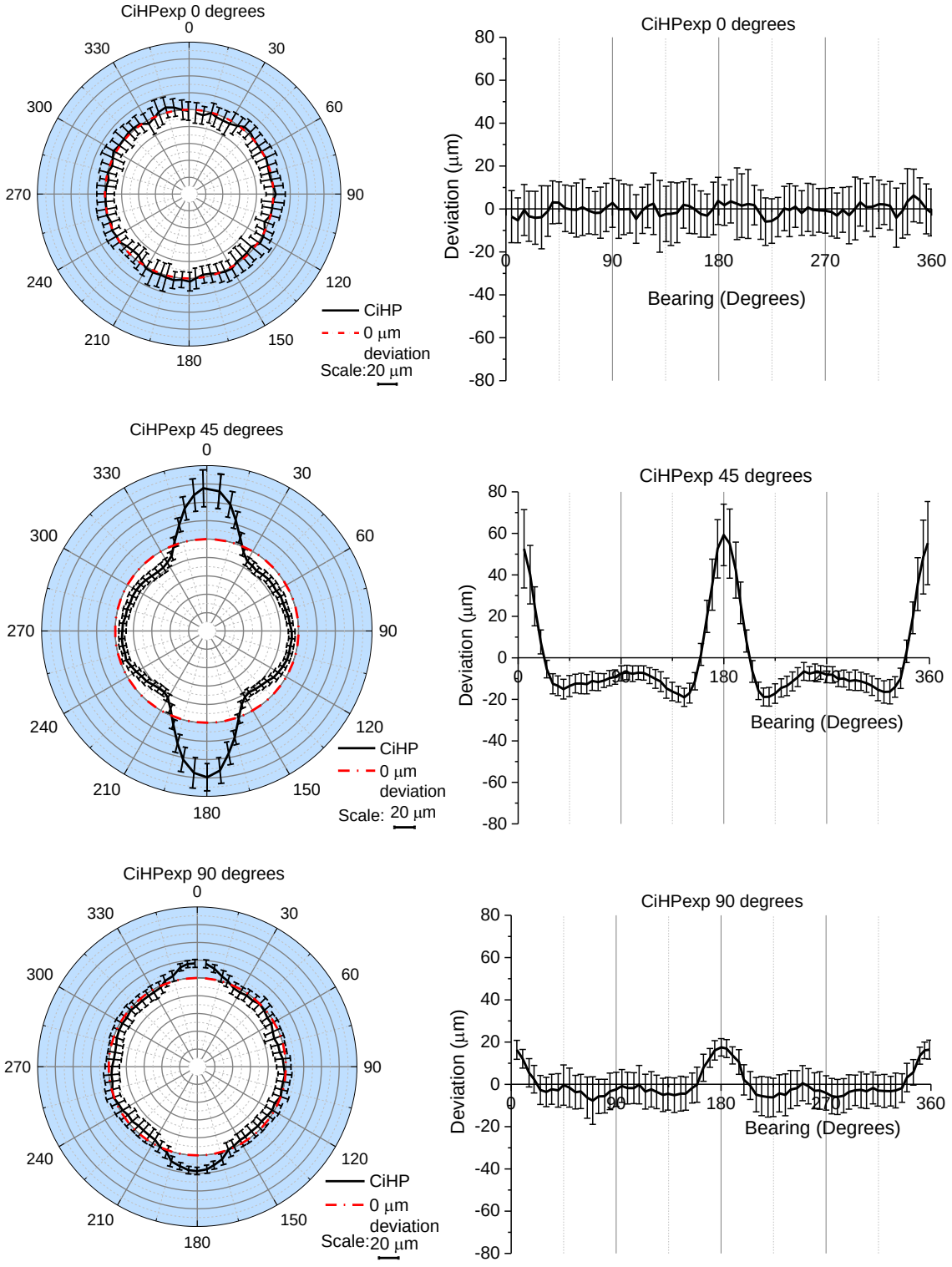

Figure 4.46 Deformation in cylinder geometry depending on angle of orientation during imaging

The greatest deviations in the cylinder fit are seen at 0° and 180°, this is at the top and bottom of the hole as it is being imaged. This matches the theory of (Tuy, 1983), in that the Tuy-Smith conditions are not met and insufficient data is collected on the surface running parallel with the Z axis (Section 2.2.6.2). Although this may contribute to the

deviations seen when the holeplate is imaged at 90° this does not explain the larger errors seen at an orientation of 45°.

Concentrating on the 45° orientation, when comparing a vertical profile of two images from the same imaging run, at two different imaging angles it is possible to see the discrepancies in the path lengths at the top and bottom of the hole (Figure 4.47) for the two views.

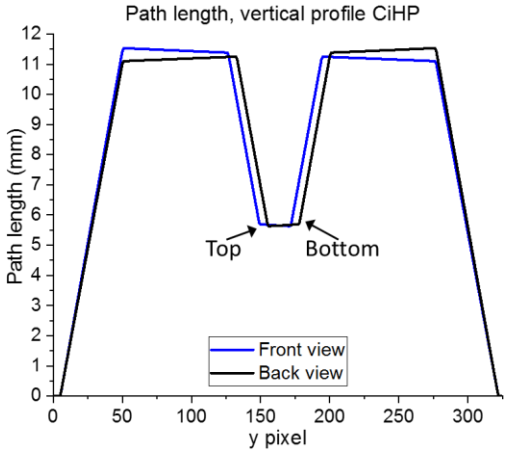

Figure 4.47 Vertical profile of path length taken down centre of CiHP from two different imaging angles (see Figure 4.48 for positon of holeplate)

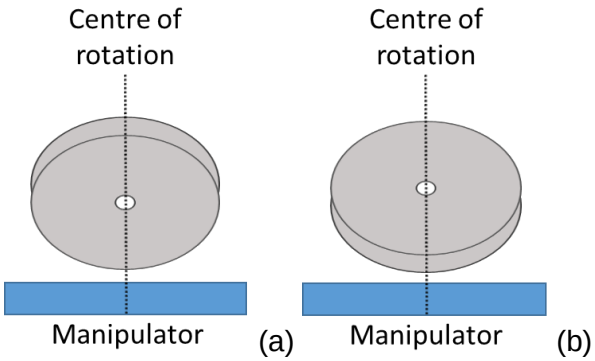

Figure 4.48 Position of holeplate discussed above. From the perspective of the detector, looking towards the source. (a) front view (b) back view

Another aspect to consider is the dramatic change in thickness of the holeplate at different imaging angles as the holeplate rotates during imaging. The maximum thickness, of 44 mm, occurs when the width of the holeplate is parallel with the X-rays, this decreases to 5 mm when the holeplate is perpendicular to the X-rays, see Figure 4.49. This minimum length is found at the top and bottom of the hole.

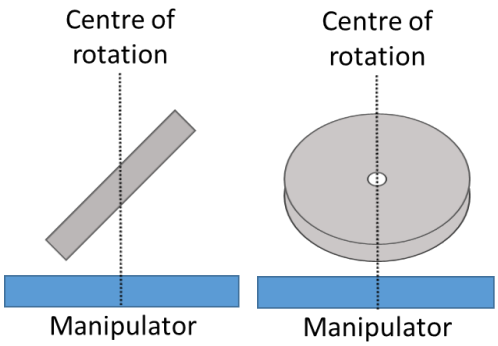

Figure 4.49 Position of holeplate discussed above. From the perspective of the detector, looking towards the source. (a) Parallel (b) Perpendicular

This difference in intensity on the images for the same part of the holeplate was also highlighted in Section 4.3.4.2.

This set of experiments highlights that the orientation of the object during imaging can have a large impact on the shape of the hole with errors of 60 µm being seen when the object is at 45°. This is the largest error seen in this work. It is believed that this could be caused either by the discrepancies between the path lengths depending on the angle at which the image is viewed at and the fact that at an angle there is a large difference between the thickest and thinnest path length of the X-rays.

4.3.9 Magnification

Depending on the size of the object being imaged on an XCT system, different magnifications can be used. For smaller objects a higher magnification may be required to decrease the voxel size and capture more detail. As previously mentioned in Section 4.2.1, the holeplates were imaged at two different magnifications, ×1.6 and ×5. These were the limits at which the holeplate could be imaged. The results, seen in Figure 4.50, indicate that the same trends in deformation are apparent in both magnifications, the only difference is the magnitude. For the lower magnification, errors are in the range of -30 µm to 35 µm with a standard deviation of 20 µm, for the higher magnification, -5 µm to 10 µm with a standard deviation of 4 µm.

The scaling of the deviations appears to be related to the voxel size, for the magnification of ×1.6 the voxel size is 125 µm, for a magnification of ×5 the voxel size is 40 µm. In both cases the deviations are approximately a quarter of the voxel size.

When fitting the cylinders to the holeplates, 10 000 points were used for both volumes. This would have resulted in a sparser population of points for the volume imaged at a higher magnification. The inverse square law, as discussed in Section 4.3.6.1 may also

have an effect on the results. The higher the magnification the closer the object is to the source; this will lead to a higher X-ray intensity for the same cross section of the object.

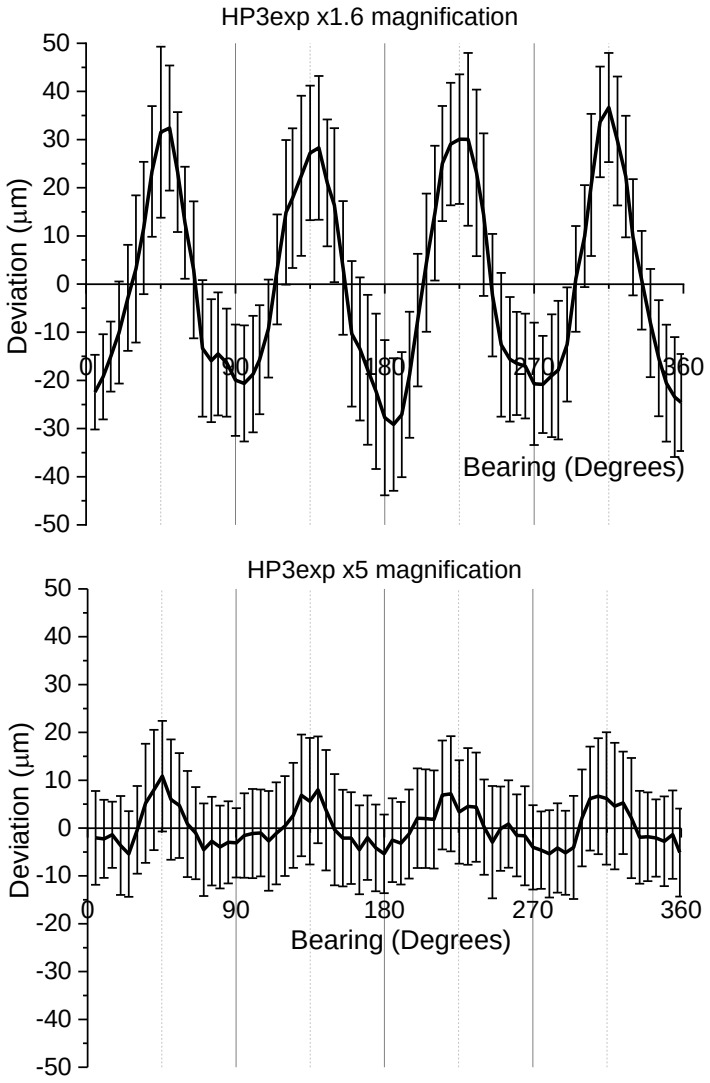

Figure 4.50 Comparison of HP3 imaged with two magnifications (×1.6 and ×5)

Using ceramic spheres of different sizes (4 mm – 50 mm) Shi et al. (2014) measured probing errors of <90 µm for a voxel size of 100 µm. This reduced to less than 20 µm at a voxel size of 40 µm. Weckenmann and Krämer (2009) used two magnifications ×1 and ×2 when imaging a 19 mm ball bar. As the magnification increased the deviations decreased from -17 µm to 7 µm.

Müller et al. (2012) used a ball plate and measured sphere distance errors. Conversely, they reported higher errors (±30 µm) when magnifications were high giving a voxel size of 28 µm and low errors of ±10 µm when the voxel size was 85 µm.

4.4 Error interactions

When all of the errors are considered together, for example orientation and position of hole within the holeplate it can be seen that the deformations occur concurrently, that is they are all present but some have a greater influence. For example, HP5 when measured at 0° as seen in Figure 4.51, has a distinctive shape with errors is the range of ±20 µm, however, when it is imaged at 45° this shape changes and the errors range from -10 µm to 40 µm. When comparing this shape to that of CiHP imaged at 45°, also seen in Figure 4.51, it can be seen that the two shapes have combined, with the effects of the orientation being greater than those of the position of the hole and the X-ray path length.

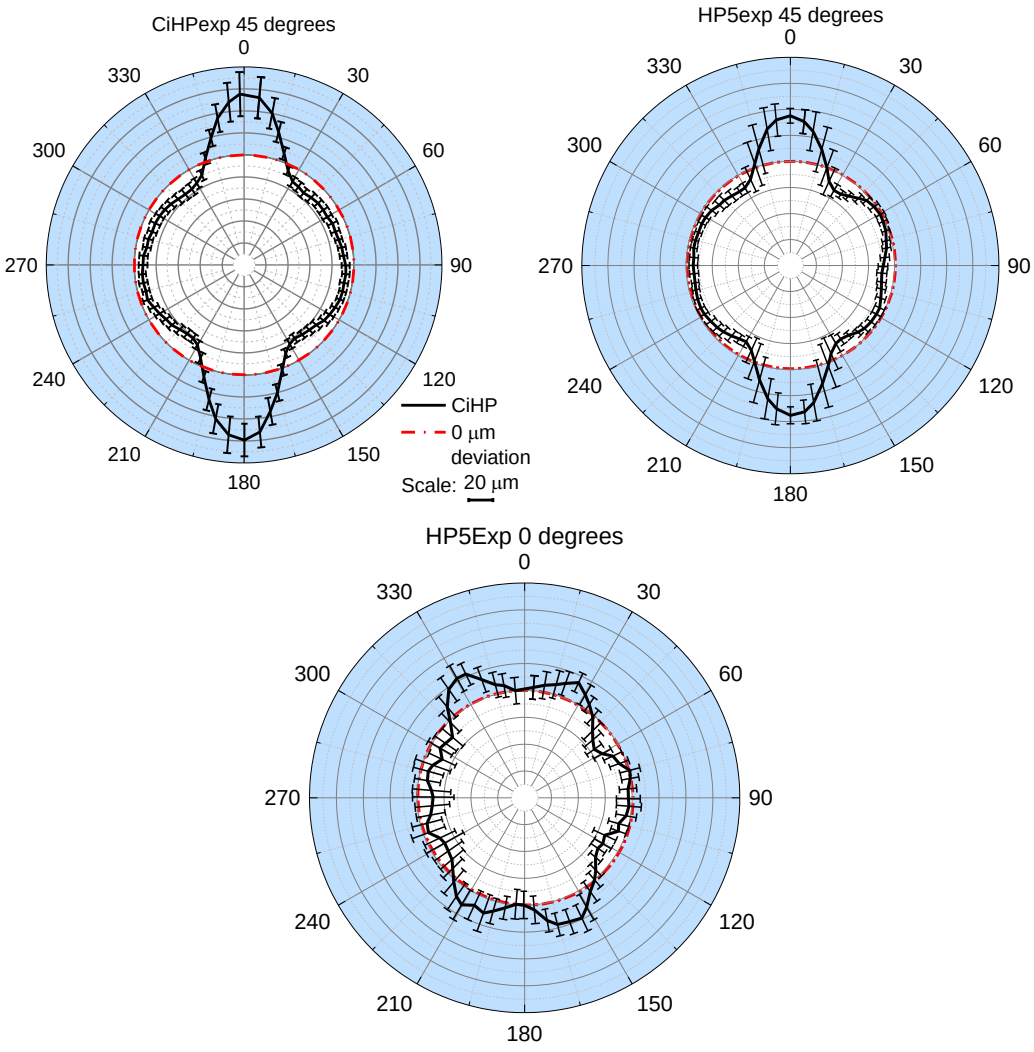

Figure 4.51 Fit point deviations for CIHP and HP5 imaged at 45° (top) and HP5 imaged at 0° (bottom)

4.5 Chapter summary

A series of holeplates was used to study the errors associated with the lengths and the geometry of holes. Factors studied were the path length of X-rays travelling through the object, the position of a hole with the holeplate, orientation of the holeplate during imaging and magnification. A summary of the errors associated with each factor can be seen in Table 4.5.

Factor considered	Observations	Magnitude of errors found in holeplate of size 48 mm x 48 mm x 8 mm with holes having a radius of 2 mm
Complex holeplate	Accuracies of bidirectional lengths and radii dependent on orientation	• Lengths ±20 µm (σ <22 µm) • Radii -11 µm to 15 µm (σ <6 µm)
Fixing during imaging	• Smoother trends in data • Reduced noise	Maximum deviation reduced from 44 µm (σ <60 µm) to 37 µm (σ <10 µm)
Path length	Geometry of hole depends on path length of X-rays	In the region of ±30 µm (σ <16 µm)
Position of hole in holeplate	Asymmetrical position in holeplate leads to asymmetrical deviations	Differences < 9 µm
Orientation during imaging	Systematic deviation in geometry dependent on orientation	At 45°: -20 µm to 60 µm (σ <20 µm)
Magnification	Magnitude of trend depends on magnification	Deviations approximately a quarter of the voxel size

Table 4.5 Factors considered in this chapter and the errors observed

With the use of a complex holeplate this chapter initially highlighted errors in the accuracy and precision of lengths and cylinder radii associated with the orientation of the object during imaging. Scaling errors were present in both the unidirectional and bidirectional lengths, with errors being larger for the bidirectional lengths. Further investigation discovered that the geometry of the hole appeared deformed. The deformation was systematic depending on the position of the hole within the holeplate.

Fixing the holeplate in a stand to prevent movement during rotation and to ensure that it was in the centre of rotation reduced the noise of the geometry data dramatically highlighting that stability of an object during imaging is essential.

The use of simple holeplates indicated that the path length of the X-rays through the holeplate was crucial to the amount of deviation caused to the geometry. Another factor was the asymmetry of the holeplate itself. The deviation on opposite sides of the holes varied depending on the amount of material on that side of the hole. This in turn is related to the position of the hole in relation to the centre of rotation. The intensity across a given cross section will vary depending on the distance from the source as a result of the inverse square law. It appears as if the algorithms used in the reconstruction process, which should take this into account, are perhaps not as robust with respects to the inverse square law and thus lead to errors when using them for metrology purposes. An incorrect interpretation of the intensity will in turn lead to an inaccurate surface being defined on the volume.

The geometry of the holes was affected the most by the orientation of the holeplates during imaging, with most deformation occurring when the holeplate was imaged at 45°. These errors may be due to the large variation in path lengths through the object as it rotates during imaging. The magnitude of the errors was also affected by the magnification. The size of the errors is related to the voxel size of the reconstructed volume.

The systematic change in the geometry explains the discrepancies in the accuracies of the bidirectional lengths in the complex holeplate. If the two points used to take the measurement were to lie on a section of the circumference where these deviations occur, the length would be systematically inaccurate.

Two types of errors have been highlighted, random and systematic. Random errors, with no obvious cause contribute to the MPE of any given system. Systematic errors seen in this chapter create large biases in the data. They are a result of the shape of the object and the set up during imaging. The systematic nature of the errors implies that they could be corrected for.

These deformations in geometry are crucial for the consideration of the holeplate as a reference object to be used with international standards for verification. It can be seen that the assessment of length measurements is vulnerable to errors caused by the deformation in the hole geometry.

Despite these experiments focussing on one type of object imaged in various conditions, creating a particular set of cases, when they are considered all together a bigger picture can be seen. The different factors can start to be considered together in order to represent a more complex object.

Overall, the holeplates provide a simple reference object that can be easily characterised with a CMM to provide reference data. Different factors can be investigated, such as orientation of object during imaging, this knowledge can then be applied to other, more complex, objects. Holeplates as references object have evolved from other verification testing for CMMs so measuring procedures are already in place, therefore it is the natural choice when considering a reference object for XCT.

Chapter 5: Simulation of X-ray images

Chapter 3 and Chapter 4 highlighted many different influences that could lead to apparent errors in the dimensional metrology of objects measured with XCT. The first, seen in Chapter 3, was the variation in intensity of the X-rays both spatially across the cone beam and throughout the measurement period. The second, seen in Chapter 4, was the orientation of the holeplate during imaging and the position of the hole within the holeplate. Both of these led to apparent deformation in the geometry of the reconstructed hole.

To try to understand these errors and potentially reduce them, a series of numerical simulations were carried out. Two methods were used, one basic simulation based on a single image of a sphere and a more complex model that simulates multiple images of the holeplates previously discussed, in a way that replicates the output from an XCT system.

5.1 Initial simulations

Initial simulations involved creating just one 2D image in aRTist, an analytical radiographic testing inspection simulation tool. In aRTist the settings were adjusted to simulate an image that would be generated by the NPL XCT system including angle of target and window material and thickness.

A 2D radiograph of a 2 mm sphere was simulated, this single image was then copied and a gradient, to simulate a non-uniform X-ray beam, was applied in MATLAB. The gradient in intensity was applied to three sets of data, each in a different direction, diagonally, horizontally and vertically, across the image. To reduce the processing time, only 360 images were produced. This is a smaller number of images (usually 3142) than would usually be used for the usual reconstruction process when imaging using the XCT system. These three sets of images were reconstructed in CTPro using the same process as the experimental images, see Section 2.4.2.

5.1.1 Results

The deviations of the fit points from the perfect sphere can be seen below in Figure 5.1. For the diagonal gradient in the images, it can be seen that the largest amount of deformation is found around the equator of the spheres. Here the errors are < - 20 µm. This deviation then reverses half way up and down the sphere and the surface becomes larger (< 20 um) than the fitted sphere. The least deformation can be seen at the poles of the sphere.

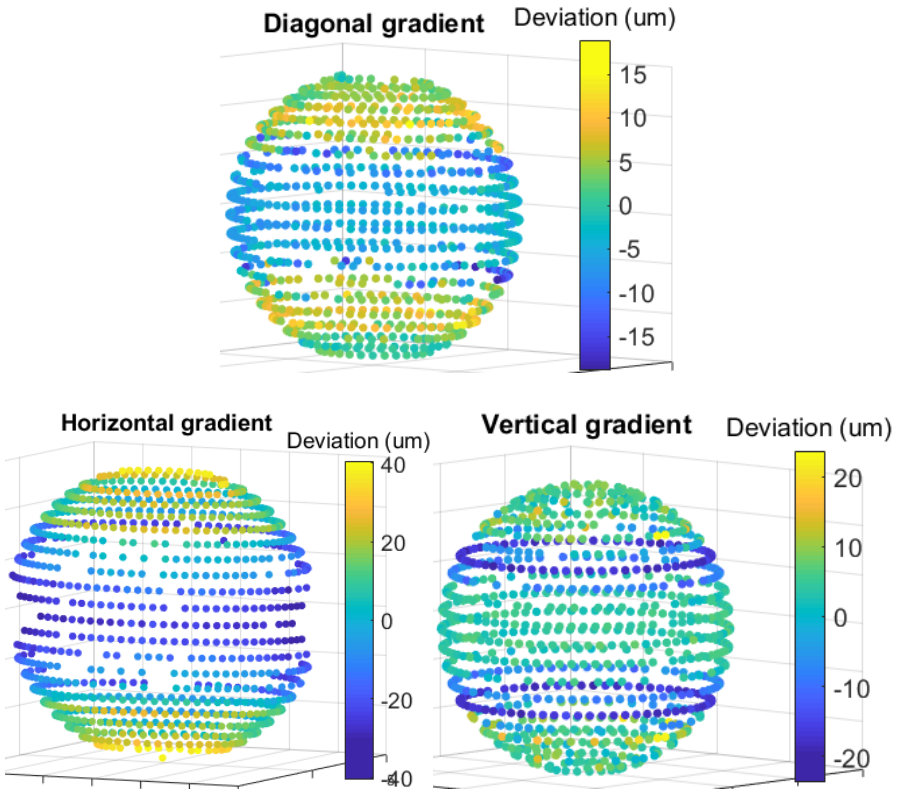

Figure 5.1 Fit point deviations when there is variation in intensity across the image (please note the varying scales in the colour bar)

The horizontal gradient seen above creates deviations in the region of ±40 µm with negative deviations seen around the equator and positive deviations at the two poles.

The vertical gradient appears to have the least impact with just two bands of < -25 µm deviation running around the sphere. The rest of the sphere has deviations of ±5 µm.

To apply these findings to the holeplates that have previously been imaged and measured in Chapter 4, a more robust numerical simulation was required.

5.2 Development of code

The simulation code was developed in MATLAB and the principle used to simulate a series of X-ray images, was to trace a line from the X-ray source to the centre of each individual pixel. Along this line the length where it is traversing through the holeplate was calculated.

It was decided to simulate the X-ray images in MATLAB, with the author writing the code from basics, to ensure that each variable, be it pixel size or X-ray spectrum, was known. Simplification of the imaging process was required, this is something that could not be achieved with commercial software packages such as Scorpius XLab® by Fraunhofer or Geant4, (see Section 2.5).

The bullet points below in Section 5.2.1 define the assumptions made during the simulation process. Figure 5.3 highlights the major steps in the three functions used in the code which are then described in more detail in Section 5.2.2 where the algorithms used are described. The MATLAB code itself can be seen in Appendix 5.

5.2.1 Assumptions

- Single point source; to replicate perfect focal spot with no blurring (Section 2.2.1.2)
- Perfect alignment of source, detector and manipulator (Figure 2.1)
- Perfect cylinder and 3D polygon (cuboid) geometry
- All measurements are in millimetres
- Identical response for each pixel of the detector
- Pixel size is 0.2 mm x 0.2 mm
- Single ray from source to pixel represents intensity of pixel. In the experimental set-up the entire area of the pixel collects the energy, see Figure 5.2 and Figure 2.15.
- Constant flux of X-rays; no spatial or temporal variation unless specified (Section 5.3)
- Expected spectrum generated in SpekCalc (Poludniowskia & Evans, 2007)
- Scatter was not taken into account; this will lead to a higher signal to noise ratio within the simulated images compared to the experimental images
- The effect of attenuation of the X-rays by air was not taken into account. For the total distance between the source and detector, the intensity of the X-rays reaching the detector, after passing through the air, is approximately 1.6% less than the initial value, it was decided that this was negligible.

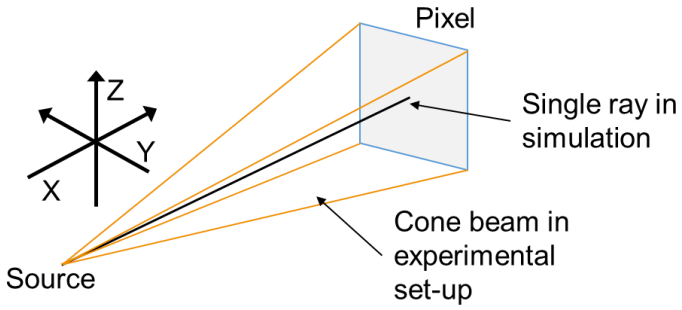

Figure 5.2 Single ray represents intensity of pixel as opposed to the whole area in the experimental set up

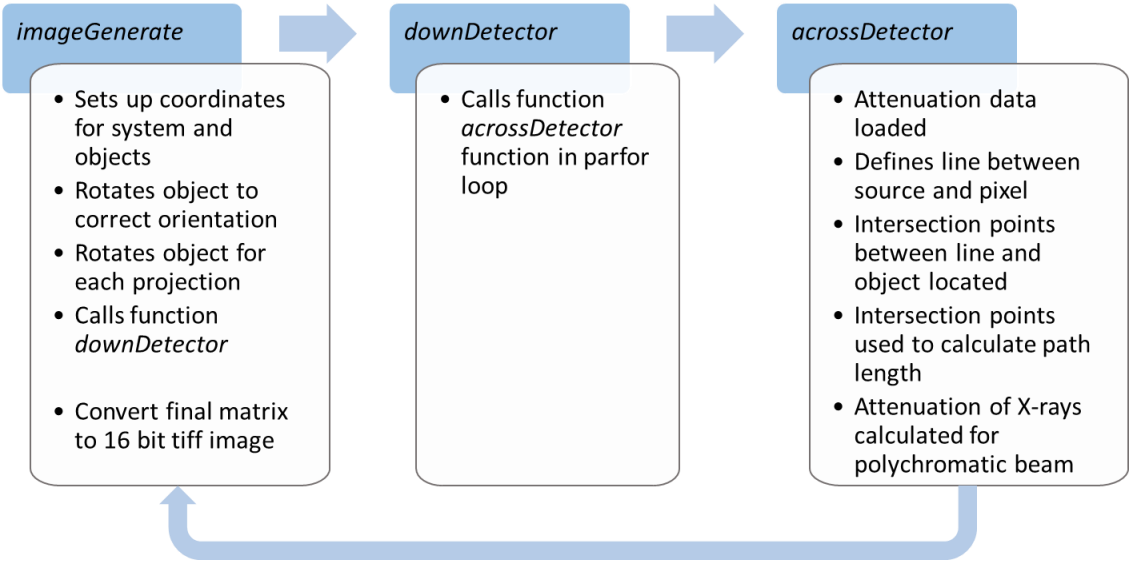

Figure 5.3 Flow diagram of major steps in algorithm for the three functions used in the simulation

5.2.2 Steps in the code

The steps, seen below, were used in the algorithms used to generate the 2D images of the holeplates. The italic text indicates the different files and functions in MATLAB.

imageGenerate

- Coordinate system for the simulation set up as seen in Figure 5.4. The origin (0, 0, 0) of the coordinate system was based around the centre of the object being imaged to allow the object to be rotated more easily in the code
- Define centre coordinates for the top and bottom of the cylinder (Cyl)
- Define corners of the 6 polygons that represent the holeplate (Poly)
- For meshes, the coordinates of the vertices for the object are imported from an .off file (object file format). The .off file was generated in MeshLab (Visual Computing Lab - ISTI - CNR) from an .stl file generated in AutoCAD®
- Magnification is input by user
- X coordinate of source defined (source to detector distance equal to 1180 mm):
  - $sourceX = -1.(\frac{source\ to\ detector\ distance}{magnification})$
- X coordinate of pixel defined:
  - $pixelX = sourceX + 1180$
- Arrays for Y and Z coordinates of pixels were propagated, Py and Pz respectively. Increments up from -199.9 to 199.9 in 0.2 intervals
- Orientation of object during imaging (as if in stand on manipulator) defined (ϑ) and input into rotation matrix:

  - $RX = \begin{bmatrix} 1 & 0 & 0 \\ 0 & \cos(\vartheta) & \sin(\vartheta) \\ 0 & -\sin(\vartheta) & \cos(\vartheta) \end{bmatrix}$ (see Figure 5.5 (a))

- Coordinates for cylinder and polygons multiplied by rotation matrix
- The increment by which the object is rotated by in between images (θ) is calculated by dividing 359.9150653° by the number of images required, 3142 unless otherwise specified. 3142 is the number of images used during experimental imaging. 359.9° was used as this is the total rotation that occurs in the Nikon XCT system.
- θ is used in the rotation matrix:
  - $RZ = \begin{bmatrix} \cos(\theta) & \sin(\theta) & 0 \\ -\sin(\theta) & \cos(\theta) & 0 \\ 0 & 0 & 1 \end{bmatrix}$ (see Figure 5.5 (b))
- The rotation matrix is multiplied by the previously rotated coordinates of the cylinder and polygons
- The function, *downDetector* is called

downDetector

- This function uses a parfor loop iterating from 1 to 2000 to represent each row of the pixel
- The function *acrossDetector* is called in the loop

acrossDetector

- Attenuation coefficients (for aluminium between 1-170 keV) and weighting data is loaded as .mat files
- Parfor loop iterating from 1 to 2000 representing the columns across the detector starts
- Line is defined by the start position (the source) and the difference in X, Y and Z
  - $dx = pixelX - SourceX$
  - $dy = \ y\ coordinate\ of\ pixel\ (Py)$
  - $dz = z\ coordinate\ of\ pixel\ (Pz)$
  - $line = [SourceX\ 0\ 0\ dx\ dy\ dz]$
- Central cylinder defined using Cyl and the radius of the cylinder
- The intersect points between the line and the cylinder and polygons are found using the function intersectLineCylinder and intersectLinePolygon3d called from MATLAB library Geom3d (Legland, 2009)
- Intersect points used to calculate path length using the equation:

- $Total\ path\ length =$

$$\sqrt{\begin{matrix}((X_2 - X_1)^2 + (Y_2 - Y_1)^2 + (Z_2 - Z_1)^2) + \\ ((X_n - X_{n-1})^2 + (Y_n - Y_{n-1})^2 + (Z_n - Z_{n-1})^2) + \cdots\end{matrix}}$$

- Equation 5.2 used to calculate the attenuation of the X-rays for that given path length (I_0 is equal to 62000 which was the average intensity of an experimental image with no object in the field of view)
- Value placed in 2D matrix, the position in the matrix corresponds to the pixel
- Loop ends

downDetector

- Loop ends

imageGenerate

- 2D matrix is converted to a 16-bit tiff image and saved in designated folder
- Code repeats for another image

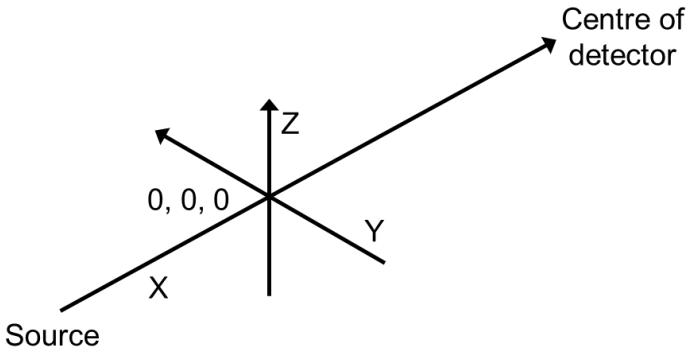

Figure 5.4 Coordinate system used in MATLAB simulations

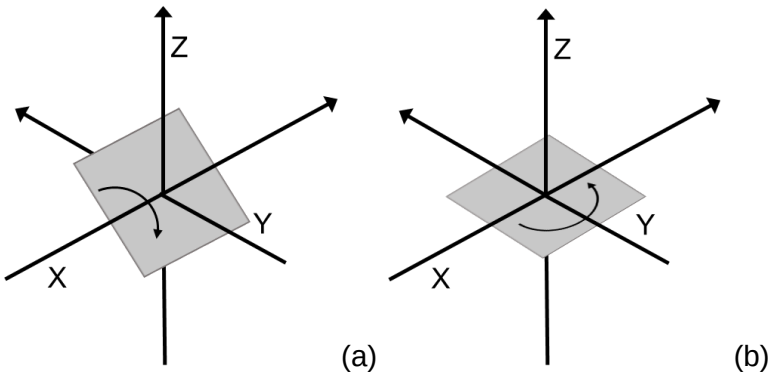

Figure 5.5 Direction of rotation of holeplate due to rotation matrices Rx (a) and Rz (b)

5.2.3 Modelling polychromatic X-rays

To model the polychromatic X-rays, the attenuation coefficients for aluminium were obtained from NIST (NIST, 2004). The data was interpolated to obtain values for each 1 keV interval from 1 to 170 keV (Figure 5.6).

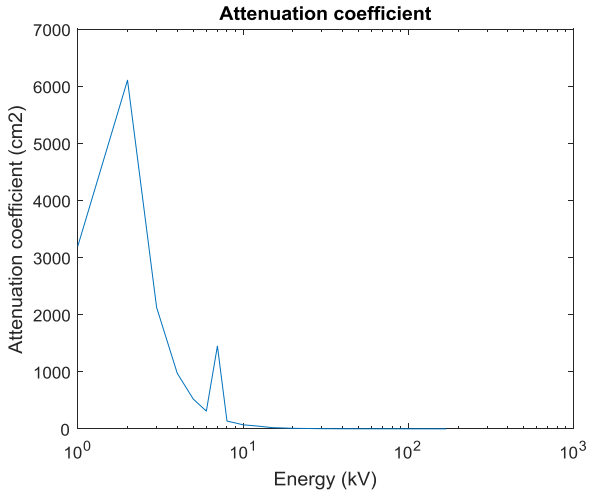

Figure 5.6 Attenuation coefficient for Aluminium

An expected spectrum for 170 kV was generated in SpekCalc (Figure 5.7). The number of photons for each 1 keV interval in the spectrum was divided by the total number of photons for the entire spectrum to give a weighting for each energy interval, i.e. the most predominant energies in the spectrum would have more influence (Figure 5.8).

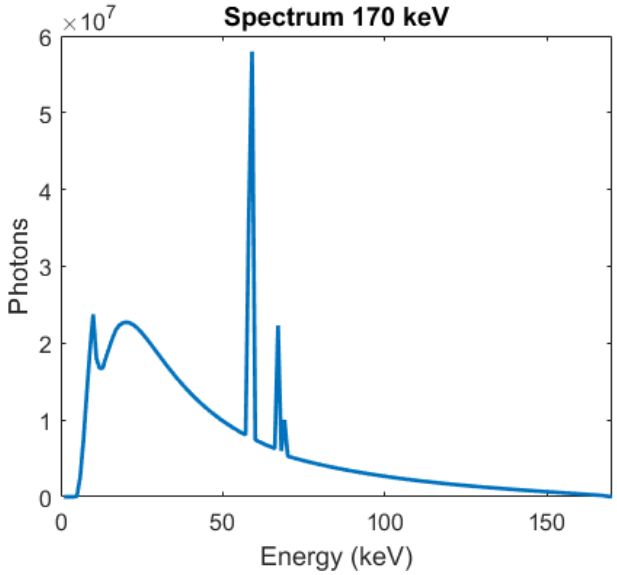

Figure 5.7 Simulated spectrum generated in SpekCalc

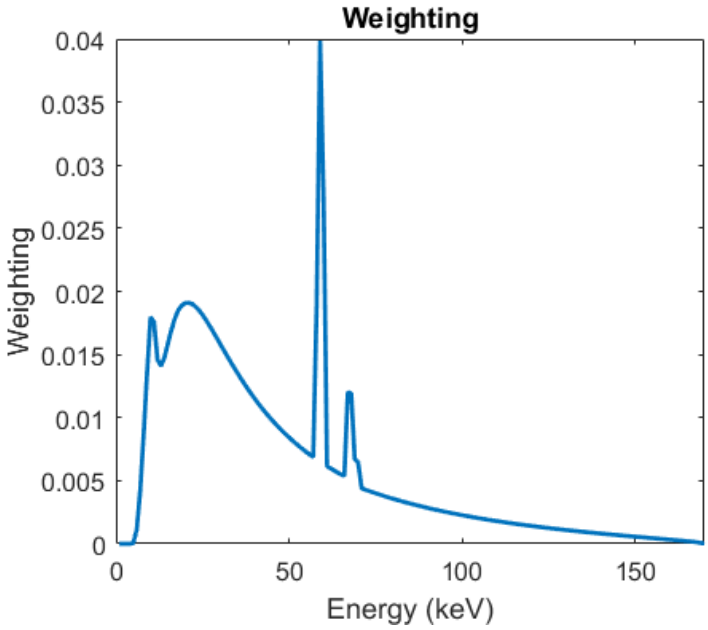

Figure 5.8 Weighting for generated spectrum

As explained in Section 2.2.3 the intensity of the X-rays is calculated using the Beer-Lambert law seen in Equation 5.1. This, however, can only be used for monoenergetic X-rays. For a polychromatic X-ray all of the attenuation coefficients for the spectrum have to be taken into account and a weighting applied depending on the shape of the spectrum.

$$I(E) = I_0(E).e^{-\mu(E).PL}$$

Equation 5.1 Intensity of x-rays I_0 is equal to original intensity, PL is equal to path length through object and μ is equal to the attenuation coefficient for a given energy and material

To take into account the polyenergetic X-rays the path length calculated with the use of the intersection points was multiplied by each value in an array containing the attenuation coefficients for each 1 keV interval. The exponential of each of these values was calculated and multiplied by the weighting. These values were summed together and multiplied by the original intensity of the X-ray (see Equation 5.2).

$$I = I_0.\sum w.e^{-\mu(E).PL}$$

Equation 5.2 Intensity of X-ray where I_0 is equal to original intensity, w is equal to the spectrum weighting, PL is equal to path length through object and μ is equal to an array containing the attenuation coefficients in 1 keV intervals

5.2.4 Reducing computational time

Initially each image, of 2000 x 2000 pixels, took approximately 1 hour to be simulated on a desktop computer with 16.0 GB RAM and 8 cores. To speed up the process in order

to fully investigate the range of holeplates and their orientations, the individual value for each pixel across the row was calculated in a parfor loop and each row going down the image was run in another parfor loop. A parfor loop in MATLAB runs each iteration of a loop in parallel using a parallel pool of workers in a multi-core computer. With the parfor loops each image took approximately 6 minutes to be simulated. Batch jobs were run on UCL's Legion cluster which allowed multiple images to be simulated concurrently. To replicate the experimental image sets, 3143 images were simulated. In Legion this would take approximately 36 hours if only one set was being generated. Running multiple jobs would increase the time taken. When testing the code, only 361 images were generated which took approximately 3 hours depending on how busy the system was with other users.

5.2.5 Code verification

The geometry of the object being simulated should not have an effect on the reconstruction, however, discrepancies in reconstructed data from initial simulations highlighted that mesh based geometry containing long thin triangles needed to be investigated. To ensure that the images were consistent with rotation, i.e. was the same image produced for the circular holeplate if it was rotated 180° in between imaging, the path lengths through the object for each image were compared for the central row of pixels, see Figure 5.9.

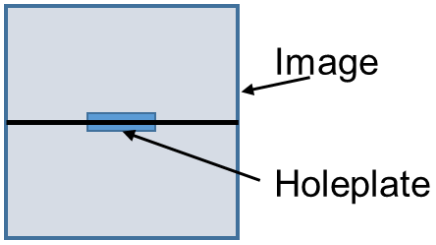

Figure 5.9 Schematic of 2D image. Path lengths taken from along black central line

5.2.5.1 Mesh vs. primitive shapes

Images generated when the holeplate was represented as a mesh highlighted differences between 0° and 180° and also 0° and 90°. Results can be seen below in Figure 5.10 and Figure 5.11 respectively.

Results for the 0°/180° comparison indicate that the images are not identical and there appeared to be discrepancies of up to 0.4 µm at the edges of the holeplate. These can be seen both in the hole and the outside edge as seen in Figure 5.10. When comparing the path lengths when there is a 90° difference in imaging (Figure 5.11), a sinusoidal trend in the data can be seen with errors of up to 140 µm. The errors seen in Figure 5.10

are smaller than the MPE of the system so are negligible. However, those seen in Figure 5.11 are much greater than the errors of <40 μm seen in the experimental results, it was therefore crucial to eliminate these sinusoidal errors.

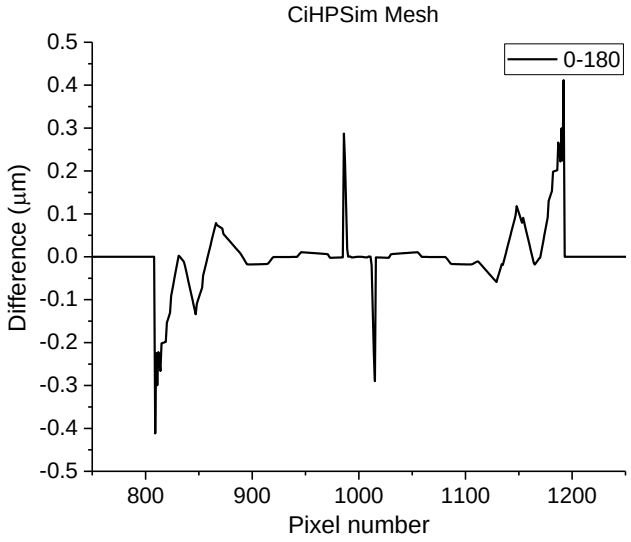

Figure 5.10 Difference in path lengths between images taken at 0° and 180°

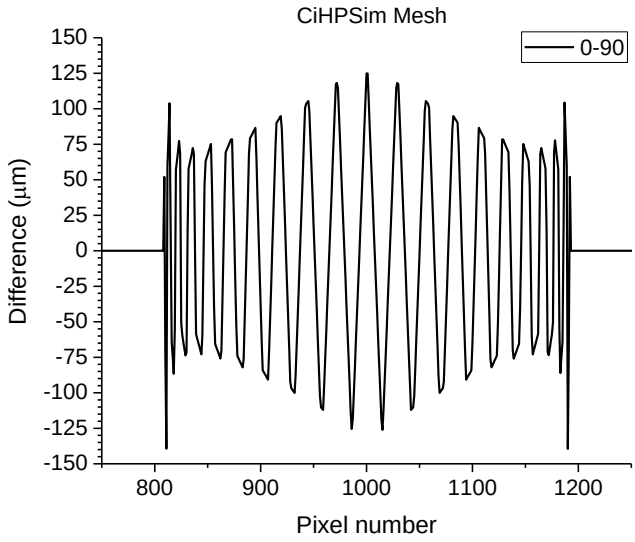

Figure 5.11 Difference in path lengths between images taken at 0° and 90°

The sinusoidal trend in the data suggested that there was a systematic error occurring. It had been determined that the middle of the object was correctly sitting at the origin as there were the same number of pixels either side of the centre of the image. Attention was then turned to the mesh and the effect the triangles that make up the mesh would have on the path lengths. The mesh, which was generated in MeshLab from a .stl generated in AutoCAD® can be seen in Figure 5.12. This and the data indicates that the triangles will not represent the hole as perfectly cylindrical.

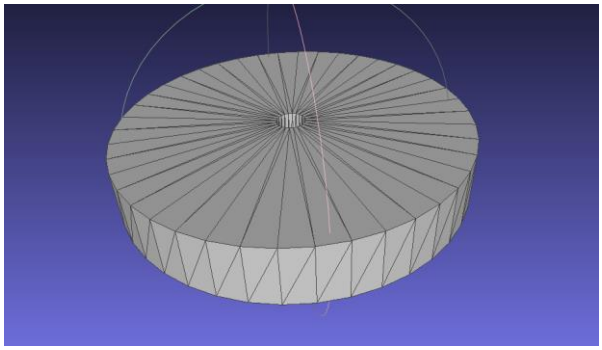

Figure 5.12 Mesh of circular holeplate

Although this was initially considered when the code for the simulation was being written, it was calculated that the radius for the central hole would have a maximum discrepancy of 2 µm when the mesh consisted of 72 triangles around the circumference. At the time, this was judged to be insignificant to the errors that were currently being seen (< 20 µm). The outside edge was not considered. However, after this experiment it was decided to investigate the effects of the mesh and to attempt to reduce the error by changing the number of vertices used to create the circular holeplate, see Figure 5.13.

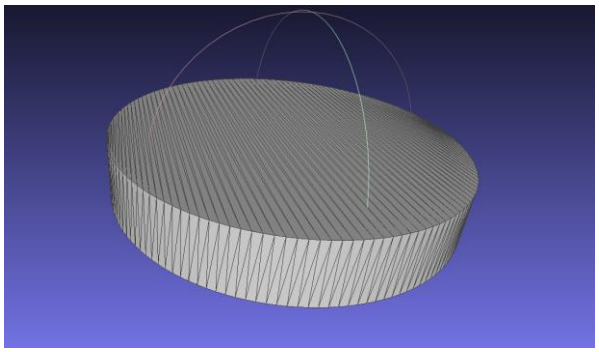

Figure 5.13 Mesh of circular holeplate with increased number of vertices

The new mesh still resulted in errors at the edges and an oscillating pattern as seen in Figure 5.14 and Figure 5.15. The errors are of the different magnitudes compared to the previous mesh and the sinusoidal pattern is repeated three times across the holeplate width. They are of the same order of magnitude as the experimental data errors in geometry and larger than the MPE of the system being modelled so still had to be removed.

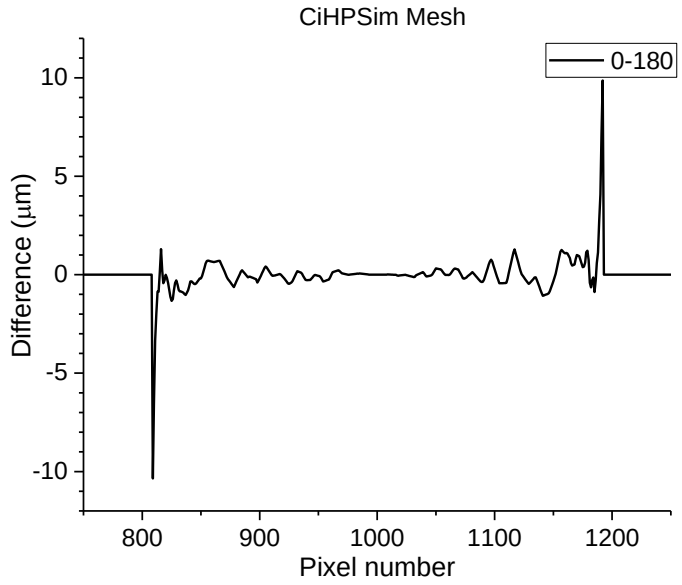

Figure 5.14 Difference in path lengths between images taken at 0° and 180°

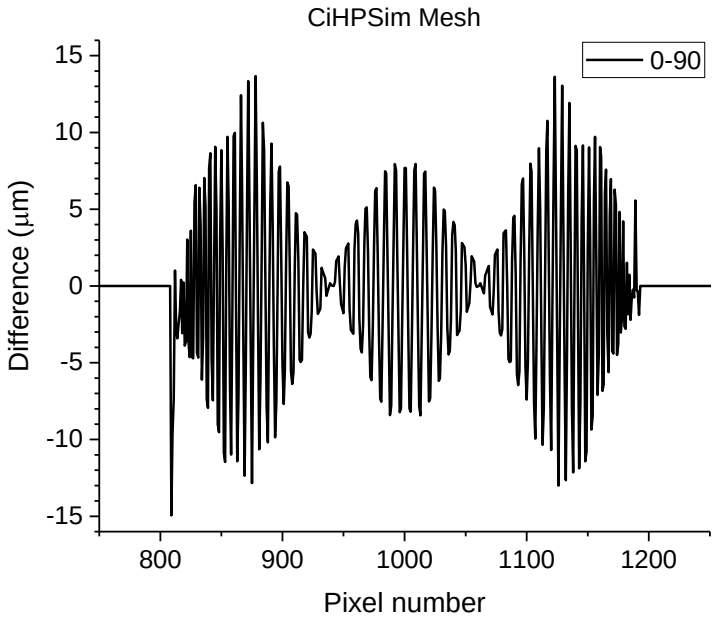

Figure 5.15 Path length between images taken at 0° and 90°

Following on from this, it was decided to completely rewrite the MATLAB code using primitive shapes to model the cylinders and cuboids found in the different holeplates. Results indicate that the mesh was indeed causing the errors. When comparing the images for the primitive shapes for the circular holeplate the differences in path lengths were all zero. The differences are also zero for HP3 at 0°and 90, 180°, 270° and 360° along with 45° and 135°.

This was conclusive evidence that the errors seen in path length were due to the use of meshes. It was decided to study a couple of variables to simulate the XCT system as

accurately as possible, these were the number of ray paths averaged for each pixel and the pixel size.

5.2.5.2 Path length averaging

As stated previously, a pixel in a detector collects the energy across the whole area of the pixel, however, this simulation calculates the path length along a single ray from the source to the centre of each pixel. Therefore, the attenuation of the X-rays through the holeplate for each pixel is based on slightly different values. To determine if this was affecting the results the number of rays being used to represent each pixel was increased.

Images were generated to simulate CiHP but this time the pixel size was reduced to 0.1 mm and 0.05 mm, compared to the usual 0.2 mm. The pixel number increased to 4000 x 4000 and 8000 x 8000 respectively compared to 2000 x 2000. The path lengths were averaged for these sets of data to provide a mean path length for each 0.2 mm pixel, see Figure 5.16.

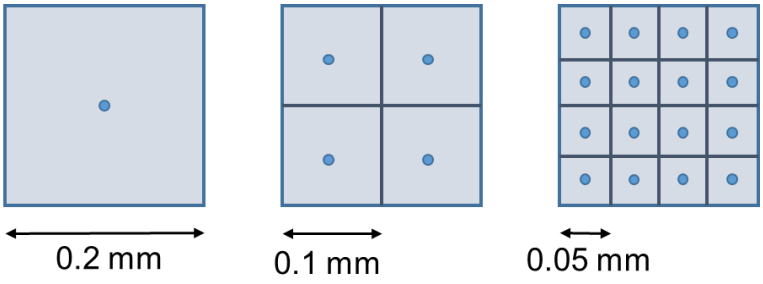

Figure 5.16 Number of points and spacing used when averaging pixels

The following graphs show the profile of the path lengths taken through the central plane of CiHP as shown in Figure 5.9. When the path lengths for the different averages are compared it can be seen there is little significant difference at the edge of the hole (Figure 5.17).

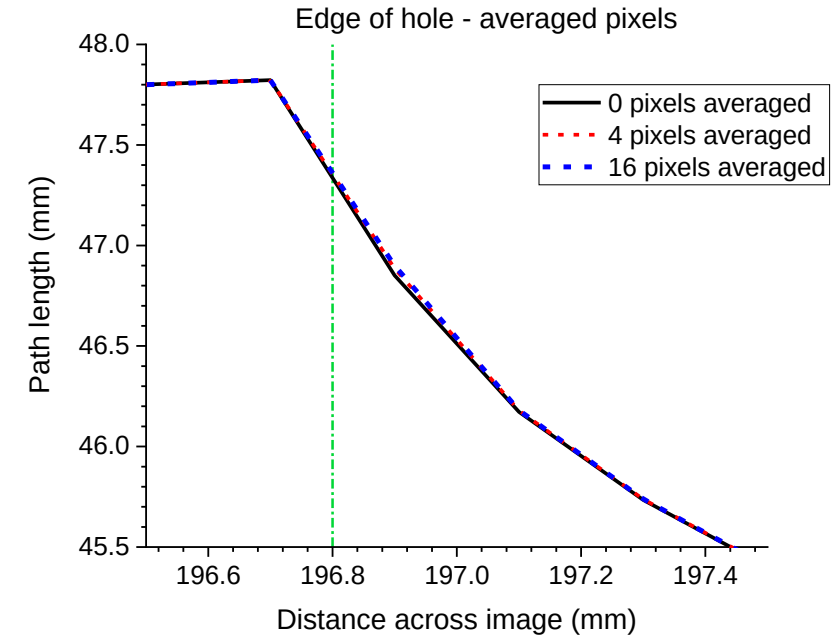

Figure 5.17 Path lengths at edge of the hole, averaged pixels (green line indicates true edge)

The main difference between the sets of data can be seen in the centre of the hole, as seen in Figure 5.18. In this case in the centre of the hole, where the length should be 44 mm, the results become more inaccurate as the number of pixels used for the averaging increases, this is because of the partial volume effect as described in Section 2.3.3. When no averaging occurs the path length is at its most accurate because it is just taking the one ray into consideration. When multiple rays are included the length will decrease as shorter rays are being taken into account.

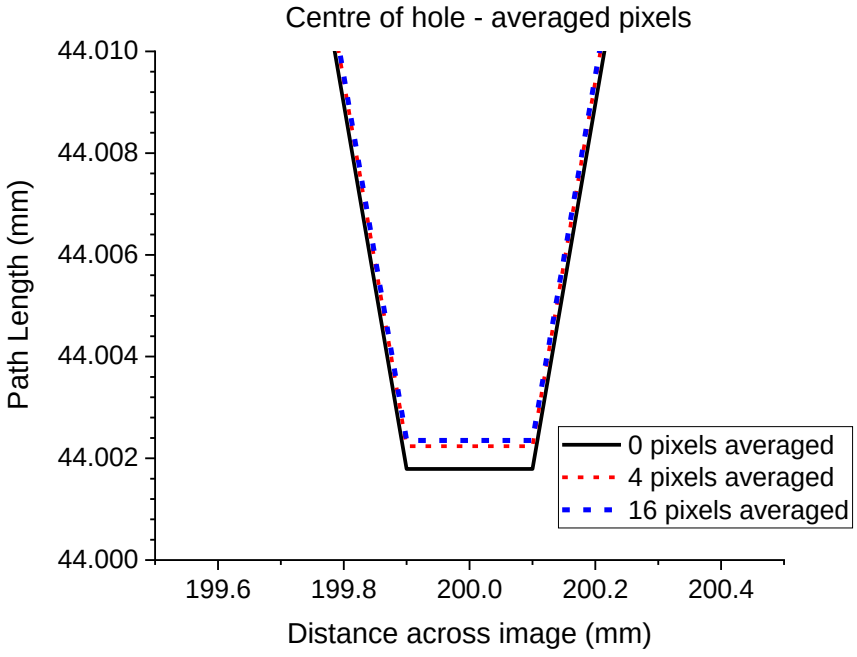

Figure 5.18 Path lengths at centre of the hole, averaged pixels

The simulated images for CiHP were reconstructed and cylinders fitted to the inside hole and outside edge, see Figure 5.19. When studying the deviations of the fit points from the fitted cylinder for both the hole and the outside cylinder when the simulation uses no averaging (Figure 5.20) it can be seen that the errors are ±3 µm. Figure 5.21 and Figure 5.22 illustrate the results for the other averaged pixels. Table 5.1 lists the range in the data for the different set ups. There is less than 1 µm difference between the various pixel averaging and the average of the standard deviations appears to increase as the number of pixels used is increased for the inside cylinder. There are distinct systematic peaks and troughs at 0°, 90°, 180 and 270° for all of the reconstructions but these will be discussed further in Section 5.4.7.

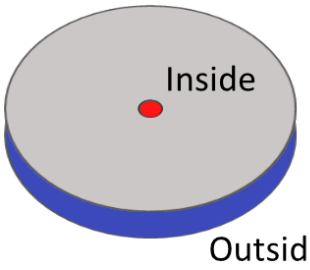

Figure 5.19 Cylinders fitted to CiHP termed in this work inside and outside

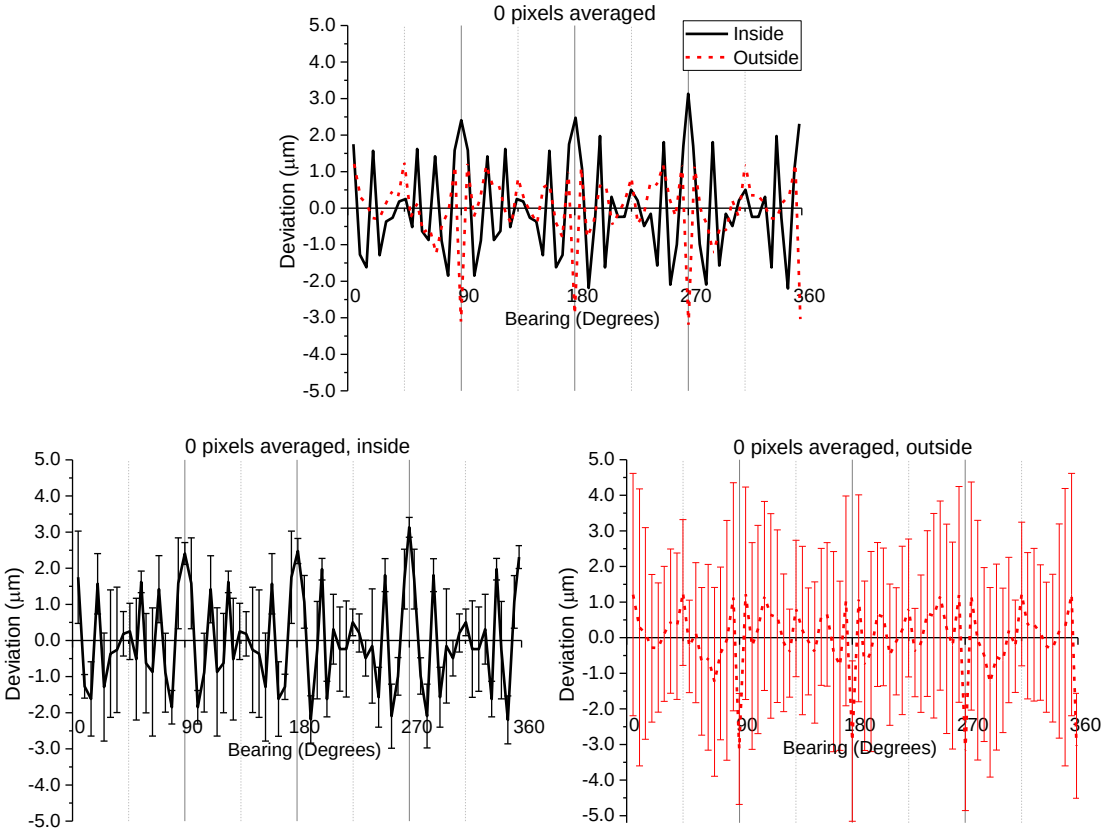

Figure 5.20 Deviation from cylinder of CiHPSim when no pixels are averaged

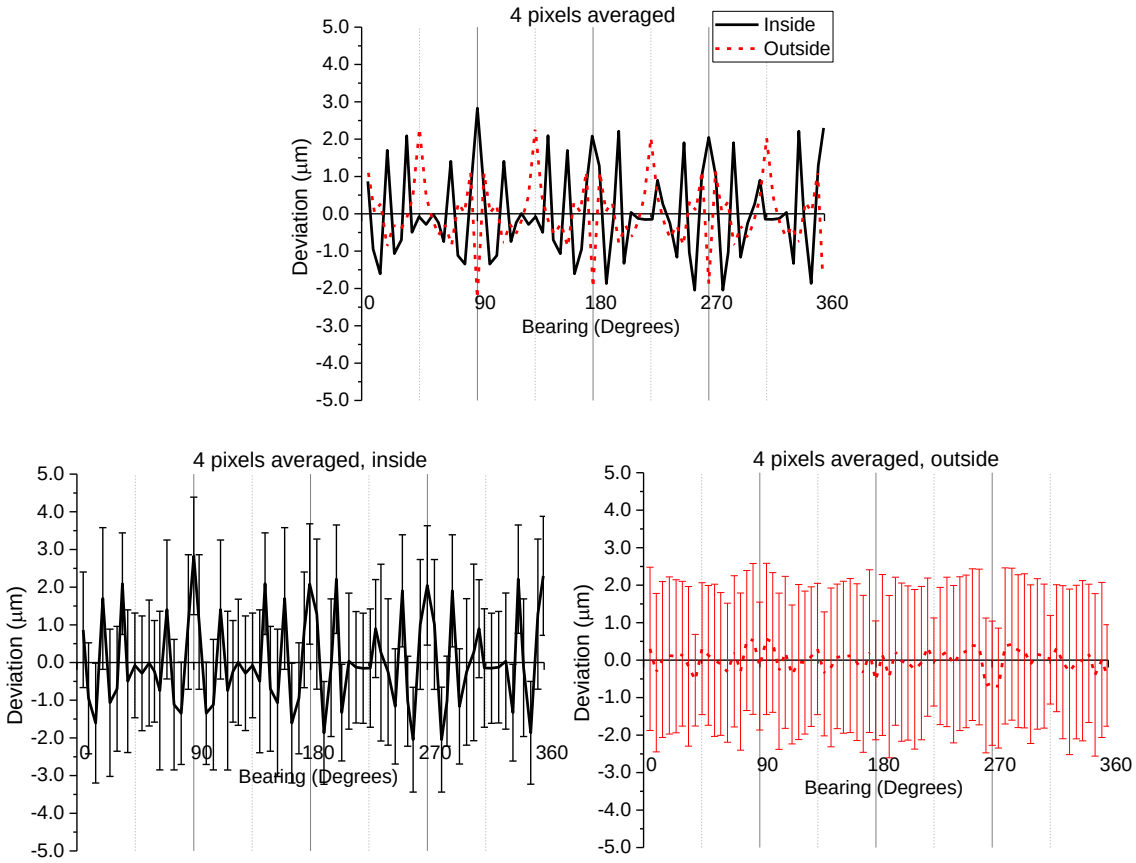

Figure 5.21 Deviation from cylinder of CiHPSim when 4 pixels are averaged

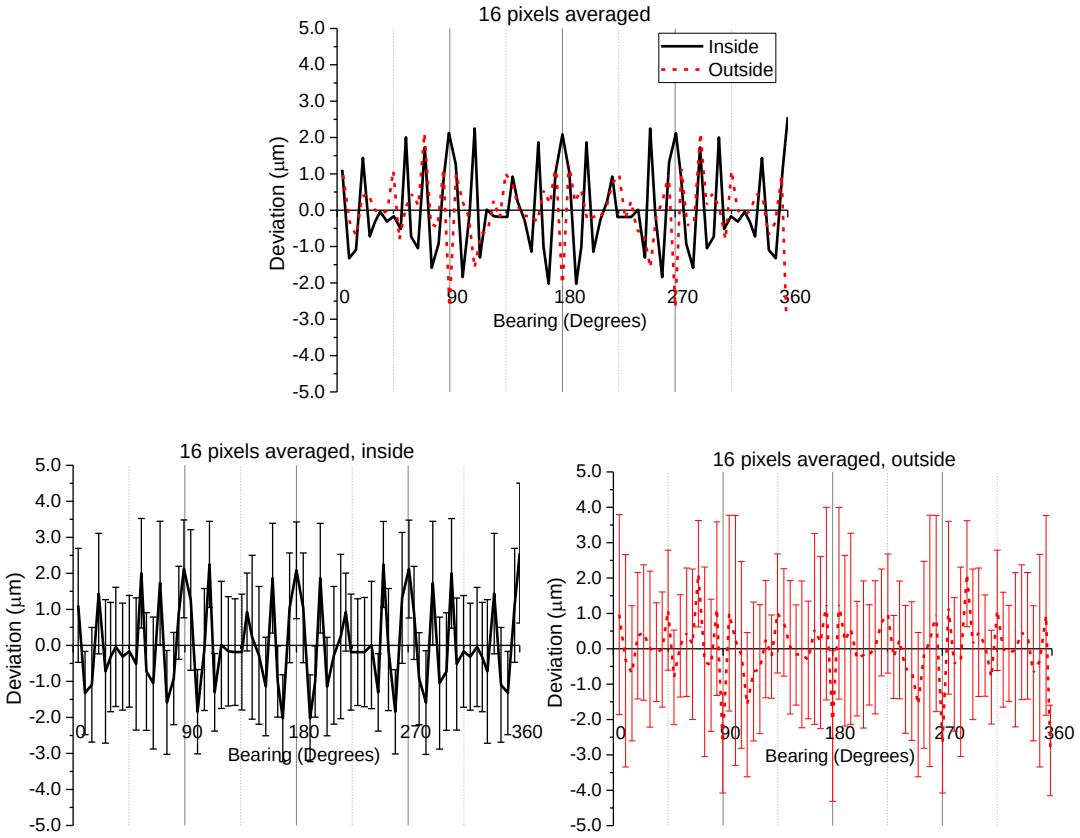

Figure 5.22 Deviation from cylinder of CiHPSim when 16 pixels are averaged

Data set	Range (µm)	Average σ (µm)
0 pixels, inside	-2.2 – 3.1	0.9
4 averaged, inside	-2.0 – 2.8	1.6
16 averaged, inside	-2.0 – 2.6	1.5
0 pixels, outside	-3.2 – 1.3	2.4
4 averaged, outside	-2.3 – 2.3	2.4
16 averaged, outside	-2.9 – 2.1	2.0

Table 5.1 Range in data and average of standard deviations for graphs in Figure 5.20, Figure 5.21 and Figure 5.22

It was decided that a reduction of less than 1 µm for the range did not justify the increase in processing time which was required. For the inside cylinder the noise in the data increased with the averaging.

5.2.5.3 Pixel size

To determine if the deformations seen are related to the sampling or pixel size, simulations were carried out where smaller pixel sizes were used, 0.1 mm and 0.05 mm with the images being 4000 x 4000 pixels and 8000 x 8000 pixels respectively.

Figure 5.23 and Figure 5.24 show that the difference in the path lengths becomes apparent with the decrease in pixel size at the edge and centre of the hole. When studying the edge of the hole, as seen in Figure 5.23, the edge of the hole moves towards the centre as the pixel size decreases, this is a result of the increased sampling. Nevertheless, none of the resolutions demonstrate the correct position for the edge of the hole although the results are becoming more accurate as the pixel size decreases.

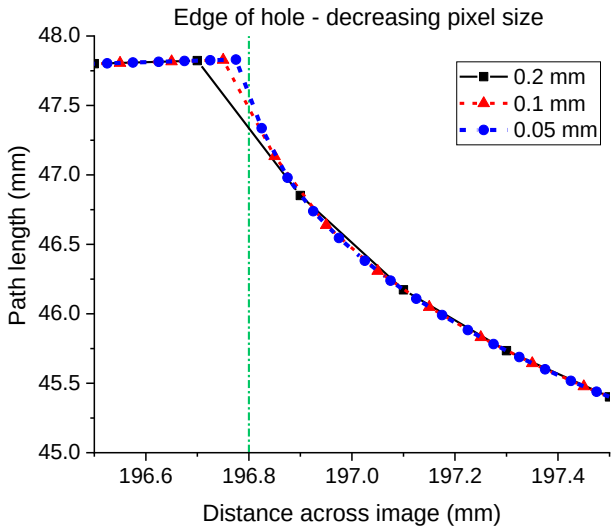

Figure 5.23 Path lengths at edge of the hole, decreasing pixel size (vertical line indicates true edge)

The decrease in pixel size allows the centre of the hole to be defined more accurately, as seen in Figure 5.24, again this is because of the increase in the number of points recorded.

Figure 5.25 illustrates the deviations in the fit points for the reconstructed holeplate when the pixels are 0.1 mm wide. The deviations are approximately a third of those seen when the pixel size was 0.2 mm, the noise is also lower. This is a result of a reduction in the voxel size in the final reconstruction which is 62.5 µm compared to 125 µm when the pixel size is 0.2 mm.

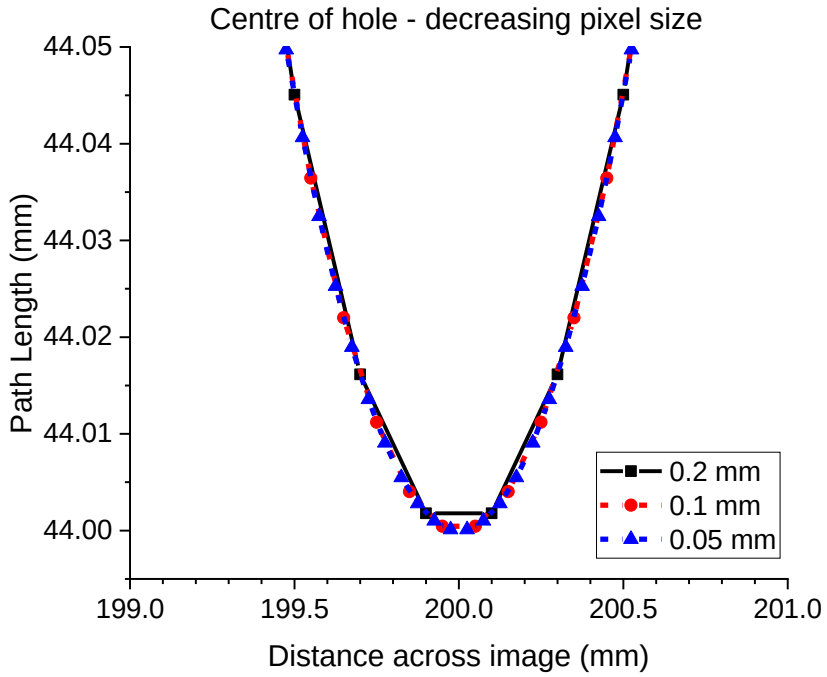

Figure 5.24 Path lengths at centre of the hole, decreasing pixel size

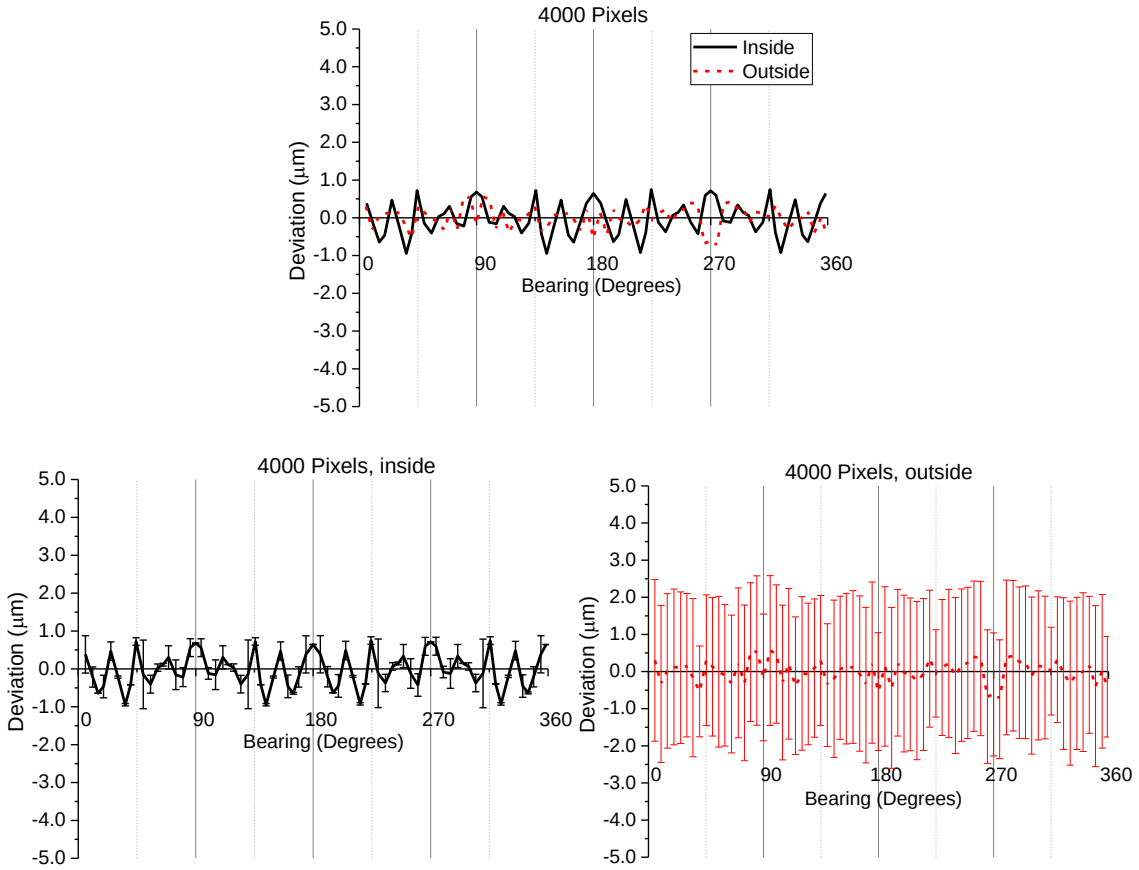

Figure 5.25 Deviation from cylinder of CiHPSim with 0.1 mm wide pixels

Unfortunately, the images that were 8000 x 8000 pixels were too large for CTPro to reconstruct, therefore the shape of the reconstructed cylinders could not be determined.

Although the smaller pixel size does decrease the errors seen, it is not representative of the NPL system and the images collected experimentally, it was therefore decided to use 2000 x 2000 pixels per image.

5.2.5.4 Image comparison

To validate the simulated images, the greyscale profiles through the holeplate will be compared to the experimental images. The two images can be seen below in Figure 5.26 and Figure 5.27.

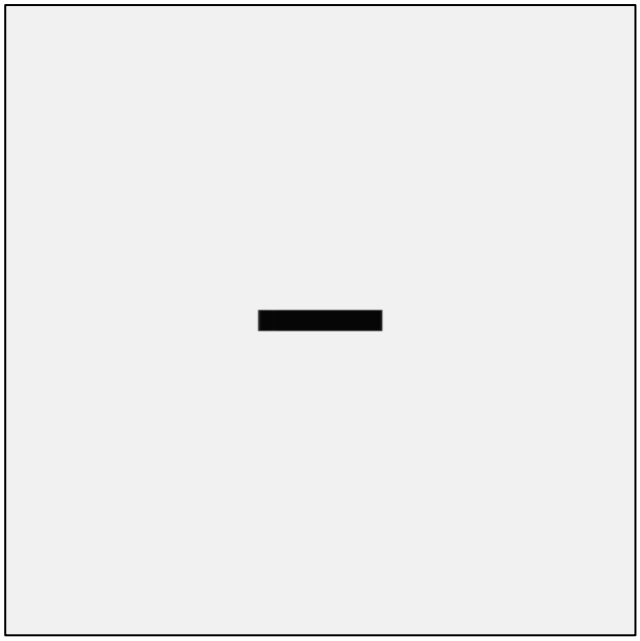

Figure 5.26 Simulated image of HP1. Black border is to show edge of image

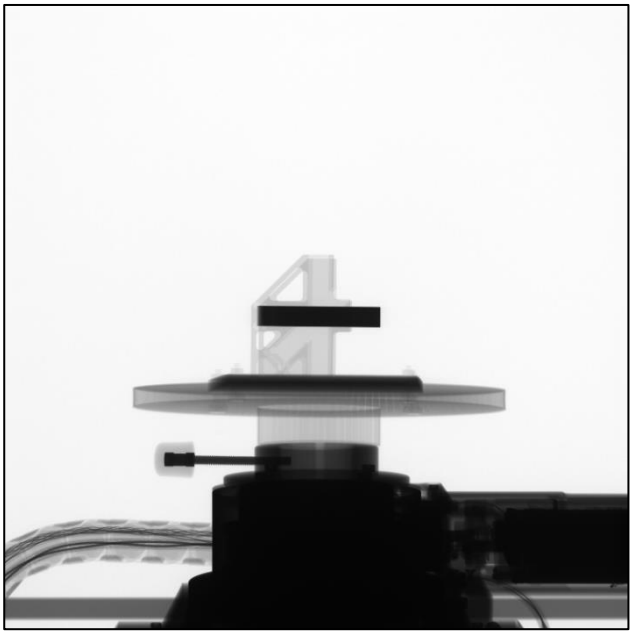

Figure 5.27 Experimental image of HP1. Black border is to show edge of image

A profile of the greyscale value was taken horizontally across both images through the holeplate, this can be seen below in Figure 5.28; the increase in greyscale seen around pixel number 180 is caused by the hole in the holeplate. The step seen in the experimental data at the left hand side of the graph is caused by the stand that the holeplate was being supported in.

The graph highlights that generally the profile of the two images is the same, the main difference is the minimum values. The larger values for the experimental image is probably caused by scattered X-rays that create an increased signal on the detector.

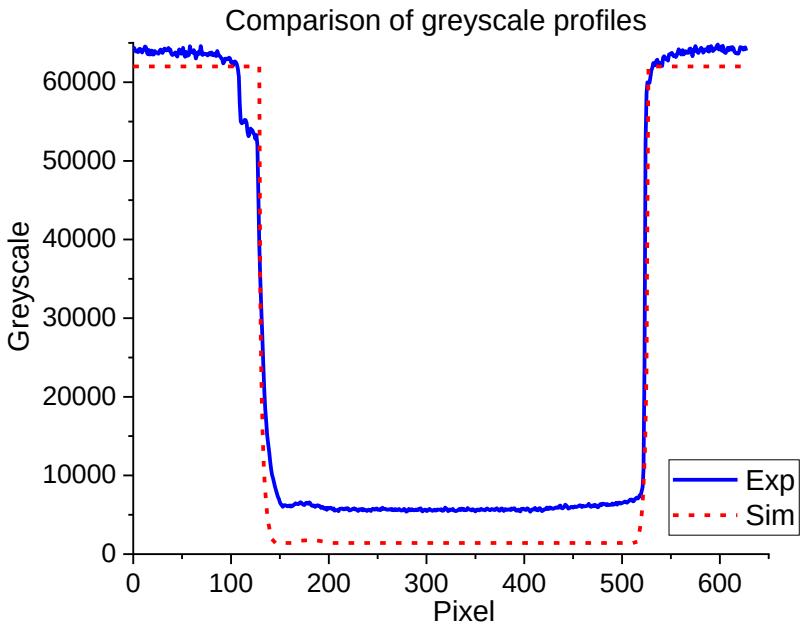

Figure 5.28 Profile of the greyscale values through the holeplate in the experimental and simulated images

The reconstructed volumes of both data sets can be seen below in Figure 5.29, the green line indicates the profile through which the cross section can be seen (smaller image). Both data sets show streaking at the corners of the holeplate. In the experimental data, shadowing occurs around the hole, the position of the shadowing relates to the deformation in the hole geometry seen in Chapter 4. Overall, it can be seen that the simulated images reconstruct well and appear to have the same characteristics as the experimental data.

A profile of the greyscale values was taken through each volume and can be seen in Figure 5.30, the simulated profile has peaks at the edges although the signals for the hole itself are very similar with an intensity drop of around 60.

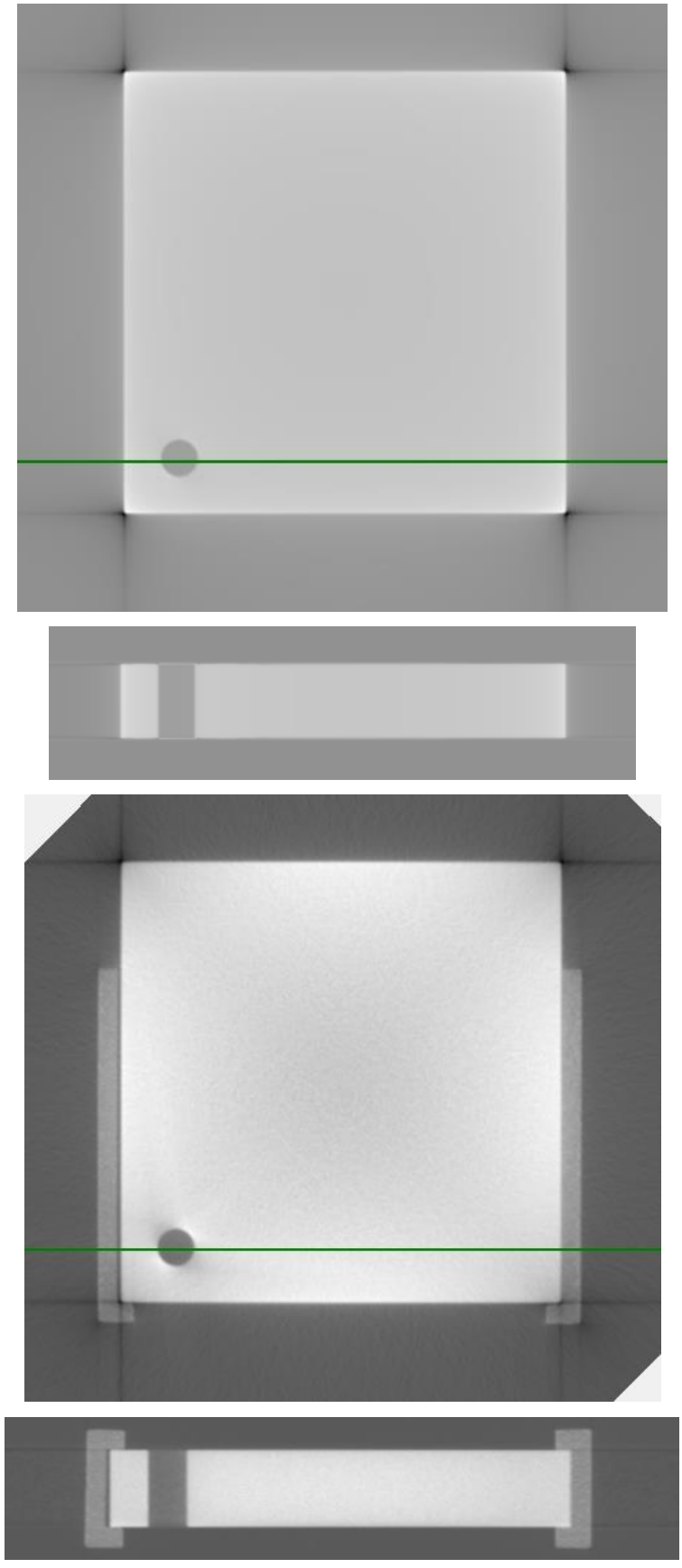

Figure 5.29 Views of reconstructed volume for simulated data (top) and experimental data (bottom). Green line indicates profile from which cross section imaged is viewed

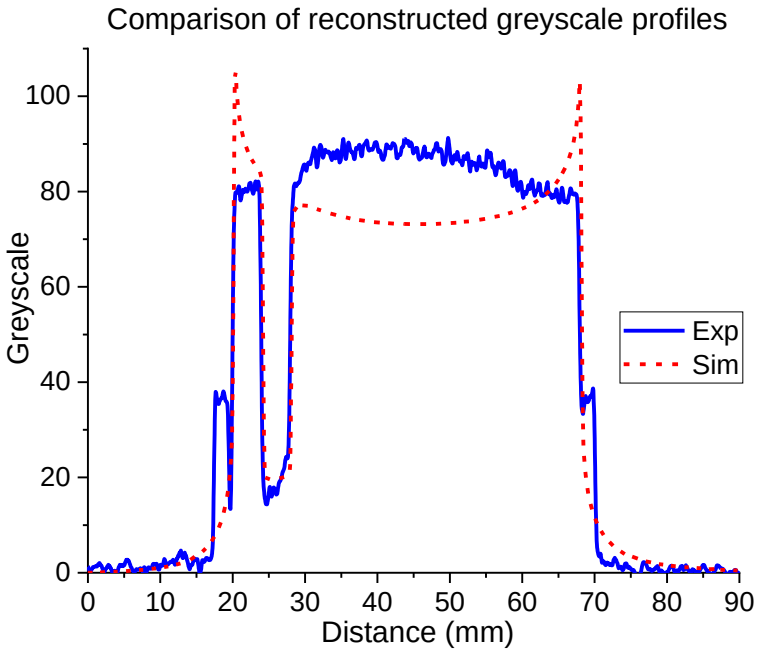

Figure 5.30 Greyscale values from profiles taken through reconstructed volumes using simulated and experimental images

A comparison of the measurements of the reconstructed volumes using the simulated and experimental images can be seen later in this chapter in Section 5.4.2.

5.3 Simulation of X-ray flux variation

To determine if the results found in Chapter 3 involving the variation in X-ray flux both spatially and temporally affect the geometry of a cylinder, it was decided to try and replicate these results using simulated images.

An initial image of a cylinder was generated using the method discussed in Section 5.2. The cylinder was 48 mm wide with a 4 mm diameter hole in the centre, this was to replicate CiHP already used in Chapter 4. The length of the cylinder was increased to 40 mm, compared to 8 mm in CiHP and the magnification was increased to x5. This change in size and magnification was to ensure that the cylinder filled a large portion of the image. If the cylinder had remained at 8 mm long and been imaged at a magnification of x1.6 it would have taken up a small amount of the image and the full impact of the intensity gradient across the image would not have been wholly exploited. Results from the ionisation chamber array experiment seen in Section 3.3.3 and Figure 3.26 indicated a 10% difference between the maximum and minimum intensity across the detector. For this reason, to replicate this spatial variation, it was decided to apply a gradient of up to 10% across the images in three different directions to the image; vertically, horizontally and diagonally (Figure 5.31). The magnitude of the gradient varied for each image, with

the maximum being 110% of the original image intensity and the minimum intensity being 90%.

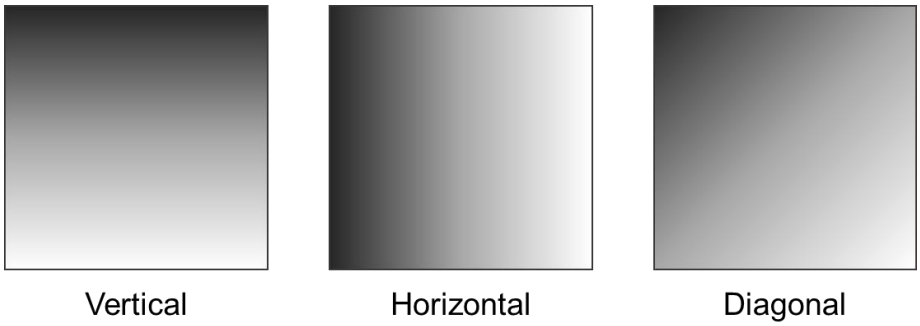

Figure 5.31 Direction of gradient applied to each image

To replicate the temporal variation, a uniform change in intensity was applied across the entire image, the amount of which varied randomly from 90% to 110% of the original image and changed for each image.

5.3.1 Results

A set of images with no gradient applied were reconstructed and a cylinder was fitted to both the inside hole and the external surface, see Figure 5.19.

The results can be seen below in Figure 5.32 and Figure 5.33. These graphs indicate that there seems to be a systematic deviation from the perfect cylinder at the four quadrants, i.e. at 0°, 90, 180° and 270°. For the inside hole, at the quadrants, the fit points are <3 µm larger than the cylinder radius, however, 5° either side of these peaks is a trough of <-3 µm. Around the rest of the circumference the deviations are between ±2 µm.

When comparing the inside cylinder with the external one it can be seen that there is again deviation around the quadrants except in this case there is a difference between the 90° and 270° pairing and the 0° and 180° pairing. At 0° and 180° the deviation is 5 µm but does not have the same trough at the shoulders of the peak seen in the inside cylinder. At 90° and 270° there is a wide section of approximately 35° where the deviation is between -2 and -4 µm with a peak of 2 µm either side. For the remaining circumference of the cylinder the deviations are within ±1 µm.

It can be noted that there is a large difference in the error bars (which are the equal to the standard deviation of the deviations for each 5° interval) seen for the different cylinders; for the internal cylinder the noise is within ±0.5 µm, however, the external cylinder has noise levels of ±6 µm. This indicates that the surface of the outside cylinder is not so smooth.

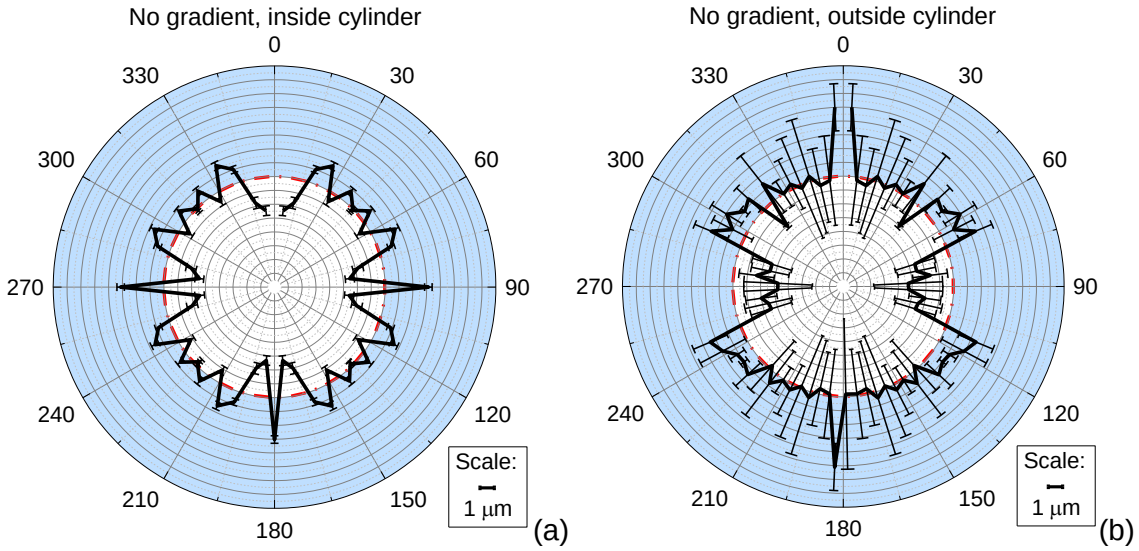

Figure 5.32 No gradient applied to images, average deviation of fit points, inside cylinder (a) outside cylinder (b)

When studying the contour graphs of the unrolled cylinder (Figure 5.33) the variation along all bearings can be seen for the inside cylinder, at the quadrants appears to have a sinusoidal trend up the cylinder for the positive deformation either side of the trough. This wave pattern appears to shorten further away from the centre of the cylinder.

This variation is not seen for the outside cylinder, where the deviation is continuous down the cylinder.

These contour graphs were drawn for all of the different gradients and all showed the same trends, they are not included in the chapter but can be found in Appendix 6.

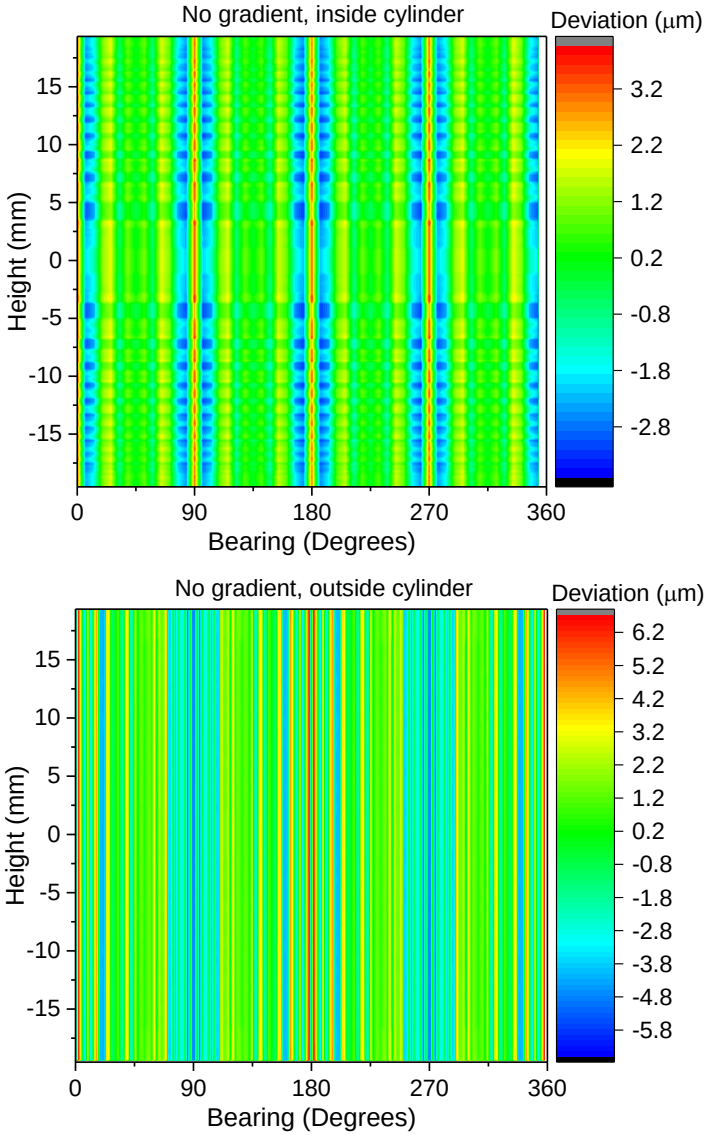

Figure 5.33 No gradient applied to images. Fit points of inside and outside fitted cylinders

Although these errors are below the manufacturer's MPE for the system, it still highlights a systematic trend that could potentially be corrected for.

5.3.1.1 Horizontal gradient

When comparing the horizontal gradient results (Figure 5.34) with those with no change in the image, it can be seen that there is not much variation between the two data sets. The errors and the noise are of the same order of magnitude. This demonstrates that the horizontal gradient does not affect the results or the software, CTPro, is effectively removing the gradient from the images.

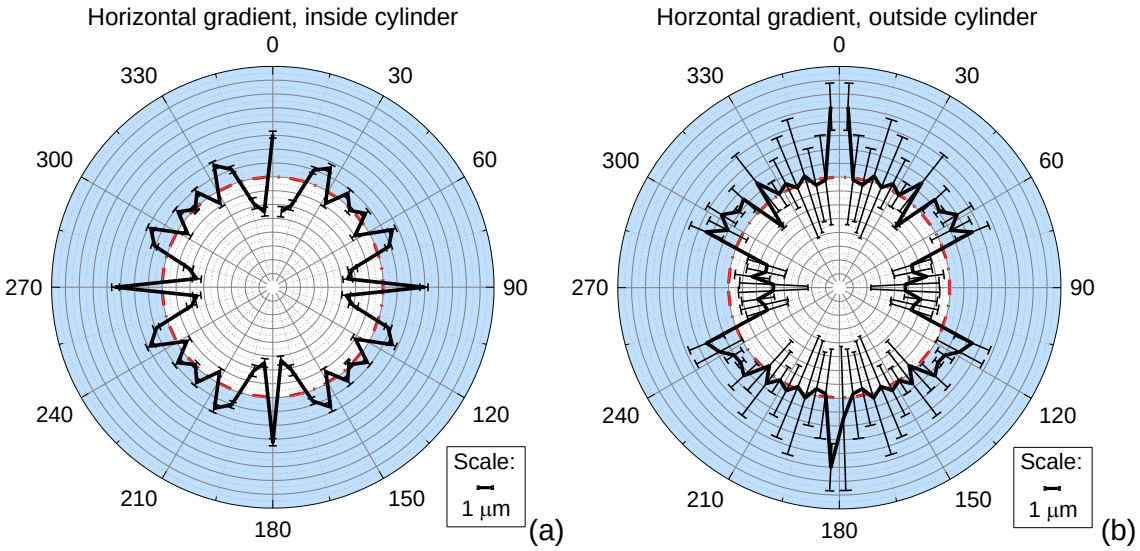

Figure 5.34 Horizontal gradient applied to images, average deviation of fit points, inside cylinder (a) outside cylinder (b)

5.3.1.2 Vertical gradient

Unlike the horizontal gradient, differences can be seen for the external cylinder when there is a vertical gradient applied to the images (Figure 5.35). The deviations no longer follow the symmetrical trend seen in the previous data. The peaks are no longer present at 0° and 180° and at 90° and 270° the deviation is completely different with the deviation at 90° being approximately 4 µm and at 270° it is -3.5 µm. No effect is see in the internal hole.

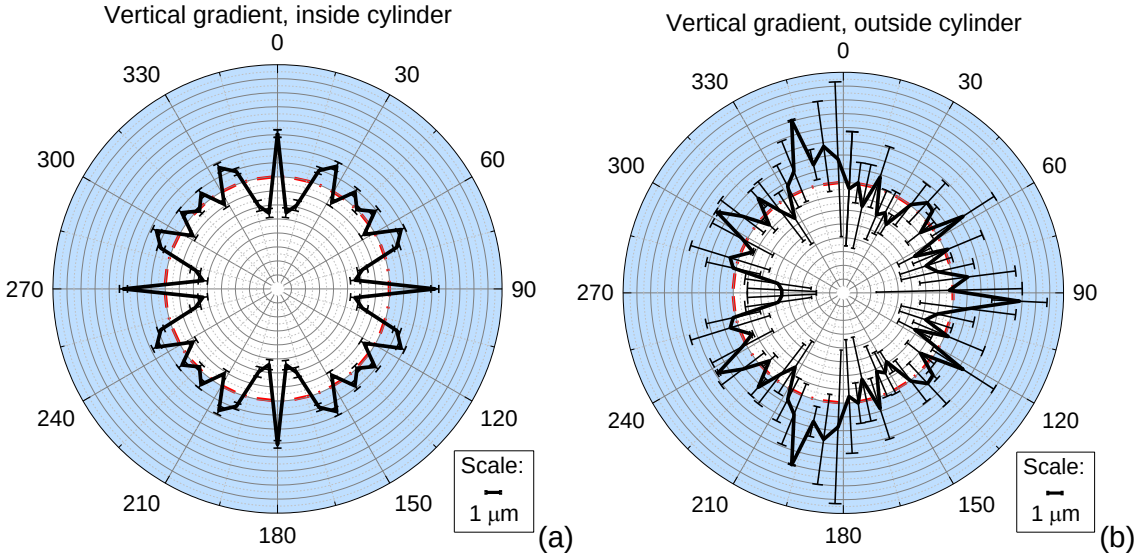

Figure 5.35 Vertical gradient applied to images, average deviation of fit points, inside cylinder (a) outside cylinder (b)

The vertical gradient does have an effect on the dimensional metrology and the gradient is not removed entirely by CTPro.

5.3.1.3 Diagonal gradient

Data for the diagonal gradient (Figure 5.36) highlights different deviations again. For the inside cylinder there is no obvious systematic trend, deviation is between ±3 µm, although there is a line of symmetry along the 90° – 270°. However, for the outside cylinder the symmetry is aligned along the 0° - 180° line with positive deviations (3 µm) seen at 0° and 180° negative deviations (-3 µm) at 90 and 270°.

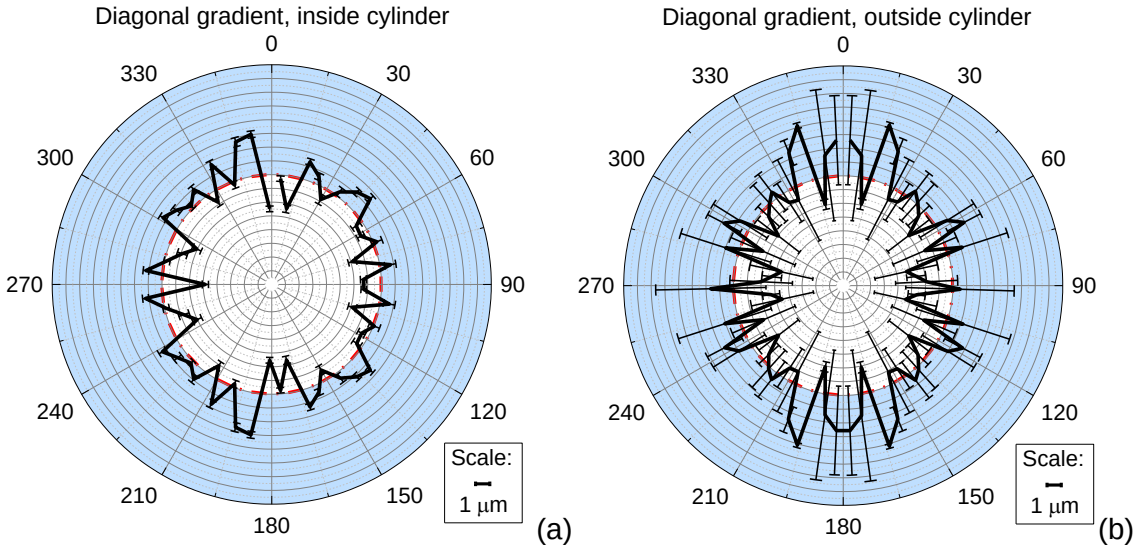

Figure 5.36 Diagonal gradient applied to images, average deviation of fit points, inside cylinder (a) outside cylinder (b)

Of all of the scenarios, the diagonal gradient has the most effect on the geometry of the holes with errors of up to 4 µm.

5.3.1.4 Temporal variation

When the overall intensity is changed for each image individually to simulate the change in the flux over time again systematic trends can be seen in the geometry of the cylinder (Figure 5.37). For the inside cylinder, the deviations range is ±2 um, there are four peaks of 2 µm at every 90° but with an offset so that they do not lie directly on the quadrants. The outside cylinder has deviations in the range of ±4 µm with the standard deviation being approximately 3 µm. Again there is a systematic trend.

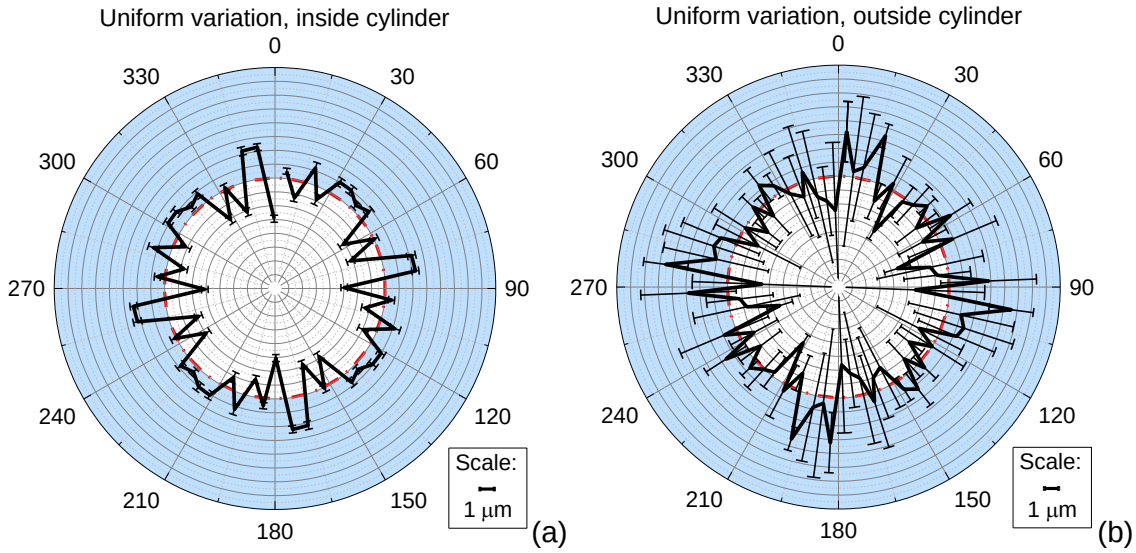

Figure 5.37 Different uniform change in intensity applied to each image, average deviation of fit points, inside cylinder (a) outside cylinder (b)

5.3.2 Discussion

These simulations indicate that a gradient applied in some directions to the images does have an impact on the geometry of the objects being imaged, in this case a cylinder. The direction in which the gradient is applied determines the apparent shape of the cylinders and also the magnitude of the deviations. The gradients appear to have a greater influence on the cylinder fitted to the outside of the cylinder, the data is also noisier in all cases. The same number of points are being used to fit both cylinders (10 000) resulting in a lower density in the outside cylinder, this therefore could be the reason for the higher standard deviation of the fit point deviations for each 5° interval.

During the reconstruction process within CTPro a filter is applied to the images, this, however, does not appear to entirely correct for any variation of intensity found within the images. Although the errors seen are within the MPE of the system used in this instance it does highlight errors. The errors are systematic within each set-up, i.e. the deviations follow sinusoidal patterns around the circumference that appear to repeat themselves. Although these trends are not repeatable between the different gradients. Therefore, it is difficult to apply a correction overall. The only way a correction could be applied is if each image was analysed for a gradient and then a correction applied to each image. The gradient would also have to be stable.

At present, on the system used for this study, a shading correction is carried out (see Section 2.4.1) but this uses a single image obtained at the start of the imaging. This is ineffective as it has been shown in Section 3.1 that the intensity varies over time. A small box placed somewhere in the image by the user also monitors the intensity over time but

this study has shown that if there is variation across the image this will also prove to be ineffective.

5.4 Simulation of holeplates

To investigate the errors seen in the experimental reconstructed holeplates, 2D images for both simple and complex holeplates were simulated and, from them, 3D volumes reconstructed. The factors studied include the orientation of the holeplates during imaging, the amount of material around the hole, the position of the hole in the holeplate with respect to the centre of rotation and the spectrum of the X-rays.

5.4.1 Orientation of holeplate during imaging

The deviations in the geometry of the hole and the outside edge of CiHPSim can be seen in Figure 5.38. The deviations are within ±5 µm for both cylinders. For the inside cylinder standard deviations are <3 µm but for the outside cylinder has noisier data and the standard deviation is <7 µm. When comparing the two graphs there is a negative correlation between the two data sets, when there are peaks in the deviation for the inside cylinder, there are corresponding troughs in the outside cylinder. This will be discussed further in Section 5.4.6.

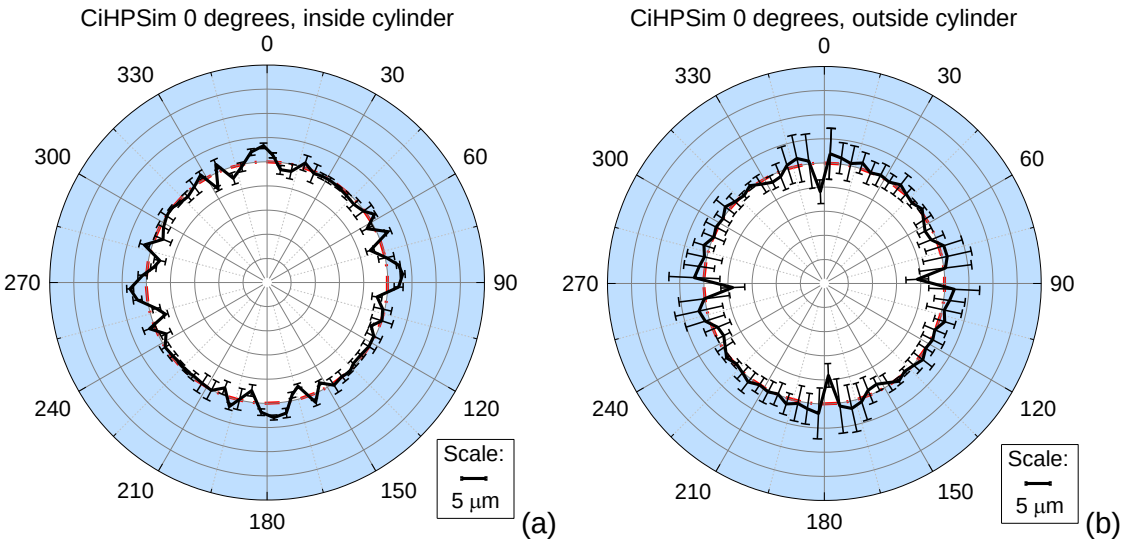

Figure 5.38 Average fit point deviations for CiHP imaged at 0° orientation, inside cylinder (a) outside cylinder (b)

Contour plots of the fit points seen in Figure 5.39, illustrate that the deformation is continuous down the cylinder for both the inside and outside cylinders.

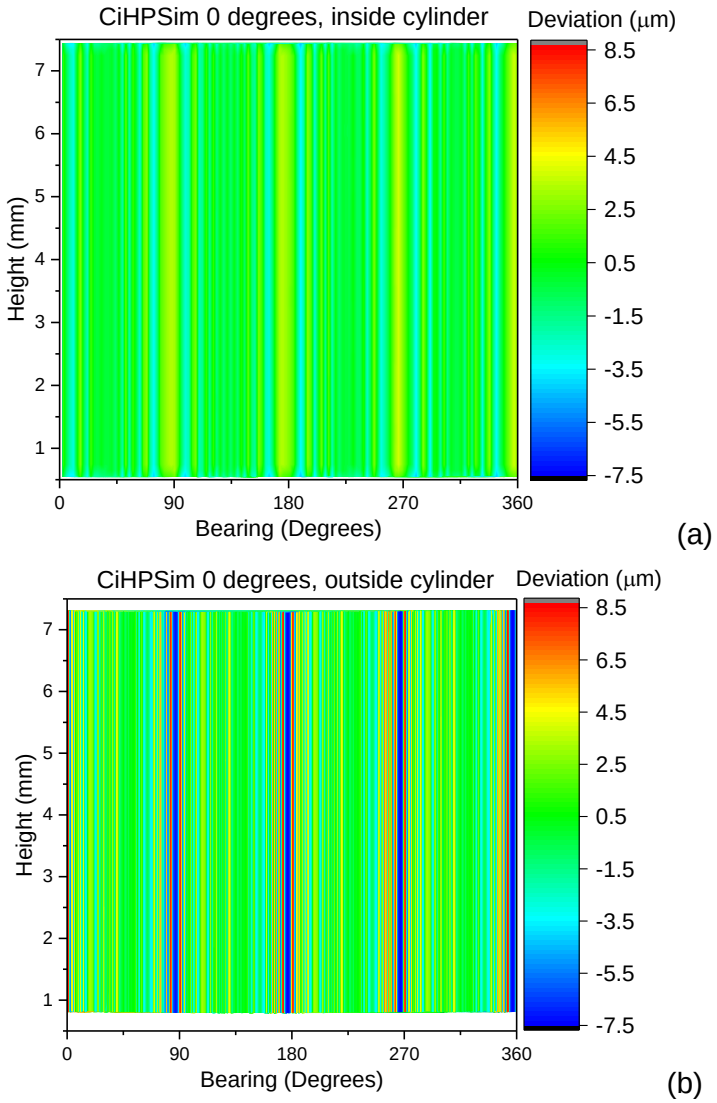

Figure 5.39 Contour plot of all fit points used for CiHPSim imaged at 0° orientation, inside cylinder (a) outside cylinder (b)

When the holeplate was orientated at 45° during imaging the same trend for the inside cylinder (Figure 5.40) can be seen in the deviation as those seen in the experimental data in Section 4.3.8. The difference between the experimental and simulation data is the magnitude of the errors. For the experimental data the range was -20 µm to 60 µm, for the simulated it was -5 µm to 17 µm, about a quarter of the size. The standard deviation follows similar trends with larger values of around 5 µm found at 0° and 180°.

The outside cylinder, which was not obtained for the experimental data due to noise around the stand, shows a similar but not identical trend as the inside cylinder. The highest deviations of around 12 µm are at 0° and 180° but it has much straighter trends in the shape of the cylinder. The noise is greatly increased for the outside cylinder; the standard deviation is <10 µm.

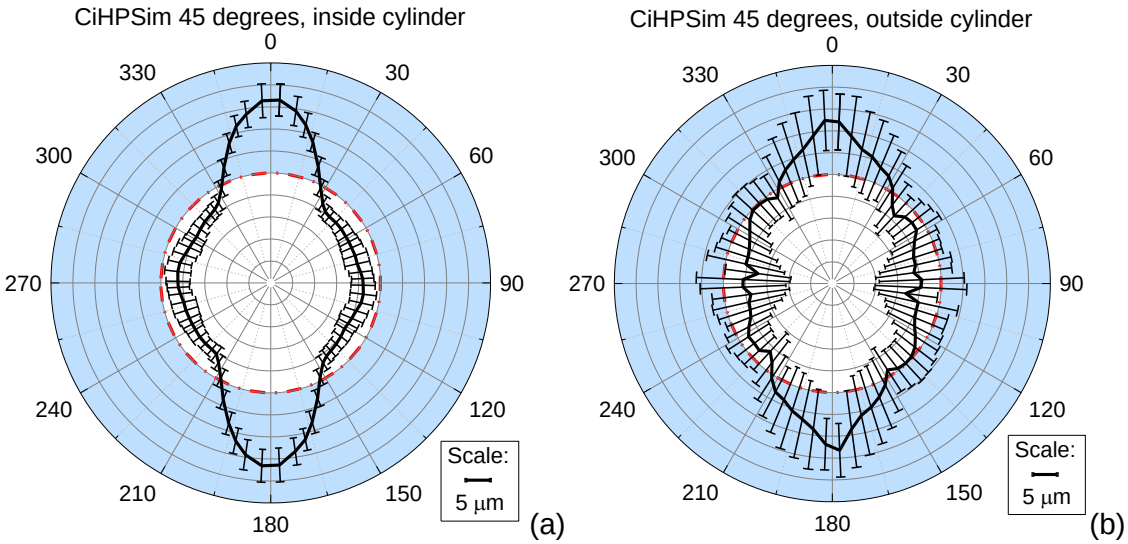

Figure 5.40 Average fit point deviations for CiHP imaged at 45° orientation, inside cylinder (a) outside cylinder (b)

The contour plots indicate that the deformation is not evenly distributed down the entire height of the cylinder (Figure 5.41). This was not evident in the radial plots seen in Figure 5.40 as these plots are the average for a given interval as explained in Section 4.2.4.2. This systematic error in the shape of the cylinders both inside and outside the holeplate could cause errors if the hole shape had just been determined with the measurement of a circle and not a cylinder.

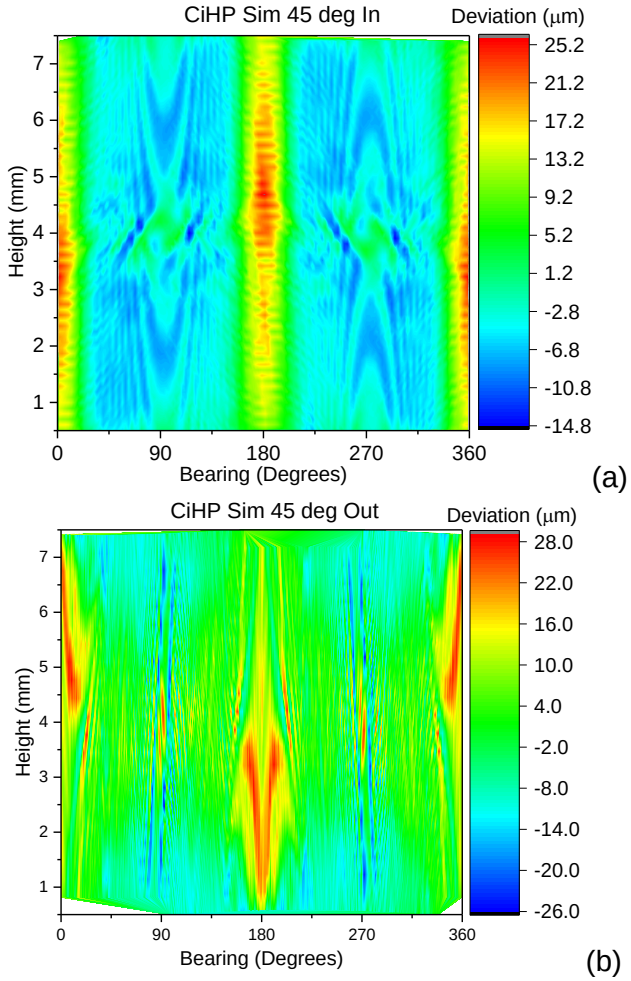

Figure 5.41 Contour plots of fit points for CiHPSim imaged at an orientation of 45°, inside cylinder (a) outside cylinder (b)

Profiles drawn across and down the unrolled cylinders can be seen in Figure 5.43, they allow the change in deviation around the circumference to be seen more clearly. For the inside cylinder the greatest change in deviations can be seen half way down the cylinder, the profile at the top and bottom of the cylinder have similar trends to those seen for the overall profile. When looking at the vertical profiles there are differences in all three profiles compared to the overall profile. The overall profile displays a deviation of approximately 0 µm apart from the top and bottom of the hole and the very centre where there is a deviation of 2 µm. The profiles taken at 90° and 270° appear to be mirror images of each other and both have deviations in the range of -8 µm to 4 µm. This indicates that the cylinder has an apparent tilt. When the cylinder was fitted a direction vector is given for the cylinder and they have values of less than 1.5 µm. The central profile taken at a bearing of 180° has deviations in the range of 13 µm to 24 µm with the smallest deviations being found at the top and bottom of the cylinder.

When considering the outside cylinder horizontal profiles (Figure 5.43), the trends are not as smooth as those seen for the inside cylinder. However, the magnitude of the errors

is of the same order. 10 000 fit points were used to fit both cylinders, therefore as the outside cylinder has a larger area the density of the points across the cylinder is less, this may contribute to the rougher trend in the data. The peak in the deviations found at 0° and 180° is much wider than the peak seen in the inside cylinder. Errors seen in the vertical profiles have much larger magnitudes compared to the inside cylinder. Overall the errors have a range of ±5 µm, nevertheless, the profiles taken at 90° and 270° exhibit errors from -19µm to 20 µm, they mirror each other again as seen above. The central profile at a 180° bearing has a much smoother trend than the equivalent profile in the inside cylinder, although the errors are much larger with deviations from -3 µm to 19 µm. The asymmetry of the profile can be seen in this profile too. These contour plots are in contrast to those seen in Figure 5.39 where the deformation is constant down the cylinder.

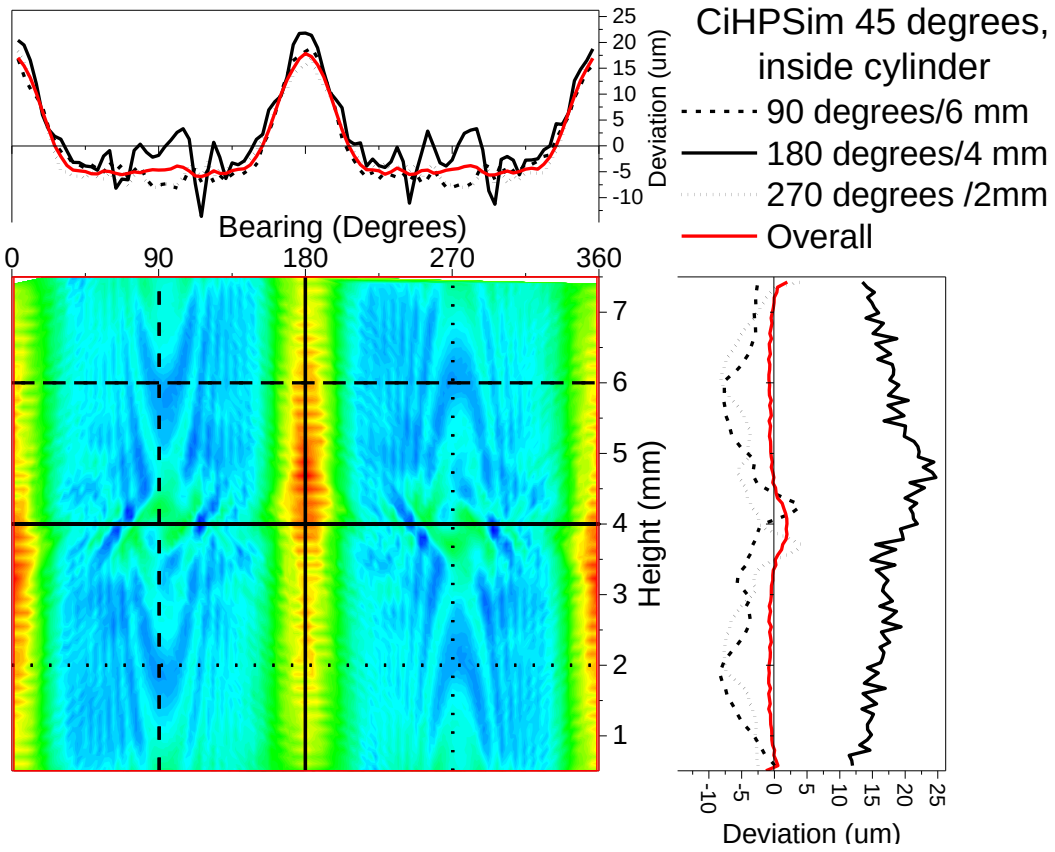

Figure 5.42 Contour and profile plot of all fit points used for inside cylinder of CiHPSim imaged at 45° orientation

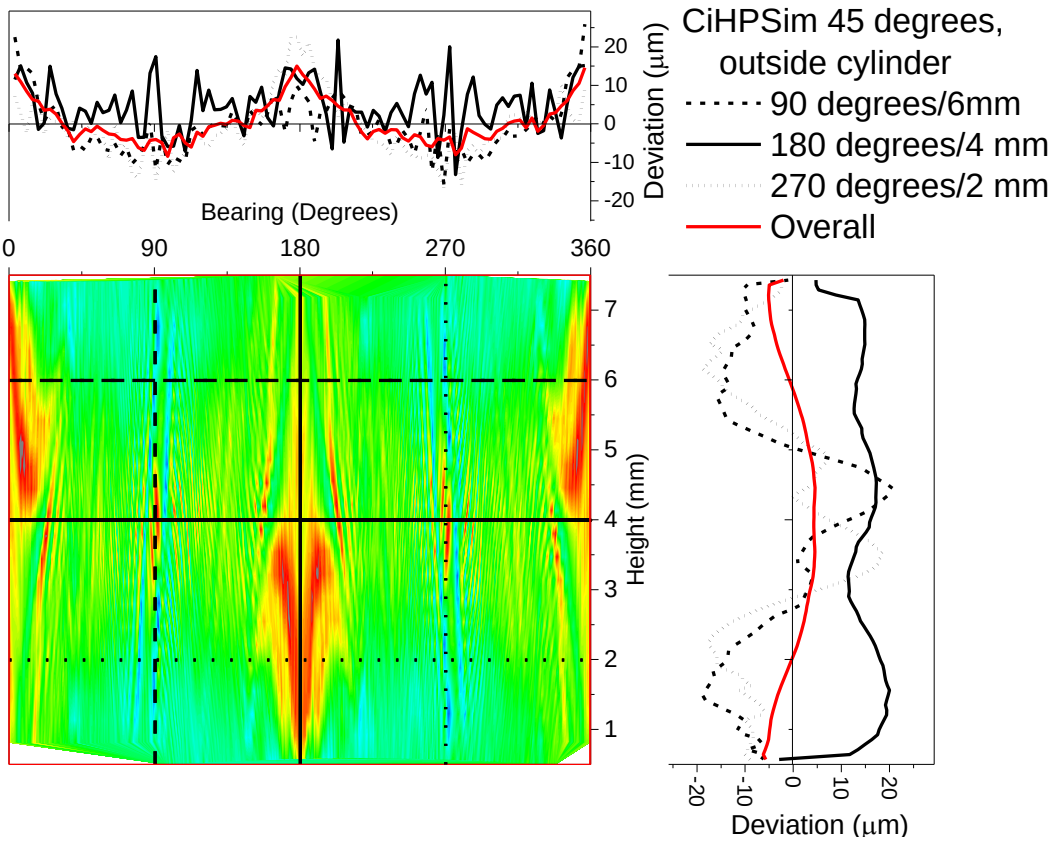

Figure 5.43 Contour and profile plot of all fit points used for outside cylinder of CiHPSim imaged at 45° orientation

This simulation highlights that errors of <±30 µm can be seen when the orientation of the object during imaging is changed. This corresponds to those errors seen in the experimental data. It can also be seen that the deformation is not equal down the length of the cylinder when imaged at 45°.

5.4.2 Amount of material – path length

The effect of the amount of material the X-rays were travelling through was investigated with the simulation of the two holeplates used in Chapter 4, namely HP1 and HP3 (Figure 5.44).

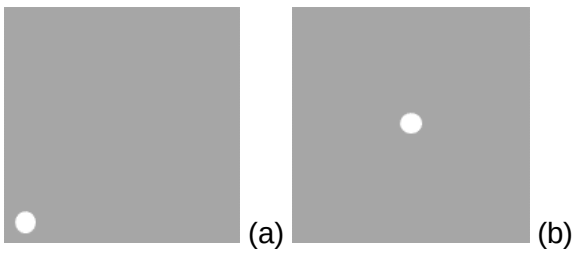

Figure 5.44 Schematic of holeplates, HP1 (a) and HP3 (b) used in numeric simulations

The contour plot for HP1 (Figure 5.45) shows that the deviation of the points is constant down the cylinder. There are distinct bands of deviation, some negative and some

positive. The asymmetric nature of the deformation around the circumference is apparent.

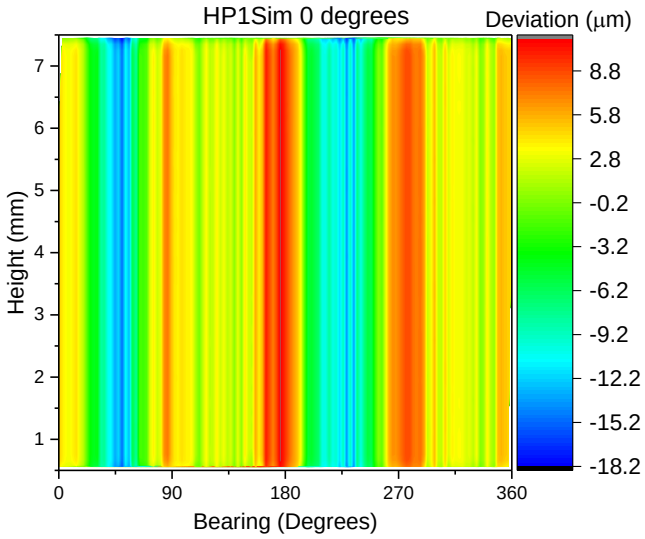

Figure 5.45 Contour plot for HP1Sim of all fit points

The radial plot of the average deviations around the circumference is seen in Figure 5.46, the deviations range from -12 µm to 10 µm. The standard deviations vary from 1 µm up to 7 µm with the noisier data being found as the deviations are becoming more negative. There is a line of symmetry along the 45° to 225° line

When comparing the experimental data to the simulation data there are differences between the two data sets. The experimental data has an elliptical trend, however, the simulated geometry has a rectangular shape. Negative deviations are found at the same positions around the circumference although the magnitude is smaller, 12 µm for the simulated data compared to 25 µm for the experimental. The maximum standard deviation for the simulated data is 6 µm whereas the experimental has standard deviations of up to 15 µm.

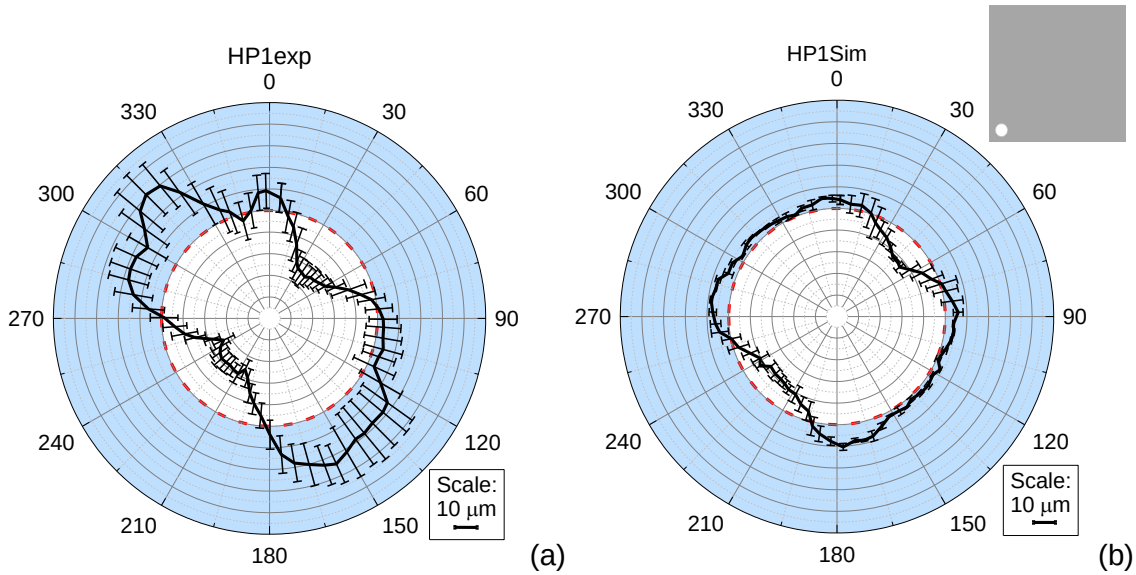

Figure 5.46 Radial plot showing fit point deviations HP1exp (a) and HP1Sim (b)

The path length of the X-rays directly through the hole and the surrounding material as the holeplate is rotated (as explained in Section 4.3.4) and the subsequent effective energy (explained further on in Section 5.4.2.1) can be seen in Figure 5.47. Both graphs exhibit angular trends, due to the square nature of the holeplate which would explain the rectangular shape of the deviation plot seen in Figure 5.46(b). This will be discussed further in Section 5.4.2.1.

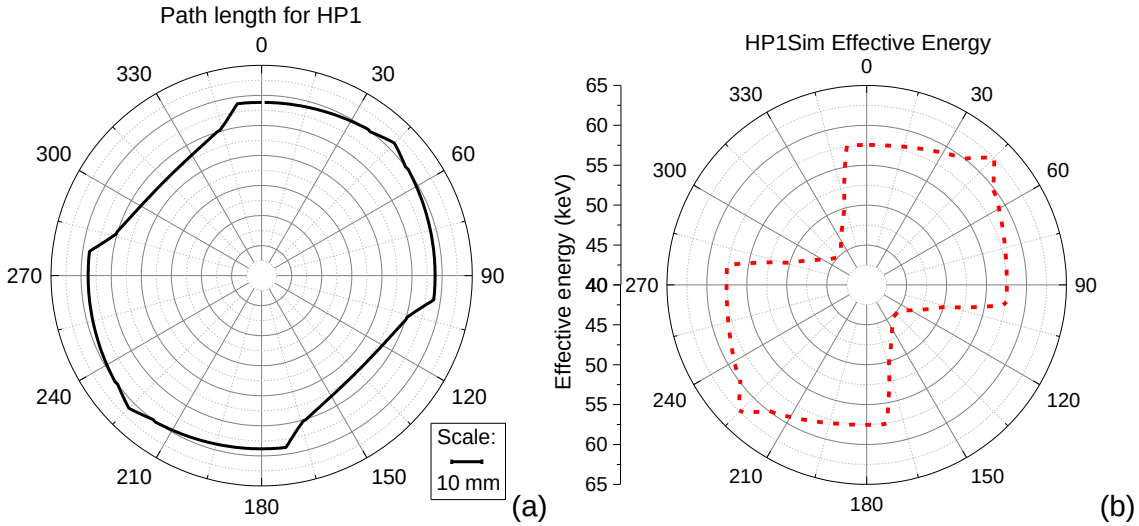

Figure 5.47 Path length (a) and effective energy (b) for HP1

Radial plots for the experimental and simulated results for HP3 can be seen in Figure 5.48, these plots show a dramatic difference in the two data sets. The magnitude of the deviations and noise is much smaller for the simulated data, <7 µm and 2 µm respectively. It can also be seen that the trend is reversed for the two data sets; the negative deviations in the experimental data are positive for the simulated data. This is most likely due to scattered radiation in the experimental data.

When comparing HP1Sim and HP3Sim, similarities can be seen, they both have a rectangular shape and the magnitude of errors are in the same region, approximately ±10 µm. Peaks in the data are found at 0°, 90°, 180° and 270° for both holeplates, however, for HP1Sim negative deviations can be seen along the axis where the longest path length is found.

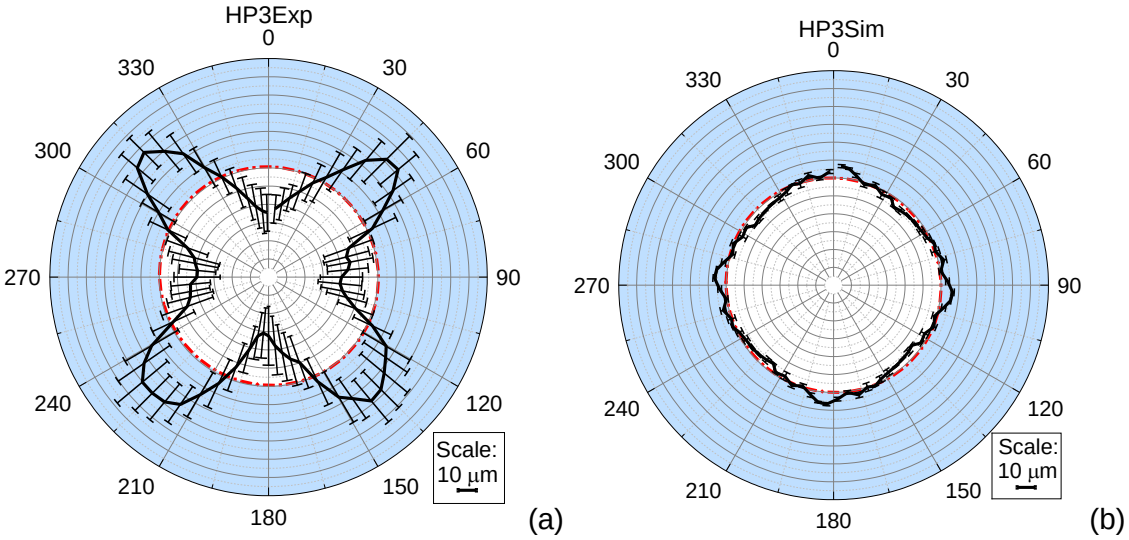

Figure 5.48 Radial plot showing fit point deviations HP3exp (a) and HP3Sim (b)

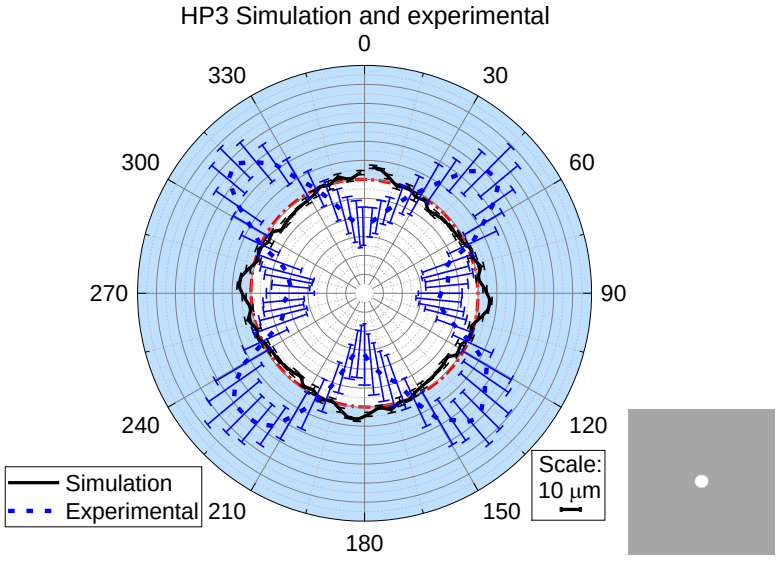

Figure 5.49 Radial plot showing fit point deviations for HP3, both simulated and experimental

Again, as seen for HP1Sim, the path length of the X-rays and the effective energies show angular trends (Figure 5.50), as previously mentioned this is discussed further in Section 5.4.2.1.

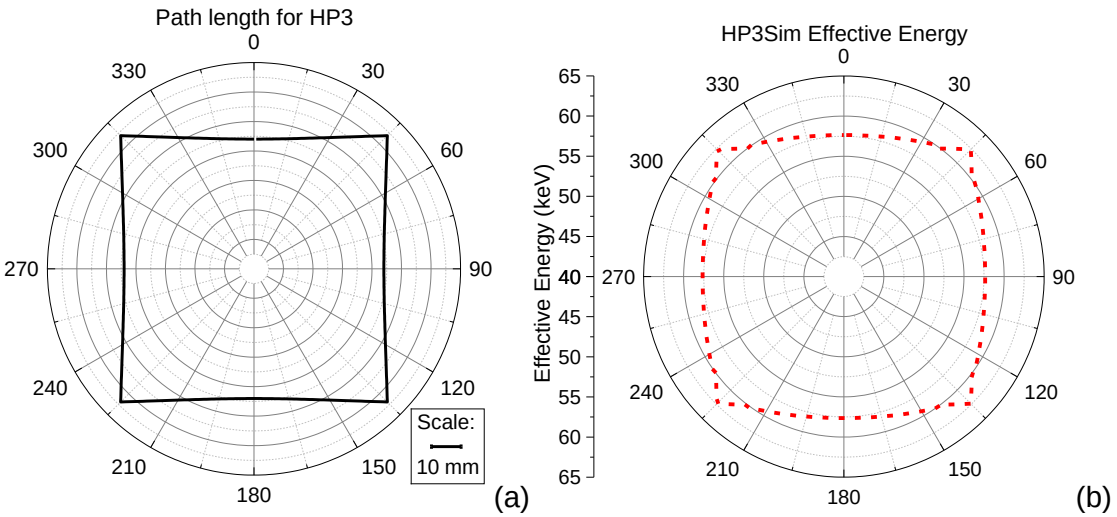

Figure 5.50 Path length (a) and effective energy (b) for HP3

5.4.2.1 Effective energy

For a polychromatic X-ray spectrum, the effective energy is defined as the energy of a mono-energetic X-ray that has the same penetrating ability as polychromatic X-rays (Sprawls, 1995). The attenuation of X-rays by a given material is characterised by the attenuation coefficient (μ). The effective energy of the spectrum can be determined by calculating the energy of a mono-energetic X-ray that has the same attenuation coefficient as the spectrum (Khan, 1953).

A simple method to calculate the length of material that the X-rays travel through was described in Section 4.3.4, this method was used again to calculate the thickness of the material that would be used in the following equations to calculate the effective energy. Although this is a very basic representation of path lengths used in the reconstruction, it is designed to get a broad overview of how the energies vary around the cylinders.

To calculate the attenuation coefficient (μ), Equation 5.1, can be rearranged, see Equation 5.3. The values for I, I_0 and t were calculated using the method seen in Section 5.2.3.

$$\mu = -\frac{\ln(\frac{I}{I_0})}{t}$$

Equation 5.3 Determination of attenuation coefficient for a given length of material

The NIST data for attenuation coefficient is given for discreet values. In the range that is required for this set up the values are given for 40 keV, 50 keV, 60 keV and 80 keV. To determine the correct value for any given energy value in between these values, a line

of best fit was determined for the three intervals. This equation was used in MATLAB to determine the energy from the attenuation coefficient calculated above.

For HP1 the results can be seen below in Figure 5.51, the data indicates a link between the deviation in the fit points and the effective energy for that given path. When the path length is at its highest, i.e. at 45° and 225° the effective energy is at its highest but the deviation is at its most negative, up to -13 µm. However, when the path length is at its shortest and therefore the effective energy is at its lowest, at 135° and 315°, the deviations are nearest zero.

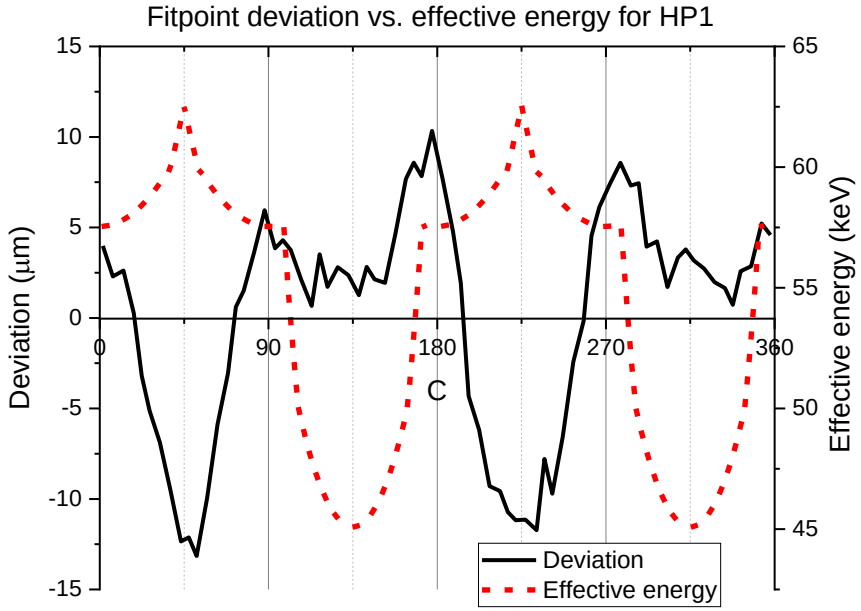

Figure 5.51 Fit point deviation verses effective energy for HP1Sim

When looking at the results for HP3, see Figure 5.52 the negative correlation between deviation and effective energy is clearly seen. Again, when the energy is at its highest the deviation is most negative (-4µm) and when the energy is at its lowest the deviations are most positive (7 µm).

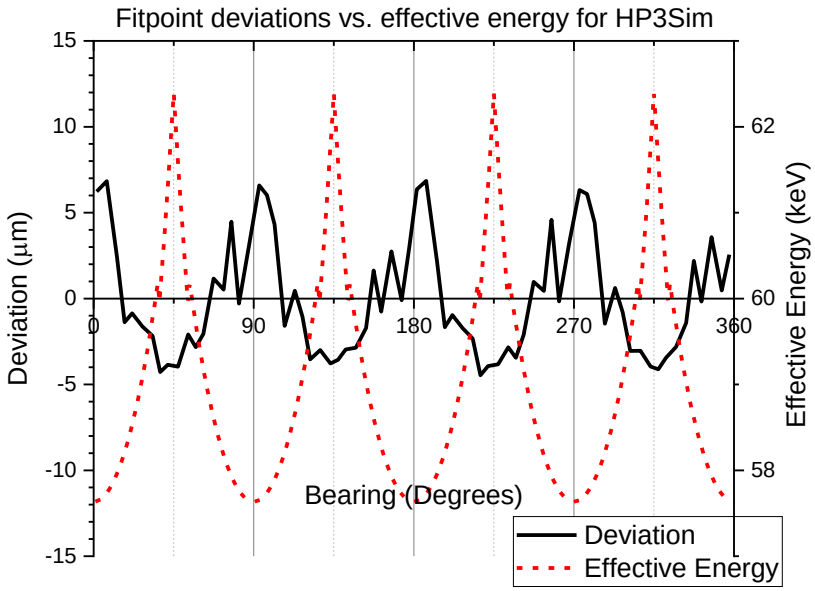

Figure 5.52 Fit point deviation verses effective energy for HP3Sim

The effective energy correlates to the intensity of the greyscale recorded for each pixel in the 2D images. The greyscale is used in the algorithms to determine the surface of the object within the reconstructed volume, therefore an accurate representation of the greyscale is crucial to define the correct position of the surface.

These experiments show that the same greyscale value is not found all the way around the circumference of the holes within the holeplates, this then leads to the apparent deformation in geometry which is seen here.

The differences between the experimental and simulated volumes will be investigated further in Section 5.4.5 which will look at the effect of slight changes in the orientation and position of the holeplate during images which may have occurred during the experimental imaging.

5.4.3 Complex holeplate

Images of the complex holeplate that was originally seen in Chapter 4 were also numerically simulated using multiple primitive cylinders in MATLAB. Three cylinders (1, 17 and 19) were compared to the experimental data of the complex holeplate that was imaged again using the purpose built stand. The results for Cylinder 1 can be seen below in Figure 5.53 and indicate that for both data sets, the deviations follow the same trends with peaks at bearings of 135° and 315° and troughs at 45° and 225°. The deviations are in the same range, however, the noise in the experimental data is higher at a maximum of 15 µm compared to <10 µm for the simulation data. The highest noise is found where the deviations are most positive.

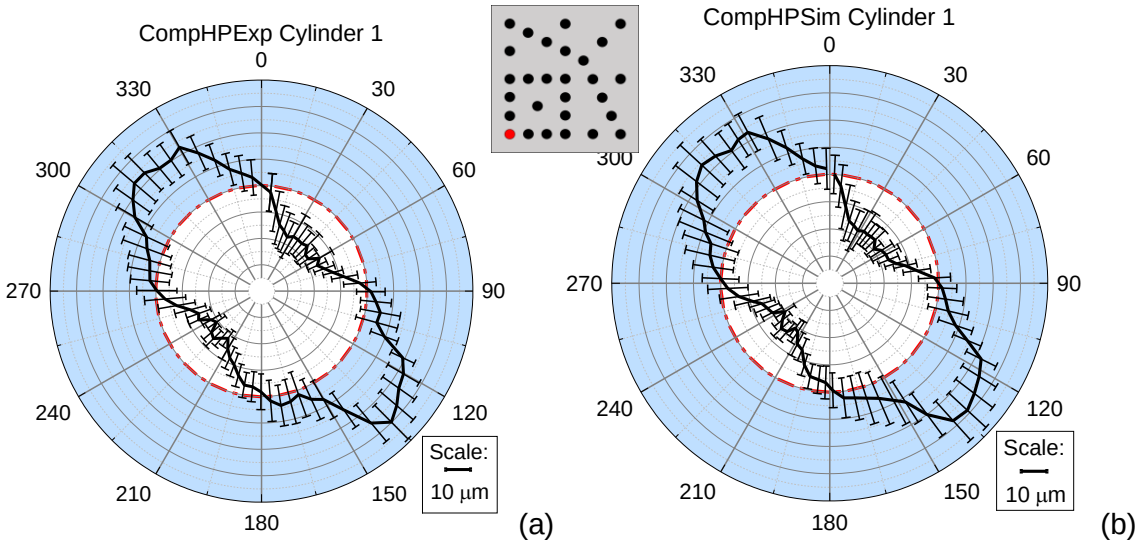

Figure 5.53 Fit point deviations for Cylinder 1 experimental (a) and simulation (b)

When comparing the deviations for Cy1Sim with the effective energy, in Figure 5.54 and Figure 5.55, the negative correlation seen for HP1Sim (Section 5.4.2.1) are also present. The trend in the effective energy data is not as smooth as that seen in HP3Sim due to the constantly changing path lengths caused by the extra holes found in the complex holeplate.

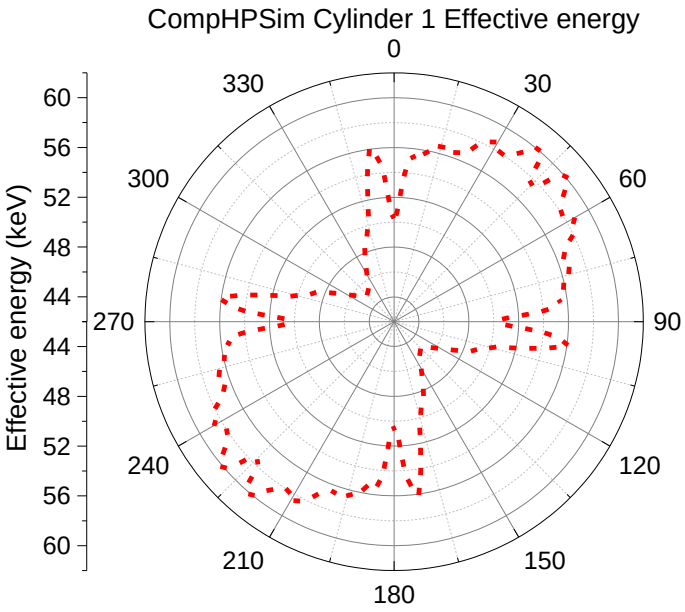

Figure 5.54 Effective energy for Cylinder 1 in CompHP

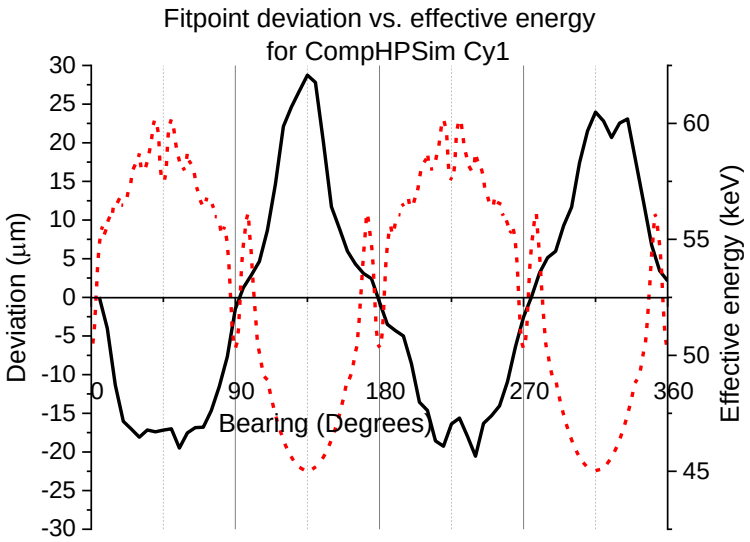

Figure 5.55 Fit point deviations of cylinder in Cylinder 1 in CompHPSim compared to effective energies around cylinder

Deviations for both the experimental and simulated Cylinder 17 can be seen in Figure 5.56. They follow the same systematic trends with peaks <40 µm at 45°, 135°, 225° and 315°. Deviations on opposite sides of the hole are not symmetrical, for example at 90° and 270°, as seen previously in Section 4.3.6. It should be noted that the holeplate is not symmetrical with three holes being found to the left of Cy 17 but only two to the right, see diagram of Complex holeplate in Figure 4.1. The side with more holes and therefore the shorter path lengths, has a more negative deviation of 25 µm compared to 15 µm at a bearing of 90°.

It should be noted that unlike HP1Sim and Cy1Sim, HP3Sim and Cy17Sim do not follow the same trend in deviations; this will be discussed further in Section 5.5.

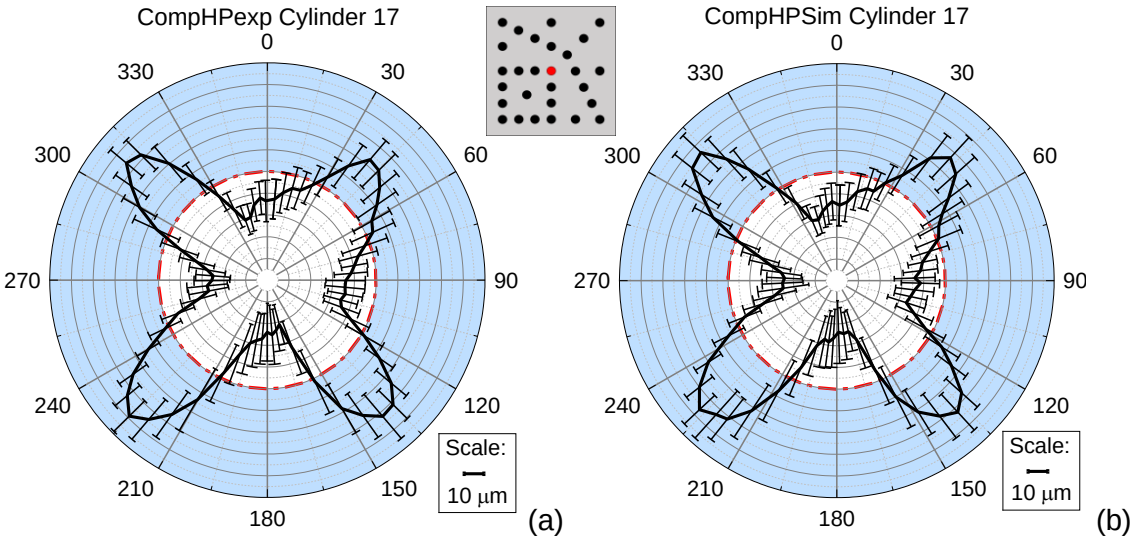

Figure 5.56 Fit point deviations for Cylinder 17 in CompHP, experimental (a) and simulation (b)

The effective energies of the X-rays around the cylinder can be seen in Figure 5.57 and Figure 5.58 and, unlike results previously seen, have a positive correlation with the deviation. The points around the circumference that have a positive deviation, i.e. the hole surface is outside the cylinder, are at the points where the effective energy is at its highest.

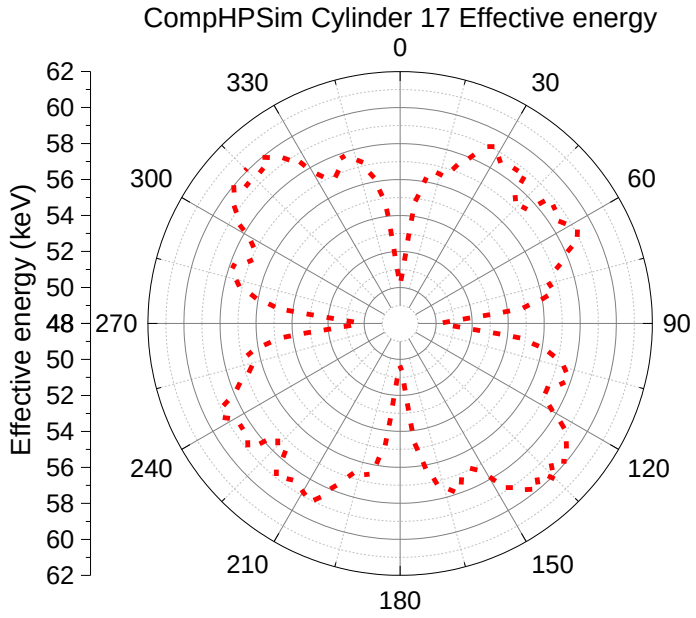

Figure 5.57 Effective energy for Cylinder 17 in CompHP

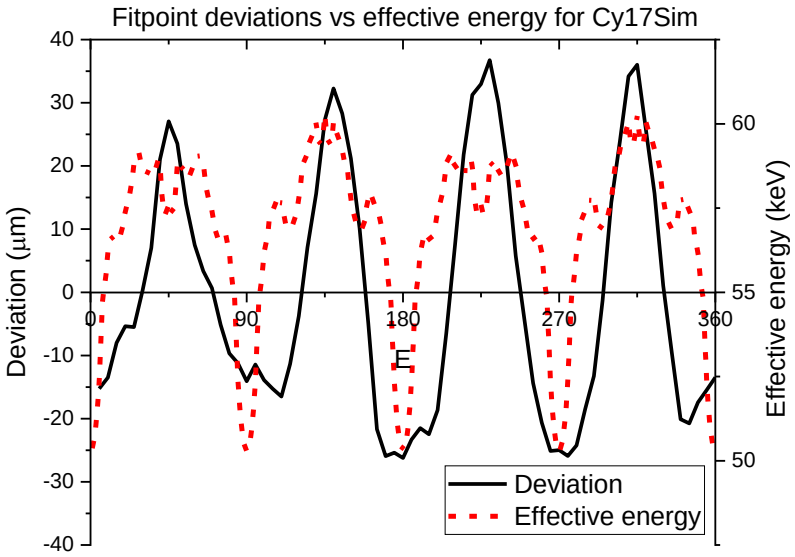

Figure 5.58 Fit point deviations of cylinder in Cylinder 17 in CompHPSim compared to effective energies around cylinder

Deviations for the experimental and simulated Cylinder 19 again follow the same trend and magnitude with respect to the deviations.

The asymmetry previously discussed in Section 4.3.6 is most extreme in this hole compared to the other holes that were investigated.

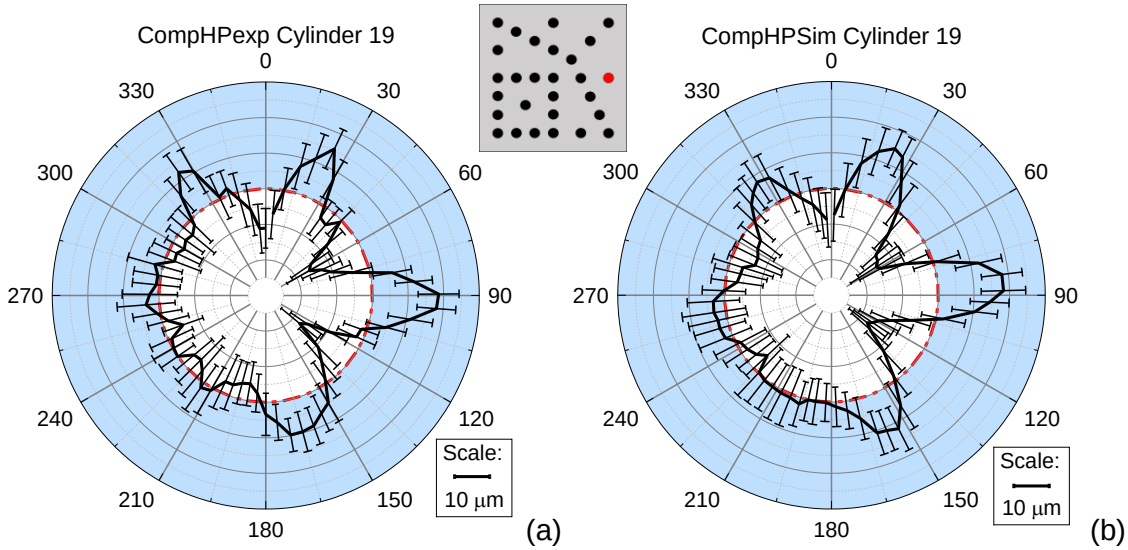

Figure 5.59 Fit point deviations for Cylinder 19 both experimental (a) and simulation

The trends for deviations and for the effective energy (Figure 5.60 and Figure 5.61) are more complex than those for Cy1 and Cy17. The correlation between the deviations and effective energy is not as well defined. In some places, e.g. at a bearing of 90°, there is a negative correlation but in other places, e.g. at a bearing of 225° there is a positive correlation.

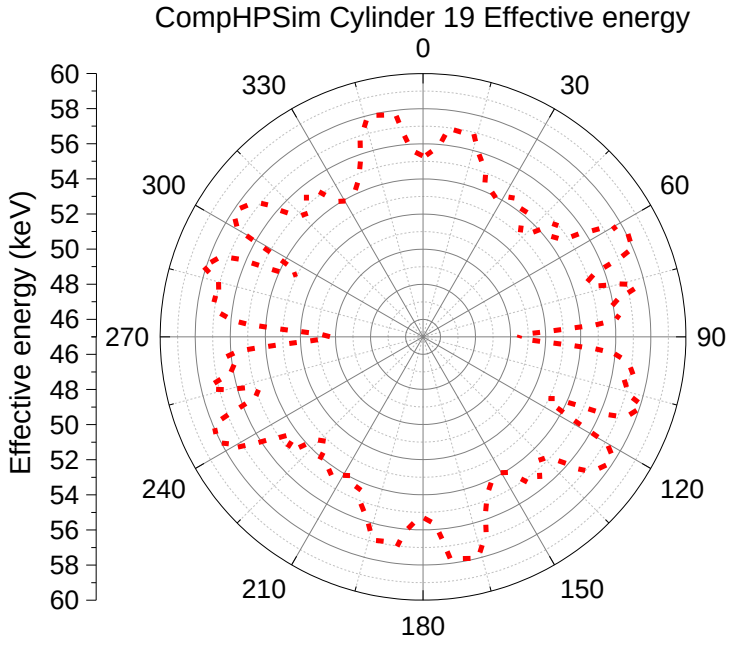

Figure 5.60 Effective energy for Cylinder 19 in CompHP

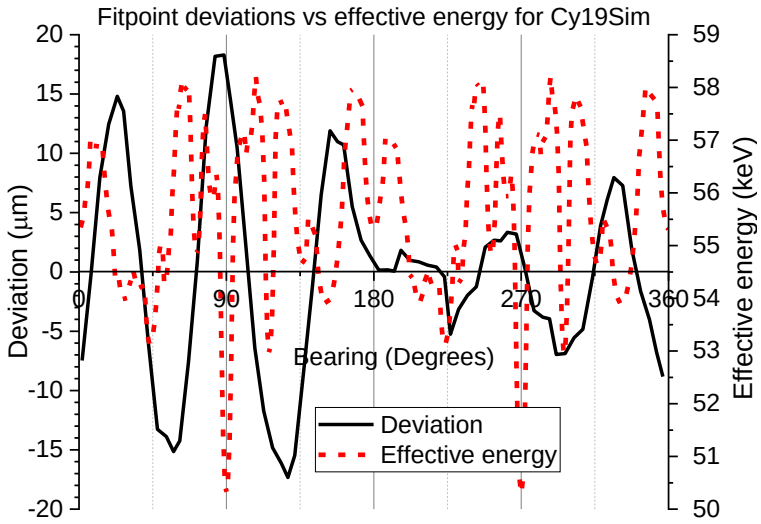

Figure 5.61 Fit point deviations of cylinder in Cylinder 19 in CompHPSim compared to effective energies around cylinder

This change from a negative correlation between deviation and effective energy seen in Cy1Sim and then a positive correlation in Cy17Sim indicates that there must be another factor involved. The only difference between the two holeplates is that the hole in HP1 is not situated in the centre of rotation, unlike the hole in HP3Sim. This will be studied further in Section 5.4.6.

Although this work focussed on the shape of the holes, Figure 5.62 illustrates the difference in the discrepancies between the measured and reference unidirectional lengths for the simulated data. It can be seen that although the spread in data is greater than the experimental data the distribution is much more even with the data spread equally across the graph. This indicates that there is no scaling error within the simulation process.

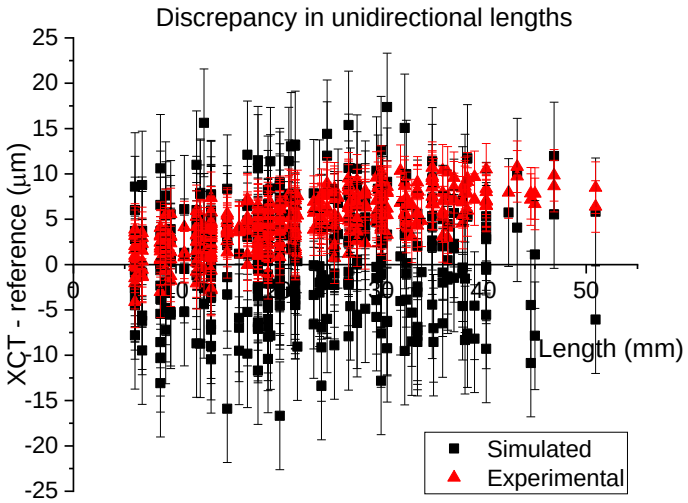

Figure 5.62 Comparison of unidirectional length discrepancy for simulated and experimental results for CompHP. Error bars equal to standard deviation of population

Overall the simulated data for the complex holeplate exhibited the same deformation in geometry as the experimental data and size of which were of the same magnitude (±40 µm).

5.4.4 Monoenergetic X-rays

Results in Section 5.4.2.1 indicate that there is a link between the effective energy of the X-rays and the deviations found along that line. To investigate this further the images for HP3 were simulated using a monochromatic X-ray beam. The holeplate was orientated at 0°. To simulate this the MATLAB code used in Section 5.2.2 was modified so that just a single value was used instead of multiple attenuation coefficients. It was decided to use the attenuation coefficient for a high energy of 500 keV to ensure that the beam transmission was high.

Results seen in Figure 5.63 indicate that although the errors are much smaller (<4 µm), there is still a systematic trend in the deviations with peaks being found at 0°, 90°, 180° and 270°. Figure 5.64 shows a comparison between the two energy types.

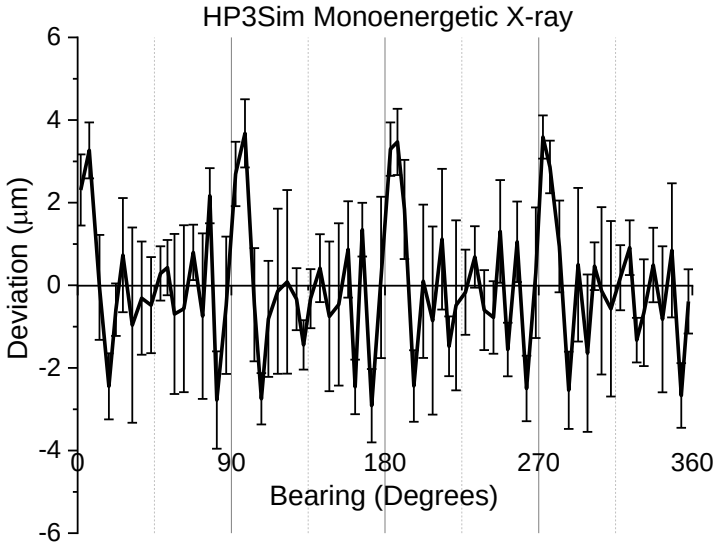

Figure 5.63 Fit point deviations for HP3Sim simulated using a monoenergetic X-rays

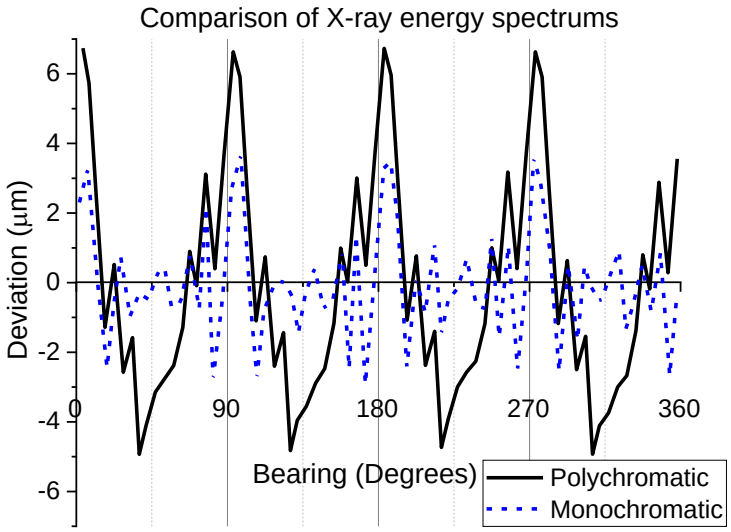

Figure 5.64 Comparison of energy spectrums when used to simulate images of HP3

These results suggests that the polychromatic X-rays and the related effective energy influences the deformation, as already discussed in Section 5.4.2.1. However, there is also a systematic error occurring which is not due to the path length of the X-rays and the effective energy probably due to the reconstruction algorithm that is being used.

5.4.5 Alignment of experimental components

The variation between the experimental and simulated data seen for HP1 and HP3 needed to be investigated further. The set-up of the point source, manipulator and detector within the simulation assumed perfect alignment between the system components and the holeplates. For the experimental set-up this alignment, no matter how accurate the calibration of the system is, will never be completely accurate, therefore it was decided to translated HP3 1 mm along the Z axis so that it was not aligned exactly with the point source and the centre of the detector.

Figure 5.65 indicates that the errors in the geometry show very little difference. There are still peaks in deformation of 6 µm and troughs of -5 µm.

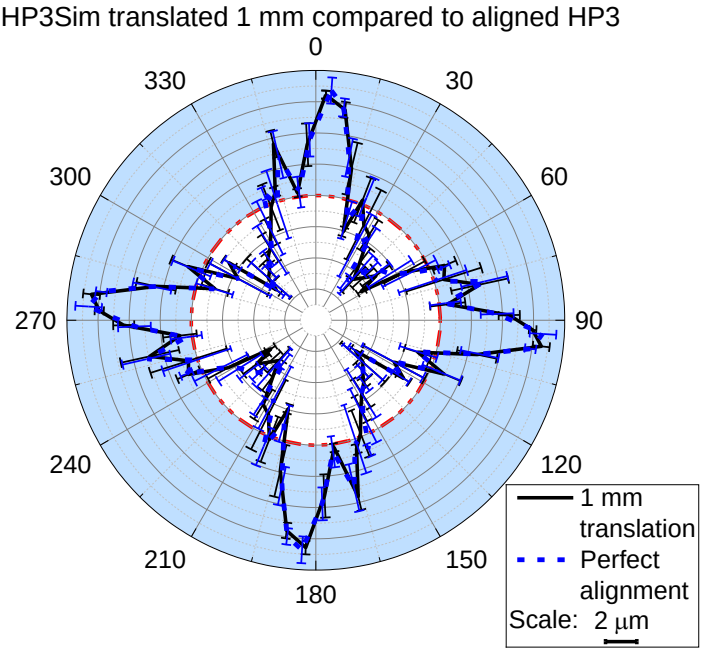

Figure 5.65 Comparison between HP3 with perfect alignment on Z axis compared to a translation of 1 mm

HP3 was also simulated with a change in orientation of 1°, unfortunately the images did not reconstruct correctly and with the limitation of time and access to the reconstruction software at NPL it was not possible to investigate further.

This simulation shows that the reconstruction algorithms still work if the object is shifted slightly in the Y axis.

5.4.6 Holeplate away from centre of rotation

To investigate the asymmetry of the deviations around the circumference, as seen in Section 4.3.6 where the hole in HP1 and HP5 was further away from the centre of rotation, images were simulated of CiHP as if it were positioned away from the centre of rotation in an experimental XCT system, see Figure 5.66. It was translated by 14.5 mm from the centre of rotation. This value was chosen as this would have been the maximum the holeplate could have been moved if the imaging had been carried out experimentally. Unfortunately access to the NPL XCT system had finished before this could be carried out. In the MATLAB code the original coordinates of the cylinders were transformed using the matrix seen in Equation 5.4.

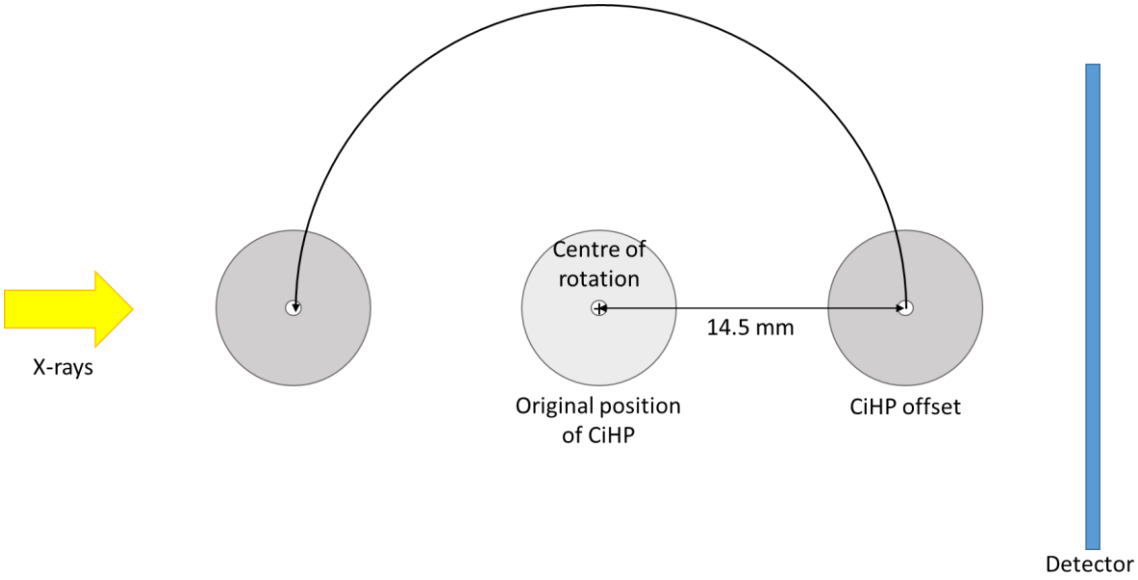

Figure 5.66 CiHPSim is positioned 14.5 mm from the centre of rotation

$$Tx = \begin{bmatrix} 1 & 0 & 0 & 14.5 \\ 0 & 1 & 0 & 0 \\ 0 & 0 & 1 & 0 \\ 0 & 0 & 0 & 1 \end{bmatrix}$$

Equation 5.4 Transformation matrix to move CiHPSim away from the centre of rotation

Results seen in Figure 5.67 show that for most of the way around the circumference, errors are within ±5 µm as seen when CiHPSim was simulated previously in the chapter. However, at a bearing of 90° there is a large peak of 17 µm for the outside cylinder.

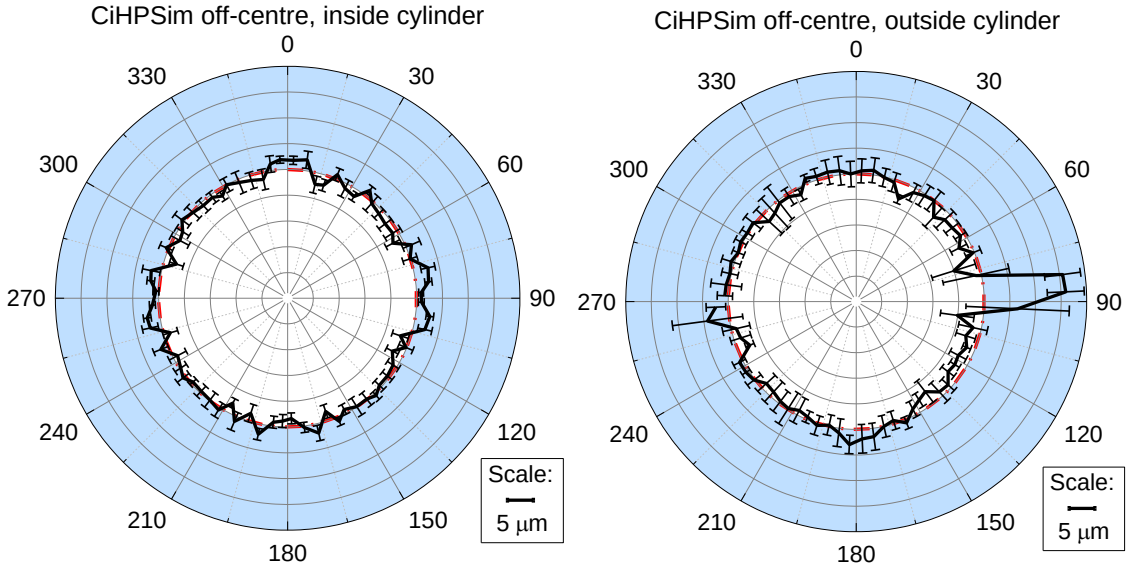

Figure 5.67 Radial plots for CiHPSim when imaged off-centre from rotational axis

Figure 5.68 illustrates the position of the holeplate and the location of the part of the holeplate where the larger deformation occurs. This is the point where the holeplate is

furthest away and then closest to the source. It is also on the extreme edges of the images. This ties in with the data seen in Chapter 4, Section 4.3.6 which illustrated asymmetrical deformation of the hole in HP1 and HP5 which was believed to be due to the change in intensity due to the inverse square law.

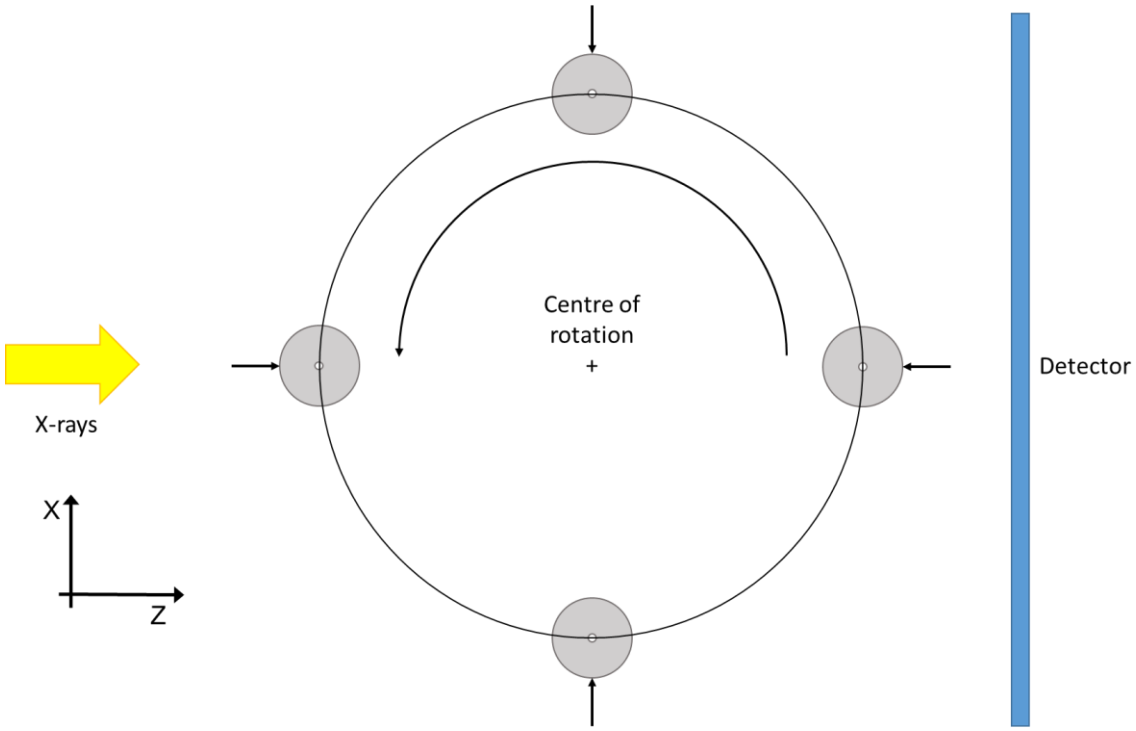

Figure 5.68 Position of CiHPSim during rotation. Arrow indicates bearing of 90° where the large deviation seen in Figure 5.67 occurs

Another factor that could be an issue is that the X-rays are glancing off the edge of the holeplate when it is at its outermost positions on the X axis.

This simulation strengthens the theory discussed in Chapter 4, Section 4.3.6.1, that if a feature within an object is not at the centre of rotation during imaging and a given cross section is imaged with different intensity X-rays during rotation; errors in the greyscale can occur at the surface where the difference in distances is most extreme.

5.4.7 Artefacts in CiHPSim deviations at 0° orientation

Systematic error can be seen in the two cylinders for CiHP when imaged at 0°, see Figure 5.69. In these two cases, they appear to mirror each other. The inside cylinder mimics the trends seen for HP3, however, the outside cylinder has large troughs of <6 µm at 0°, 90°, 180° and 270°. These are at the bearings where the inside deviations are at their most positive. These results would indicate an apparent increase in the thinning of the holeplate at these bearings, which is not the case as the simulations use perfect primitive shapes.

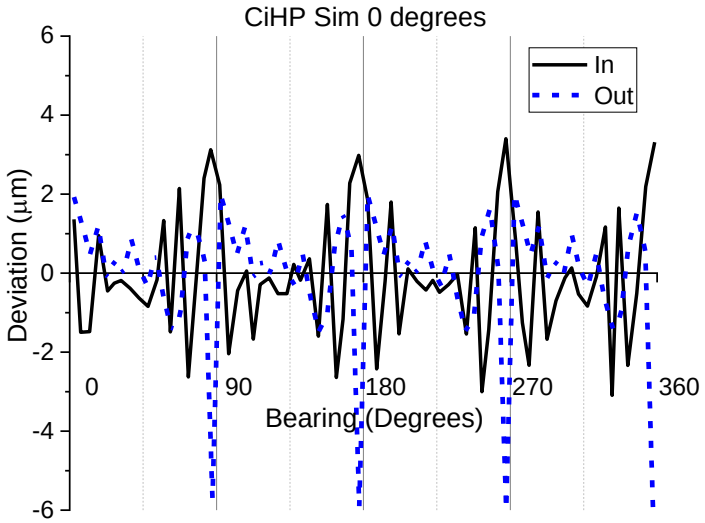

Figure 5.69 Deviations for inner and outer cylinder fitted to CiHPSim imaged at 0°

Both the results for CiHPSim and HP3Mono indicate that there is a systematic error potentially occurring in the reconstruction process. Although the errors lie below the MPE of the system they are highly systematic indicating that they could be corrected for.

To try to identify why these errors were occurring the same images used for CiHP above were reconstructed again but the initial angle was altered to 35° in the .xtekct file that is loaded into CT Pro. Results seen in Figure 5.70 indicate that for the inner cylinder, the deviations show the same trend in the deviations with the same magnitude as the data seen in Figure 5.69. However, for the outside cylinder, although the trend is the same the magnitude of the errors is much smaller with a maximum of -2 µm compared to 6 µm seen at 0°, 90°, 180° and 270°.

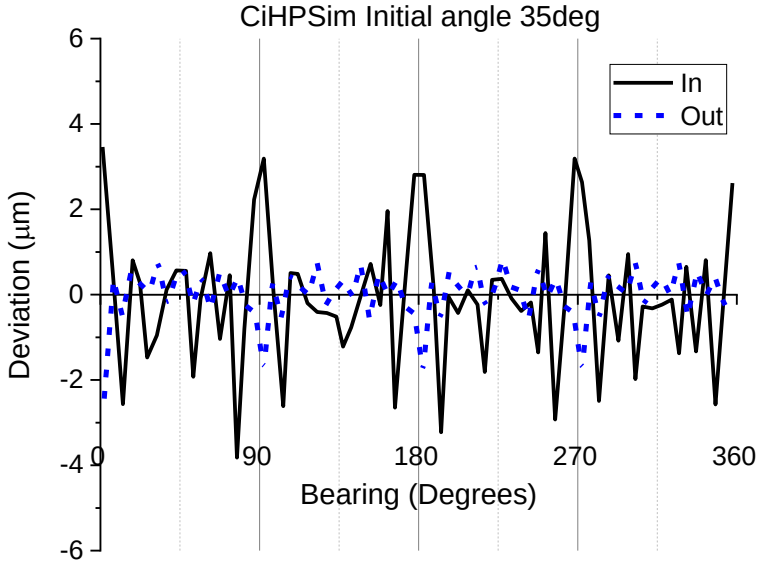

Figure 5.70 Deviations for inner and outer cylinder fitted to CiHPSim. Reconstructed with a 35° initial angle

To investigate this further, the original images were again reconstructed but when the volume was imported it was registered to a CAD model of the holeplate that had been rotated 35° in an anti-clockwise direction. These results can be seen in Figure 5.71 and show the same magnitude of errors as those seen for the original CiHPSim data. They follow the same trend but the peaks and troughs are shifted to the left by 35°. This indicates that the deformation of the shape occurs in the reconstruction and not the cylinder fitting process.

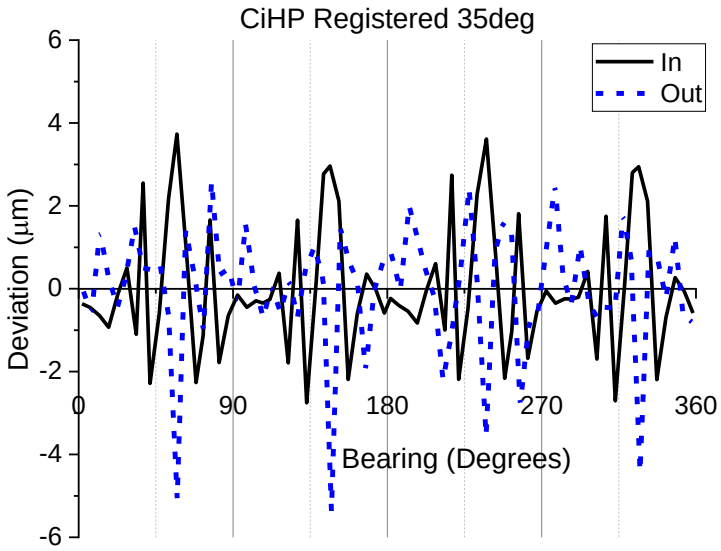

Figure 5.71 Deviations for inner and outer cylinder fitted to CiHPSim when volume rotated 35° in VGStudio Max

The cause for these trends in inexplicable and cannot at this point in time be explained.

5.5 Discussion

Systematic trends can be seen throughout this chapter both in the investigation into the X-ray flux variation across the images and with the simulation of the different holeplates.

The change in apparent geometry was observed in Section 4.3.8 with deviations of < 60 µm being found when the holeplate was orientated at 45° during imaging. This geometry was replicated in the simulated volumes although the deviations were less than 17 µm. The geometry of the surfaces was found to vary depending on whether it was the outside edge or the inside edge.

Apparent geometry deformation also appears to be related to the position of the hole within the holeplate itself. The simulated volumes of HP1 and HP3 show similar angular geometry, however, the shapes do vary slightly (Figure 5.72) with negative deviations of around 10 µm being seen at a bearing of 45° and 225° for HP1. One difference between the two holeplates is that the hole in HP1 is situated away from the centre of rotation. To

investigate if this would have any effect on deviations, a simulation of CiHP moved away from the centre of rotation was carried out and a significant level of deviation was found on the outside cylinder (<15 µm). This deformation occurred at the edge of the holeplate that was far away and near the source. This ties in with the inverse square law that indicates that the intensity of the X-rays for a given cross-section will decrease the further away from the source the cross-section is.

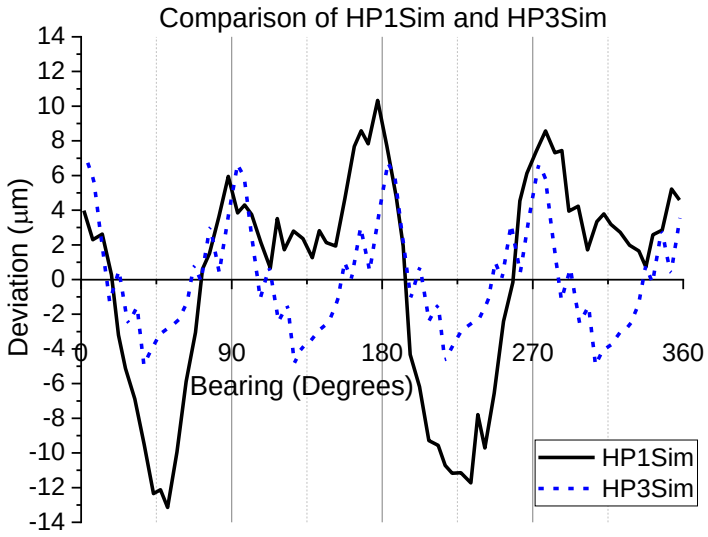

Figure 5.72 Comparison of fit point deviations for HP1Sim and HP3Sim

The discrepancy in the intensity and therefore the greyscale appears to affect the reconstruction of the volume and deforms the geometry of the shape.

Another difference is the amount of material around the holes. As illustrated the path lengths vary for each holeplate and these path lengths are negatively correlated to the effective energy of the X-rays.

The asymmetry between opposite sides of the holes appears to be related to the amount of material either side of the hole. Although the intensity measured at the detector is a result of the total path length, which is the same length no matter which way it is viewed from, there does appear to be a discrepancy. This again is related to the inverse square law.

The simulations for HP1 and HP3 do not match with the experimental data, see Figure 5.73 which highlights the differences between the datasets. HP1Sim indicates a similar trend but the magnitude of the errors is smaller than the experimental data. The trend in the geometry for HP3Sim is opposite to the experimental data and the magnitude of the errors is smaller. However, when comparing the experimental and simulated results for the holes in the complex holeplate there is little difference in the magnitude of the errors,

the only difference is that the noise in the data is less for the simulated results, see Figure 5.74.

These differences in magnitude in deviations, for the simple holeplate, between the simulated and experimental data may be due to scattering of the X-rays in the experimental data. Scatter causing errors in dimensional measurements was discussed in Section 2.8.5, Angel *et al.*, (2015) found errors of 7 µm in 2 mm unidirectional and bidirectional measurements. Results in 3.2.2 indicated that scatter was present within the X-ray system especially at higher voltages.

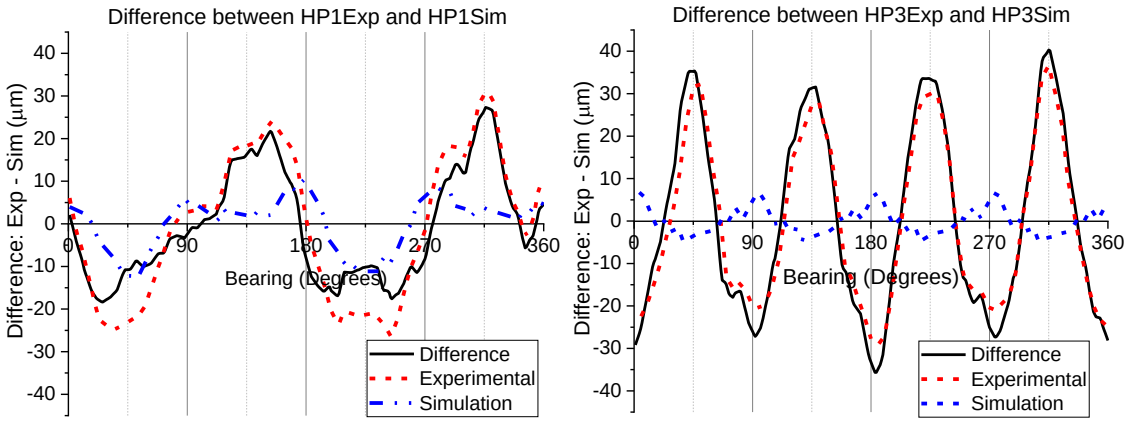

Figure 5.73 Comparison of HP1 and HP3 for the experimental and simulated data

Another result that is not expected is that the results that Cy17 (both for experimental and simulation) have a positive correlation between the deviations and effective energy. This is unlike all the other data sets where there is a negative correlation.

Deviations of up to 6 µm are seen in simulations for CiHP at 0° 90°, 180° and 270°. The direction of these deviations varies for the inside and outside cylinders. They appear to be a result of the reconstruction and positioning of the voxels, this is shown when different set-ups were tested in the reconstruction process. These artefacts were also seen when HP3 was images with a monochromatic X-ray spectrum.

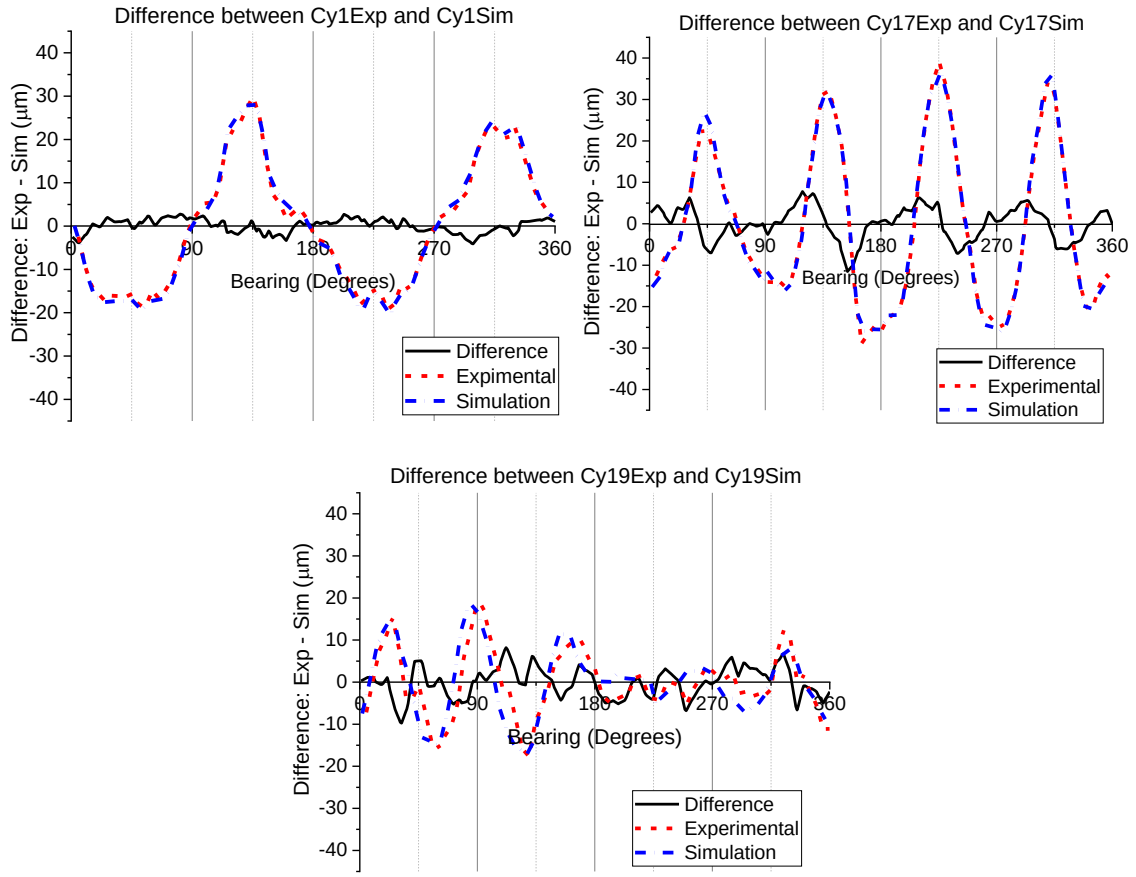

Figure 5.74 Comparison of Cy1, Cy17 and Cy17 in CompHP for the experimental and simulated data

5.6 Potential correction

The systematic nature of the trends would allow a possible correction to be calculated. This could involve using a detector that measures the spectrum to be used when imaging the holeplates. From this the effective energy could be measured, this value could then be used to correct the greyscale values in the volume.

5.7 Impact of simulation

The simulation provided a useful tool in the determination of factors associated with deformation of the apparent geometry of objects. The simulation takes into account a particular geometry and interaction of the X-rays with the given material of a specific density. The initial, perfect alignment which would not be available in an experimental environment allowed the individual factors to be studied. For example, when the orientation of the object during imaging was being studied, this simulation allowed everything in the system to stay constant apart from the orientation. The discrepancies were then purely down to the change in orientation.

The small changes made to the geometry of the system seen in Section 5.4.5 indicates the potential that the simulation holds. In this instants the orientation of the holeplate was altered slightly, this could replicate a tilt in the manipulator. The height of the object was also changed to represent the X-rays hitting the target not quite perpendicularly. The coordinates of the detector could also be manipulated to replicate a tilt on the detector.

Discrepancies between the simulated and experimental data were highlighted in Figure 5.73 and Figure 5.74 and indicate that, for the complex holeplate, the maximum difference are approximately ±5 µm on a systematic deformation of ±30 µm. This indicates that for the complex holeplate, which is being considered as a reference object for an ISO standard, the simulation provides a good representation where errors can be predicted.

For the simple holeplates the discrepancies between the experimental and simulated data are much higher (±45 µm) indicating that there some other unidentified factors that have not been taken into account in the simulation. As previously mentioned scatter was not included in the simulation, the discrepancies seen between the simulated and experimental data for the simple holeplates may indicate that scatter is more predominant in the simple holeplates and therefore has a larger effect.

Potential errors that result from the simulation include errors associated with the intensity of the pixel being represented by a single ray trace instead of a cross section as seen with a detector. This may lead to partial volume effects whereby very small features (<2 µm) may not be identified, for the purpose of the 4 mm diameter holes seen in the work it is not a problem.

5.8 Chapter Summary

This chapter is focussed entirely on the simulation of X-ray images which are then reconstructed to create a 3D volume. The simulation was adapted to include some factors that were discussed in Chapter 3 and Chapter 4, including orientation of the object during imaging, the path length of the X-rays through the object and the position of the feature of interest with respect to the centre of rotation.

A simple simulation was originally tested to determine the influence of the issues discussed in Chapter 3 on the dimensions of a sphere. Errors of ±20 µm were noted so it was decided to build a more complex simulation in MATLAB to simulate the NPL system along with other factors that were seen in Chapter 4 which were believed to cause errors.

The simulation was based on tracing a line from a point source to the centre of each pixel. The points of intersection between the line and the holeplate were calculated and then used to determine the path length and subsequent attenuation of the X-rays for a polychromatic X-ray. Meshes were used originally to represent the holeplates but this led to systematic errors so were changed to primitive shapes.

When replicating conditions found in Chapter 3 by applying gradients to individual images, results indicate that errors, if present, depend on the direction of the gradient. Errors of <5 µm were seen in the geometry.

Simulations of the simple holeplates, HP1 and HP3 indicate the same systematic trends as seen for the experimental data, the only difference is the magnitude of the errors which are <10 µm. For the complex holeplate, the trends are again the same as the experimental results and have the same magnitude (±10 µm). These errors in deviation have a negative correlation with the effective energy.

When comparing the simulation results with the experimental results, when the orientation of the object during imaging varies, it can be seen that the same systematic trends in data can be seen with errors of <17 µm being present.

As discussed in Chapter 4 the intensity of the X-rays as they travel further away from the source decrease with respect to the inverse square law. To test this a simulation was run where the holeplate was placed away from the centre of rotation. On the edge with the most extreme distances relative to the source, errors in the geometry of <16 µm were found.

When simulating CiHP, where the path lengths are all equal, errors of up to 6 µm were seen at the quadrants, these were also seen in a monoenergetic simulation of HP3. This indicates an artefact, the cause of which is unknown at this time.

Chapter 6: Conclusions and further work

This research was sponsored by the Engineering and Physical Sciences Research Council (EPSRC) and the National Physical Laboratory (NPL) and was motivated by NPL's contribution to the international effort to establish traceability of dimensional measurements acquired with X-ray computed tomography (XCT).

Work carried out by the author for an MRes highlighted fundamental issues in XCT imaging that needed to be further understood, these included the systematic errors associated with the orientation of the object during imaging and a gradient in the greyscale values of the 2D projections, resulting in an incorrect surface threshold being defined. This led to an investigation in this EngD into the spectral and temporal variation of the X-ray flux in the NPL XCT system, this involved measuring the X-ray intensity with an ionisation chamber and the dose across the cone beam. It was found that after the initial warming up period, the X-ray intensity remained fairly stable at voltages less than 200 kV. The dose across the cone beam exhibited a bulls-eye shape which was not centred on the detector. This led to a gradient in intensity being present across the detector.

Concurrently, the use of a complex aluminium holeplate was being considered as a reference object for ISO10360-11 as a similar test object is used for traceability of coordinate measuring machines. It was therefore decided to image a similar holeplate with a size of 48 mm x 48 mm x 8 mm. It contained 28 holes, all of which had a nominal diameter of 4 mm. Systematic errors in unidirectional and bidirectional length measurements were found, <10 µm and ±50 µm respectively. Further investigation into these errors followed, looking particularly at the geometry of the individual holes within the holeplate. These errors in geometry became the main focus of the research.

The complex deformation signatures found in the geometry of the holes led to the design and construction of four simple holeplates, all of which were of the same size as the original holeplate but only contained one hole. These holeplates illustrated systematic deviations in geometry that appears to be related not only to the position of the hole in the holeplate (±40 µm), but to the orientation of the holeplate during the image acquisition process (<60 µm).

To determine the cause and to study these errors further, numerical simulations were carried out to produce 2D projection images of the holeplates. These simulated images, when reconstructed into a volume, demonstrated the same trends in hole deformation

as the experimental data, although for the simple holeplates the magnitude of the errors was smaller (<10 µm).

Many examples of test objects used to identify the cause of errors along with the magnitude of the errors in question can be seen in Section 2.8. A few, relevant references are listed here and all indicate errors in the same region as those seen in this thesis. Kasperl et al., (2014) carried out simulations of a similar complex holeplate and found probing errors of between 55 µm and 85 µm. Bartscher et al., (2014) have also imaged a similar holeplate and found length measurement errors in the range of ±11 µm. Using step gauges, errors of <7 µm were found in 2 mm length measurements by Angel et al., (2015). Sphere centre to centre distance errors of ±30 µm were found by Müller et al., (2012) when imaging ruby spheres of 5 mm diameter. The use of a test object is widely practised in the field to establish the cause of errors and to identify ways of minimising them.

6.1 Contributions to knowledge

With the use of experimental and simulated data, the cause of errors in the geometry of a series of holeplates has been partly identified, allowing the errors to be reduced below the MPE of the system (9 + L/50) µm where L is in mm, the evidence of which can be seen below.

In Chapter 3, a series of experiments was carried out to investigate the stability of the X-ray flux over the time it takes to image an object (50 minutes) and across the cone beam itself. Results indicated that there was a drift in the intensity of approximately 2% over time, variation in intensity of 10% was also found across the detector. The measurement of the dose indicated a bullseye pattern, this is to be expected as the X-rays travel out from a point source in a spherical nature, however, the peak in intensity was not found in the centre of the image as expected. The dose across the detector was found to have a gradient of 20% as well. A comparison of the measured spectrum and a simulated spectrum indicated that the X-rays appear to be filtered before reaching the sample, this therefore would reduce the amount of beam hardening in the object being imaged. This could be due to the X-rays passing through the X-ray gun housing which is discussed further in Section 3.3.2.

Chapter 4 focussed on the imaging and measurement of a complex holeplate and four simple holeplates, all of which were 48 mm x 48 mm x 8 mm in size and made of aluminium. A selection of factors influencing the geometry of the hole (diameter of 4 mm) within the holeplates were considered including; orientation and stability of the holeplate

during imaging, position of the hole within the holeplate and magnification used in the set up.

Bidirectional and unidirectional lengths, along with reconstructed cylinder radii were measured for the complex holeplate (CompHP). Results for the bidirectional lengths and cylinder radii demonstrated discrepancies in accuracy and precision from measurements acquired with a coordinate measuring machine. These discrepancies were related to the orientation of the holeplate during imaging. For example, when the holeplate was at 0° to horizontal the radii were <17 µm too small and <15 µm too large when the holeplate was at 90°. There were also similar trends in the bidirectional lengths. To investigate this further, the geometry of the individual holes was studied, the trends of which appear to systematically change for each hole. Below in Figure 6.2 and Figure 6.3 some sample data can be seen which highlights the typical trends seen in the geometry of the holes.

To study these complex trends further, three simple square holeplates (HP1, HP3 and HP5, see Figure 6.1) were manufactured, all of which only had one hole in them. The position of the hole was different for each plate but the position of the hole corresponded to one that was also found in CompHP. The amount of material around each hole in CompHP was very imbalanced, to simplify this imbalance and to make it as extreme as possible, the holes in the simple holeplates were positioned in a corner, in the centre and at the edge of the different holeplates.

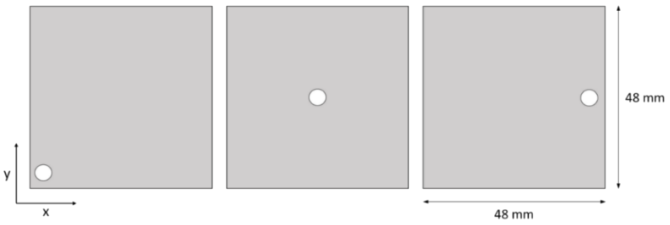

Figure 6.1 Schematic of simple holeplates, HP1, HP3 and HP5 from left to right

Systematic trends in the deviation of the geometry varied for each holeplate, as seen in Figure 6.2, indicating that the position of the hole within the holeplate is crucial to the accuracy of the results. HP1 and HP5 exhibit asymmetrical deformation around the circumference of the hole. Errors bars, representing 1 sigma or the standard deviations of the cylinder fit point deviations for each 5° interval, are different for each data set, 5 µm (HP1), 10 µm (HP5) and 15 µm (HP3). Since the observed deviations are greater than the error bars, all trends are significant.

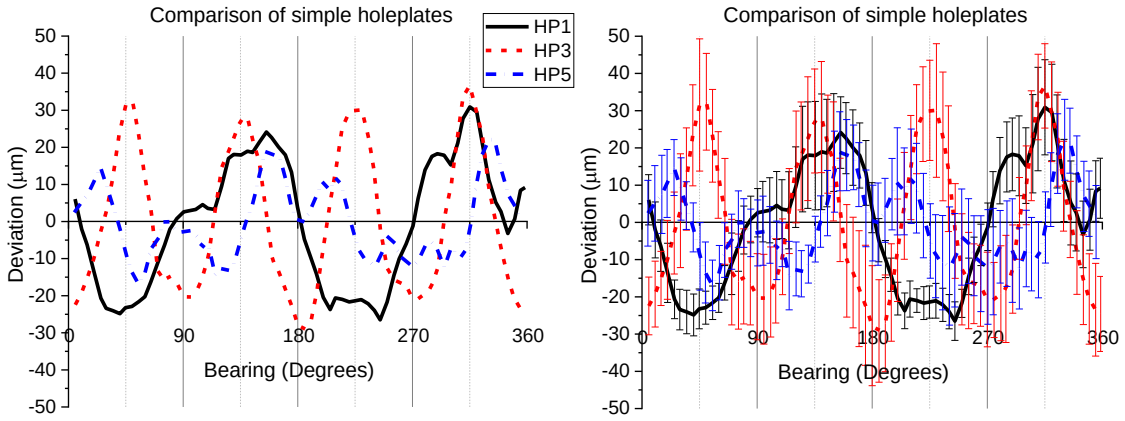

Figure 6.2 Comparison of simple holeplates experimentally imaged at 0° (with and without error bars)

To investigate the trends observed with the change in orientation a circular holeplate (CiHP) was manufactured to eliminate any effects of the path length of the X-rays varying. CiHP had a single, 4 mm diameter, hole in the centre but was still 48 mm wide like the other holeplates. It was imaged at 0°, 45° and 90° to horizontal. Errors between -20 µm and +60 µm were found when the holeplate was imaged at 45°, see Figure 6.3. In this case the error bars indicate that only the trends seen at an orientation of 45° and 90° are significant as they are larger than the error bars. However, for an orientation of 90° this is only the case for the deformation seen at a bearing of 0° and 180°.

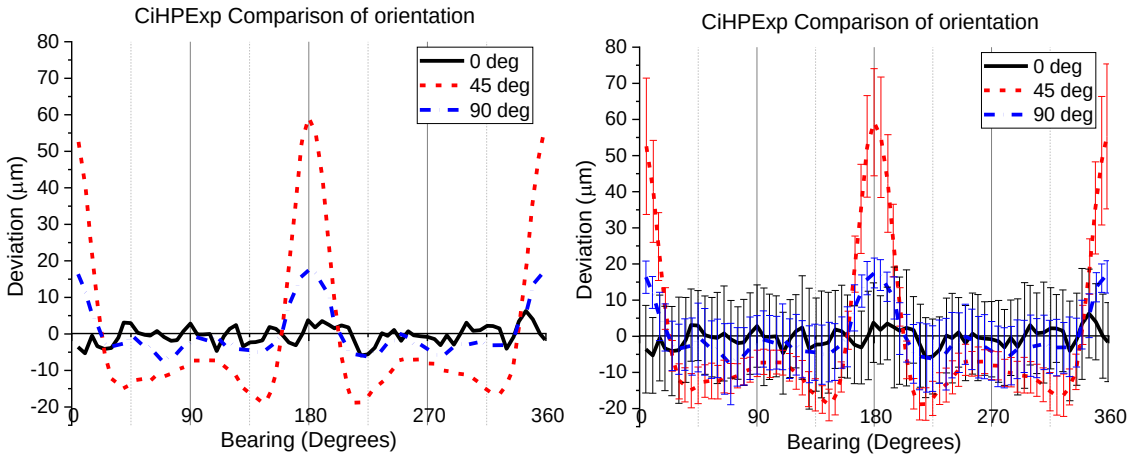

Figure 6.3 Comparison of CiHPExp imaged at different orientations (with and without error bars)

A comparison between HP3 and CiHP imaged at 0° indicated that the path length of the X-rays through the material affected deviations. Errors in the geometry of ±30 µm were found, see Figure 4.29 in Section 4.3.4.1.

Fixing the holeplates in a purpose built stand to ensure stability and repeatability during imaging reduced systematic deviations from 44 µm to 37 µm. The main factor associated

with this, however, was the reduction in the standard deviation of the fit points' deviations which decreased from 60 µm to 10 µm, see Figure 4.26 in Section 4.3.2. This experiment showed an improvement in the results and highlights the importance of the use of a purpose built holder to ensure stability of the object during imaging. With this holder, results are improved and it ensures repeatability and the driving down of errors seen previously. This test would prove useful to a user who is achieving results at the limit of their system's capability, fixing the object in the centre of the image ensures repeatability and an assurance of the results.

An experiment on the effects of varying magnification indicated that, although the trends remain the same, the magnitude of the errors in deviations from a perfect cylinder are smaller, see Figure 4.50 in Section 4.3.9. Two magnifications were used, x1.6 and x5, which were the minimum and maximum magnifications that could be used with the system. Errors were in the range of ±30 µm and ±10 µm for each magnification, x1.6 and x5 respectively. This is approximately a quarter of the voxel size in both cases. This change in magnitude does not contribute to the geometric deformation, only the size of the error. For the user, this demonstrates that the correct magnification should be chosen depending on the features being imaged.

Chapter 5 is based on numerical simulations. 2D X-ray images of the holeplates were simulated in MATLAB using a ray-tracing method. The geometry of the holeplates was represented with the use of primitive shapes such as planes and cylinders. The discrepancies in the flux both spatially and temporally that were highlighted in Chapter 3 were replicated in the simulated images. Systematic errors of <5 µm were seen in the geometry of the cylinder. The shape of the systematic distortion depended on the direction in which the gradient in the intensity was applied to the images, see graphs in Section 5.3.1.

When images of HP1 were simulated the resulting deviations in the fit points had the same trend as the experimental data, however, the magnitudes were up to 17 µm smaller for the simulated volume. The simulation of HP3 showed a different trend that was opposite to the experimental data and had errors that were approximately 30 µm smaller.

The simulations of CompHP demonstrated the same shape deviations as the experimental data and the errors were also of the same magnitude (<30 µm when the holeplate is fixed in the custom made stand), see graphs in Section 5.4.3.

When the holeplate is orientated at different angles the simulation data has the same trend as the experimental data but the magnitudes of the greatest errors are

approximately a quarter of the size, 60 µm for experimental, versus 15 µm for the simulated.

Simulated images of CiHP positioned away from the centre of rotation highlighted fit point errors of 15 µm on the outside edge that is closest to both the source and the detector as it is rotated during imaging (see Section 5.4.6). This is an indication that the errors seen for HP1 and HP5, are partly due to the holes being away from the centre of rotation. This illustrates that the intensity of the 2D images and subsequently the geometry of the reconstructed volume is impacted by the fact that the X-ray intensity varies with respect to the distance from the source. It also indicates that if the object is near the edge of the image errors could occur.

Chapters 4 and 5 illustrated that the main sources of errors in XCT metrology are the orientation of the object during imaging, in this case the worst errors (<60 µm) were found at an orientation of 45°. Another major factor associated with the geometry error was the position of the hole within the holeplate which is in turn relates to the path length of the X-rays and the effective energy of the X-rays when they reach the detector.

6.2 Novelty

Exploratory tests on the holeplate, measuring unidirectional and bidirectional lengths and the radii of the cylinders led this thesis to focus on the geometry or shape of the holes within the holeplate and the factors that caused the deformation. This resulted in several novel outcomes.

Five factors which affect the geometry of a hole within a holeplate were studied. These are, in order of impact: orientation, path length of X-rays, position of hole in holeplate, fixing of holeplate during imaging and gradient in 2D projections caused by X-ray flux variations.

Although the length measurements within the holeplate had been studied before by other authors, for example Kasperl et al., (2014) and it had been noted that the cylinders had some deviation in geometry, no other studies have investigated the trends in geometry for the different holes in such detail. The apparent distortion in the geometry of a perfect cylinder is crucial for the manufacturing industry when they are using XCT for non-destructive testing. A manufactured part could potentially be discarded as they appear to be deformed when this is not in fact the case.

The method to calculate the bearing of the fit points around the cylinder was a novel method based on the author's land surveying background. These bearings were then used to average the fit point deviations for every 5° interval around the circumference.

This in-depth study of the data using this averaging method was also novel, previous work by other authors had only worked with all of the fit points and used a qualitative approach.

The simple holeplates that were designed and manufactured during this study are the first of their kind. They allowed investigation into the systematic but complex trends in the hole's geometry seen in the complex holeplate. The simple holeplates are easier and cheaper to manufacture and therefore may offer an alternative to the complex holeplate when studying geometrical errors relating to orientation and position of a feature. The idea behind the simple holeplates is easily transferrable to other shapes and materials and could potentially be used to calculate errors found in the geometry of complex shapes.

The numerical simulation of the 2D images started with a basic ray tracing technique and evolved to accommodate the use of polychromatic X-rays. It originally used meshes to represent the holeplates but was developed to use primitive shapes which allowed for increased accuracy in the path length calculations. The principles behind the simulation code allow it to be adapted to accommodate changes in source position, detector position and alignment as well as different X-ray spectrums. This would allow further issues to be studied in depth.

The simulation allows certain factors to be taken into account, i.e. orientation of the object whilst eliminating others, e.g. polychromatic X-rays, allowing the errors for each factor to be calculated and corrected for. For example, an object is simulated at 0° and at 45°, the difference between the two could be found and this value then subtracted from the experimental data thereby correcting for the effects of orientation. Any errors seen after this correction are from other errors, such as position of object with respect to the centre of the rotation or another error that is still unaccounted for, these include scatter and an imperfect mechanical set up of a system.

This thesis has shown that although holeplates are not the ideal test object to use for acceptance and verification of XCT systems, due to the errors in the hole geometry, they provide a simple object, made of a uniform material that can be easily characterised and calibrated. Similar objects are used in the verification of coordinate measuring machines, therefore the principles and procedures are already in place making the holeplate a desirable test object. This series of tests, although individually simple, can be combined to form a larger picture to the issues surrounding dimensional metrology and XCT.

Due to the nature of X-rays there will always be some variation in the intensity of X-rays. This variation in intensity is due to the fact that the production of X-rays is a random

process and depends on the number of photons that leave the source. However, as far as the author is aware, no previous work has been carried out to determine the effects this would have on the measured dimensions and geometry of an object being imaged. Measurement of the X-ray intensity was carried out with the help of the medical physics department at NPL and used instruments usually employed to calibrate medical devices. New methods had to be developed to create a measurement strategy that would work with an industrial XCT system, capturing data not usually recorded.

With the use of a numerical simulation these intensity variations were applied to images and results showed that the direction of the gradient in the image systematically affects the shape of the geometry. At this stage the errors are small (<4 µm) and below the MPE of the system, but with the driving down of other errors, such as those discussed in this thesis, the errors due to flux variation may start to become crucial with respect to traceability of measurements. Although this thesis only looked at the effects on simple objects (sphere and cylinder), it highlights that the problem exists and should be studied further.

Lessons learnt from the simulation include the fact that the orientation of the object and X-ray path length are crucial. In the case of the simple holeplates the deformation seen in the geometry of the holes was of a lower magnitude (±10 µm) than the experimental data (±35 µm), this is believed to be due to scatter not being included in the simulation.

Overall the highest accuracy and precision of dimensional measurements acquired with XCT can be found if the amount of material around the feature being measured is of equal thickness. The object must also be imaged horizontally at 0°. The feature being measured must be in the centre of rotation and fixed securely in position. If these conditions are met the accuracy of the shape of a 4 mm radius cylinder is ±6 µm. Repeated measurements indicate that the precision is 5.5 µm.

In XCT metrology the main error sources are the object being imaged at an orientation other than horizontal, with maximum errors in shape of 60 µm seen when the holeplate was imaged at 45° to horizontal. A non-uniform path length of the X-rays around the feature being measured also has a major impact with errors of ±30 µm seen in the geometry of cylinder of 4 mm. A more detailed outline of error sources can be seen in Table 4.5

6.3 Link to International Standard and recommendations

ISO10360 is an international standard that details the acceptance and reverification tests for coordinate measuring systems. The part known as ISO10360-11 would be solely

dedicated to coordinate measuring machines that use the principle of X-ray computed tomography and is still being revised. It will provide users with a confidence in the results that are being acquired, along with giving designers the ability to propose smaller and more intricate structures in the knowledge that they can be accurately measured to a specific design requirement.

As previously discussed in Section 2.8.1, the complex holeplate is being considered as a reference object for the standard ISO10360-11. The standard will use many measurements, e.g. probing size error and circle probing form error. Cylinder probing form error and bidirectional lengths are also included in the standard; these measurements will be particularly susceptible to the apparent deformation in the reconstructed hole's geometry. However, as has been proven in this thesis, due the systematic nature of some of the errors (such as deformation depending on the position of the hole) the errors could be accounted for and corrected.

This thesis also highlights the systematic errors in the geometry of the holes that is associated with the orientation of the holeplate during imaging. The optimum orientation at which the holeplate should be imaged at would have to be included in the standard. It could possibly be recommended that the holeplate is imaged in multiple orientations to determine the average deviation in geometry.

This research is important as it highlights that ISO test results need to be robust to the systematic variations seen in this thesis. For example, large deformations may be apparent on a given part of a cylinder but if a bidirectional length is taken from a point on the circumference of the cylinder that has little deformation the results will be biased. If the errors could not be corrected for, it is then important to take a large enough array of results to encompass all of the varying magnitudes of the errors.

The use of simple holeplates in the standard could simplify results as it provides a simpler process when simulating results along with being able carry out more fundamental tests without having to measure multiple holes. The simple holeplates would allow for a straightforward indication of the quality of results for a given system. As stated previously the simple holeplates are much cheaper to manufacture and could be offered as an alternative to XCT users who perhaps do not require a definite statement of accuracy for their system but would like an estimate as to how their system is performing.

A report outlining recommendations when using the holeplate has been written by the author to be submitted to the committee, it can be seen in Appendix 8.

An alternative to a holeplate would be a free form shape that incorporates internal feature that are orientated at multiple angles, for example, an internal tube that snakes its way through an object. With the tube moving around inside the object the thickness of the material and therefore the path lengths of the X-rays would be varying along with the orientation of the tube. It should be remembered, though, that a more complex object would be difficult to calibrate and reference measurements would be hard to obtain. This again highlights the important position that simple holeplates have within the verification process.

Recommendations for XCT metrology would include, if an object has features at multiple orientations, to be aware that the orientation would affect the geometry of the feature. The object should potentially be umaged multiple times at different orientations to obtain accurate results. Another recommendation would be to position the feature being measured in the centre of rotation, this would reduce the errors associated with the change in intensity of the X-rays due to the inverse square law as seen in Sections 4.3.6.1 and 5.4.6. The issues relating to the varying path lengths of the X-rays is harder to rectify as the shape of the object cannot be changed, however, the user should be aware of the issues and image the object in an orientation that limits the extremes in path lengths.

6.4 Further work

This thesis has highlighted the cause of many errors that affect the geometry of a reconstructed object. Starting with systematic errors in the order of ±60 µm, this work has highlighted the causes of the errors so that errors of only of ±4 µm are seen, i.e. if the object is imaged at 0° and has a constant amount of material around the feature being measured. The focus of the further work suggested for this thesis is the continuation of identifying the cause of other, smaller errors observed in this thesis, thereby continuing the work of reducing the discrepancies between the simulated and experimental data. If the simulations can replicate the results seen in experimental data more accurately, then it can be used in a correction.

The most critical error, which is the error seen when the object is simulated at an orientation of 45° and 90°, show identical trends to those seen in the experimental data, however, the simulated data has smaller magnitudes, <60 µm versus <15 µm. An area that needs inclusion in the simulation is the simulation of scatter, both within the XCT cabinet and the object itself, to ascertain if this reduces the discrepancies seen between the experimental and simulated data.

As mentioned in Section 2.2.4 the use of a collimated fan beam system can reduce the amount of scatter collected on the detector, with this in mind the holeplates could be imaged on a fan beam system and the geometry and size of deformation could be studied.

Work seen in Sections 4.3.4.2 and 5.4.2.1 indicated that the effective energy of the X-rays plays a crucial part in the deformation of the reconstructed hole's geometry. In most cases, as the effective energy increases the deviations becomes more negative, i.e. the surface moves towards the centre of the cylinder. If the X-ray spectrum could be measured for each pixel as the images are being acquired and previous knowledge of form of the object was taken into account, the effects due to the effective energy changes could be corrected for.

Another error which remains unsolved is that seen in the simulated circular holeplate imaged at an orientation of 0°. In this instance errors of ±5 µm at a bearing of 0°, 90°, 180° and 270° are seen, similar results are also seen for HP3Sim. Further work is needed to characterise these errors; they can then be used in a correction. This would then allow a potential decrease in the MPE of a system. The errors are seen in volumes reconstructed from images acquired with both polychromatic and monochromatic X-rays indicating that the errors are associated with the reconstruction process and not the interaction of X-rays with the material.

Although the variation of the X-ray flux was investigated with the simulation of images of a cylinder it would be important to apply the same gradients to images of the holeplates. The errors associated with a more complex object could then be determined, this would allow discussion of the impact of the variations in an industrial situation.

Building on the user survey a set of simple holeplates could be distributed to industry to gauge if variations seen in this thesis are found in the growing number of XCT systems found in industry.

References and bibliography

Affenzeller, C., Gusenbauer, C., Reiter, M. & Kastner, J. (2015) Measurement uncertainty evaluation of an X-ray computed tomography system. In: *Digital Industrial Radiology and Computed Tomography*. 2015 Ghent. pp. 22–25.

Agostinelli, S., Allison, J., Amako, K., Apostolakis, J., et al. (2003) GEANT4 - A simulation toolkit. *Nuclear Instruments and Methods in Physics Research, Section A: Accelerators, Spectrometers, Detectors and Associated Equipment*. [Online] 506 (3), 250–303. Available from: doi:10.1016/S0168-9002(03)01368-8.

Allisy-Roberts, P. & Williams, J. (2008) *Farr's Physics for Medical Imaging*. 2nd edition. Edinburgh, Elsevier.

American Society for Testing and Materials (2014) *ASTM E1441-11: Standard Guide for Computed Tomography (CT) Imaging*. [Online]. Available from: doi:10.1520/E1441-11.

Ametek (2017) *X-123CdTe Complete X-Ray & Gamma Ray Spectrometer*. [Online]. 2017. Available from: https://amptek.com/products/x-123-cdte-complete-x-ray-gamma-ray-spectrometer-with-cdte-detector/#6 [Accessed: 19 March 2018].

Angel, J., De Chiffre, L., Kruth, J.-P., Tan, Y., et al. (2015) Performance evaluation of CT measurements made on step gauges using statistical methodologies. *CIRP Journal of Manufacturing Science and Technology*. [Online] 11, 68–72. Available from: doi:10.1016/j.cirpj.2015.08.002.

Araujo, G.P., Oliveira, A.H., Carneiro, A.C., Carneiro, C.J.G., et al. (2011) Fluctuations on the x-ray intensity beam using a portable x-ray probe based on 6 Lii(Eu) crystal. In: *International Nuclear Atlantic Conference*. 2011 Brazil. p. 6.

Baek, J., De Man, B., Harrison, D. & Pelc, N.J. (2015) Raw data normalization for a multi source inverse geometry CT system. *Optics Express*. [Online] 23 (6), 7514. Available from: doi:10.1364/OE.23.007514.

Barrett, J.F. & Keat, N. (2004) Artifacts in CT: recognition and avoidance. *Radiographics : a review publication of the Radiological Society of North America, Inc*. [Online] 24 (6), 1679–1691. Available from: doi:10.1148/rg.246045065.

Bartscher, M., Illemann, J. & Neuschaefer-Rube, U. (2016) ISO test survey on material influence in dimensional computed tomography. *Case Studies in Nondestructive Testing and Evaluation*. [Online] 6, 79–92. Available from:

doi:10.1016/j.csndt.2016.04.001.

Bartscher, M., Sato, O., Härtig, F. & Neuschaefer-Rube, U. (2014) Current state of standardization in the field of dimensional computed tomography. *Measurement Science and Technology*. [Online] 25 (6), 064013. Available from: doi:10.1088/0957-0233/25/6/064013.

Becares, V. & Blazquez, J. (2012) Detector dead time determination and optimal counting rate for a detector near a spallation source or a subcritical multiplying system. *Science and Technology of Nuclear Installations*. [Online] 2012. Available from: doi:10.1155/2012/240693.

Bellon, C., Deresch, A., Gollwitzer, C. & Jaenisch, G.-R. (2012) Radiographic Simulator aRTist: Version 2. In: *Proc. of 18th World Conference on Nondestructive Testing*. 2012 Durban, South Africa. pp. 16–20.

Boas, F.E. & Fleischmann, D. (2012) CT artifacts: causes and reduction techniques. *Imaging in Medicine*. [Online] 4 (2), 229–240. Available from: doi:10.2217/iim.12.13.

Braun, H., Kyriakou, Y., Kachelriess, M. & Kalender, W.A. (2010) The influence of the heel effect in cone-beam computed tomography: artifacts in standard and novel geometries and their correction. *Physics in medicine and biology*. [Online] 55, 6005–6021. Available from: doi:10.1088/0031-9155/55/19/024.

Britannica Academic (2018) *Sound*. [Online]. 2018. Britannica Academic. Available from: http://academic.eb.com/levels/collegiate/article/sound/109557#63975.toc [Accessed: 19 January 2018].

British Standards Institution (2011) *BS EN 16016-3:2011 Non destructive testing — Radiation methods — Computed Tomography Part 3 : Operation and interpretation*.

British Standards Institution (2010) *BS EN ISO 286-1:2010 Geometrical product specifications (GPS) - ISO code system for tolerances on linear sizes*.

Brunke, O. (2012) Fully-Automated 3D Metrology and Defect Analysis with High-Resolution 300 kV Microfocus Computed Tomography. In: *18th World Conference on Non destructive testing*. 2012 Durban, South Africa. pp. 16–20.

Buzug, T.M. (2010) *Computed Tomography From Photon Statistics to Modern Cone-Beam CT*. 1st edition. Heidelberg, Springer-Verlag.

Cantatore, A. & Müller, P. (2011) *Introduction to computed tomography*. DTU Mechanical Engineering, Kgs. Lyngby.

Carmignato, S. (2012) Accuracy of industrial computed tomography measurements: Experimental results from an international comparison. *CIRP Annals - Manufacturing Technology*. [Online] 61 (1), 491–494. Available from: doi:10.1016/j.cirp.2012.03.021.

Carmignato, S., Dreossi, D., Mancini, L., Marinello, F., et al. (2009) Testing of x-ray microtomography systems using a traceable geometrical standard. *Measurement Science and Technology*. [Online] 20 (8), 084021. Available from: doi:10.1088/0957-0233/20/8/084021.

Cheng, C.C., Ching, Y.T., Ko, P.H. & Hwu, Y. (2018) Correction of center of rotation and projection angle in synchrotron X-ray computed tomography. *Scientific Reports*. [Online] 8 (1), 1–9. Available from: doi:10.1038/s41598-018-28149-8.

Cherry, S.., Sorenson, J.A. & Phelps, M.E. (2012) *Physics in Nuclear Medicine*. 4th edition. Philadelphia, Elsevier Saunders.

De Chiffre, L., Carmignato, S., Kruth, J.-P., Schmitt, R., et al. (2014) Industrial applications of computed tomography. *CIRP Annals - Manufacturing Technology*. [Online] 63 (2), 655–677. Available from: doi:10.1016/j.cirp.2014.05.011.

Corcoran, H.C. (2014) *MRes dissertation: A study into the effects on XCT dimensional measurements*. University College London.

Corcoran, H.C., Brown, S.B., Robson, S., Speller, R.D., et al. (2016) Observations on the performance of X-Ray computed tomography for dimensional metrology. In: *International Archives of the Photogrammetry, Remote Sensing and Spatial Information Sciences - ISPRS Archives*. [Online]. 2016 p. Available from: doi:10.5194/isprsarchives-XLI-B5-25-2016.

Cuadra, J.A., Divin, C. & Panas, R.M. (2017) Uncertainty Quantification of an X-ray Computed Tomography System. In: *Dimensional Accuracy and Surface Finish in Additive Manufacturing*. 2017 Leuven, Belgium. pp. 1–4.

Dössel, O. & Schlegel, W.C. (2009) *World Congress on Medical Physics and Biomedical Engineering*. Olaf Dössel & Wolfgang C Schlegel (eds.). Munich, Germany, Springer Science & Business Media, 2010.

Evans, R.D. (1955) *The Atomic Nucleus*. 1st edition. New York, Tata McGraw-Hill.

Excillum (2015) *Metal jet anode*. [Online]. 2015. Available from: http://www.excillum.com/technology.html [Accessed: 4 December 2015].

Feldkamp, L.A., Davis, L.C. & Kress, J.W. (1984) Practical cone-beam algorithm. *Journal of the Optical Society of America A*. [Online] 1 (6), 612. Available from: doi:10.1364/JOSAA.1.000612.

Ferrucci, M., Leach, R.K., Giusca, C.L., Dewulf, W., et al. (2015) Towards geometrical calibration of X-ray computed tomography systems - A review. *Measurement Science and Technology*. [Online] 26, 30. Available from: doi:10.1088/0957-0233/26/9/092003.

Flay, N. (2016) *An investigation of the factors associated with the x-ray tube and their influence on dimensional measurement in micro-focus cone-beam industrial x-ray computed tomography systems*. University of Southampton.

Flay, N., Sun, W., Brown, S.B., Leach, R.K., et al. (2015) Investigation of the Focal Spot Drift in Industrial Cone-beam X-ray Computed Tomography. In: *Digital Industrial Radiology and Computed Tomography*. 2015 Ghent. pp. 22–25.

Fosbinder, R. & Orth, D. (2011) *Essentials of Radiologic Science*. Lippincott Williams & Wilkins.

Fritz, S.L. & Livingston, W.H. (2009) A comparison of computed and measured heel effect for various target angles. *Medical physics*. [Online] 9 (1982), 216–219. Available from: doi:10.1118/1.595074.

GE Measurement and Control (2013) *speed|scan CT 64 Brochure*. (October 2013).

Hermanek, P. & Carmignato, S. (2017) Porosity measurements by X-ray computed tomography: Accuracy evaluation using a calibrated object. *Precision Engineering*. [Online] 49, 377–387. Available from: doi:10.1016/j.precisioneng.2017.03.007.

Hermanek, P., Oliveira, F.B. De, Carmignato, S. & Bartscher, M. (2017) Experimental investigation of new multi-material gap reference standard for testing computed tomography systems. In: *7th Conference on Industrial Computed Tomography*. 2017 Leuven, Belgium. pp. 1–10.

Hiller, J., Kasperl, S., Schön, T., Schröpfer, S., et al. (2010) Comparison of Probing Error in Dimensional Measurement by Means of 3D Computed Tomography with Circular and Helical Sampling. In: *2nd International Symposium on NDT in Aerospace*. 2010 Hamburg. pp. 1–7.

Hiller, J. & Reindl, L.M. (2012) A computer simulation platform for the estimation of measurement uncertainties in dimensional X-ray computed tomography.

Measurement: Journal of the International Measurement Confederation. [Online] 45 (8), 2166–2182. Available from: doi:10.1016/j.measurement.2012.05.030.

Hsieh, J., Nett, B., Yu, Z., Sauer, K., et al. (2013) Recent Advances in CT Image Reconstruction. *Current Radiology Reports*. [Online] 1 (1), 39–51. Available from: doi:10.1007/s40134-012-0003-7.

International Organization for Standardization (1993) *International Vocabulary of Basic and General Terms in Metrology*.

International Organization for Standardization (2012) *ISO 1101:2012(E) Geometrical product specifications (GPS) — Geometrical tolerancing — Tolerances of form, orientation, location and run-out*.

International Organization for Standardization (2002) *ISO 15708-2 Non-destructive testing - Radiation Methods - Computed Tomography Part 2: Examination practices*.

Johns, H.E. & Cunningham, J.R. (1983) *The Physics of Radiology*. 4th edition. Springfield, Charles C Thomas.

Kalender, W.A. (2011) *Computed Tomography: Fundamentals, System Technology, Image Quality, Applications*. 3rd edition. Erlanger, Publicis Publishing.

Kalender, W.A. & Kyriakou, Y. (2007) Flat-detector computed tomography (FD-CT). *European Radiology*. [Online] 17, 2767–2779. Available from: doi:10.1007/s00330-007-0651-9.

Kasperl, S., Bauscher, I., Hassler, U., Markert, H., et al. (2002) Reducing artefacts in industrial 3D computed tomography (CT). In: *Vision, Modeling, and Visualization*. 2002 Erlangen. pp. 51–57.

Kasperl, S., Franz, M. & Karl, M. (2013) Fully Automatic Analysis of Standard CT Characteristics by means of Simulation. In: *ICTMS*. 2013 Ghent, Belgium. pp. 321–324.

Kasperl, S., Schielein, R., Sukowski, F., Hornberger, P., et al. (2014) CT simulation study to demonstrate material impact using hole plates. In: *European Conference on Non-Destructive Testing (ECNDT)*. 2014 Prague, Czech Republic. pp. 1–10.

Kiekens, Frank, W., Tan, Y., Bleys, P., et al. (2010) A test object for calibration and accuracy assessment in X-ray CT metrology. In: *10th International Symposium on Measurement and Quality Control*. 2010 Osaka. pp. 5–8.

Kiekens, K., Welkenhuyzen, F., Tan, Y., Bleys, P., et al. (2011) A test object with parallel

grooves for calibration and accuracy assessment of industrial computed tomography (CT) metrology. *Measurement Science and Technology*. [Online] 22 (11), 115502. Available from: doi:10.1088/0957-0233/22/11/115502.

Knoll, G.F. (2010) *Radiation Detection and Measurement*. 4th edition. Hoboken, John Wiley and Sons.

Kraemer, A., Stolfi, A., Schneider, T., Chiffre, L. De, et al. (2017) Traceability investigation in Computed Tomography using industry-inspired workpieces Traceability investigation in Computed Tomography using industry - inspired workpieces. In: *7th Conference on Industrial Computed Tomography*. 2017 Leuven, Belgium. pp. 1–9.

Kruth, J.-P., Bartscher, M., Carmignato, S., Schmitt, R., et al. (2011) Computed tomography for dimensional metrology. *CIRP Annals - Manufacturing Technology*. [Online] 60 (2), 821–842. Available from: doi:10.1016/j.cirp.2011.05.006.

Legland, D. (2009) *geom3D*. [Online]. 2009. Matlab File Exchange. Available from: http://uk.mathworks.com/matlabcentral/fileexchange/24484-geom3d [Accessed: 2 March 2017].

Léonard, F., Brown, S.B., Withers, P.J., Mummery, P.M., et al. (2014) A new method of performance verification for x-ray computed tomography measurements. *Measurement Science and Technology*. [Online] 25 (6), 065401. Available from: doi:10.1088/0957-0233/25/6/065401.

Lifton, J.J. (2017) The influence of scatter and beam hardening in X-ray computed tomography for dimensional metrology. *Measurement Science and Technology*. [Online] 28, 229. Available from: doi:10.3233/XST-140471.

Lifton, J.J., Malcolm, A.A. & Mcbride, J.W. (2013) The Application of Beam Hardening Correction for Industrial X-ray Computed Tomography. In: *5th International Symposium on NDT in Aerospace*. 2013 Singapore. p.

Lyra, M., Ploussi, A., Rouchota, M. & Synefia, S. (2014) Filters in 2D and 3D cardiac SPECT image processing. *Cardiology Research and Practice*. [Online] 2014, 11. Available from: doi:10.1155/2014/963264.

Maire, E. & Withers, P.J. (2014) Quantitative X-ray tomography. *International Materials Reviews*. [Online] 59 (1), 1–43. Available from: doi:10.1179/1743280413Y.0000000023.

Menefee, J., Cho, Y. & Swinehart, C. (1967) Sodium activated Cesium Iodide as a gamma ray and charged particle detector. *IEEE Transactions on Nuclear Science*. [Online] 14 (1), 464–467. Available from: doi:10.1109/TNS.2000.856533.

Muders, J., Hesser, J., Lachner, A. & Reinhart, C. (2011) Accuracy evaluation and exploration of measurement uncertainty for exact helical cone beam reconstruction using katsevich filtered backprojection in comparison to circular Feldkamp reconstruction with respect to industrial CT metrology. In: *International Symposium on Digital Industrial Radiology and Computed Tomography*. 2011 Berlin, Germany. pp. 1–8.

Müller, P., Hiller, J., Cantatore, A., Bartscher, M., et al. (2012) Investigation on the influence of image quality in X - ray CT metrology. In: *Conference on Industrial Computed Tomography*. 2012 Wels. pp. 1–10.

Nardelli, V.C., Arenhart, F.A., Donatelli, G.D., Porath, M.C., et al. (2012) Feature-based analysis for quality assessment of x-ray computed tomography measurements. *Measurement Science and Technology*. [Online] 23 (10), 105006. Available from: doi:10.1088/0957-0233/23/10/105006.

National Institute of Standards & Technology (2012) *Standard Reference Material 2087*. [Online]. 2012. Available from: https://www-s.nist.gov/srmors/certificates/2087.pdf?CFID=21722562&CFTOKEN=d9f1409c89ed992f-8553664C-D518-382D-C49B4DE9F49C01A2 [Accessed: 21 July 2015].

Van Nieuwenhove, V., De Beenhouwer, J., De Carlo, F., Mancini, L., et al. (2015) Dynamic intensity normalization using eigen flat fields in X-ray imaging. *Optics Express*. [Online] 23 (21), 27975. Available from: doi:10.1364/OE.23.027975.

Nikl, M. (2006) Scintillation detectors for x-rays. *Measurement Science and Technology*. [Online] 17 (4), R37–R54. Available from: doi:10.1088/0957-0233/17/4/R01.

Nikon Metrology (2013a) *CT Pro User manual*.

Nikon Metrology (2014) *High voltage microfocus CT for inspection of dense, complex parts*. [Online]. 2014. Available from: https://blog.nikonmetrology.com/high-voltage-microfocus-ct-inspection-dense-complex-parts/ [Accessed: 4 June 2018].

Nikon Metrology (2013b) *Inspect-X 3.1.12, X-Tek X-ray and CT inspection manual*.

Nikon Metrology (2015) *XT H Series Brochure*.

NIST (2018) *Getting the Inside Story on Products with Computed Tomography*. [Online].

2018. Available from: https://www.nist.gov/news-events/news/2017/02/getting-inside-story-products-computed-tomography [Accessed: 31 May 2018].

NIST (2013) *Two-Sample t-Test for Equal Means*. [Online]. 2013. Available from: https://www.itl.nist.gov/div898/handbook/eda/section3/eda353.htm [Accessed: 22 October 2018].

NIST (2004) *X-Ray Mass Attenuation Coefficients*. [Online]. 2004. Available from: https://physics.nist.gov/PhysRefData/XrayMassCoef/tab3.html [Accessed: 8 June 2018].

NSI (2018) *Castings*. [Online]. 2018. Available from: https://4nsi.com/application-studies/castings [Accessed: 16 April 2018].

NSI (2017) *X5000*. [Online]. 2017. X5000 brochure. Available from: https://4nsi.com/brochures/x5000-brochure.pdf [Accessed: 22 March 2018].

Oberg, E., Jones, F.D., Horton, H.L. & Ryffel, H.H. (2016) *Machinery's Handbook*. 30th edition. South Norwalk, Industrial Press.

Pelc, N.J. (2014) Recent and future directions in CT imaging. *Annals of Biomedical Engineering*. [Online] 42 (2), 260–268. Available from: doi:10.1007/s10439-014-0974-z.

Poludniowski, G., Landry, G., DeBlois, F., Evans, P.M., et al. (2009) SpekCalc: a program to calculate photon spectra from tungsten anode x-ray tubes. *Physics in Medicine and Biology*. [Online] 54 (19), N433–N438. Available from: doi:10.1088/0031-9155/54/19/N01.

Poludniowskia, G.G. & Evans, P.M. (2007) Calculation of x-ray spectra emerging from an x-ray tube. Part I: Electron penetration characteristics in x-ray targets. *Medical physics*. [Online] 34 (6), 2164–2174. Available from: doi:10.1118/1.2734726.

PTB, P.B. (2000) *Multi-wave Standards a Breakthrough in Form Measurement*. [Online]. 2000. Available from: https://www.ptb.de/cms/en/presseaktuelles/journals-magazines/ptb-news/ptb-news-ausgaben/archivederptb-news/news00-2/multi-wave-standards-a-breakthrough-in-form-measurement.html [Accessed: 4 April 2017].

Radon, J. (1917) Über die Bestimmung von Funktionen durch ihre Integralwerte längs gewisser Mannigfaltigkeiten. *Mathematische-Physikalische Klasse*. 69, 262–267.

Redus, R.H., Pantazis, J.A., Pantazis, T.J., Huber, A.C., et al. (2009) Characterization

of CdTe detectors for quantitative X-ray spectroscopy. *IEEE Transactions on Nuclear Science*. [Online] 56 (4), 2524–2532. Available from: doi:10.1109/TNS.2009.2024149.

Reid-Paul, T.S. (2012) *Radiologic Technology at a Glance*. 1st edition. New York, Delmar.

Schuetz, P., Jerjen, I., Hofmann, J. & Plamondon, M. (2014) Reducing the influence of environmental scattering in industrial computed tomography by system optimisation and correction algorithms. In: *11th European Conference on Non-Destructive Testing*. 2014 Prague, Czech Republic. p.

Schulze, R., Heil, U., Groß, D., Bruellmann, D.D., et al. (2011) Artefacts in CBCT: A review. *Dentomaxillofacial Radiology*. [Online] 40 (5), 265–273. Available from: doi:10.1259/dmfr/30642039.

Seco, J., Clasie, B. & Partridge, M. (2014) Review on the characteristics of radiation detectors for dosimetry and imaging. *Physics in Medicine and Biology*. [Online] 59 (20), R303–R347. Available from: doi:10.1088/0031-9155/59/20/R303.

Shi, Y., Gao, S., Song, X., Li, D., et al. (2014) The assessment of industrial CT's probing error. In: *Optical Metrology and Inspection for Industrial Applications III*. [Online]. 2014 Beijing. p. Available from: doi:10.1117/12.2071795.

Smith, S.W. (1997) The Scientist and Engineer's Guide to Digital Signal Processing. *The Scientist and Engineer's Guide to Digital Signal Processing*. [Online] 423–450. Available from: doi:10.1016/B978-0-7506-7444-7/50062-5.

Sprawls, P. (1995) *The Physical Principles of Medical Imaging*. Medical Physics Publishing Corporation.

Sun, W., Brown, S.B. & Leach, R.K. (2012) *NPL REPORT ENG 32 An overview of industrial X-ray computed tomography*.

Tan, Y., Kiekens, K., Welkenhuyzen, F., Angel, J., et al. (2014) Simulation-aided investigation of beam hardening induced errors in CT dimensional metrology. *Measurement Science and Technology*. [Online] 25 (6), 064014. Available from: doi:10.1088/0957-0233/25/6/064014.

Titarenko, V., Titarenko, S., Withers, P.J., De Carlo, F., et al. (2010) Improved tomographic reconstructions using adaptive time-dependent intensity normalization. *Journal of Synchrotron Radiation*. [Online] 17 (5), 689–699. Available

from: doi:10.1107/S0909049510024908.

Tuy, H.K. (1983) An inversion formula for cone-beam reconstruction. *Society for Industrial and Applied Mathematics*. 43 (3), 546–552.

Uren, J. & Price, B. (2010) *Surveying for Engineers*. Fifth. Basingstoke, Palgrave Macmillian.

VDI/VDE-Richtlinien (2010) *VDI 2630-1.2 Computed tomography in dimensional measurements*.

Villarraga-Gómez, H., Amirkhanov, A. & Smith, S.T. (2016) A study of uncertainties from workpiece tilt in dimensional computed tomography. In: *31st ASPE Annual Meeting*. 2016 Portland, USA. p.

Villarraga-Gómez, H., Lee, C.B. & Smith, S.T. (2018) Dimensional metrology with X-ray CT: A comparison with CMM measurements on internal features and compliant structures. *Precision Engineering*. [Online] 51, 291–307. Available from: doi:10.1016/j.precisioneng.2017.08.021.

Villarraga-Gómez, H. & Smith, S.T. (2015) Optimal Specimen Orientation in Cone-Beam X-Ray Ct Systems (for Dimensional Metrology). In: *ASPE Annual Meeting*. [Online]. 2015 Austin. p. Available from: doi:10.13140/RG.2.1.3320.7282.

Visual Computing Lab - ISTI - CNR (n.d.) *MeshLab*.

Vogeler, F., Verheecke, W., Voet, A. & Kruth, J. (2011) Positional stability of 2D X-ray images for computer tomography. In: *International Symposium on Digital Industrial Radiology and Computed Tomography*. 2011 Berlin. pp. 1–9.

Weckenmann, A. & Kramer, P. (2009) Application of computed tomography in manufacturing metrology. *Technisches Messen*. 76 (340–346).

Weckenmann, A. & Krämer, P. (2009) Assessment of measurement uncertainty caused in the preparation of measurements using computed tomography. In: *XIX IMEKO World Congress: Fundamental and Applied Metrology*. 2009 Lisbon. pp. 1888–1892.

Wenig, P. & Kasperl, S. (2006) Examination of the measurement uncertainty on dimensional measurements by X-ray computed tomography. In: *European Conference on Non-Destructive Testing*. 2006 Berlin. pp. 1–10.

Yagüe-Fabra, J.A., Ontiveros, S., Jiménez, R., Chitchian, S., et al. (2013) A 3D edge detection technique for surface extraction in computed tomography for dimensional

metrology applications. *CIRP Annals - Manufacturing Technology*. [Online] 62 (1), 531–534. Available from: doi:10.1016/j.cirp.2013.03.016.

Young, H.D. & Freedman, R.A. (2008) *Sears and Zemansky's University physics: with modern physics*. 13th edition. [Online]. Boston. London, Mass. Addison-Wesley. Available from: doi:10.1017/CBO9781107415324.004.

Yxlon (2016) *Foundries*. [Online]. 2016. Available from: https://www.yxlon.com/applications/foundries [Accessed: 16 April 2018].

Appendices

The specifications for the different XCT systems and detectors can be seen in Appendix 1. As mentioned in the thesis many graphs showed similar trends as those described. To aid the flow of the thesis they are included in in an appendix. Appendices 1, 2 and 3 contain data from Chapter 4, Appendix 6 contains data from Chapter 5. Appendix 5 contains the MATLAB code written by the user to simulate the 2D X-ray images.

The results of the survey sent to XCT users can be seen in Appendix 7.

To obtain an extra 3 months funding from the UCL VEIV doctoral centre, a technical report was written by the author. This was intended to provide recommendations to the committee working towards the international standard ISO 10360-11 and can be seen in Appendix 8.

Appendix 1: System specifications

Nikon XTH 225 M

Accuracy (µm)* MPE	9+L/50 (L in mm)
Sample size (maximum)	Diameter 250 mm Height 450 mm
Sample weight (maximum)	50 kg (maximum) 5 kg (for metrology applications)
Manipulator travel	(X) 400 mm (Y) 300 mm (Z) 730 mm R 360° continuous
Source to detector	1180.071 mm (nominal)
Detector	16 bit 4 Mpixels (2000 x 2000 pixel)
Magnification	1.6x to 150x
X-ray source	225 kV / 225 W open tube
X-ray spot	3 µm micro-focus (up to 7W)
Target material	Tungsten
Target type	Reflection
Enclosure temperature	19 to 21° C
Ambient temperature	17 to 25° C
Radiation protection (DIN 54113-2, IRR99)	< 1µSv/hr
Cabinet dimensions	2414 mm x 1275 mm x 2205 mm
System weight	4200 kg

*Applies only to single material samples with a maximum diameter of 250mm and maximum height of 250mm

NSI X5000

Geometric magnification	>3000x
Overall maximum system resolution	~500 nm
X-ray source voltage range	10 kV to 240 kV
Minimum focal spot size	~500 nm
Detector size	40 cm x 40 cm
Maximum sample weight	227 kg
Axis travel	Vertical: 121 cm Horizontal: 81 cm Tilt: +20° / -20° Rotation:360° continuous
Nominal part envelope	81 cm x 121 cm
Cabinet size	271 cm x 203 cm x 233 cm
Cabinet weight	6170 kg

Perkin Elmer XRD Detector

Detector size	41 cm x 41 cm
Resolution	200 µm pixel size
Interface	Fibre optics
Housing	Standards 8” & 16”
Electronics	0.5 pF – 8 pF
Scintillator	CsI & Al metalized carbon fibre
Version	Continuous scan 16”

Appendix 2: Complex holeplate

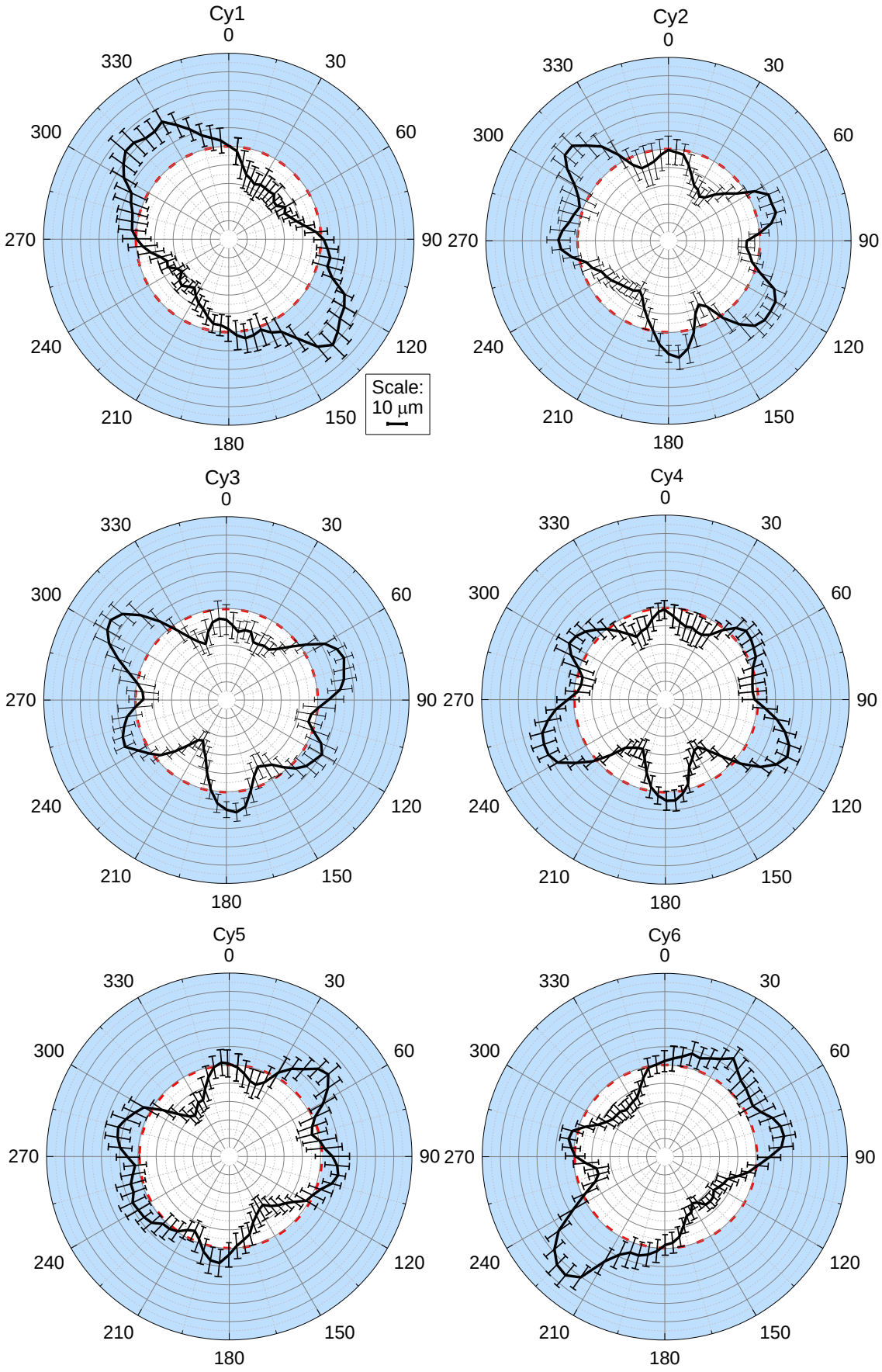

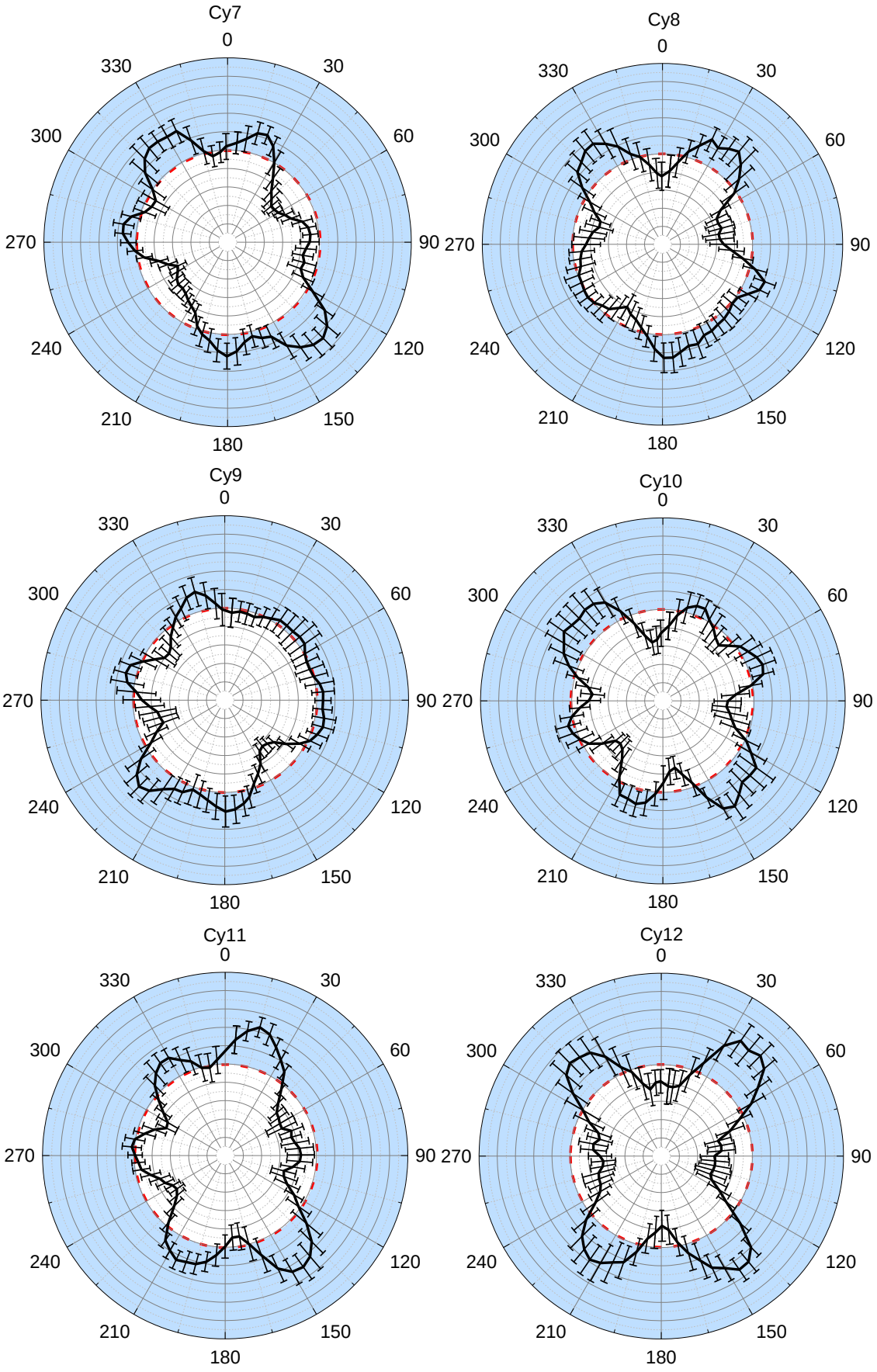
Cy7
Cy8
Cy9
Cy10
Cy11
Cy12
0
30
60
90
120
150
180
210
240
270
300
330

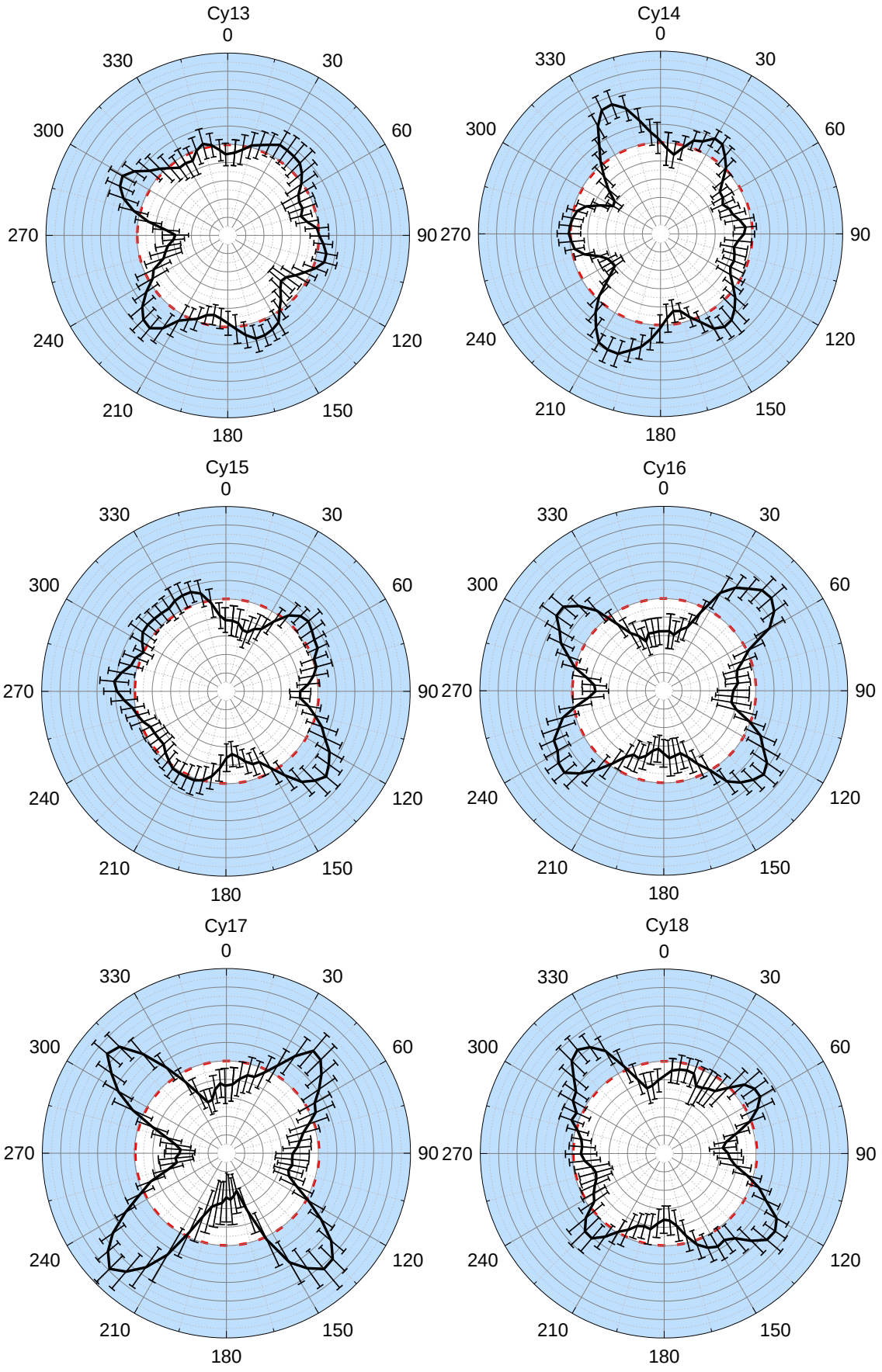
Cy13
Cy14
Cy15
Cy16
Cy17
Cy18
0
30
60
90
120
150
180
210
240
270
300
330

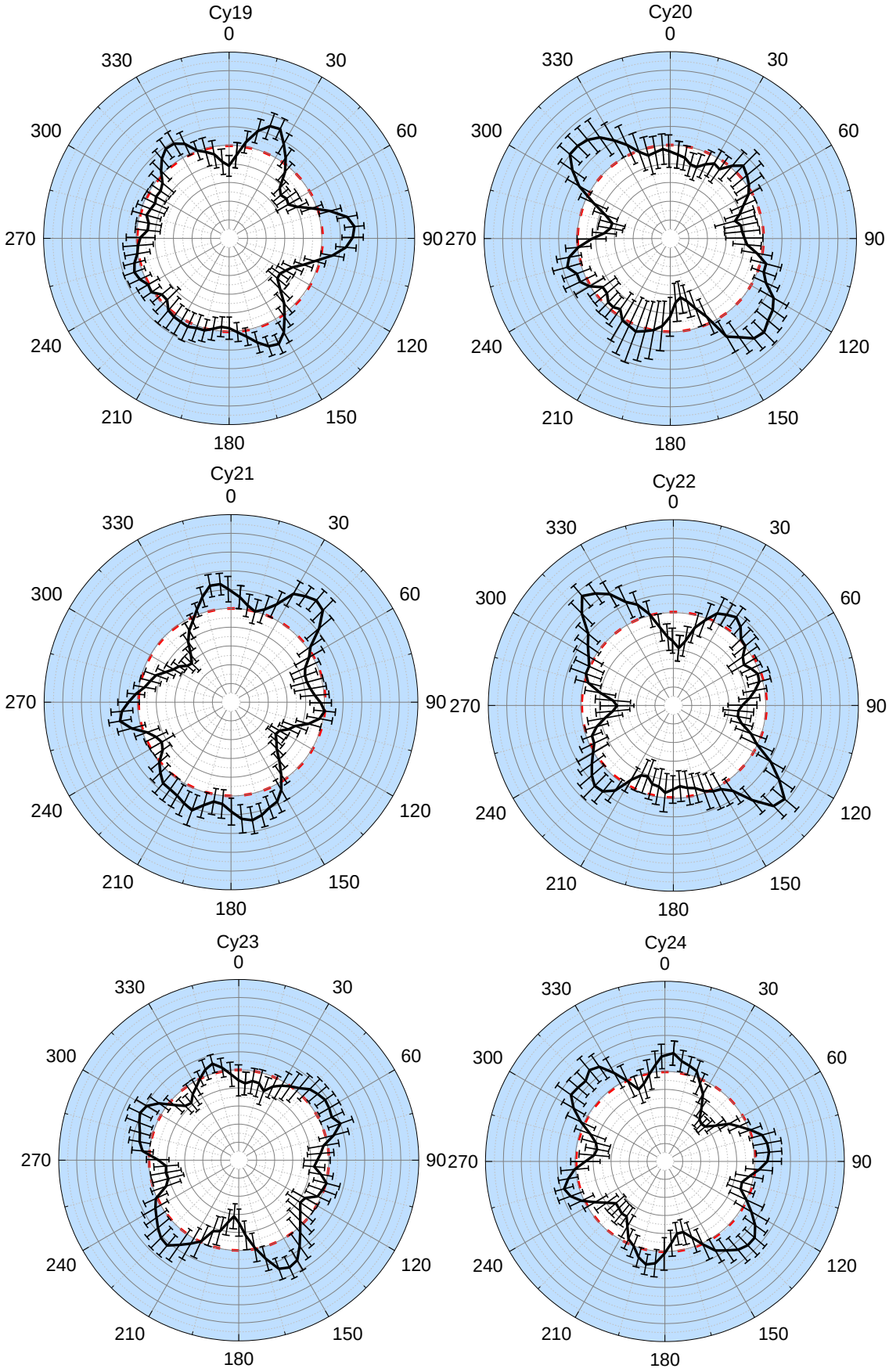
Cy19
Cy20
Cy21
Cy22
Cy23
Cy24
0
30
60
90
120
150
180
210
240
270
300
330

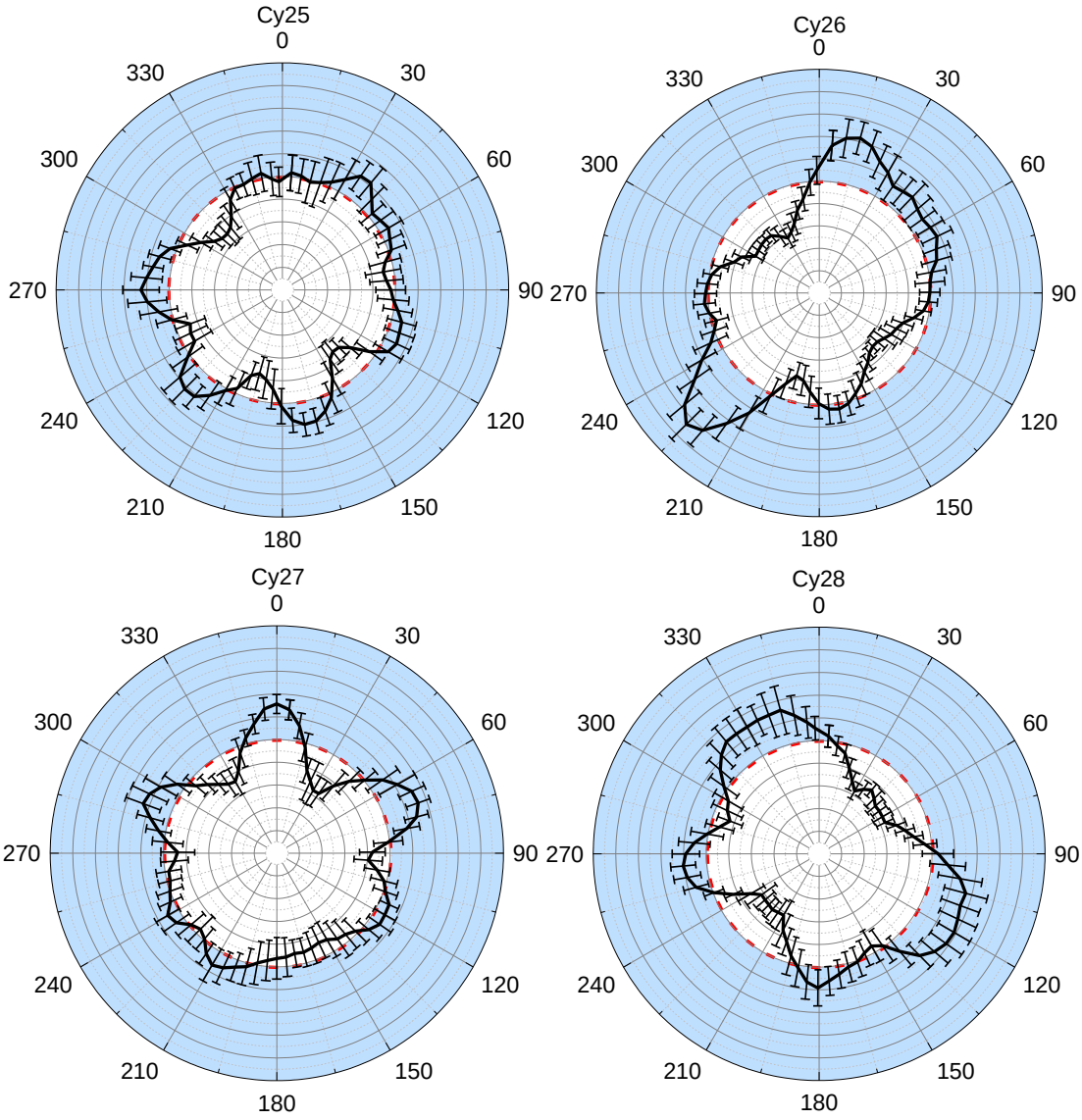
Cy25
0
30
60
90
120
150
180
210
240
270
300
330
Cy26
0
30
60
90
120
150
180
210
240
270
300
330
Cy27
0
30
60
90
120
150
180
210
240
270
300
330
Cy28
0
30
60
90
120
150
180
210
240
270
300
330

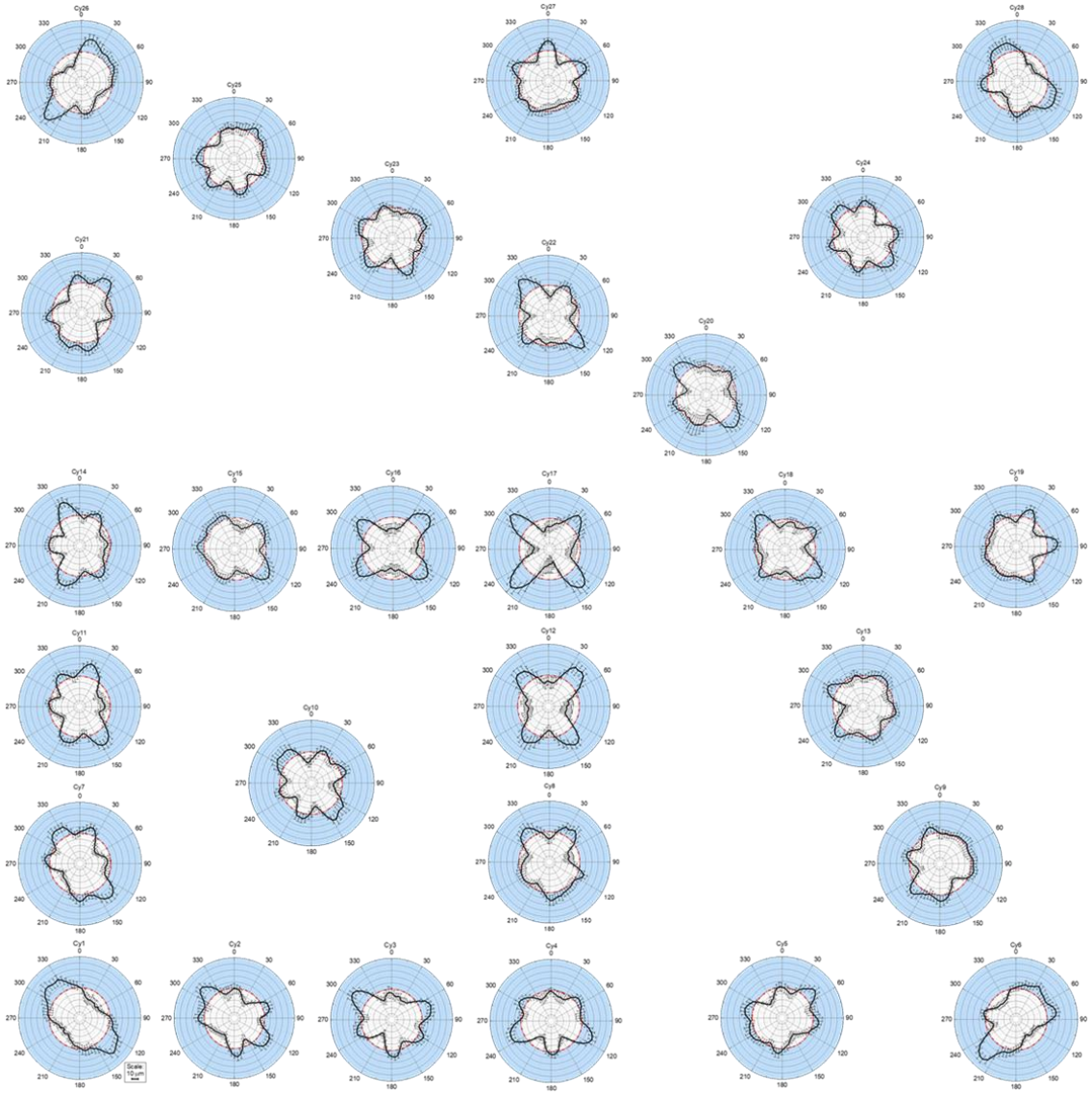
Cy26
Cy25
Cy27
Cy28
Cy23
Cy24
Cy21
Cy22
Cy20
Cy14
Cy15
Cy16
Cy17
Cy18
Cy19
Cy11
Cy12
Cy13
Cy10
Cy7
Cy8
Cy9
Cy1
Cy2
Cy3
Cy4
Cy5
Cy6
Scale
10 µm

Appendix 3: Orientation

Simple holeplates imaged at 45°

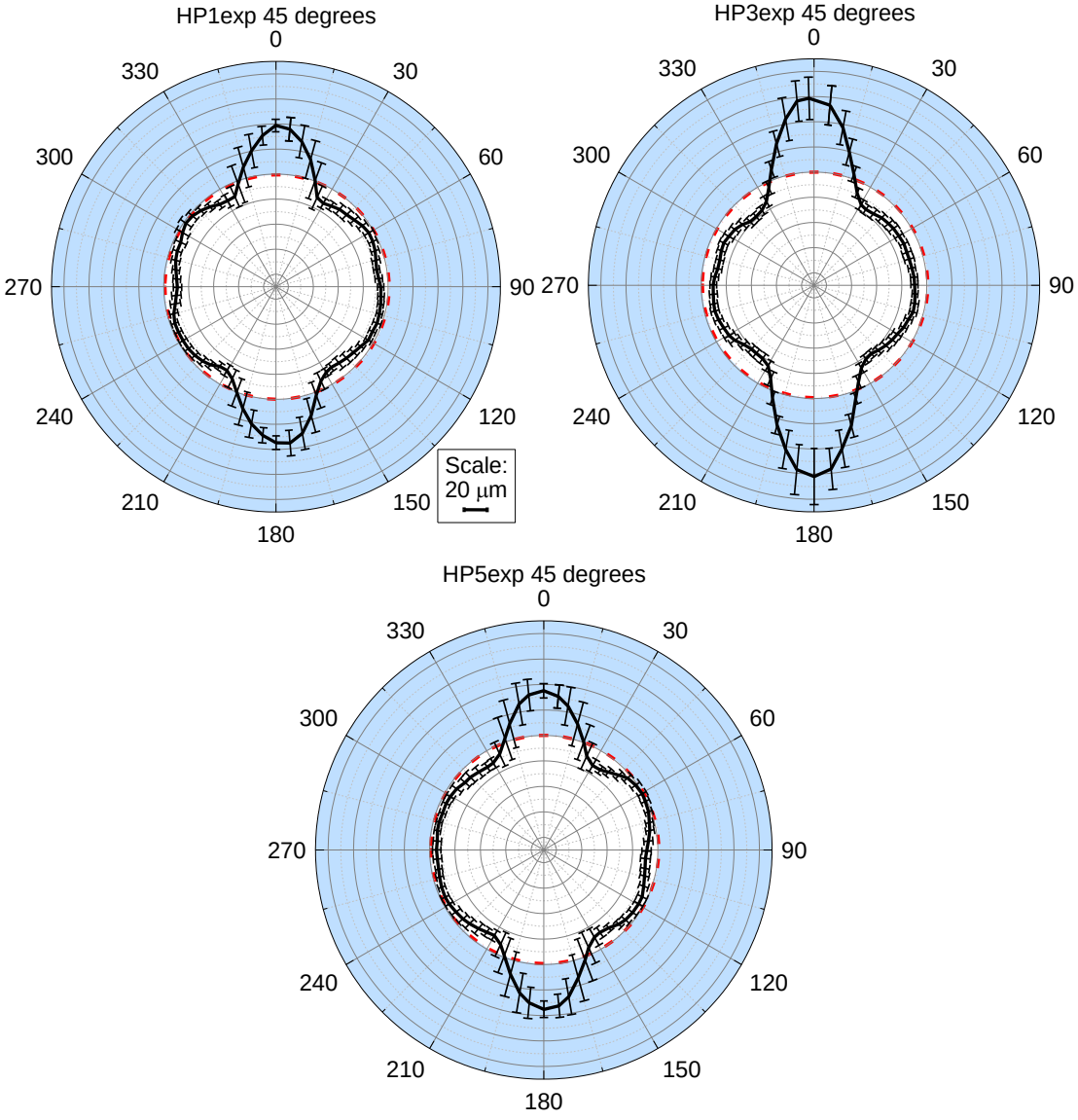

Simple holeplates imaged at 90°

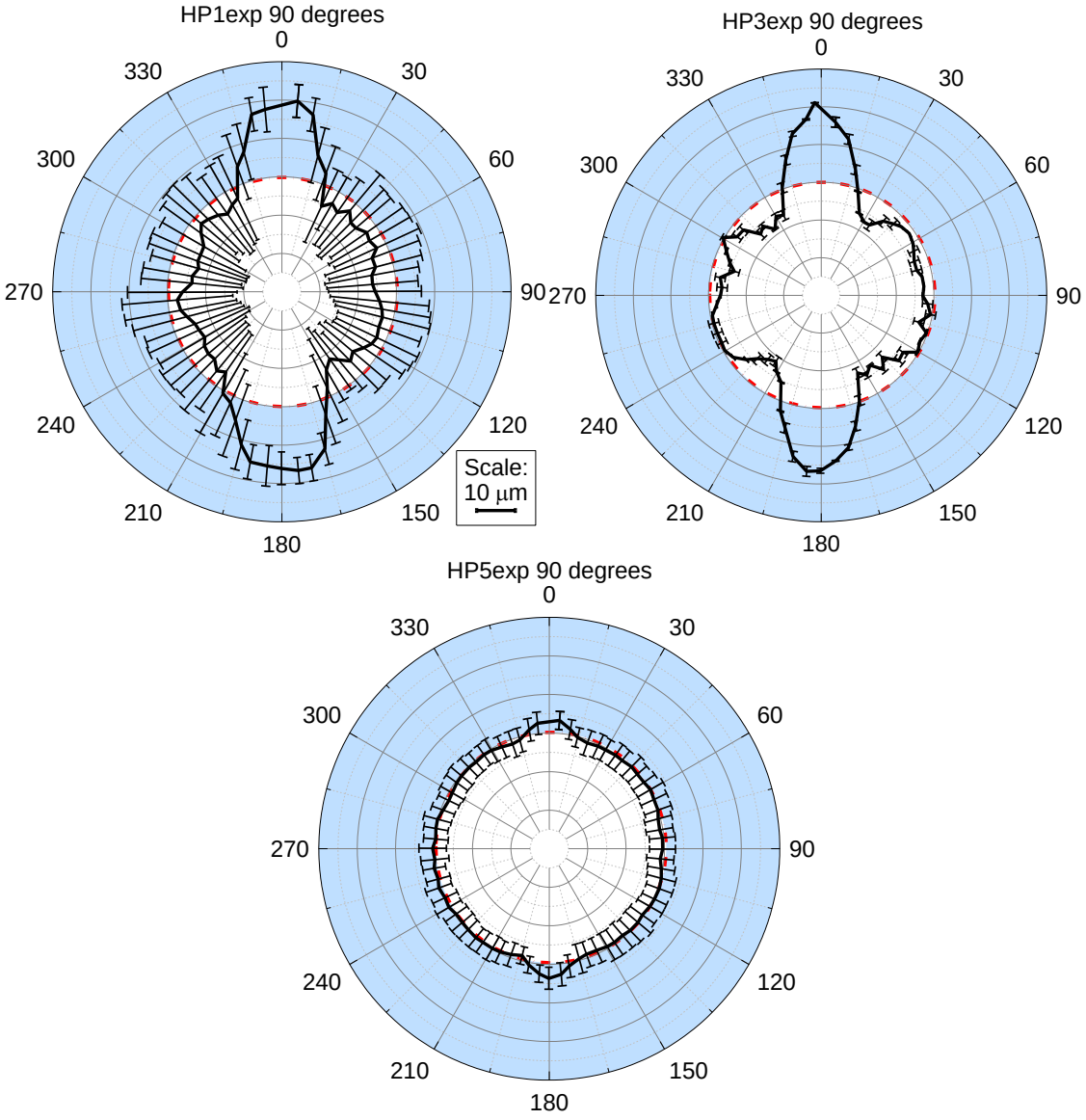

Appendix 4: Repeatability

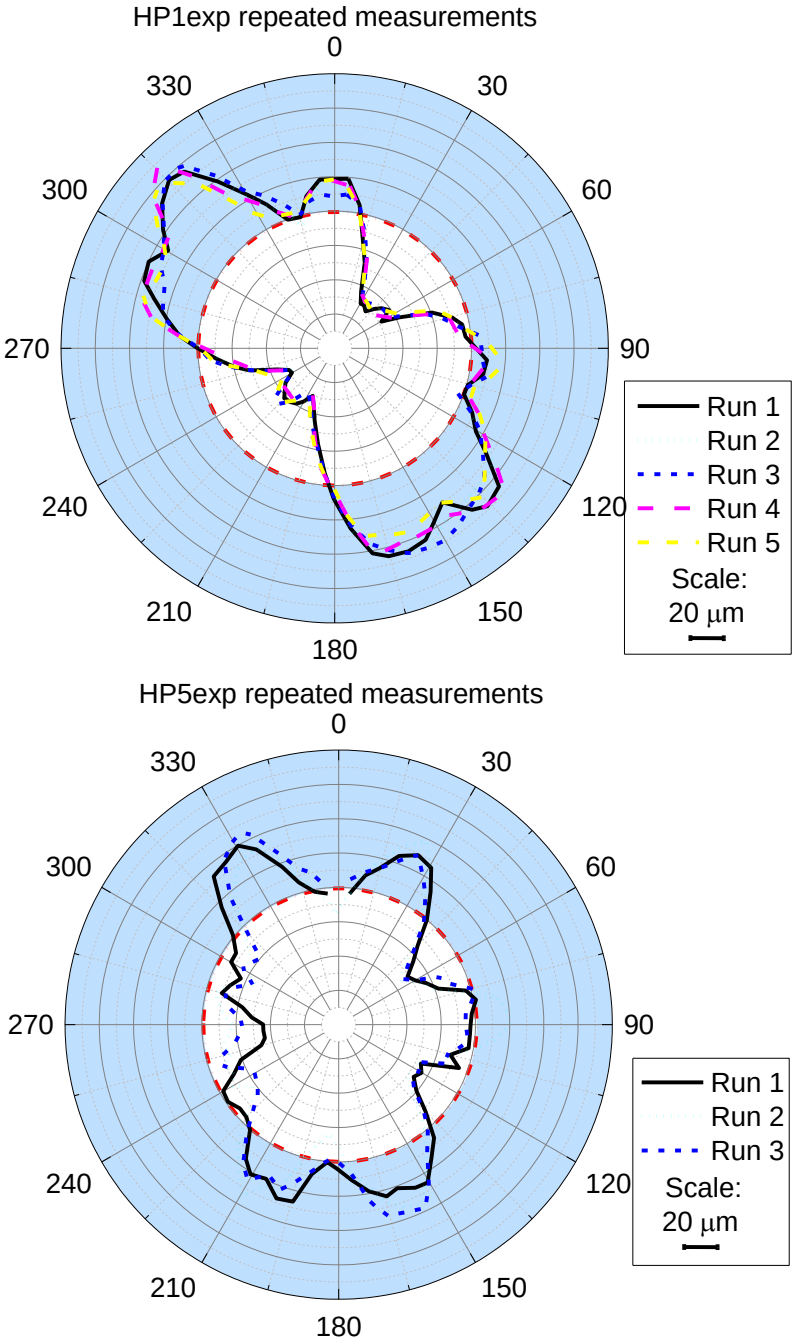

Appendix 5: MATLAB code

MATLAB code written by the author and used in Chapter 5 to simulate 2D image. A description of the code can be found in Chapter 5.

imageGenerate

```
% addpath to folders containing geom3d and geom2d libraries
addpath('/scratch/scratch/uceshcc/geom3d/meshes3d')
addpath('/scratch/scratch/uceshcc/geom2d/polygons2d')

% defining individual polygons for each side of the holeplate
topPoly = [-24 -24 4;24 -24 4;24 24 4;-24 24 4];
bottomPoly = [-24 -24 -4;24 -24 -4;24 24 -4;-24 24 -4];
frontPoly = [-24 -24 4;-24 24 4;-24 24 -4;-24 -24 -4];
backPoly=[24 -24 4;24 24 4;24 24 -4;24 -24 -4];
leftPoly= [-24 24 4;24 24 4;24 24 -4;-24 24 -4];
rightPoly=[-24 -24 4;24 -24 4;24 -24 -4;-24 -24 -4];

% Define Cylinder (centre of top and bottom)
CYLINDER = [-18 -18 -4; -18 -18 4];

mag = 1.6; % define magnification
SourceX = -1*(1180/mag); % define X coordinate for source
PixelX = SourceX + 1180; % define X coordinate for pixel

% Y and Z coordinates for pixels on detector
P2y = -199.9:0.2:199.9; % y coordinate of pixel
P2z = 199.9:-0.2:-199.9; % z coordinate of pixel

%object angle
R= 45;
Rdeg = deg2rad(R);

%rotate plate by R deg
Rx = [1,0,0;0,cos(Rdeg),sin(Rdeg);0,-sin(Rdeg),cos(Rdeg)];
RotCyl = CYLINDER*Rx;
OriTop = topPoly*Rx;
```

```
OriBottom = bottomPoly*Rx;
OriFront=frontPoly*Rx;
OriBack=backPoly*Rx;
OriLeft=leftPoly*Rx;
OriRight=rightPoly*Rx;

% Rotate vertices around the centre of the HP
Step = 359.9150653/3142; % Rotation interval
i = str2num(getenv('SGE_TASK_ID')); % task ID in Legion
% Angle HP is rotated by after each image
AngRad = deg2rad(i*Step);

% rotation matrix
Rz = [cos(AngRad), sin(AngRad), 0; -sin(AngRad), cos(AngRad), 0 ; 0, 0, 1 ]; % rotates anticlockwise (Transpose (Rz') for clockwise)
"http://mathworld.wolfram.com/RotationMatrix.html"

% coordinates for polygons and cylinder multiplied by rotation matrix
topPolyRot = OriTop*Rz;
bottomPolyRot = OriBottom*Rz;
leftPolyRot = OriLeft*Rz;
rightPolyRot = OriRight*Rz;
frontPolyRot = OriFront*Rz;
backPolyRot = OriBack*Rz;
CylRotStep = RotCyl *Rz;

% required for running on Legion
distcomp.feature('LocalUseMpiexec',false)

% Calls function downDetector. Creates 1050 x 1300 matrix of calculated intensity values. Cropped for speed.
AllPaths =
downDetector(CylRotStep,leftPolyRot,rightPolyRot,topPolyRot,bottomPolyRot,frontPolyRot,backPolyRot,P2y,P2z,SourceX,Pixelx);

% Pads matrix out to 2000 x 2000
AllPathsPad = padarray(AllPaths, [950 700],'post');
```

```
AllPathsPad(AllPathsPad==0)=62000;

%Convert to 16 bit unsigned integer
img16_2 =uint16(AllPathsPad);

% writes .tif image to designated folder
imwrite(img16_2,
['/scratch/scratch/uceshcc/Results/Final/HP1Primative/HP1_',num2str(i,'%04i'),'.tif']
,'compression','none')
```

---

downDetector

```
% Runs loop of acrossDetector for rows of pixels down detector
function [AllPaths] =
downDetector(leftPolyRot,rightPolyRot,topPolyRot,bottomPolyRot,frontPolyRot,backPo
lyRot,P2y,P2z,SourceX,Pixelx,CylRotStep)

parfor k = 950:1050
        AllPaths(k,:) =
    acrossDetector(k,leftPolyRot,rightPolyRot,topPolyRot,bottomPolyRot,frontPolyR
    ot,backPolyRot,P2y,P2z,SourceX,Pixelx,CylRotStep);
end
```

---

acrossDetector

```
function[AllPaths]=acrossDetector(k,CylRotStep,leftPolyRot,rightPolyRot,topPolyRot,bo
ttomPolyRot,frontPolyRot,backPolyRot,P2y,P2z,SourceX,Pixelx)

%Load attenuation coefficient and spectrum data

data = load('AC.mat');

AC = data.AC;

data2 = load('weightedArea.mat');
```

```
weightedArea = data2.weightedArea;

% parfor loop calculates final intensity of pixels after X-rays are attenuated by object.
Each pixel in column calculated individually in parallel

 parfor j = 700:1300

        dx = Pixelx-SourceX; % Define line

        dy = P2y(j); % Define Y coordinate of pixel

        dz = P2z(k); % Define Z coordinate of pixel

         LINE = [SourceX 0 0  dx dy dz]; % Define line along which intersection points
        % with object are found

        % Intersection points for cylinder

        CylInt = [CylRotStep(1,:) CylRotStep(2,:)  2];

        CylPOINTS = intersectLineCylinder(LINE, CylInt);


        interBack = intersectLinePolygon3d(LINE, backPolyRot);

        interBack(any(isnan(interBack)), :) = [];


        interFront = intersectLinePolygon3d(LINE, frontPolyRot);

        interFront(any(isnan(interFront)), :) = [];


        interLeft = intersectLinePolygon3d(LINE, leftPolyRot);

        interLeft(any(isnan(interLeft)), :) = [];


        interRight = intersectLinePolygon3d(LINE, rightPolyRot);

        interRight(any(isnan(interRight)), :) = [];


        interTop = intersectLinePolygon3d(LINE, topPolyRot);
```

```
interTop(any(isnan(interTop)), :) = [];


interBottom = intersectLinePolygon3d(LINE, bottomPolyRot);

interBottom(any(isnan(interBottom)), :) = [];

% Intersection points combined in one matrix (AllPoints). They are sorted,
%smallest to largest

AllPoints = [interBack; interFront; interLeft; interRight; interTop;
InterBottom;CylPOINTS];

        if isempty(AllPoints)

                AllPoints = [0 0 0];

        end

AllPoints(any(isnan(AllPoints), 2), :) = [];

intSize =size(AllPoints);

E = 14-(intSize(1,1));

[values, order] = sort(AllPoints(:,1));

sortedINTERS = AllPoints(order,:);

padInters = padarray(sortedINTERS, [E 0],'post');

% Path length calculated using intersection points

PathLength = (sqrt(((padInters(2,1)-padInters(1,1))^2)+((padInters(2,2)-
padInters(1,2))^2)+((padInters(2,3)-padInters(1,3))^2))) +(sqrt(((padInters(4,1)-
padInters(3,1))^2)+((padInters(4,2)-padInters(3,2))^2)+((padInters(4,3)-
padInters(3,3))^2))) +(sqrt(((padInters(6,1)-padInters(5,1))^2)+((padInters(6,2)-
padInters(5,2))^2)+((padInters(6,3)-padInters(5,3))^2))) +(sqrt(((padInters(8,1)-
padInters(7,1))^2)+((padInters(8,2)-padInters(7,2))^2)+((padInters(8,3)-
padInters(7,3))^2))) +(sqrt(((padInters(10,1)-
padInters(9,1))^2)+((padInters(10,2)-padInters(9,2))^2)+((padInters(10,3)-
padInters(9,3))^2))) +(sqrt(((padInters(12,1)-
padInters(11,1))^2)+((padInters(12,2)-padInters(11,2))^2)+((padInters(12,3)-
padInters(11,3))^2))) +(sqrt(((padInters(14,1)-
```

```
        padInters(13,1))^2)+((padInters(14,2)-padInters(13,2))^2)+((padInters(14,3)-
        padInters(13,3))^2)));

        % attenuation calculated using path length

        Atten=AC*(PathLength/10);

        expAtten=exp(Atten);

        WeightedAtten = expAtten.*weightedArea';

        finalInt = 62000*(sum(WeightedAtten));

        % All intensities collected in a single matrix

        AllPaths(j) = finalInt;

end
```

Appendix 6: Image intensity gradient

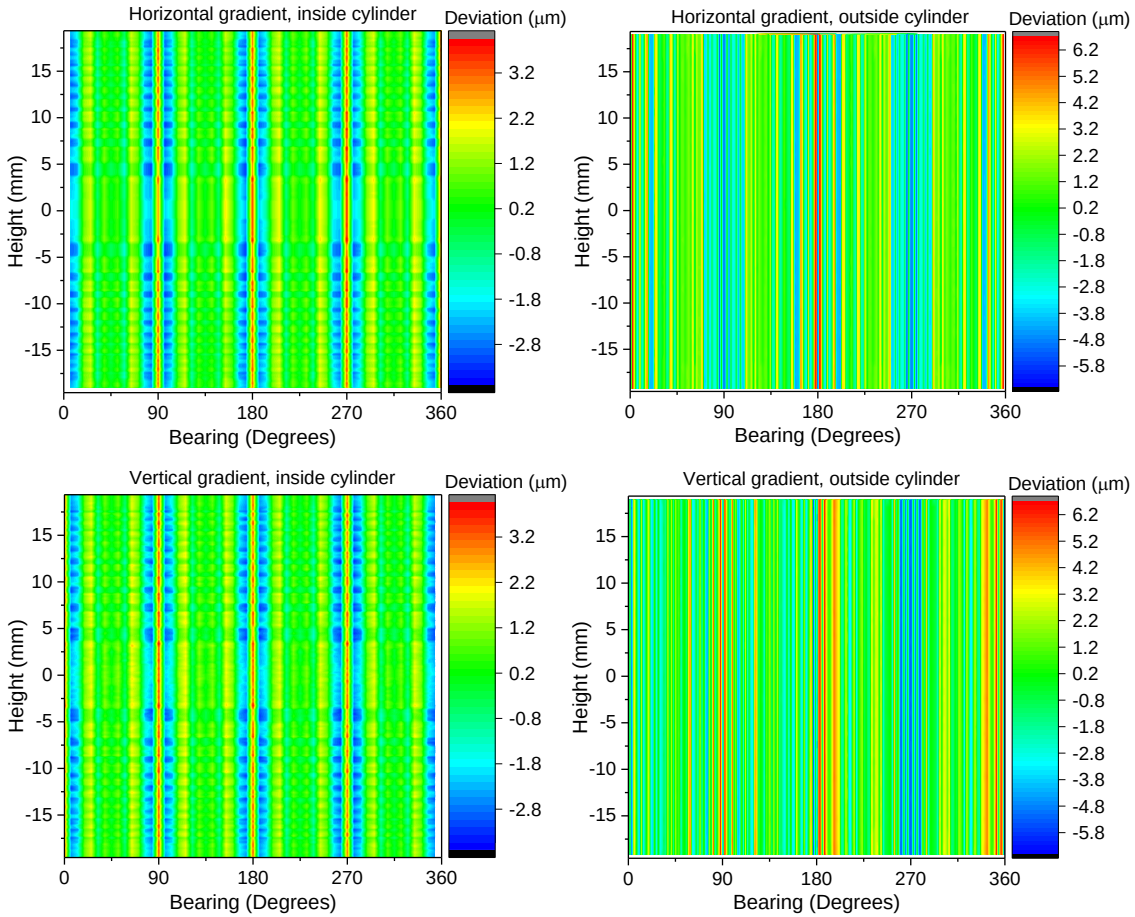

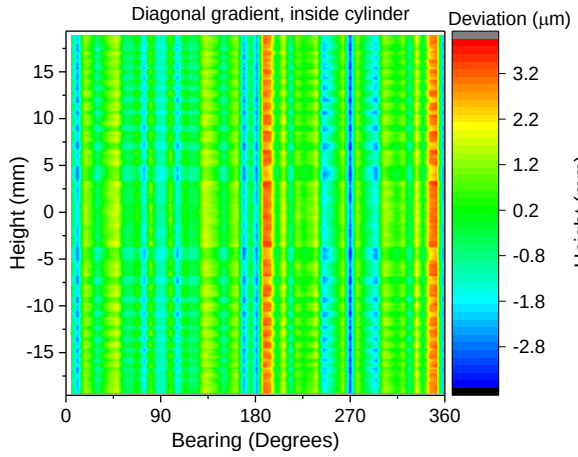
Diagonal gradient, inside cylinder
Deviation (μm)
3.2
2.2
1.2
0.2
-0.8
-1.8
-2.8
Height (mm)
15
10
5
0
-5
-10
-15
0
90
180
270
360
Bearing (Degrees)

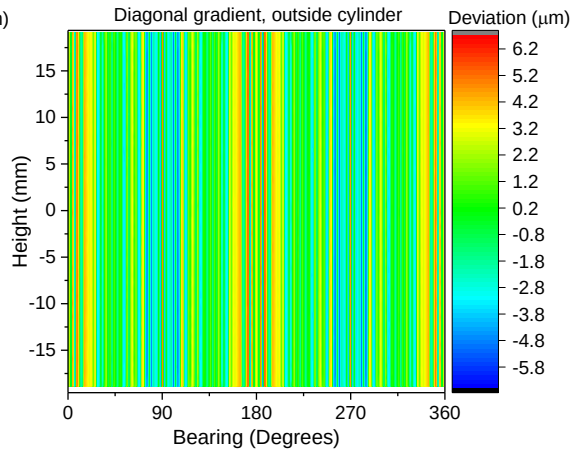
Diagonal gradient, outside cylinder
Deviation (μm)
6.2
5.2
4.2
3.2
2.2
1.2
0.2
-0.8
-1.8
-2.8
-3.8
-4.8
-5.8
Height (mm)
15
10
5
0
-5
-10
-15
0
90
180
270
360
Bearing (Degrees)

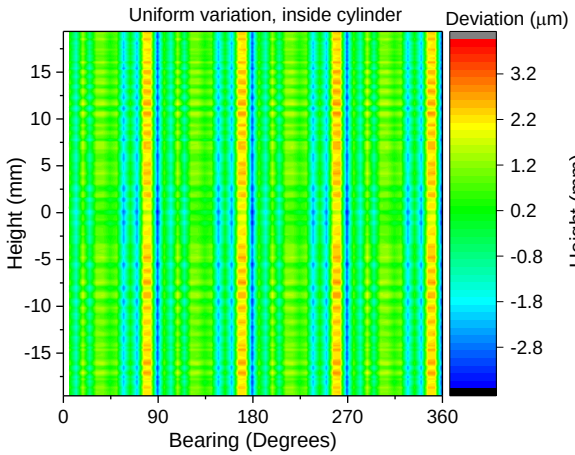
Uniform variation, inside cylinder
Deviation (μm)
3.2
2.2
1.2
0.2
-0.8
-1.8
-2.8
Height (mm)
15
10
5
0
-5
-10
-15
0
90
180
270
360
Bearing (Degrees)

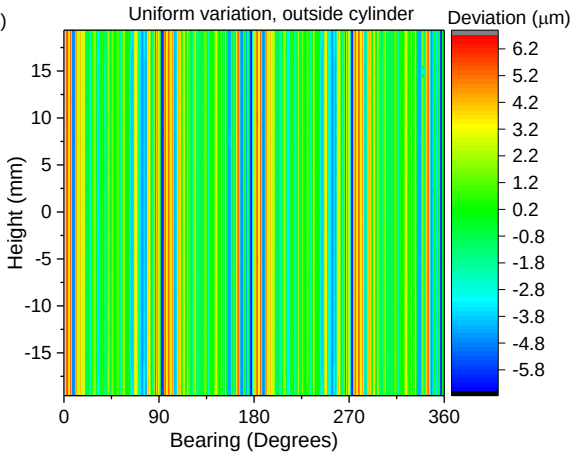
Uniform variation, outside cylinder
Deviation (μm)
6.2
5.2
4.2
3.2
2.2
1.2
0.2
-0.8
-1.8
-2.8
-3.8
-4.8
-5.8
Height (mm)
15
10
5
0
-5
-10
-15
0
90
180
270
360
Bearing (Degrees)

Appendix 7: Survey results

In which sector is your industry?	Count
Manufacturing	10
Automotive	9
Casting	5
Aerospace	8
Electronics	4
Medical	60
Dental	7
Geological science	3
Military/defence	4
Oil	3
Research	23
Other	Veterinary Watch industry
What do you use XCT for?	
Dimensional metrology	21
Defect, void and crack analysis	23
Medical diagnostics	60
Reverse engineering	10
Material composition analysis	17
Other	Visualising internal structures
What materials do you image?	
Castings – metal	19
Castings – plastic	17
Biological samples - bone	14
Biological samples – soft tissue	14
Additive manufacturing	16
Plastics	18
Geological	14
Concrete	7
Electrical components	14
Other	Foam

What systems do you use?	
GE	11
Siemens	11
Toshiba	6
Nikon	10
Zeiss	2
Philips	4
YXLON	1
Proprietary	1
Target type	
Reflective	27
Transmission	19
Target material	
Tungsten	40
Copper	4
Rhenium	4
Molybdenum	8
Maximum energy	
150 keV	25
225 keV	16
350 keV	2
450 keV	2
>450 keV	0
Detector brand	
Siemens	5
GE	4
Stellar	2
Philips	4
Aquilion	1
Perkin Elmer	6
YXLON	1
Varian	1
Hamamatsu	1
Toshiba	2

Smallest detail measured (mm)	
0.0001 – 0.001	5
0.001 – 0.01	5
0.01 – 0.1	2
0.1 – 1.0	8
1 – 10	5
How important are dimensional measurements to you?	
Very important	9
Fairly important	12
Important	3
Slightly important	4
Not at all important	0
What is your greatest limitation?	
Beam hardening	11
Noise	12
Insufficient accuracy	3
Time	10
Other	Size/resolution trade off
What are your priorities?	
Visualisation	19
Dimensional measurements	9
Qualitative comparison to CAD	5
Other	Quantitative characterisation of features

Appendix 8: ISO report

Considerations when using a holeplate as a reference object for ISO10360-11

Hannah C Corcoran[1]

[1] Civil, Environmental and Geomatic Engineering, University College London, London, United Kingdom

Introduction

Dimensional measurements were acquired from a series of holeplates for the completion of an Engineering Doctorate at University College London. The work was sponsored by the Engineering and Physical Sciences Research Council (EPSRC) and the National Physical Laboratory (NPL) who are part of the international effort to achieve traceability of dimensional results obtained using X-ray computed tomography (XCT).

The main focus of the project was to identify the cause of errors in the geometry of the holes within the holeplates. Once the source of the error is ascertained it may be possible to reduce the size of the errors to below the MPE of a given system.

The first holeplate was an aluminium, complex holeplate (CompHP) based on a design by Bartscher et al., (2014) with a size of 48 mm x 48 mm x 8 mm, contained 28 holes, all of which had a diameter of 4 mm, see Figure 1. Along with this complex holeplate, four other simple holeplates were manufactured. They had the same dimensions as the complex holeplate but only contained one hole. For three of them the hole was positioned to have the largest imbalance of material, i.e. the biggest variation in path lengths around the hole, see Figure 2. The final holeplate (CiHP) was circular and had a hole in the centre to insure a constant amount of material around the hole. The main focus of the work was the apparent deformation of holes within the holeplates along with the causes of these deformations. The shape of the deformation appears to be related to the path length of the X-rays through the material, the position of the hole within the holeplate and the orientation of the holeplate during imaging. Both experimental and numerical simulation work was carried out to study factors associated with the errors.

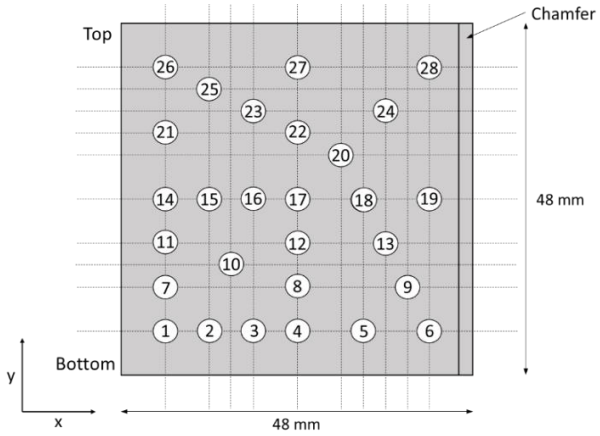

Figure 1 Schematic of complex holeplate. Numbers denote cylinder number used in report

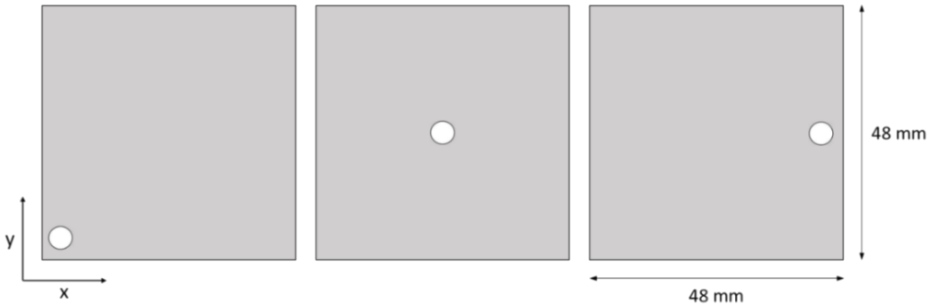

Figure 2 Simple holeplates, from left to right, HP1, HP3 and HP5

Measurements acquired

The holeplates were imaged at an orientation of 0°, 45° and 90° to horizontal and were held in place during imaging using a custom built stand to ensure stability during imaging and to guarantee the holeplates were all in the same position during imaging.

Initial measurements taken of the aluminium holeplate were unidirectional and bidirectional lengths and the radii of the holes. The holeplate was measured on a coordinate measuring machine (measurement accuracy (1.2 + L/400) µm) at NPL which provided reference lengths that could be compared to the measurements obtained using XCT. This follows similar methods that provide traceability of measurements.

Along with the length measurements, which are frequently used in the study of holeplates, the geometry of the holes was examined. This was carried out by recording the fit point data used to fit cylinders to the holes in VGStudio Max. The data comprised of the x, y and z coordinate of the point and the deviation of the fit point from the fitted cylinder. A bearing for each point around the cylinder was calculated using the coordinates and the centre of the sphere and an average deviation was taken for all the points within each 5° interval down the cylinder, see Figure 3.

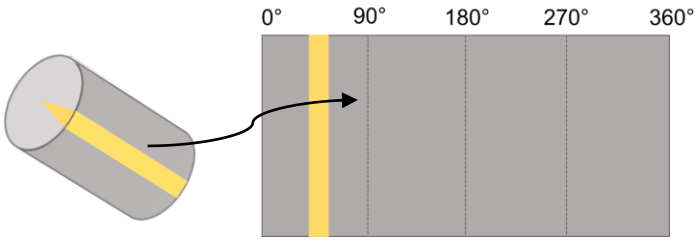

Figure 3 Schematic of area from which the mean deviation of fit points are taken

Along with the reconstruction of experimental images, 2D projections were simulated using a ray tracing method implemented in MATLAB. The holeplates were modelled using primitive shapes and the intensity of each pixel was determined by calculating the attenuation of a polychromatic X-ray for each ray path.

Results

The largest discrepancies between XCT and CMM results can be seen in the bidirectional lengths, (Figure 4). These errors, with a range of ±60 µm, are greater than the MPE of the system used to image the holeplate ((9 + L/50) µm where L is in mm). This, therefore, illustrates that the holeplate is not the ideal reference object to be used unless the causes of these errors are identified and removed.

It has been identified that the large errors in the bidirectional lengths are due to the apparent deformation in the geometry of the cylinders. Factors effecting the geometry include the orientation of the object during imaging and the position of the hole within the holeplate. These factors that affect the lengths are not ideal with respects to deploying a reference object to establish traceability in dimensional measurements.

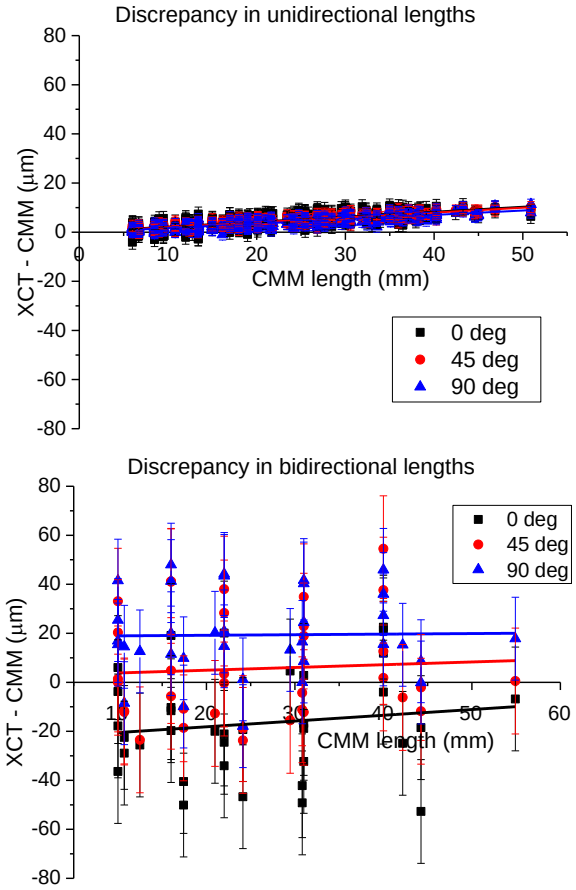

Figure 4 Unidirectional (left) and bidirectional (right) lengths. Discrepancy between XCT and CMM results. Error bars equal to standard deviation of population

Simulation and experimental work demonstrates that the largest influence on the geometry is the orientation of the holeplate during imaging. CiHP was imaged at three different orientations, 0°, 45° and 90°. Errors of up to 60 µm can be seen when the holeplate is at 45°, see Figure 5.

Another significant factor is the position of the hole within the holeplate, the geometry of three cylinders from CompHP can be seen in Figure 6 when the holeplate was imaged at 0°. The shape of the hole is different for every hole, but each hole shows systematic trends in the errors that are in the range of ±40 µm.

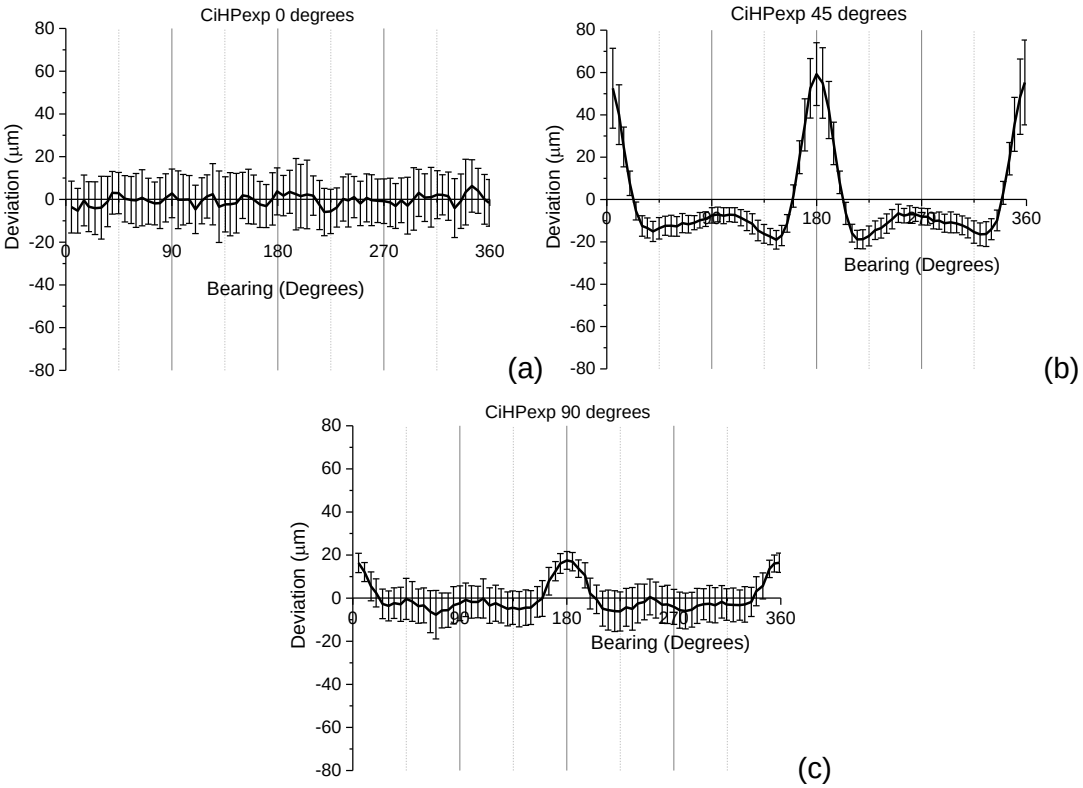

Figure 5 Deformation in cylinder geometry of CiHP depending on orientation during imaging. (a) 0°, (b) 45° and (c) 90°

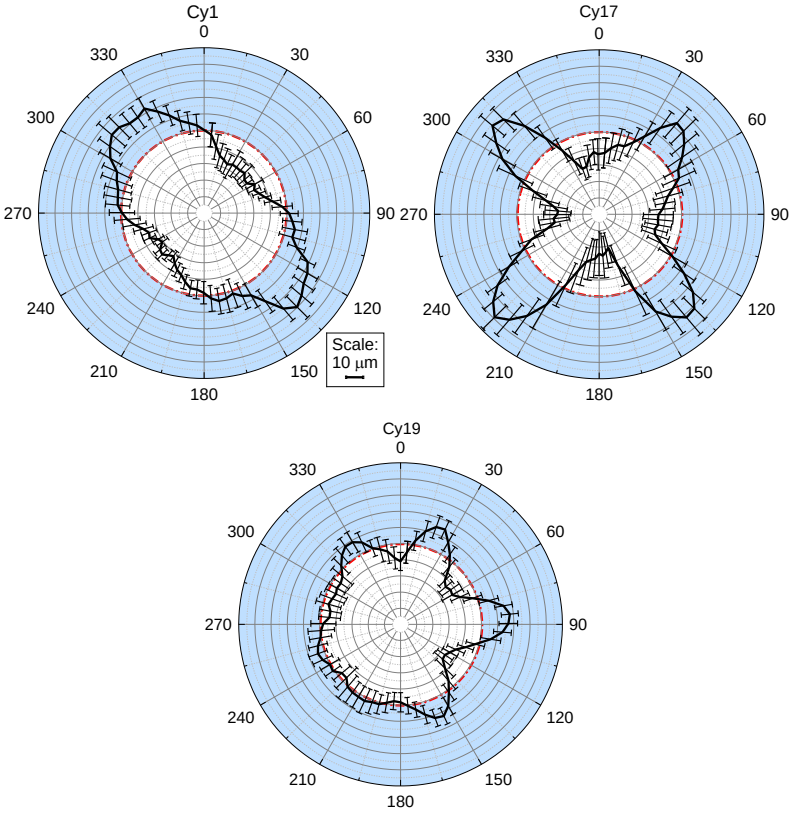

Figure 6 Fit point deviations for Cylinders 1, 17 and 19 (left to right). Error bars equal to standard deviation of points in each 5° interval. Red dashed line is equal to zero deviation

To study these effects further, three simple holeplates were imaged, as mentioned above, and the geometry of the holes can be seen below in Figure 7. Similar trends are seen for those of the corresponding holes in the complex holeplate, the deviations, however, have a smoother and simpler shape. It can be seen that the deformation has lines of symmetry that follow the lines of symmetry of the holeplate itself.

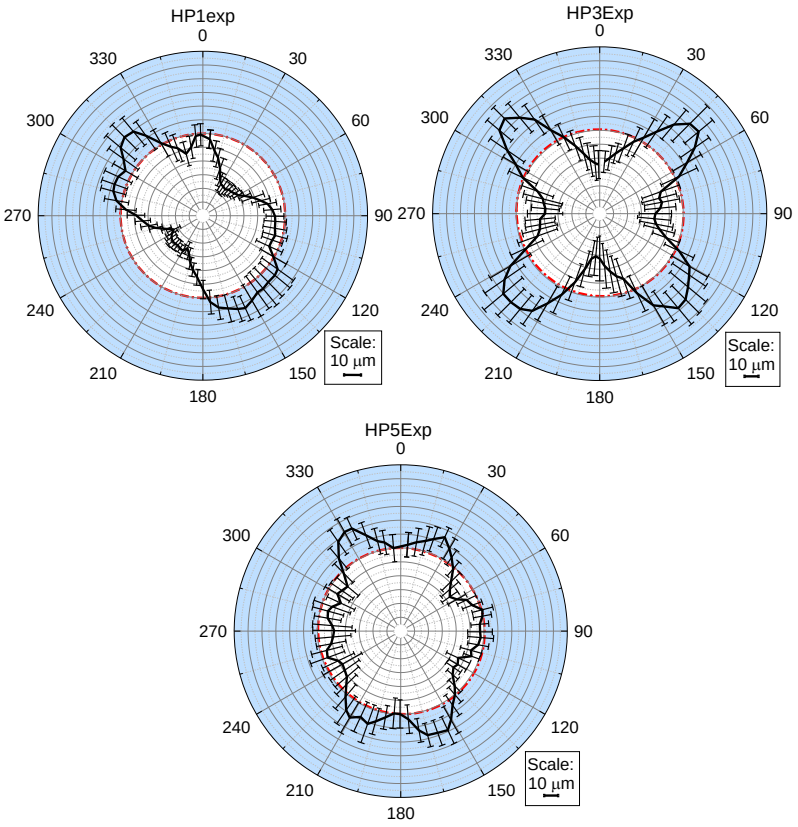

Figure 7 Fit point deviations for simple holeplates from left to right: HP1, HP3 and HP5

A comparison between CiHP and HP3, see Figure 8, highlights the influence of the path length of the X-rays through the material on the deformation in the geometry. Where the path lengths are at their longest (at 45°, 135°, 225° and 315°) the deviations are at their most positive and vice versa for the shortest path lengths. These errors appear to be related to the effective energy of the X-rays along the given path length.

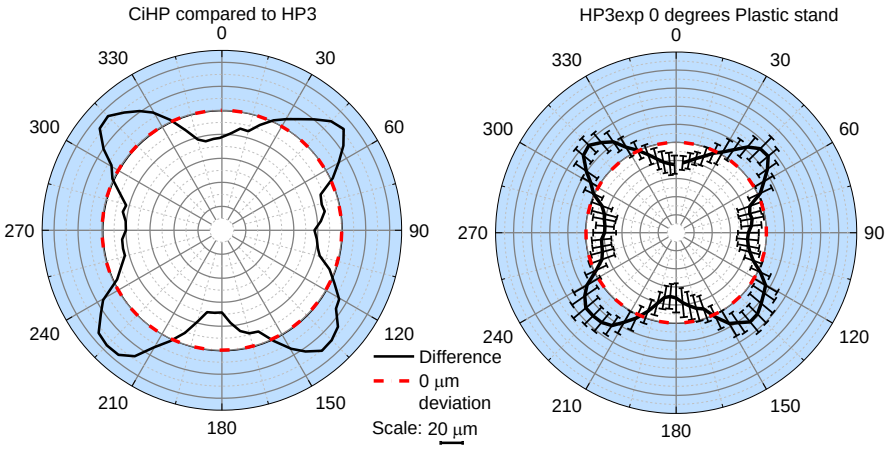

Figure 8 Difference in fit point deviations between CiHP and HP3

An important factor that was highlighted during this work was how crucial it is to keep the object stable and within the centre of rotation during imaging. Results of deviations of a holeplate imaged with and without a custom made stand highlight the increase in noise in the data when the holeplate is not fixed in position but is just resting on a stand. Standard deviations are reduced from 67 µm to 18 µm when the holeplate is fixed (Figure 9). The use of a stand ensures repeatability in position when imaging the same holeplate repeatedly or imaging multiple holeplates along with preventing any movement during imaging.

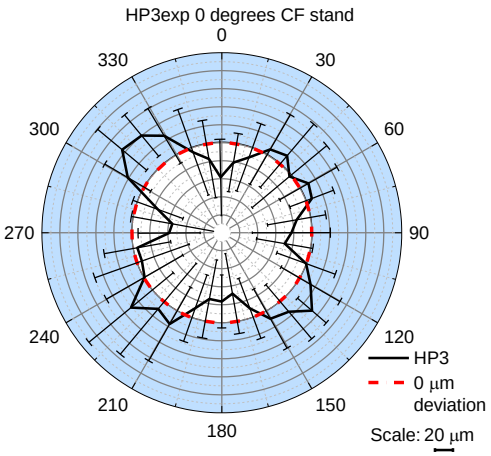

Figure 9 Deformation of HP3 with holeplate not fixed (left) and fixed (right) during imaging

Recommendations

The use of simple holeplates should be considered when trying to establish traceability of dimensional measurements using XCT. They are more easily manufactured than the complex one and are therefore cheaper. They provide a quick method to determine potential errors associated with features in objects. Although in this case the holeplates

are square, others could be designed to replicate other geometries used in industry from which the errors for that given geometry could be determined.

If an object contains features orientated at multiple angles it should be imaged at various orientations and the results averaged in an attempt to eliminate the deviations seen in the geometry.

Experiments with the simple holeplate, HP3, highlighted the importance of fixing the holeplate in the centre of the image to prevent movement as it is rotated during imaging.

The bidirectional length results seen in Figure 4 are taken for multiple points on all of the cylinders, most of which are affected by the geometry errors. Below is a table and diagram illustrating measurements that would not be affected by these deformations. There is a combination of lengths, these include the longest and shortest distance between the cylinders, see Figure 11.

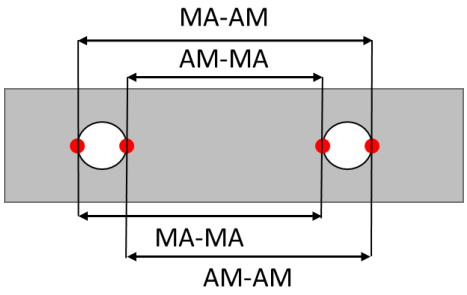

Figure 10 Different length measurements where MA means the boundary between material and air and AM means air to material

Start	End	Boundary type
1(0)	7(0)	AM-AM
1(0)	11(180)	AM-MA
1(0)	14(0)	AM-AM
1(0)	14(180)	AM-MA
1(0)	26(180)	AM-MA
1(90)	4(90)	AM-MA
1(90)	6(270)	AM-MA
1(270)	4(270)	MA-MA
1(270)	6(270)	MA-MA
2(0)	25(0)	AM-AM
2(0)	25(180)	AM-MA
6(180)	19(180)	MA-MA
13(0)	24(180)	AM-MA
14(45)	27(225)	AM-MA
14(270)	19(270)	MA-MA
26(90)	28(90)	AM-AM
26(270)	28(90)	MA-AM

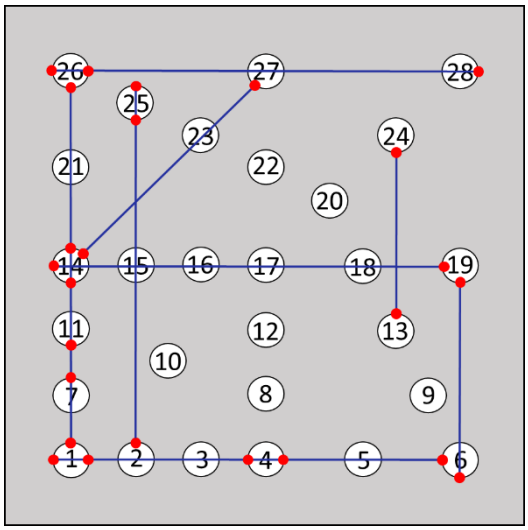

Figure 11 Suggested length measurements. Number represents hole number, number in brackets corresponds to bearing around hole with 0° at the top

References and bibliography

Bartscher, M., Sato, O., Härtig, F. & Neuschaefer-Rube, U. (2014) Current state of standardization in the field of dimensional computed tomography. Measurement Science and Technology. [Online] 25 (6), 064013. Available from: doi:10.1088/0957-0233/25/6/064013.